



HAL
open science

Electronic transport in graphene

Keyan Bennaceur

► **To cite this version:**

Keyan Bennaceur. Electronic transport in graphene. Condensed Matter [cond-mat]. Université Paris Sud - Paris XI, 2010. English. NNT: . tel-00584925

HAL Id: tel-00584925

<https://theses.hal.science/tel-00584925>

Submitted on 11 Apr 2011

HAL is a multi-disciplinary open access archive for the deposit and dissemination of scientific research documents, whether they are published or not. The documents may come from teaching and research institutions in France or abroad, or from public or private research centers.

L'archive ouverte pluridisciplinaire **HAL**, est destinée au dépôt et à la diffusion de documents scientifiques de niveau recherche, publiés ou non, émanant des établissements d'enseignement et de recherche français ou étrangers, des laboratoires publics ou privés.

Transport électronique dans le graphène

Keyan Bennaceur

Thèse de Doctorat de l'université Paris XI



Jury de thèse

Christian Glattli (directeur de thèse)

Christophe Chaubet (rapporteur)

Duncan Maude (rapporteur)

Hélène Bouchiat (examineur)

Francis Williams (examineur)

Mark-Olivier Göerbig (examineur)

Remerciements

Durant ces 3 années de Doctorat j’aurai beaucoup appris. Bien sûr, cela m’a permis d’aller beaucoup plus loin en physique. Cette thèse aura aussi été une leçon de vie, ces trois ans qui m’ont été donnés pour réaliser un projet de recherche ont été plus qu’instructionnels. Tant sur le point de vue humain que professionnel, ce projet m’a donné l’occasion d’interagir avec beaucoup de monde, chercheurs, techniciens, ingénieurs... Cela a été très riche et j’aimerais les remercier ici pour l’aide et le soutien qu’ils ont pu m’apporter.

Tout d’abord merci à mon directeur de thèse Christian Glattli. Tu m’as permis de vivre cette riche expérience en m’accueillant au sein de l’équipe Nanoélectronique. Discuter de physique avec toi a toujours été très riche et un grand plaisir pour moi, tu mets en mots simple des concepts compliqués. Puis, malgré toutes les responsabilités que tu as, tu as toujours été concerné par les problèmes que j’ai pu rencontrer.

Patrice Jacques, je te remercie pour ton aide précieuse et ta disponibilité, tes doigts de fée ont permis de résoudre bien des difficultés techniques, et m’ont beaucoup aidé à avancer dans mon travail de recherche, j’ai aussi beaucoup apprécié ta disponibilité qui pouvait te mener à remplir le cryostat d’hélium pendant les vacances, ce qui était indispensable pour que les expériences continuent à tourner. Claudine Chaleil, je te remercie chaleureusement pour l’aide que tu m’as apporté en microfabrication, les heures que tu as passées en salle blanche pour m’aider et la disponibilité que tu as eue.

Fabien Portier et Patrice Roche, membres du groupe nanoélectronique, je vous remercie pour votre accueil au sein du groupe nanoélectronique, pour les bons moments passés ensemble, comme les déjeuners et les joggings le midi, les discussions physiques intéressantes, et pour tous les petits services rendu comme ta voiture Fabien, tes programmes Patrice ou les perles de mon oral de thèse.

Tito Williams, je te remercie pour ta présence et les riches discussions que l’on a eu durant ces trois années, merci également de m’avoir invité à donner un séminaire en Hongrie, et surtout un grand merci pour tes nombreuses relectures de mon manuscrit sur laquelle tu as dû t’arracher plus d’un cheveu avec mon anglais.

Merci Denis Vion pour ta précieuse aide en nanofabrication, pour tous tes conseils et la formation aux outils qui m’étaient indispensables pour réaliser des microcircuits, tu ne comptais pas le temps et tu as toujours été très concerné par les problèmes que je pouvais rencontrer, ce qui a toujours rendu agréable le fait

de venir te demander conseil. Je remercie aussi le reste du groupe Quantronique Hugues Potier, Patrice Bertet, Philippe Joyez, Cristian Urbina Marcelo Goffman et Daniel Estève, pour les riches discussions que ce soit sur la physique, mais aussi la musique, la gastronomie, l'Amérique du sud. . .

Patrick Paris, Philippe Forget, Matthieu de Combarieu, merci d'avoir toujours été dans les parages pendant ma thèse, j'ai un grand sourire en me rappelant toute nos discussions photos ! Merci aussi pour vos conseils et votre aide précieuse en cryogénie.

Jean Noel Fuchs et Mark Goerbig, je vous dois un grand merci pour votre cours sur le graphène qui était particulièrement clair et qui a inspiré la première partie de ce manuscrit ainsi que pour le temps que vous avez pris à répondre à toutes mes questions.

Hélène Bouchiat, Miguel Monteverde, et toute l'équipe de physique mésoscopique du LPS, merci pour notre collaboration et tous les riches échanges que j'ai pu avoir avec vous.

Roland Tourbot, Pierre-Francois Orfila merci à vous pour votre aide précieuse pendant laquelle vous ne comptiez pas votre temps sur les nombreux instruments du SPEC.

Vincent Padilla, Jean-Claude Tack, Jacques Proudowski, votre travail de précision au sein de l'atelier a bien contribué à la fabrication d'un réfrigérateur adapté au graphène et je vous en remercie.

Eric Vincent, responsable du SPEC, Sandrine Thunin, Nathalie Royer, Murielle Zyla, secrétaires, merci pour votre accueil au SPEC, votre travail et votre disponibilité qui font du SPEC un laboratoire accueillant et efficace.

Je voudrais remercier l'équipe de thésards et post-doctorants. J'ai passé des moments très agréables avec vous, je garde en tête ces grands pique-niques, ces longues discussions autour d'un thé, ces pots à la sortie du RER B et bien d'autres souvenirs, merci à vous Julie Dubois, Geneviève Fleury, Geremie Guignard, Phuong-anh Huynh, Quentin Le Masne, Gabriel Lemarié, François Nguyen, Florian Ong, Agustín Palacios-Laloy, Ivana Petkovic, Jean Damien Pillet, Predene Roulleau, Eva Zakka-Bajjani.

Merci également aux stagiaires qui sont venus travailler avec moi , Nadège Kaina, Julien Boët, Thibault Brezillon et un clin d'œil spécial à Andrey Mostovov qui est maintenant en thèse et prend la suite de mon travail sur le graphène.

Michaela Hénocque-Smart et Claire Bollerot merci beaucoup pour vos relectures de mon manuscrit avec un regard extérieur très affuté.

Bien sûr merci à mes amis, vous avez permis d'adoucir les moments difficiles et donné de la joie. Ici je ne peux pas être exhaustif, certains sont déjà cités plus haut j'aimerais quand même citer quelques personnes, Delphine merci pour les beaux moments que l'on a passé. Rafael tu as supporté mon bazar dans notre collocation et c'était un grand plaisir d'habiter avec toi. De rédiger avec toi ainsi qu'avec Pauline aura permis d'adoucir ce moment. Claudia, au cours de cette thèse nous avons été colocataires et collaborateurs et ça a été très agréable. Mathilde, Céline, Elsa, merci pour tous les bons dîners que l'on a pris ensemble et le soutien psychologique tournant pour nos thèses ou recherches d'emplois.

Mathieu et Dorian merci pour les projets sur l'écologie que vous avez initié et qui m'ont beaucoup " nourri " durant cette thèse.

Ma famille aussi aura été très importante. Sofiane, mon frère, merci de ta présence très agréable et souvent réconfortante. Mes oncle et tantes que je ne cite pas tous ici, merci pour m'avoir à maintes reprises accueilli chez vous et partagé ces bons moments.

Papa et Maman c'est à vous que je dois le plus grand merci car sans vous je n'en serais jamais arrivé là, merci pour votre soutien sans faille dans mes études, merci pour votre amour.

Et, j'aimerais ici avoir une petite pensée pour toi ma grand-mère qui était très fière de son petit-fils quand il entré en thèse mais ne l'aura pas vu la finir.

Amma, merci de m'avoir donné un exemple très inspirant et qui m'a permis de surmonter bien des difficultés.

Contents

| | | |
|----------|---|-----------|
| I | The physics of graphene | 17 |
| 1 | Electronic structure of graphene | 18 |
| 1.1 | Introduction | 18 |
| 1.2 | Graphene atomic structure | 20 |
| 1.3 | Electronic properties | 21 |
| 1.3.1 | Introduction to bandstructure calculation | 22 |
| 1.3.1.1 | Bravais lattice | 22 |
| 1.3.1.2 | Bloch's theorem | 22 |
| 1.3.1.3 | Tight binding approximation | 22 |
| 1.3.2 | Bandstructure | 23 |
| 1.3.2.1 | Honeycomb lattice | 23 |
| 1.3.2.2 | Nearest neighbor hopping | 25 |
| 1.3.2.3 | Low energy linearization | 27 |
| 1.3.2.4 | Energy scale and limit of the linearization approximation | 31 |
| 1.3.3 | The Dirac equation and some of its special properties | 32 |
| 1.3.3.1 | Dirac's Equation | 33 |
| 1.3.3.2 | Valley, band and chirality | 37 |
| 1.3.3.3 | Berry's phase | 38 |
| 1.3.3.4 | Klein Tunneling | 39 |
| 1.4 | Bilayer graphene | 43 |
| 2 | Electronic Transport | 47 |
| 2.1 | Mesoscopic physics | 47 |
| 2.2 | Two-dimensional electron gases | 48 |
| 2.3 | Lengthscales | 49 |
| 2.4 | Transport, from macro to micro via meso | 50 |
| 2.4.1 | Drude model | 50 |
| 2.4.1.1 | Collision time τ | 51 |
| 2.4.2 | Coherent diffusive transport | 52 |
| 2.4.3 | Weak localization | 53 |
| 2.4.4 | Universal conductance fluctuations (UCF) | 55 |
| 2.4.5 | Einstein-Smoluchowski's diffusion approach | 56 |
| 2.4.6 | Landauer's description of quantum transport | 56 |

| | | |
|----------|---|-----------|
| 2.5 | Transport in graphene | 57 |
| 2.5.1 | Magnitudes | 58 |
| 2.5.2 | Incoherent diffusive transport | 59 |
| 2.5.3 | Scattering processes | 60 |
| 2.5.3.1 | Resonant impurities | 60 |
| 2.5.3.2 | Charged impurities | 62 |
| 2.5.4 | Experimental transport results | 63 |
| 2.5.5 | Adsorption on Graphene | 64 |
| 2.5.6 | Approaching the Dirac point | 66 |
| 2.5.7 | Quality of the graphene as a function of the substrate. . . | 67 |
| 3 | Quantum Hall effect | 68 |
| 3.1 | Motion of an electron in a magnetic field | 69 |
| 3.2 | Classical Hall effect | 72 |
| 3.3 | The Landau quantization | 73 |
| 3.3.1 | Bohr's semi-classical quantization | 73 |
| 3.3.2 | Quantum mechanical computation | 74 |
| 3.3.3 | Eigenfunctions in the Landau gauge | 77 |
| 3.4 | Zeeman splitting | 78 |
| 3.5 | Landau Levels in graphene | 79 |
| 3.5.1 | Monolayer graphene | 79 |
| 3.5.2 | Bilayer Graphene | 81 |
| 3.6 | Landau levels comparison | 82 |
| 3.7 | Shubnikov-De Haas (SDH) oscillations, a first observation of Landau quantization | 83 |
| 3.8 | Transport in the regime of Integer Quantum Hall effect | 85 |
| 3.8.1 | Hall bar geometry | 85 |
| 3.8.1.1 | Four probe measurement | 85 |
| 3.8.1.2 | Hall bar, a 6 probe geometry to measure separately Hall and longitudinal resistance | 85 |
| 3.8.2 | Landau level in presence of an external edge confinement potential | 86 |
| 3.8.3 | Edge states | 89 |
| 3.8.4 | Buttiker equation for transport | 90 |
| 3.8.5 | Quantum Hall transport in graphene | 91 |
| 3.8.5.1 | Monolayer | 91 |
| 3.8.5.2 | Bilayer | 94 |
| 3.8.6 | Corbino geometry | 94 |
| 3.8.7 | Compressibility | 96 |
| 3.8.8 | Disorder and localization | 97 |
| 3.8.9 | Broadening of the Landau levels | 99 |
| 3.9 | Metal insulator transition | 99 |
| 3.9.1 | Localization length | 99 |
| 3.10 | Finite energy Quantum Hall effect | 101 |
| 3.10.1 | Thermal activation | 102 |
| 3.10.2 | Transport through localized states. | 104 |

| | | |
|------------------------|---|------------|
| 3.10.2.1 | Variable Range Hopping (VRH) | 104 |
| 3.10.2.2 | Variable range hopping and quantum hall effect | 106 |
| 3.10.3 | Breakdown of the QHE | 108 |
| 3.10.4 | Hall Field distribution | 110 |
| 3.10.5 | Width of the ρ_{xx} peak | 111 |
| 3.10.5.1 | Pruisken theory, Anderson Transition | 111 |
| 3.10.5.2 | VRH | 113 |
| 3.10.5.3 | To summarize: | 114 |
| 3.11 | Metrology | 115 |
| II Experimental | | 117 |
| 4 | Graphene Fabrication | 118 |
| 4.1 | Obtaining graphene | 118 |
| 4.1.1 | Epitaxy | 118 |
| 4.1.1.1 | Epitaxy on SiC | 118 |
| 4.1.1.2 | Epitaxy on Ruthenium | 119 |
| 4.1.2 | Liquid phase exfoliation | 119 |
| 4.1.3 | Chemical Vapor Deposition (CVD) | 119 |
| 4.1.4 | Exfoliation | 119 |
| 4.1.4.1 | Preparation of the substrate. | 119 |
| 4.1.4.2 | Graphite exfoliation | 120 |
| 4.1.5 | Deposition | 121 |
| 4.1.6 | Removing the tape | 122 |
| 4.2 | Location of the graphene | 122 |
| 4.2.1 | Optical microscope and CCD imagery | 124 |
| 4.3 | Lithography | 125 |
| 4.3.1 | UV lithography | 125 |
| 4.3.2 | E-beam Lithography | 126 |
| 4.4 | Metal deposition: Physical vapor deposition | 127 |
| 4.4.1 | E-beam Vapor deposition (EBPVD) | 127 |
| 4.4.2 | Joule evaporator (JPVD) | 127 |
| 4.5 | plasma etching | 127 |
| 4.6 | Device Fabrication | 128 |
| 4.7 | Corbino | 130 |
| 4.7.1 | Metallic air bridges | 130 |
| 4.8 | Suspended Sample | 132 |
| 4.9 | Contacting the sample | 133 |
| 4.10 | Cause of death during the fabrication | 134 |
| 5 | Phonons and Raman spectroscopy in Graphene | 136 |
| 5.0.1 | Different phonon modes in graphene | 136 |
| 5.1 | Raman Spectroscopy, a way to ensure that we have monolayers | 138 |
| 5.1.1 | Raman principle | 140 |
| 5.1.2 | Raman spectroscopy of graphene | 141 |

| | | |
|----------|---|------------|
| 5.1.3 | Measurement of Raman on graphene | 143 |
| 6 | Setup and basic electronic Measurements | 147 |
| 6.1 | Cleaning the graphene | 148 |
| 6.1.1 | Annealing the sample in Situ: | 148 |
| 6.1.2 | Current annealing: | 148 |
| 6.1.3 | AR/H ₂ Heating | 150 |
| 6.2 | Doping graphene using gates | 151 |
| 6.2.1 | Back gate | 151 |
| 6.2.2 | The side Gate | 152 |
| 6.3 | Transport measurement | 153 |
| 6.3.1 | Devices | 153 |
| 6.3.2 | Conductance and mobility | 156 |
| 6.3.2.1 | Monolayers | 156 |
| 6.3.2.2 | Bilayer | 158 |
| 6.3.3 | Universal Conductance Fluctuations | 160 |
| 6.4 | Quantum Hall measurements | 161 |
| 6.4.0.1 | 3-point measurements | 161 |
| 6.4.0.2 | Measurements on other samples. | 163 |
| 6.4.1 | The effect of the contacts | 165 |
| 6.5 | Corbino measurements on a bilayer | 166 |
| 7 | Measurement of the transport and elastic scattering time | 168 |
| 8 | Mechanism of the disappearance of the QHE at finite energy | 174 |
| 8.1 | Transport measurement procedure and overview of the transport data. | 175 |
| 8.1.1 | Temperature measurements | 175 |
| 8.1.2 | Bias Current measurements | 178 |
| 8.1.3 | Analysis of the data | 180 |
| 8.2 | High energy transport: thermal Activation energy | 183 |
| 8.3 | Breakdown of QHE at high bias current? | 188 |
| 8.4 | Low energy transport, Mott or Efros-Shklovskii variable range hopping? | 190 |
| 8.4.1 | Variable range hopping with temperature | 190 |
| 8.4.1.1 | VRH observation under large bias currents | 194 |
| 8.5 | Universal laws in QHE | 199 |
| 8.5.1 | Universal localization length scaling exponents | 200 |
| 8.6 | Transition between Hall plateaus: Evidence for a Universal Regime driven by VRH | 202 |
| 8.7 | Conclusion | 205 |
| 9 | Conclusion | 206 |
| 9.1 | Conclusion | 206 |

| | | |
|------------|---|------------|
| III | Appendix | 208 |
| 10 | Variable temperature insert | 209 |
| 10.1 | Remarks on thermal exchanges in a solid | 209 |
| 10.1.1 | Phonons | 210 |
| 10.1.2 | Electrons | 211 |
| 10.2 | The cryostat | 211 |
| 10.3 | The insert assembly | 212 |
| 10.3.1 | Bonding techniques | 213 |
| 10.3.2 | The body | 213 |
| 10.3.3 | Connection head tulip | 214 |
| 10.3.4 | 1K Pot | 214 |
| 10.3.5 | thermalization of measurement wires | 215 |
| 10.3.6 | The sample Holder | 217 |
| 10.3.7 | Thermometer | 217 |
| 11 | Additional measurements | 218 |

Preface

Version Française

Ce travail porte sur l'étude du transport électronique dans le graphène, en particulier à fort champs magnétique, en régime d'Effet Hall Quantique. Il a pu être mis en évidence les mécanismes de transport électronique à énergie finie dans ce régime, les lois d'universalité de l'effet Hall quantique observées dans les gaz bidimensionnels d'électrons ont été retrouvées. Nous avons aussi pu observer pour la première fois la transition entre un régime de transport avec interactions et un sans interaction électronique grâce aux effets d'écrantage de la grille permettant de doper le graphène. Cette transition permet de confirmer une loi de saut à pas variable donnée par Efros-Shklovskii comme mécanisme de transport dominant dans l'effet Hall quantique.

Très récemment découvert le graphène a beaucoup retenu l'attention de la communauté scientifique ces 6 dernières années, et ses découvreurs, Andrey Geim et Kostya Novoselov viennent juste d'être récompensés du prix Nobel de physique 2010.

Nous allons voir que le graphène est particulier en bien des aspects. D'abord c'est le premier solide cristallin naturel à 2 dimensions qui ait pu être observé. Ce n'est ni un métal ni vraiment un semi-conducteur, les électrons se propageant à l'intérieur sont décrit par une équation bien particulière qui est l'équation de Dirac ultra relativiste normalement réservé aux particules sans masses de très haute énergie.

L'effet Hall quantique est aussi un sujet passionnant se apparaissant dans les gaz bidimensionnels d'électrons dans lequel se manifeste une résistance transverse appelé résistance de Hall, quantifié en paliers de h/e^2 en fonction d'un champ magnétique appliqué perpendiculairement. Cet effet a donné lieu à deux prix Nobel, un en 1985 à K.v.Klitzing pour la découverte de l'effet Hall quantique entier et l'autre en 1998 à D.C. Tsui, H.L.Störmer (expérience) et R.B Laughlin (théorie) and pour la découverte de l'effet Hall quantique fractionnaire.

L'effet Hall quantique entier a été observé dans le graphène en 2005 simultanément par l'équipe de A.Geim et celle de P. Kim révélant expérimentalement

la nature particulière des porteurs de charges. Dans ce matériau cet effet montre des points communs avec celui observé par K.V.Klitzling dans les gaz d'électrons régis par une relation de dispersion conventionnelle ainsi que d'importantes différences qui permettent d'étudier l'effet Hall quantique sous un nouvel angle.

Cette thèse se constitue en deux parties d'abord une partie résumant les propriétés physique du graphène et de l'effet Hall quantique puis une partie expérimentale.

La première partie offre d'abord une introduction générale sur le graphène. Puis le calcul de la relation de dispersion dans le graphène est rappelé à partir de l'approximation des liaisons fortes. De ce calcul et, due au réseau en nid d'abeille, on peut déduire que la relation de dispersion à basse énergie peut s'assimiler à celle donnée par l'équation de Dirac où la vitesse de la lumière est remplacé par la vitesse de Fermi. Ceci débouche sur une présentation de l'équation de Dirac et certaines propriétés particulières à cette équation se retrouvant dans la physique du graphène.

Nous nous intéresserons ensuite aux phénomènes de transport électronique à deux dimensions dans un domaine dit diffusif et cohérent, où la longueur de cohérence de phase électronique est du même ordre que celle de l'échantillon autorisant l'observation d'effets d'interférences quantiques. Pour cela nous adapterons les équations de Drude et de diffusion d'Einstein à ce type de transport.

Enfin un chapitre est réservé à l'effet Hall quantique qui est le cœur de ma thèse, dans ce chapitre la physique de cet effet est détaillée. Nous aborderons d'abord le calcul des niveaux de Landau dans les gaz conventionnels d'électrons ainsi que dans le graphène. Puis nous nous intéresserons aux propriétés de transport électronique dans ce régime. Dans la suite il sera présenté une étude qui se veut la plus exhaustive possible sur les mécanismes de la rupture de l'effet Hall quantique à énergie finie ainsi que la transition métal isolant. Ces sujets ont longuement été débattus dans les années 90, et sont toujours d'actualité. La rupture de l'effet Hall quantique peut être vue comme due à la conduction à travers l'échantillon perpendiculairement au courant alors que la quantification de l'énergie cyclotron alliée au principe de Pauli empêche normalement l'existence de chemin continu au niveau de Fermi d'un bord à l'autre de l'échantillon. Différents mécanismes expliquent ce transport en fonction de l'énergie mise en jeu. Quand l'énergie est comparable à l'écart entre niveaux d'énergie, l'activation thermique vers des niveaux de Landau non occupés explique ce processus. Nous nous arrêterons plus longuement sur les processus de basse énergie se produisant à l'intérieur du niveau de Landau rempli le plus proche de l'énergie de Fermi et perturbé par le désordre, en particulier sur la description de Poliakov et Shklovskii en termes de saut inélastique à portée variable entre états localisés au niveau de Fermi. La transition métal isolant s'observe quand l'énergie se rapproche d'un niveau de Landau (ou exactement sur le niveau de Landau pour un échantillon de taille infinie à température nulle),

cette transition est associée à une divergence de la longueur de localisation, où au-delà d'une certaine limite les états localisés s'étendent pour offrir un passage continu d'un bord à l'autre de l'échantillon. Fait remarquable, cette divergence suit une loi de puissance avec un exposant universel expliqué en termes de percolation quantique. Nous pourrions voir que deux visions s'opposent pour la transition de plateau à plateau, celle de Poliakov-Shklovskii l'expliquant avec la loi de saut à portée variable et celle de Pruisken l'expliquant via une transition métal isolant basée sur la comparaison entre la longueur de localisation et la longueur de cohérence de phase.

Nous arrivons ensuite à la deuxième partie, la partie expérimentale, où est d'abord présenté la fabrication d'échantillons permettant de mesurer les propriétés électroniques graphène. Celle-ci délicate a occupé une bonne partie de mon travail de thèse. La méthode utilisée pour obtenir du graphène est similaire à celle mis au point par K.Novoselov et consiste en l'exfoliation de graphite naturel. Le dépôt de contacts se fait essentiellement grâce aux techniques de lithographie électroniques et évaporation de métal après avoir caractérisé le graphène. Nous nous arrêterons sur le repérage et la caractérisation du graphène car ces étapes ne sont pas triviales. En effet trouver un feuillet de 3 Angström d'épaisseur pour quelques dizaines à centaines de microns carré de surface et pourvoir déterminer si il s'agit d'une ou plusieurs couche n'a rien de simple. Une méthode efficace pour discriminer entre une ou plusieurs couches de graphène qui sera décrite est la spectroscopie Raman basée sur l'étude des propriétés vibratoire d'un cristal.

Ensuite sont présentés des résultats de transport électronique élémentaire caractérisant le graphène. Ces résultats, bien que pas novateurs car déjà mesurés par plusieurs équipes ces dernières années, sont importants car ils illustrent les propriétés particulières du graphène et sont une étape clés dans la caractérisation, la compréhension et l'amélioration du graphène.

Puis il est présenté une étude sur les temps de transport réalisée par l'équipe d'Hélène Bouchiat à laquelle j'ai eu la chance de participer. Cette étude a permis la mesure du temps électronique de transport entrant dans la conductivité de Drude et le temps de vie électronique qui est le temps entre 2 collisions. De par le rapport de ces deux temps, il peut être déduit des propriétés importantes sur la nature des impuretés limitant la mobilité électronique. Ici cette étude aura permis de conclure que les impuretés limitantes dans des échantillons typique de graphène exfolié sont de petits (taille bien inférieur à la longueur d'onde de Fermi, de l'ordre de la distance entre 2 atomes du graphène) défauts neutres, tel par exemple des trous dans le réseau cristallin, ou des atomes adsorbés sur la surface du graphène.

Enfin les résultats sur la rupture de l'effet Hall quantique à énergie finie et la transition plateau-plateau dans le graphène qui représentent le cœur de mon travail de thèse sont présentés. En particulier nous avons pu mesurer que la rup-

ture de l'effet Hall quantique suivait des lois similaires à celles observées dans les gaz 2D conventionnels mais avec des énergies caractéristiques plus importantes, ce qui pourrait être très intéressant pour des applications métrologiques. Nous avons aussi pu observer que la divergence de la longueur de localisation à l'approche de la transition métal-isolant suivait les mêmes lois d'universalité que celles observées précédemment dans le régime d'effet Hall quantique avec des hétérojonctions de semiconducteurs. Le résultat le plus marquant de cette étude est sans doute l'observation du passage entre deux régimes de transport inélastiques à travers le centre de l'échantillon toujours en régime d'effet Hall quantique grâce à l'écrantage des interactions électronique par la grille métallique utilisée pour régler la densité du graphène. Ces régimes sont le variable range hopping de Mott (sans interaction) et le variable range hopping d'Efros-Shklovskii (avec interactions). Ce résultat apporte un argument expérimental essentiel permettant de clore une question longuement débattue sur la nature des mécanismes de transport dominant dans l'effet Hall quantique au voisinage de la transition entre plateaux de Hall.

Dans le dernier chapitre de la partie expérimentale nous découvrirons l'insert cryogénique fabriqué durant ma thèse qui est un élément essentiel pour les mesures de transport électronique à basse température. Ce dispositif permet d'effectuer des mesures sous vide cryogénique à une température de 1,6K au centre d'une bobine permettant d'appliquer un champ magnétique de 20 Tesla. La particularité de cet insert est que une fois plongé dans l'hélium liquide nous avons la possibilité d'élever la température de l'échantillon jusqu'à 450K, permettant de faire dégazer le graphène ce qui, nous allons le voir améliore considérablement les propriétés électroniques.

English version

This work deals with the electronic transport in graphene, particularly at high magnetic fields under quantum Hall effect. The finite energy mechanisms of transport have been established, confirming the universal laws of the quantum Hall effect observed in two-dimensional electron gases. We first observed the cross-over between two transport mechanisms, with and without electronic interactions thanks to screening by the backgate used to control the density of carriers in graphene. This cross-over confirmed the Efros-Shklovskii variable range hopping (VRH) law as the dominant mechanism of transport under quantum Hall effect conditions.

Since its recent discovery graphene has drawn much of the scientific community's attention these last six years. The discoverers of graphene, Andrey Geim and Kostya Novoselov, have just been awarded the 2010 Nobel Prize in Physics.

We will see that graphene is very special in many aspects. First of all, it is the first two-dimensional natural crystalline (without any confinement potential) solid to be observed. It is neither metal nor conventional semiconductor. The

propagation of electrons in graphene is described by an ultra-relativist Dirac equation, normally reserved for high energy or massless particles.

The quantum Hall effect (QHE) is in itself an exciting phenomenon which occurs in two-dimensional electron gases. Under QHE conditions a transverse potential appears which is linearly related to the current by a Hall resistance which is quantized in multiples of h/e^2 as a function of a perpendicular magnetic field. This effect led to the attribution of two Nobel Prizes, one in 1985 to K. von Klitzing for the integer quantum Hall effect, the other in 1998 to D.C. Tsui, R.B Laughlin and H.L. Störmer for the fractional quantum Hall effect.

In 2005, the integer quantum Hall effect in graphene was observed simultaneously by A. Geim's and P. Kim's teams and seen to show the peculiar nature of charge carriers obeying a Dirac like equation of motion. The quantum Hall effect in this new material has aspects in common with the observed by K. von Klitzing in electron gases subject to a conventional dispersion relation but also differences that give a new angle to the quantum Hall effect.

This thesis is divided into two parts, the first one will summarize the physical properties of graphene and the quantum Hall effect while the second will deal with the experiments done in this work.

The first part is a general introduction about graphene and the calculation of the dispersion relation deduced from a tight-binding approximation. From this calculation and as a result of the honeycomb lattice, it is seen that the low energy dispersion relation can be assimilated to the massless Dirac equation. A presentation of the Dirac equation with some peculiar properties applicable to graphene will be done.

In order to understand the two-dimensional electronic transport in the diffusive and in the coherent regime where the phase coherence length is of the same order of the sample's length which enables the observation of quantum interferences effects, we recall how the Drude approach and the Einstein diffusion relation can be adapted to this type of transport.

Finally, a full chapter is devoted to the quantum Hall effect, which is the core of this thesis. We will first study Landau levels in conventional electron gases and then in graphene, to see how their structure affects the electronic transport properties in this regime. This will be followed by an as exhaustive as possible study of the quantum Hall effect breakdown mechanisms at finite energy and the metal insulator transition. These subjects were much debated in the nineties and are still open topics. The disappearance of the quantum Hall effect can be seen as of conduction throughout the sample, in contradiction to the low temperature situation where the quantization of the cyclotron energy together with the Pauli principle normally prevents the existence of a continuous path at Fermi level between the two edges of the sample. Various mechanisms may explain this transport as a function of the energy involved. When the energy is comparable to the Landau level energy gap, the thermal activation towards non occupied Landau levels explains this process. We will focus on the low-energy processes occurring inside the filled Landau level closest to Fermi level, and particularly on the description by Polyakov and Shklovskii based on

variable range hopping between states at the Fermi level. The metal insulator transition is observed when the Fermi energy is close to a Landau level (or on a Landau level in an infinite sample at zero temperature). This transition is associated with a divergence of the localization length, where beyond a certain limit, localized states extend to provide a continuous path from one side to the other in the sample. Remarkably, this divergence follows a power law with a universal exponent explained in terms of quantum percolation. We will see that two opposing views for the transition from plateau to plateau were proposed: that of Poliakov-Shklovskii explaining it with the variable range hopping law and that of Pruisken explaining it via a metal-insulator transition based on the comparison between the localization length and the phase coherence length.

In the second experimental, part starts with the presentation of the making of samples for measuring graphene electronic properties. This delicate task took up a considerable part of the time allotted to my thesis. The method used to obtain graphene is similar to that developed by K. Novoselov and consists of exfoliating natural graphite. The deposition of contacts was performed essentially by using the techniques of lithography and evaporation of metal after graphene has been identified and characterized. I focus on the identification and characterization of graphene as these steps are delicate. In point of fact, finding a three-angstrom-thick layer for several tens to hundreds of microns square surface and being able to determine if there are one or more layers is not straightforward. An efficient method to discriminate between one or several layers of graphene is based on the Raman spectroscopy which makes it possible to study the vibrational properties of a crystal.

Afterwards, we will present the results of the elementary electronic transport characterizing graphene. These results, measured by several groups in recent years, are not innovative, but are important in that they illustrate the peculiar properties of graphene and are a key step in the characterization, understanding and improvement of the samples.

This will be followed by a study on transport scattering times by the team of Helene Bouchiat in which I had the chance to participate. This study resulted in the measurement of the electronic transport time entering the Drude conductivity and that defining the lifetime of an electronic state, which is the time between two collisions. By the ratio of these two times, important properties can be inferred about the nature of impurities limiting electrons mobility. In this regard, the study has found that impurities limiting the mobility in typical samples of exfoliated graphene are small neutral defects (well below the Fermi wavelength and in the range of the distance between two atoms of graphene) such as vacancies in the crystal lattice, or adsorbed atoms on the surface of the graphene.

A final section will present the results on the disappearance of the quantum Hall effect at finite energy and the plateau-plateau transition in graphene, which are the core of my thesis. In particular we were able to show that the disappearance of the quantum Hall effect follows laws similar to those seen in conventional 2D electron gases, but with higher characteristic energies, which could be very

interesting for metrological applications. We also observed that the divergence of the localization length on approaching the metal-insulator transition followed the same law of universality as previously observed in the conventional quantum Hall effect regime. The most striking result of this study is probably the observation of the cross-over between two inelastic bulk transport regimes revealed by the screening of electron interactions by the metal backgate used to tune the density of graphene. These regimes are Mott's variable range hopping (without interaction) and the Efros-Shklovskii's variable range hopping (with interactions). This result provides experimental evidence, to conclude a long debate about the nature of the dominant transport mechanisms in the quantum Hall effect near the transition between Hall plateaus.

In the last chapter of the experimental section, the cryogenic insert built during my thesis will be described. It is essential for measurements of electronic transport at low temperature. This device enables measurements under cryogenic vacuum at a temperature of 1.6 K, at the center of a coil permitting the application of a magnetic field of up to 20 Tesla. The particularity of this insert is that once it is immersed in liquid helium, the temperature of the sample can be raised to 450K, enabling degassing of adsorbed molecules from the graphene, which, we will later see, greatly improves its electronic properties.

Part I

The physics of graphene

Chapter 1

Electronic structure of graphene

1.1 Introduction

Graphene is a two-dimensional crystal of carbon atoms arranged in a honeycomb lattice.

Carbon, the very well-known sixth element of Mendeleev table is the fifteenth most abundant element on Earth and the fourth in the universe [1]. It is also the second most abundant element in the human body. It forms more compounds than any other material and is central to life on Earth through the carbon cycle.

Carbon has many properties: it is transparent and insulating in diamond, opaque in graphite, and its allotropes vary considerably in terms of thermal and electrical conductivity. It has been known since Human prehistory as charcoal or soot, and was probably used by the Chinese in its diamond form as early as 2500 BCE [2]. Graphite, one of carbon's many allotropes, came into common use in 1564 with the invention of pencils.

The knowledge that all these allotropes (diamond, graphite, amorphous carbon) come from one element is quite recent: in 1772, Lavoisier showed that a diamond is composed of carbon and, in 1779, Carl Wilhelm Scheele showed that graphite, which had been believed to come from lead, produces the same amount of carbon dioxide gas per gram as amorphous carbon.

In 1889, a report on carbon filaments was presented to the French Academy of Science [3]; these were later recognized as carbon nanotubes in 1952 by Radushkevich and Lukyanovich[4]. [5]. In 1991, Iijima's observation of nanotubes drew the attention of the scientific community to that allotrope of carbon, which has since become an intense field of research in materials science.

More recently, in 1985, the fullerene allotrope of carbon was discovered by Robert Curl, Harold Kroto and Richard Smalley, who were awarded the Nobel prize in chemistry for their discovery.

Although its band structure was calculated as early as 1947[6], graphene did

not become a laboratory reality until the work of A.K Geim and K.Novoselov in 2004[7].

Graphite, nanotubes, fullerenes, and graphene have one common point: they are all composed of a honeycomb lattice of carbon atoms. Graphene is a purely two-dimensional crystal, consisting of a monolayer of carbon atoms arranged as a honeycomb lattice. A carbon nanotube can be seen as a rolled graphene sheet. A fullerene molecule, also known as a Buckyball, can be described as a soccer football made with graphene where some hexagons have been replaced by pentagons (the basic ball is composed of 60 carbon atoms).1.1

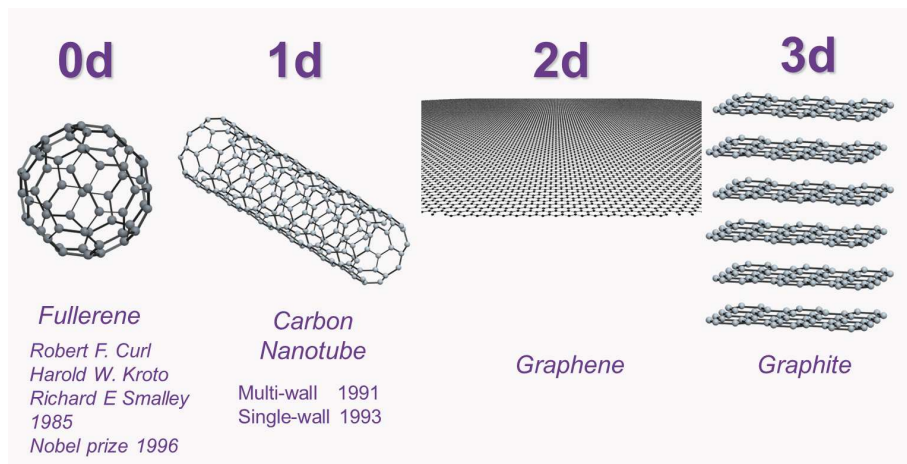


Figure 1.1: Figure from K.Novoselov

Several reasons can explain the recent interest shown by the scientific community in studying graphene which is illustrated by figure 1.2. Firstly, the combination of its conductivity and two-dimensional nature makes it the ultimate two-dimensional charge gas. Secondly, we are currently reaching the limit of silicon's capacity in terms of size (50nm) and Geim reports the engineering of a field device [7] smaller than the smallest presently engineered electronic transistor which allows one to think that it could be a good candidate for replacing silicon. There is, in addition, the possibility of controlling the carrier density through zero.

Its electronic properties are perhaps the most exciting aspect from a fundamental point of view. Due to its honeycomb lattice, the charge carriers have a linear energy-momentum relationship at the Fermi energy and obey a 2D massless Dirac equation appropriate to ultrarelativistic particles (such as neutrinos) with the speed of light replaced by a Fermi velocity ($v_F \sim c/300$). That makes it a toy for doing "benchtop" Quantum electrodynamic experiments.

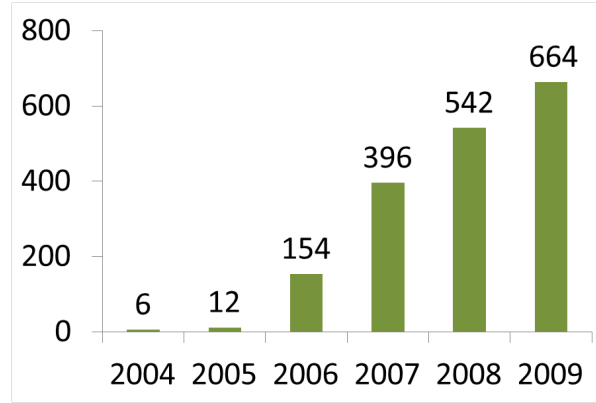


Figure 1.2: Number of preprint on arXiv with graphene in the title

1.2 Graphene atomic structure

Carbon has a nucleus of 6 protons and 6 neutrons. It is surrounded by 6 electrons which, are in the atomic configuration $1s^2 2s^2 2p^2$. In this configuration, there are two electrons in the inner 1s shell, very close to the nucleus, making them irrelevant for chemical reactions of the four outer electrons, 2 of which are in the 2s shell and 2 in the 2p shell, the latter having an energy about 4eV above the former. However, in the presence of other atoms like H, O, C etc. a covalent bond of lower energy can advantageously be formed by exciting an electron of the 2s band.

The covalent bonds are described by a combination of four states: $|2s\rangle$, $|2p_x\rangle$, $|2p_y\rangle$, $|2p_z\rangle$. A quantum superposition of the state $|2s\rangle$ with n $|2p_j\rangle$ is called sp^n hybridization.

Graphene is sp^2 hybridized, which means in orbital terms

$$|sp_1^2\rangle = \frac{1}{\sqrt{3}}|2s\rangle - \sqrt{\frac{2}{3}}|2p_x\rangle \quad (1.1)$$

$$|sp_2^2\rangle = \frac{1}{\sqrt{3}}|2s\rangle + \sqrt{\frac{2}{3}}\left(\frac{\sqrt{3}}{2}|2p_y\rangle + \frac{1}{2}|2p_x\rangle\right) \quad (1.2)$$

$$|sp_3^2\rangle = -\frac{1}{\sqrt{3}}|2s\rangle + \sqrt{\frac{2}{3}}\left(-\frac{\sqrt{3}}{2}|2p_y\rangle + \frac{1}{2}|2p_x\rangle\right) \quad (1.3)$$

These hybridizations are shown schematically in fig. 1.3

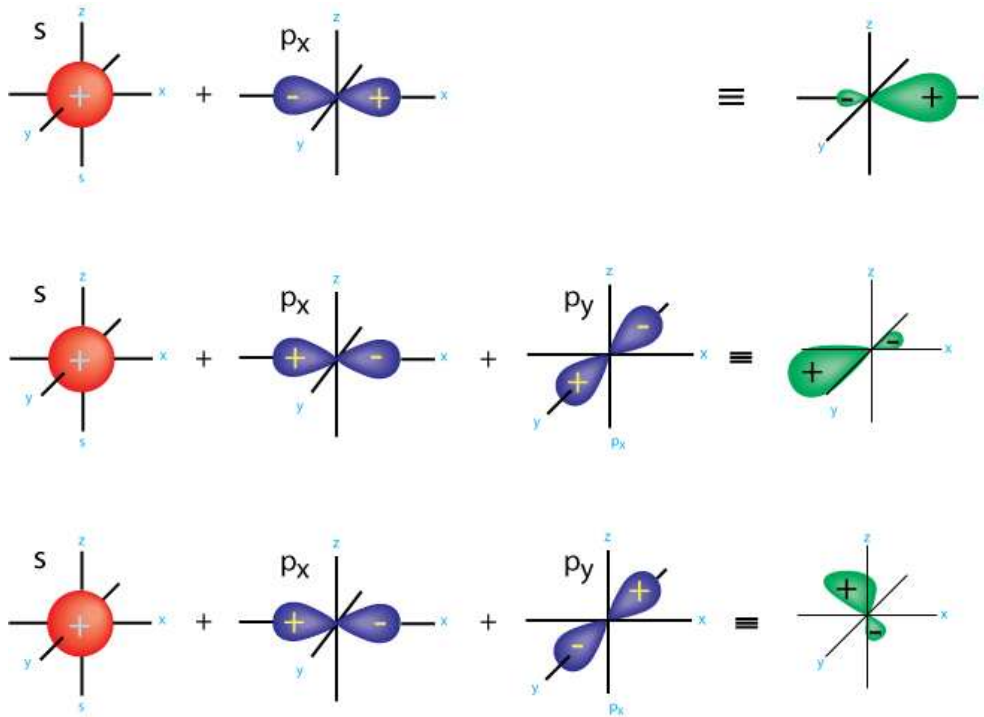


Figure 1.3: schema of the different hybridizations

These hybrid orbitals create σ bonds between carbon atoms, which are strong bonds between in-plane orbitals. The electron in the remaining p_z orbital is free to move and accounts for electron transport. In the following sections, we will only consider the p_z electrons, since they are the only mobile electrons.

1.3 Electronic properties

Drawing on ref [8, 9, 10, 11], we saw that the electrons which account for electronic transport are those in the p_z orbital. In order to compute the electronic bandstructure in graphene, we will examine the properties of electrons in this orbital, which are less bound to the atoms than are the core electrons. To do this, we will use Schrödinger's equation in an atomic potential $H = \frac{p^2}{2m} + V(\vec{r})$. The lattice symmetries are very important here and will make it possible for us to compute this equation for an infinite number of atoms.

In later sections, we will introduce the necessary tools before outlining the calculation specific to graphene.

1.3.1 Introduction to bandstructure calculation

1.3.1.1 Bravais lattice

A Bravais lattice is a lattice where one can find all nodes of the lattice knowing the position of one node and N vectors (where N is the dimension). In 2D we can write

$\vec{R} = n_1 \vec{a}_1 + n_2 \vec{a}_2$ where n_1, n_2 are integers and \vec{a}_2, \vec{a}_1 are linearly independent vectors.

A reciprocal lattice facilitating a Fourier analysis can be computed from the Bravais lattice to obey the condition using $e^{i\vec{K} \cdot \vec{R}} = 1$. This is a very powerful tool to calculate bandstructures using the symmetries of the lattice.

In the Bravais lattice, we can define a primitive cell called Wigner-Seitz cell. This cell is the region surrounding a node of the lattice which is nearer to this node than to any other node.

The reciprocal cell of the Wigner-Seitz cell is called the first Brillouin zone.

A honeycomb lattice is not a Bravais lattice. Figure 1.4 shows that B atoms see three A atoms, one up left, one up right and one down; contrarily, A atoms see the B atoms on their down right, down left and top. The way to construct the reciprocal lattice in graphene is to take a triangular lattice with two atoms per unit cell or two triangular sublattices. The reciprocal lattice of a triangular lattice is also a triangular lattice rotated by $\pi/2$.

1.3.1.2 Bloch's theorem

In the Hamiltonian $H = \frac{p^2}{2m} + V(\vec{r})$, V is the atomic potential and has a translation symmetry implying that $V(\vec{r} + \vec{R}) = V(\vec{r})$ for all \vec{R} belonging to the Bravais lattice.

This symmetry imposes a Hamiltonian which is invariant under all discrete translations $T(\vec{R})$ from which Bloch's theorem results.

We use Schrödinger's equation: $H\psi_{n\vec{k}}(\vec{r}) = \varepsilon_n(\vec{k})\psi_{n\vec{k}}(\vec{r})$ where n stands for all the quantum numbers linked to observables.

Bloch's theorem stipulates that the wave function can be written as $\psi_{n\vec{k}}(\vec{r}) = e^{i\vec{k} \cdot \vec{r}} u_{n\vec{k}}(\vec{r})$ where $u_{n\vec{k}}(\vec{r}) = u_{n\vec{k}}(\vec{r} + \vec{R})$.

As a result, we have $\psi_{n\vec{k}}(\vec{r} + \vec{R}) = e^{i\vec{k} \cdot \vec{r}} \psi_{n\vec{k}}(\vec{r})$ and also the modulus of the wavefunction is preserved for Bravais lattice translations $|\psi_{n\vec{k}}(\vec{r} + \vec{R})|^2 = |\psi_{n\vec{k}}(\vec{r})|^2$

A consequence of Bloch's theorem is that $\psi_{\vec{k}}(\vec{r}) = \psi_{\vec{k} + \vec{K}}(\vec{r})$ and $\varepsilon(\vec{k} + \vec{K}) = \varepsilon(\vec{k})$ where \vec{K} is a lattice vector of the reciprocal lattice.

1.3.1.3 Tight binding approximation

In an atomic lattice, there are different situations possible for the charge transport. The simplest case is that of atoms very far from one another, where the

atomic wavefunctions do not overlap and the electrons can be considered located in atomic levels on the lattice node.

The tight binding approximation applies to situations where atomic wavefunctions are overlapping enough to allow electron transfer but not enough to make an atomic description totally inappropriate.

This approximation consists of taking electrons in an atomic potential and allowing hopping from one atom to another with a barrier of height t to the nearest neighbors.

1.3.2 Bandstructure

We use a tight binding model to compute the bandstructure of graphene.

1.3.2.1 Honeycomb lattice

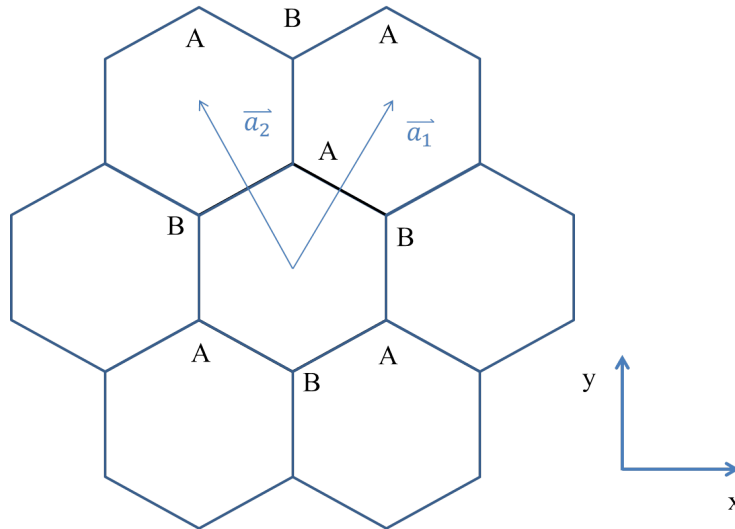


Figure 1.4: hexagonal lattice showing the vectors of the Bravais lattice

First of all, we need to define the Bravais lattice in which we will work and its associated first Brillouin zone. We take vectors as defined on figure 1.4. Note that many other choices would have led to the same final result. The point here is to find the most convenient basis vectors in the Bravais lattice for computation. We have:

$$\vec{a}_1 = \frac{a_0}{2}(\sqrt{3}, 3), \quad \vec{a}_2 = \frac{a_0}{2}(-\sqrt{3}, 3) \quad (1.4)$$

where a_0 is the distance between two carbon atoms (~ 1.42).

Also, it is important to know the position of the nearest neighbors of A and B atoms. For an A atom at (0,0) the positions of the 3 B atoms surrounding it are:

$$\vec{\delta}_1 = \frac{a_0}{2}(\sqrt{3}, 1), \quad \vec{\delta}_2 = \frac{a_0}{2}(-\sqrt{3}, 1), \quad \vec{\delta}_3 = a_0(0, -1) \quad (1.5)$$

A B atom is surrounded by 3 A atoms at relative positions $\vec{\delta}'_1 = -\vec{\delta}_1$, $\vec{\delta}'_2 = -\vec{\delta}_2$, and $\vec{\delta}'_3 = -\vec{\delta}_3$.

The reciprocal lattice is calculated in accordance with the condition $\vec{a}_i \cdot \vec{b}_j = 2\pi\delta_{ij}$:

$$\vec{b}_1 = \frac{2\pi}{3a_0}(\sqrt{3}, 1), \quad \vec{b}_2 = \frac{2\pi}{3a_0}(-\sqrt{3}, 1) \quad (1.6)$$

As mentioned previously, the reciprocal lattice for a hexagonal lattice has the same shape: it is composed of two triangular sublattices subtending a hexagon. As a consequence, the first Brillouin zone is a hexagon, the symmetry labels being Γ for the center and K and K' for the two groups of three equivalent points at the six corners. The reciprocal lattice hexagons are rotated by $\pi/2$ with respect to the real space hexagons.

The positions of K and K' are

$$\vec{K} = \frac{2\pi}{3a_0}\left(\frac{1}{\sqrt{3}}, 1\right), \quad \vec{K}' = \frac{2\pi}{3a_0}\left(-\frac{1}{\sqrt{3}}, 1\right) \quad (1.7)$$

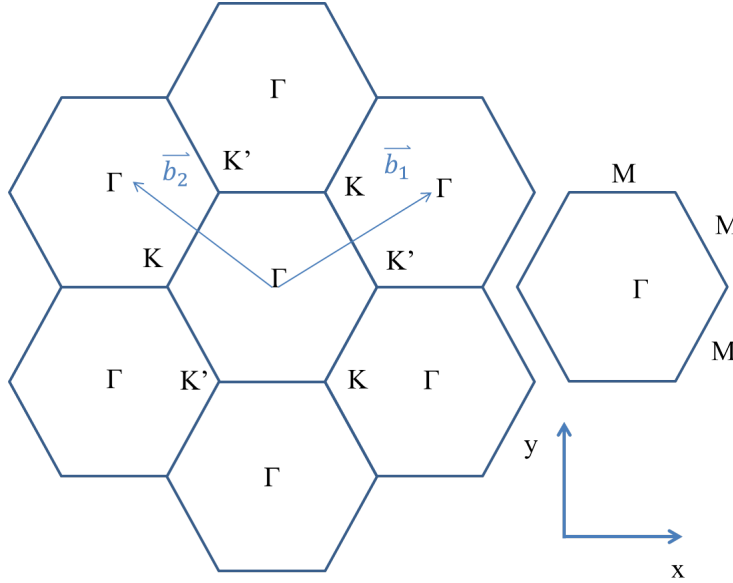


Figure 1.5: Reciprocal lattice: the hexagons defines the First Brillouin zone where Γ is the center of the FBZ and K and K' its corners; M is located on a side of the FBZ between a K and K' point.

1.3.2.2 Nearest neighbor hopping

We will slightly diverge from the classical tight binding model by applying the principle of tight bonding to models with two atoms per cell. Therefore, we need to take two-component wavefunctions

$$\psi(\vec{r}) = \sum_{\mathbf{k}} [\alpha_{\mathbf{k}} \psi_{\mathbf{k}}^A(\vec{r}) + \beta_{\mathbf{k}} \psi_{\mathbf{k}}^B(\vec{r})]$$

with a hopping probability t between A and B sites.

It is useful to write the wavefunction in the form of a two-components spinor where the sites A and B are represented by the two pseudo-spin components

$$\psi_{\mathbf{k}} = \begin{pmatrix} \alpha_{\mathbf{k}} \\ \beta_{\mathbf{k}} \end{pmatrix}$$

Both α and β are Bloch wavefunctions, so they can be written in the form of

$$\begin{pmatrix} \alpha_{\mathbf{k}} \\ \beta_{\mathbf{k}} \end{pmatrix} = \sum_i \exp i\mathbf{k} \cdot \mathbf{R}_i \begin{pmatrix} a_{\mathbf{k}} \phi_{\mathbf{k}}^{(A)}(\vec{r}) \\ b_{\mathbf{k}} \phi_{\mathbf{k}}^{(B)}(\vec{r}) e^{i\mathbf{k} \cdot \delta_i} \end{pmatrix} \quad (1.8)$$

Here we have set the origin R_0 on an A atom.

We must now solve Schrödinger's equation:

$$H\psi_{\mathbf{k}} = E_{\mathbf{k}}\psi_{\mathbf{k}} \quad (1.9)$$

In order to have a scalar equation, we multiply it from the left by $\psi_{\mathbf{k}}^\dagger$:

$$\psi_{\mathbf{k}}^\dagger H\psi_{\mathbf{k}} = E\psi_{\mathbf{k}}^\dagger \psi_{\mathbf{k}} \quad (1.10)$$

$$\begin{pmatrix} \alpha_{\mathbf{k}}^* & \beta_{\mathbf{k}}^* \end{pmatrix} \begin{pmatrix} \Delta V^{AA} & \Delta V^{AB} \\ \Delta V^{BA} & \Delta V^{BB} \end{pmatrix} \begin{pmatrix} \alpha_{\mathbf{k}} \\ \beta_{\mathbf{k}} \end{pmatrix} = E \begin{pmatrix} \alpha_{\mathbf{k}}^* & \beta_{\mathbf{k}}^* \end{pmatrix} \begin{pmatrix} \alpha_{\mathbf{k}} \\ \beta_{\mathbf{k}} \end{pmatrix} \quad (1.11)$$

$$H_{\mathbf{k}} = E_{\mathbf{k}} S_{\mathbf{k}} \quad (1.12)$$

The Hamiltonian can be written as a 2×2 matrix:

$$H_{\mathbf{k}} = \begin{pmatrix} t_{\mathbf{k}}^{AA} & t_{\mathbf{k}}^{AB} \\ t_{\mathbf{k}}^{BA} & t_{\mathbf{k}}^{BB} \end{pmatrix} \quad (1.13)$$

To compute $t_{\mathbf{k}}^{AB}$ and $t_{\mathbf{k}}^{BA}$ we have to consider that 3 atoms surround the A (or B) atom, resulting in a phase shift

$$t_{\mathbf{k}}^{AB} = t \sum_l e^{i\mathbf{k} \cdot \delta_l} = t\gamma_{\mathbf{k}}, \quad t_{\mathbf{k}}^{BA} = t \sum_l e^{i\mathbf{k} \cdot \delta_l'} = t\gamma_{\mathbf{k}}^* \quad (1.14)$$

$$\gamma_{\mathbf{k}} = e^{-ik_y a_0} \left(1 + 2e^{+3ik_y a_0/2} \cos \frac{k_x a_0 \sqrt{3}}{2} \right) \quad (1.15)$$

$$\gamma_{\mathbf{k}}^* = e^{+ik_y a_0} \left(1 + 2e^{-3ik_y a_0/2} \cos \frac{k_x a_0 \sqrt{3}}{2} \right) \quad (1.16)$$

The distance between 2 nearest-neighbor A or B atoms is around 1.7 times smaller than the distance between a pair of A or B atoms. As the probability of hopping diminishes exponentially with the distance we can neglect the hopping between A and A or B and B atoms, as confirmed by experiments [12] from which $t' \sim 0.1t$ was assessed.

$$S_{\mathbf{k}} = \begin{pmatrix} \alpha_{\mathbf{k}}^* \alpha_{\mathbf{k}} & \alpha_{\mathbf{k}}^* \beta_{\mathbf{k}} \\ \beta_{\mathbf{k}}^* \alpha_{\mathbf{k}} & \beta_{\mathbf{k}}^* \beta_{\mathbf{k}} \end{pmatrix} = \begin{pmatrix} s_{\mathbf{k}}^{AA} & s_{\mathbf{k}}^{AB} \\ s_{\mathbf{k}}^{BA} & s_{\mathbf{k}}^{BB} \end{pmatrix}$$

For the overlap matrix, we can reasonably suppose that the overlap of the A and B wavefunctions is very low because, as said in section 1, the electrons which account for transport are in p_z orbitals, which have a small spatial extension in the x,y plane. Therefore, we will ignore non-diagonal terms s^{AB} and s^{BA} . Normalization of the wavefunction imposes $s_{\mathbf{k}}^{AA} = s_{\mathbf{k}}^{BB} = 1$.

We can now simplify equation 1.10

$$\begin{pmatrix} E_{\mathbf{k}} & t_{\mathbf{k}}^{AB} \\ t_{\mathbf{k}}^{BA} & E_{\mathbf{k}} \end{pmatrix} = 0 \quad (1.17)$$

which results in

$$E_{\mathbf{k}}^2 = t^2 \gamma_{\mathbf{k}} \gamma_{\mathbf{k}}^* \quad (1.18)$$

$$E_{\mathbf{k}} = \pm t \sqrt{1 + 4 \cos \frac{k_x a_0 \sqrt{3}}{2} \cos \frac{3k_y a_0}{2} + \cos^2 \frac{k_x a_0 \sqrt{3}}{2}} \quad (1.19)$$

From this equation, we notice that the energy vanishes at two inequivalent points:

$$\vec{K} = \frac{2\pi}{3a_0} \left(\frac{1}{\sqrt{3}}, 1 \right), \quad \vec{K}' = \frac{2\pi}{3a_0} \left(-\frac{1}{\sqrt{3}}, 1 \right) \quad (1.20)$$

We saw earlier that these points are the corners of the first Brillouin zone. This is a special and central property of graphene: its valence and conduction bands cross. As a consequence, graphene is neither a semiconductor nor a metal, and is often referred to as a zero-gap semiconductor. Plots of the bandstructure are given in fig.1.6a and 1.7.

1.3.2.3 Low energy linearization

We can linearize the energy dispersion around the crossing points as follows

$$\vec{K} = \frac{4\pi}{3\sqrt{3}a_0} \vec{e}_x, \quad \vec{K}' = -\frac{4\pi}{3\sqrt{3}a_0} \vec{e}_x$$

Where vectors K and K' are the same as defined before, apart from a translation by a reciprocal lattice vector for simplifying the calculation.

$$\gamma_{\mathbf{k}} = \exp\left(ik_x \frac{a_0\sqrt{3}}{2} + ik_y \frac{a_0}{2}\right) + \exp\left(-ik_x \frac{a_0\sqrt{3}}{2} + ik_y \frac{a_0}{2}\right) + \exp(-ik_y) \quad (1.21)$$

For the linearization around the K point we define the wave vector

$$\vec{k}' = \vec{k} - \vec{K}$$

in terms of which we have

$$\gamma_{\mathbf{k}'} = \exp\left(ik'_x \frac{a_0\sqrt{3}}{2} + ik'_y \frac{a_0}{2} - 2i\frac{\pi}{3}\right) + \exp\left(-ik'_x \frac{a_0\sqrt{3}}{2} + ik'_y \frac{a_0}{2} + 2i\frac{\pi}{3}\right) + \exp(-ik'_y) \quad (1.22)$$

For this linearization, we consider only the first-order terms. We will see later that this linearization is well adapted for most experiments at realistic situation for transport.

$$\gamma_{\mathbf{k}'} = \left(-\frac{1}{2} - i\frac{\sqrt{3}}{2}\right) \left(1 + i\frac{a_0}{2} (k'_x\sqrt{3} + k'_y)\right) + \left(-\frac{1}{2} + i\frac{\sqrt{3}}{2}\right) \left(1 + i\frac{a_0}{2} (-k'_x\sqrt{3} + k'_y)\right) + 1 - ik'_y \quad (1.23)$$

$$\boxed{\gamma_{\mathbf{k}'} = \frac{3a_0}{2} (k'_x - ik'_y)} \quad (1.24)$$

For the linearization around the K' point we define the wave vector

$$\vec{k}'' = \vec{k} - \vec{K}'$$

$$\boxed{\gamma_{\mathbf{k}''} = -\frac{3a_0}{2} (k''_x + ik''_y)} \quad (1.25)$$

In a similar way, we can compute the results for B atoms:

$$\boxed{\gamma_{\mathbf{k}'}^* = \frac{3a_0}{2} (k'_x + ik'_y)} \quad (1.26)$$

$$\boxed{\gamma_{\mathbf{k}''}^* = -\frac{3a_0}{2} (k_x'' - ik_y'')} \quad (1.27)$$

These results highlight the necessity of including both sublattices A and B as well as both crossing points K and K' in our wave functions, which are noted $\psi_{\pm}^{A/B}$, where \pm is the valley indice.

$$\Psi = \begin{pmatrix} \psi_{+}^A \\ \psi_{+}^B \\ \psi_{-}^A \\ \psi_{-}^B \end{pmatrix}$$

We set $\gamma_{\mathbf{k}} = \frac{3a_0}{2} (k_x - ik_y)$ and by remarking that $\gamma_{\mathbf{k}''}^* = -\gamma_{\mathbf{k}'}$ we can write the following Hamiltonian

$$H = t \begin{pmatrix} 0 & \gamma_{\mathbf{k}} & 0 & 0 \\ \gamma_{\mathbf{k}}^* & 0 & 0 & 0 \\ 0 & 0 & 0 & \gamma_{-\mathbf{k}}^* \\ 0 & 0 & \gamma_{-\mathbf{k}} & 0 \end{pmatrix} \quad (1.28)$$

Note that this linearization precludes charge carriers from passing from K to K' valleys and vice versa.

We set $v_F = 3a_0t/2\hbar$, denoting the Fermi velocity: $v_F = 1.10^6 m/s \simeq c/300$.

By choosing this wavevector, the diagonalized Hamiltonian for the K band is equal to that for K'

$$H = \hbar v_F \begin{pmatrix} \sqrt{\gamma_{\mathbf{k}}\gamma_{\mathbf{k}}^*} & 0 \\ 0 & -\sqrt{\gamma_{\mathbf{k}}^*\gamma_{\mathbf{k}}} \end{pmatrix} \quad (1.29)$$

The eigenvalues of this Hamiltonian are:

$$\boxed{\varepsilon_{\xi=\pm}^{\lambda} = \lambda \hbar v_F |\vec{k}|} \quad (1.30)$$

Where λ is the band subscript, $\lambda = +$ applies to the conduction band with positive energy and $\lambda = -$ to the valence band associated with negative energy.

We can remark that charge carriers in the different sublattices will propagate with a momentum phase shifted by $\theta_{\mathbf{k}} = \arctan(k_y/k_x)$.

The minus sign in γ of the K' band brings forward the notion of chirality (which will be detailed in section 1.3.3.2). To have a simple view, if the angle between the k_x and k_y in the K band is represented by the angle of the thumb and forefinger of the right hand, in K' valley it would be represented by the same angle in the left hand.

All these parameters can be expressed in the wavefunction:

$$\Psi = \begin{pmatrix} \psi_+^A \\ \psi_+^B \\ \psi_-^B \\ \psi_-^A \end{pmatrix} = \begin{pmatrix} 1 \\ \lambda e^{i\theta_{\mathbf{k}}} \\ 1 \\ -\lambda e^{i\theta_{\mathbf{k}}} \end{pmatrix} \varphi$$

Note that the A and B sublattices are exchanged in the K' spinor for convenience.

The Hamiltonian for such a wavefunction is:

$$H = \hbar v_F \begin{pmatrix} \boldsymbol{\sigma} \cdot \mathbf{k} & 0 \\ 0 & -\boldsymbol{\sigma} \cdot \mathbf{k} \end{pmatrix} \quad (1.31)$$

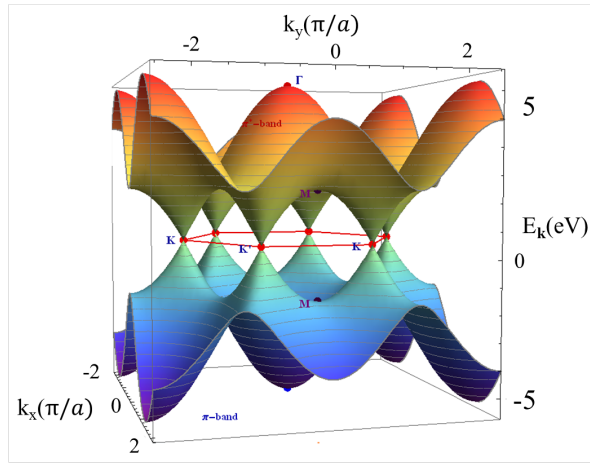
where σ are the Pauli matrices representing a pseudo-spin

$$\sigma_x = \begin{bmatrix} 0 & 1 \\ 1 & 0 \end{bmatrix}, \quad \sigma_y = \begin{bmatrix} 0 & -i \\ i & 0 \end{bmatrix}$$

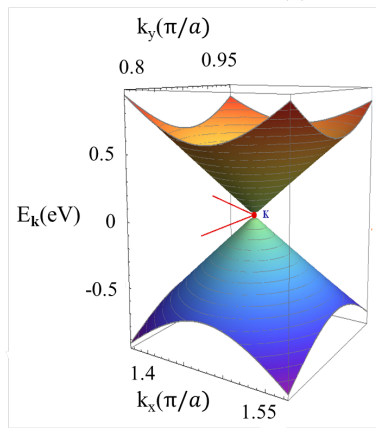
$$H = \hbar v_F \vec{\alpha} \vec{k} \quad (1.32)$$

With $\alpha = \begin{pmatrix} \boldsymbol{\sigma} & 0 \\ 0 & -\boldsymbol{\sigma} \end{pmatrix}$.

The pseudospin represents the weight on the A and B sublattices.



(a)



(b)

Figure 1.6: Bandstructure of graphene. On the left, for the full Brillouin zone and, on the right, the low energy linear relation around K point.

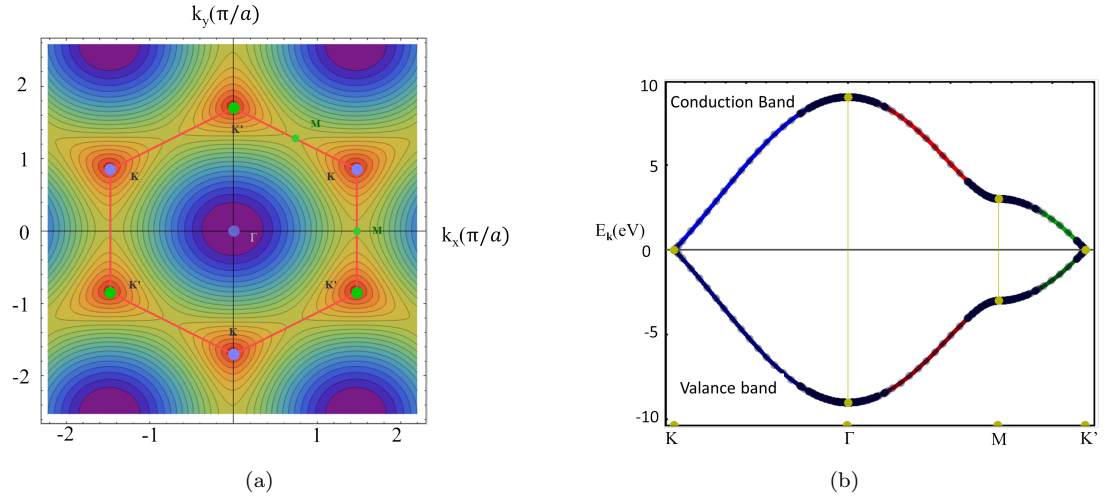


Figure 1.7: 2D views of the bandstructure of graphene. (a) is a view from the top and while (b) is a plot of energy versus position in the FBZ cell.

As shown in fig. 1.8, the bandstructure of graphene was experimentally measured by angle resolved photo-emission (ARPES).

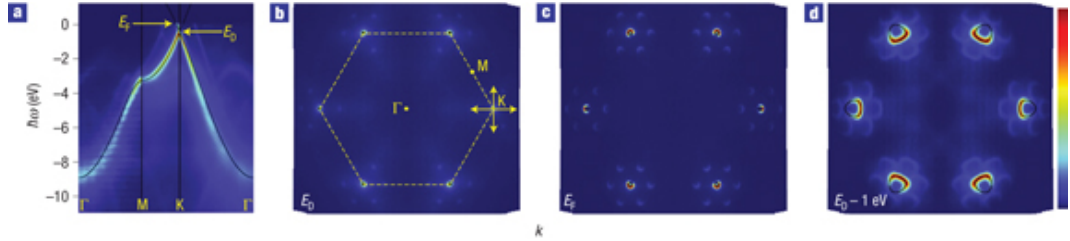


Figure 1.8: ARPES measurement of graphene on SiC substrate in ref [12]. (a) Experimental energy distribution of states as a function of momentum along principal directions; (b) Constant-energy map of the states at binding energy corresponding to Dirac energy and Brillouin zone boundaries (dashed line); (c) Constant-energy map at Fermi level; (d) ED-1 eV

1.3.2.4 Energy scale and limit of the linearization approximation

The previous section contained a linearization focusing only on the first-order terms in the Hamiltonian, the validity of which must now be examined.

Because in experiments the density is linearly tuned by backgate to sample potential (see section 6.2), it should prove useful to express all energies in terms of density.

Typical gate efficiency leads to $n = \alpha V_g$ where $\alpha = 7.10^{14} m^{-2} \cdot V^{-1}$, where the maximum achievable gate voltage (above which graphene is destroyed) is

$V_{gmax} \approx 100V$ leading to a density $n \approx 7.10^{16}m^{-2}$, therefore, we will consider $n_{max} = 1.10^{17}m^{-2}$.

In two dimensions linear dispersion $E_F = \hbar v_F k_F$ and a four fold degeneracy, $n = k^2/\pi$, which implies that:

$$E_F = \hbar v_F \sqrt{\pi n}$$

$$n = 3,7.10^{17}.m^{-2} * E(eV)^2$$

Therefore, the maximum attainable energy in typical electronic measurements is

$$E_{max} \approx 0.5eV$$

where

$$k_F^{max} \approx 6.10^8 m^{-1}, \quad \lambda_F^{min} \approx 1.10^{-8} m$$

The linearization described in paragraph 1.3.2.3 implied that $k_F a \ll 1$, or $\lambda \gg a$, therefore, if we consider that $a = 1,42.10^{-10}m$, we can reasonably conclude that this approximation remains valid for all our electronic measurements. On a more quantitative note, we can compare the second-order term of $k_F a$

$$\frac{(k_F^{max} a)^2}{k_F^{max} a} = 8.5\%$$

1.3.3 The Dirac equation and some of its special properties

Quantum mechanics is usually described using Schrödinger's equation, which is focused on non-relativistic particles. In 1928, Dirac formulated a quantum description for relativistic fermions by way of the so-called Dirac equation.

A major point of his formulation is the discovery of the concept of antiparticles. Indeed this equation has two solutions: one with positive energy and another with negative energy (identified as anti particles). In 1932, the positron, the antiparticle of the electron was observed by Carl Anderson, thus demonstrating the validity of the novel concepts expressed in Dirac's equation.

The ultra-relativistic Dirac equation is usually linked with high energy particles (like neutrinos) and predicts some novel effects.

Due to the honeycomb lattice structure of graphene, an effective ultra-relativistic Dirac equation can be used to describe the electron while making it possible to observe some of the novel effects predicted by Dirac's equation.

1.3.3.1 Dirac's Equation

This part is largely inspired by [8, 13].

Klein-Gordon's equation was the first to be proposed for the description of a relativistic particle within a quantum mechanics approach.

It is constructed in a similar way to Schrödinger's equation where

$$H = \frac{p^2}{2m} \quad (1.33)$$

and we make the substitution $H \rightarrow i\hbar \frac{\partial}{\partial t}$ and $\vec{p} \rightarrow -i\hbar \vec{\nabla}$ and apply these operators to a wavefunction Ψ

$$i\hbar \frac{\partial}{\partial t} \Psi = \frac{1}{2m} (-i\hbar \vec{\nabla})^2 \Psi \quad (1.34)$$

The Klein-Gordon equation is built from a relativistic Hamiltonian

$$H^2 = p^2 c^2 + m^2 c^4 \quad (1.35)$$

A substitution in 1.33 gives us:

$$\left(\frac{1}{c^2} \frac{\partial^2}{\partial t^2} - \Delta + \frac{m^2 c^2}{\hbar^2} \right) \Psi = 0 \quad (1.36)$$

This equation is a second-order in time and differs from Schrödinger's in that the knowledge of the state vector $\psi(\vec{r}, t = 0)$ is not sufficient to describe it at subsequent times.

To restore a first-order equation in time, we can use multi-component wavefunctions and write Eq. 1.36 as

$$\left(1 + \frac{i\hbar}{mc^2} \frac{\partial}{\partial t} \right) \left(1 - \frac{i\hbar}{mc^2} \frac{\partial}{\partial t} \right) \Psi = \frac{\hbar^2}{mc^2} \Delta \Psi \quad (1.37)$$

Where we set $\Psi_A = \Psi + \frac{i\hbar}{mc^2} \frac{\partial \Psi}{\partial t}$ and $\Psi_B = \Psi - \frac{i\hbar}{mc^2} \frac{\partial \Psi}{\partial t}$ to obtain a system of differential equations of first order in time as expressed by:

$$i\hbar \frac{\partial \Psi}{\partial t} \begin{bmatrix} \Psi_A \\ \Psi_B \end{bmatrix} = \begin{bmatrix} mc^2 - \frac{\hbar^2}{2m} \Delta & -\frac{\hbar^2}{2m} \Delta \\ \frac{\hbar^2}{2m} \Delta & -mc^2 + \frac{\hbar^2}{2m} \Delta \end{bmatrix} \begin{bmatrix} \Psi_A \\ \Psi_B \end{bmatrix} \quad (1.38)$$

Most of the problems posed by this equation can be solved. However, one part of it will, by nature, prevent the description of relativistic fermions.

The two components are non symmetric: in the non-relativistic limit, Ψ_B is of the order of zero whereas Ψ_A is of the order of 1. Which leaves us with a one-component wavefunction that is not sufficient to describe the electron spin.

A four-components wave function is needed if space and time coordinates are to play a symmetric role: Ψ_μ where $\mu = (1, 2, 3, 4)$ can be written has a column matrix

$$\Psi = \begin{bmatrix} \Psi_1 \\ \Psi_2 \\ \Psi_3 \\ \Psi_4 \end{bmatrix}$$

We will see later that all the components correspond to physical quantities: in a combination of spin and helicity, both of which can take 2 values.

The position probability is then given by

$$P(\vec{r}, t) = \sum_{\mu=1}^4 |\Psi_\mu|^2$$

The equation is in the form

$$i \frac{\partial \Psi}{\partial t} = H_D \Psi$$

In the case of a particle without external field, H_D has to be invariant to translation, thus independent of \vec{r} and t

$$H_D = \vec{\alpha} \cdot \vec{p} c + \beta m c^2 \quad (1.39)$$

Where \vec{p} corresponds to $\vec{p} \rightarrow -i\nabla$. $\vec{\alpha} = (\alpha_x, \alpha_y, \alpha_z)$ and β denotes 4 hermitean operators acting on the four-component wavefunction, all of which mix the components of the wavefunction.

We can now express the Dirac equation with $E = i\hbar \frac{\partial}{\partial t}$

$$[E - c\vec{\alpha} \cdot \vec{p} - \beta m c^2] \Psi(\vec{r}, t) = 0 \quad (1.40)$$

Our next step is to determine $\vec{\alpha}$ and β . To do so, we use the correspondence principle, bearing in mind that the solutions of this equation must satisfy Klein-Gordon's equation

$$[E^2 - \vec{p}^2 c^2 - m^2 c^4] \Psi(\vec{r}, t) = 0 \quad (1.41)$$

When we multiply eq.1.40 by $[E + \vec{\alpha} \cdot \vec{p} + \beta m]$, we obtain :

$$\left[E^2 - \sum_k (\alpha^k)^2 (p^k)^2 - \beta^2 m^2 - \sum_{k < l} (\alpha^k \alpha^l + \alpha^l \alpha^k) p^k p^l - \sum_k (\alpha^k \beta + \beta \alpha^k) m p^k \right] \Psi = 0$$

This expression was simplified by setting $c = 1$, however, coming back to usual notation can easily be performed by dimensional argument.

By identification with equation 1.41 we have

$$\begin{aligned} (\alpha^k)^2 &= 1 & \alpha^k \alpha^l + \alpha^l \alpha^k &= 0 & (k \neq l) \\ \beta^2 &= 1 & \alpha^k \beta + \beta \alpha^k &= 0 \end{aligned} \quad (1.42)$$

Solving these equations gives us

$$\vec{\alpha} = \begin{bmatrix} 0 & \vec{\sigma} \\ \vec{\sigma} & 0 \end{bmatrix}, \beta = \begin{bmatrix} \mathbf{1} & 0 \\ 0 & -\mathbf{1} \end{bmatrix}$$

where $\vec{\sigma}$ are the Pauli matrices

$$\sigma_x = \begin{bmatrix} 0 & 1 \\ 1 & 0 \end{bmatrix}, \sigma_y = \begin{bmatrix} 0 & -i \\ i & 0 \end{bmatrix}, \sigma_z = \begin{bmatrix} 1 & 0 \\ 0 & -1 \end{bmatrix}.$$

We can now express the Dirac equation in an external field quite easily by making the substitution:

$$E \rightarrow E - V, \quad \vec{p} \rightarrow \vec{p} - e\vec{A}$$

to obtain

$$\boxed{\left[(E - V) - \vec{\alpha}(\vec{p}\vec{c} - e\vec{A}) - \beta mc^2 \right] \Psi = 0} \quad (1.43)$$

If we consider the case of a free electron without field to find stationary states, we can set

$$\Psi(\vec{r}, t) = e^{\frac{Et}{\hbar}} \psi(\vec{r}) \quad (1.44)$$

$$E\psi(\vec{r}) = H_D\psi(\vec{r}) \quad (1.45)$$

Now, if we decompose the wavefunction in terms of planar waves $\psi_\mu(\vec{r}) = e^{i\vec{k}\cdot\vec{r}} C_\mu(\vec{k})$, where $C_\mu(\vec{k})$ is independent of \vec{r} ($\mu = 1, 2, 3, 4$), we have

$$(c\hbar\vec{k}\cdot\vec{\alpha} + \beta mc^2) C_\mu(\vec{k}) = E C_\mu(\vec{k})$$

Solving this equation gives eigenvalues:

$$\boxed{E = \pm \sqrt{(mc^2)^2 + (pc)^2}} \quad (1.46)$$

This result shows two possible eigenvalues for energy: one positive, the other negative. A priori a negative value for energy has no physical meaning and can be ignored, however we can imagine some experiments where it can not be ignored like in the Klein paradox (described in 1.3.3.4). This led Dirac to postulate that all negative states are occupied by electrons in the “vacuum”. If we add one electron to this vacuum, it will necessarily be in a positive energy state because all negative states are full and electrons obey Fermi-Dirac statistics. Dirac asserts that the possible negative energy states are holes or missing electrons in a sea of electrons. Thus, the hole differs from the missing electron in that it has an opposite charge, energy and impulsion, which means that the hole would carry a charge $+e$ and have its momentum \vec{p} antiparallel to its velocity \vec{v} . Dirac’s postulates led to the novel concept of antiparticle. In 1932, four years after Dirac’s prediction, Carl D. Anderson observed an electron antiparticle for the first time and named it a positron.

The inherently problematic aspect of this theory is that it presupposes that the negative energy states are filled by an infinity of electrons while it is a one-electron theory. Furthermore, the idea of electrons not interacting in the vacuum appears fairly suspicious. Both problems are solved in the framework of quantum electrodynamics, notwithstanding, Dirac's equation gives a good picture of simple quantum relativistic problems and accurate predictions for many phenomena. As we will see later, some of the phenomena which were predicted by Dirac's equation can be observed in graphene.

If we express the ultra-relativistic Dirac Hamiltonian in 2 dimensions without a mass, we obtain

$$H_D = \vec{\alpha} \cdot \vec{p}c = \hbar c \vec{k} \cdot \vec{\alpha} \quad (1.47)$$

where α is now composed of the two Pauli matrices σ_x and σ_y . Here it denotes the isospin, which is linked to helicity in the case of neutrinos. This Hamiltonian is remarkably similar to that for graphene, while, in the latter, c , the speed of light is replaced by the Fermi velocity, the Pauli σ matrices act on the pseudospin and the two-component state vectors represent a superposition of the sublattices. The similarity does end with the comparison of the Hamiltonians, for the effects predicted by Dirac's equation should find their equivalent in graphene, making it a nice tool to examine phenomena of usually very high energy with a low-energy physical system.

It is also interesting to note that the disappearance of the mass leads to a constant velocity; the β matrices, which are linked to time transformation disappear. As a conclusion, the energy depends only on the wavevector, which is proportional to the inverse wavelength.

1.3.3.2 Valley, band and chirality

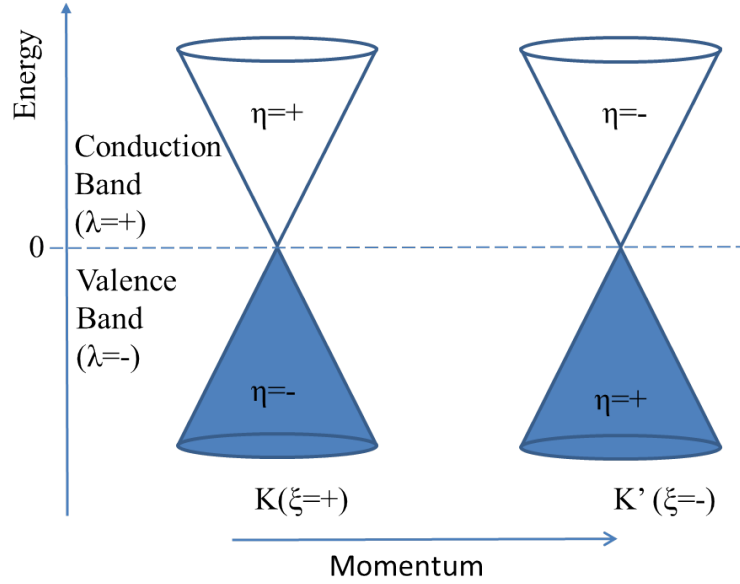


Figure 1.9

There is a set of parameters which are important to know in order to understand the properties of an electron in graphene.

Chirality, helicity. A figure is said to be chiral if it is not identical to its mirror image. For example, our hands are chiral, the image of our right hand in a mirror, as a rule, is our left hand. We can distinguish right from left chirality. It is interesting to note that most of the molecules constituting living beings on Earth have a left chirality.

A DNA helix or a propeller plane provide simple examples of helicity, which is the projection of the rotating direction on the direction of motion. The conventional approach for describing rotation is used to determine right- and left-handed helicity: we assume that a standard clock, tossed face forward, has a left-handed helicity. As is the case with chirality, nature manifestly favors left-handed helicity as demonstrated by DNA or neutrinos, for instance.

For particles which obey the Dirac equation we can define helicity as the projection of its spin onto the propagation direction: $h = \frac{\vec{p} \cdot \vec{\sigma}}{|\vec{p}|}$. It is a hermitian operator with eigenvalues $\eta = \pm$:

$$h | \eta = \pm \rangle = \pm | \eta = \pm \rangle \quad (1.48)$$

As mentioned, all neutrinos in nature are “left-handed” which means that $\eta = -$ whereas all antineutrinos are right-handed ($\eta = +$).

For a massless Dirac equation, helicity commutes with the Hamiltonian, which results in a good quantum number. Also, for massless particles helicity is the same as chirality. Due to its too abstract nature, the chirality of massive Dirac particles will not be dealt with here.

For graphene, which obeys a massless Dirac equation, chirality and helicity are the same. As the two different projections of pseudospin result in a chiral image, chirality is the expression generally used to describe the projection of the pseudospin onto the propagation direction.

The Band (valence band or conduction band). A major difference between dispersion relation in graphene and Dirac's equation is that the negative part of the Dirac cones are truly filled with the Valence Band electrons. As we can tune the density in graphene, the Fermi level can lie in the conduction band (positive energy) or in the valence band (negative energy). This is not possible with the Dirac equation (and a bit paradoxical): we can not remove "vacuum electrons" (by electron-positron pair creation).

The band index is labeled λ , and considered positive for the conduction band and negative for the valence band.

The valley (K or K') We saw earlier that charge carriers are doubly degenerate and can propagate in the K or K' valley, with opposite chiralities. Here we will define the valley subscript by ξ , which can take ± 1 values, positive for K and negative for K'.

The relation which links valley, band and chirality is

$$\boxed{\lambda = \xi\eta} \tag{1.49}$$

This relation is shown in figure 1.9.

1.3.3.3 Berry's phase

Berry introduced the notion for quantum mechanics of a phase acquired by the wavefunction in a cyclic adiabatic process.

As shown in fig.1.10, a simple view of a Berry's phase can be obtained by imagining the trajectory of a point on a sphere with which, 2 vectors are associated, one always parallel to the propagation direction and the other always perpendicular. At the end of a loop on the sphere, there is an angle corresponding to a rotation between the initial and final position of the vectors.

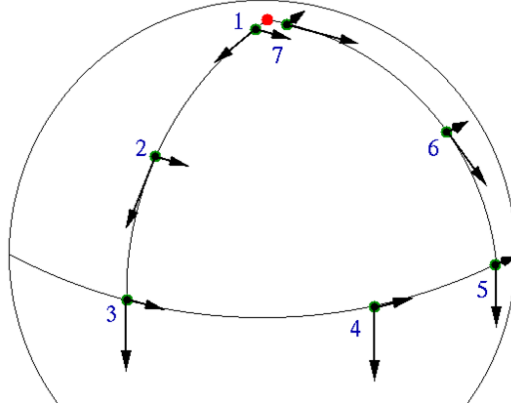


Figure 1.10: Berry's phase

In the case of graphene a Berry's phase of π is acquired along a rotation of the Pseudospin.

A simple view of this phase can be obtain recalling the wave function in the K valley:

$$\Psi(\mathbf{k}) = \begin{pmatrix} 1 \\ \lambda e^{i\theta_{\mathbf{k}}} \end{pmatrix} \varphi$$

The phase ϕ ($\Psi(\mathbf{k})e^{i\phi}$) accumulated along one adiabatic rotation of the wavevector \mathbf{k} during a time $t = T$ can be expressed as follows:

$$\phi = -i \int_0^T \langle \Psi(\mathbf{k}(t)) | \frac{\partial}{\partial t} \Psi(\mathbf{k}(t)) \rangle dt = \pi$$

This phase shift was observed [14] and leads to interesting phenomena such as weak antilocalization (describe in 2.4.3).

For a graphene bilayer Berry's phase is 2π .

1.3.3.4 Klein Tunneling

The massless nature of the charge carriers has an interesting effect: it causes an observable Klein paradox within the Dirac equation. Such a phenomenon is intuitively understandable since there is no bandgap in the massless Dirac equation. As a result, a tunnel barrier shifts the energies by a potential V_0 ; whatever the value of V_0 , there will always be available states for electrons to go.

In high-energy physics, this effect occurs for ultrarelativistic particles, like neutrinos, for which a tunnel barrier is transparent in the case of perpendicular incidence.

We should now consider the details of this phenomenon.

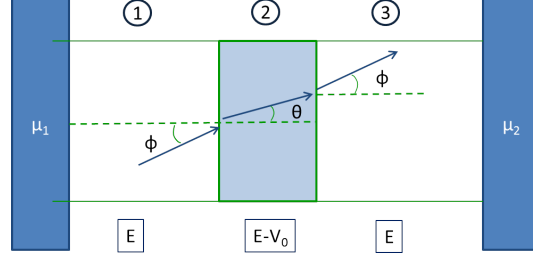


Figure 1.11: Potential barrier in graphene

In figure 1.11, three regions are defined: regions 1 and 3 are the “normal” regions of zero-applied potential. Region 2 corresponds to the tunnel barrier at potential V_0 .

The equation of motion for regions 1 and 3 is

$$H\Psi = E\Psi$$

whereas for region 2

$$H\Psi = (E - V_0)\Psi$$

The calculation is done for valley K and would have the same results if done with the other valley; also, scattering between valleys is highly improbable. We consider two component wave functions composed of incident and reflected waves:

$$\begin{aligned}\psi_1 &= e^{ik_x x + k_y y} \begin{pmatrix} 1 \\ \lambda e^{i\phi} \end{pmatrix} + r e^{-ik_x x + k_y y} \begin{pmatrix} 1 \\ -\lambda e^{-i\phi} \end{pmatrix} \\ \psi_2 &= t' e^{iq_x x + q_y y} \begin{pmatrix} 1 \\ \lambda' e^{i\theta} \end{pmatrix} + r' e^{-iq_x x + q_y y} \begin{pmatrix} 1 \\ -\lambda' e^{-i\theta} \end{pmatrix} \\ \psi_3 &= t e^{ik_x x + k_y y} \begin{pmatrix} 1 \\ \lambda e^{i\phi} \end{pmatrix}\end{aligned}$$

$k_F = 2\pi/\lambda$, $k_x = k_F \cos \phi$ and $k_y = k_F \sin \phi$, $q_x = \sqrt{(E - V_0)^2/\hbar^2 v_F^2 - k_y^2}$, $\theta = \tan^{-1}(k_y/q_x)$, λ is the band subscript, for K valley $\lambda = +$ in the conduction band (for positive energy) and $\lambda = -$ in the valence band (negative energy) so we can set $\lambda = \text{sign}E$, also $\lambda' = \text{sign}(E - V_0)$.

To compute the transmission t and reflection r parameters, we have to equate the following pairs of wave functions:

$$\begin{aligned}\psi_1(0, y) &= \psi_2(0, y) \\ \psi_2(d, y) &= \psi_3(d, y)\end{aligned}\tag{1.50}$$

Which leads to the system of equations:

$$\begin{cases} 1 + r = t' + r' \\ \lambda(e^{i\phi} - re^{-i\phi}) = \lambda'(t'e^{i\theta} - r'e^{-i\theta}) \end{cases} \quad (1.51)$$

$$\begin{cases} t'e^{iq_x d} + r'e^{-iq_x d} = te^{ik_x d} \\ \lambda'(t'e^{i(q_x d + \theta)} - r'e^{-i(q_x d + \theta)}) = \lambda te^{i(k_x d + \phi)} \end{cases} \quad (1.52)$$

If we consider $V_0 \gg E$, θ angles can be neglected implying that for $\lambda = 1$, $\lambda' = -1$:

$$\begin{cases} 1 + r = t' + r' \\ (1e^{i\phi} - re^{-i\phi}) = -(t' - r') \end{cases} \quad (1.53)$$

$$\begin{cases} t'e^{iq_x d} + r'e^{-iq_x d} = te^{ik_x d} \\ -(t'e^{iq_x d} - r'e^{-iq_x d}) = te^{i(k_x d + \phi)} \end{cases} \quad (1.54)$$

From the second system of equation we have

$$t' = r' \frac{e^{-2iq_x d}(1 - e^{i\phi})}{1 + e^{i\phi}}$$

From the second equation of the first system we have

$$r' = \frac{(e^{i\phi} - re^{-i\phi})(1 + e^{i\phi})}{2e^{-iq_x d}(i \sin(q_x d) + e^{i\phi} \cos(q_x d))}$$

$$t' = \frac{(e^{i\phi} - re^{-i\phi})(1 - e^{i\phi})}{2e^{iq_x d}(i \sin(q_x d) + e^{i\phi} \cos(q_x d))}$$

Thus with the first equation of the first system we obtain

$$r = \frac{ie^{i\phi} \sin(q_x d) \sin \phi}{\cos \phi \cos(q_x d) - i \sin(qd)}$$

Here we are interested in the transmission probability $T = |t|^2 = 1 - |r|^2$. Solving these equations we get:

$$\boxed{T = \frac{\cos^2 \phi}{1 - \cos^2(q_x d) \sin^2 \phi}} \quad (1.55)$$

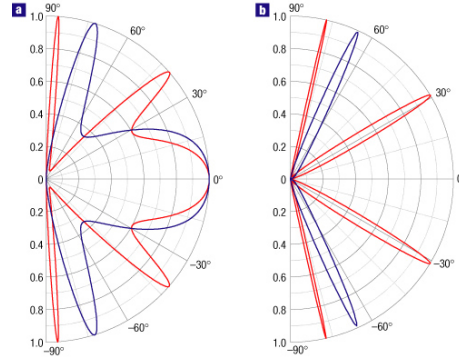


Figure 1.12: Calculation from M.I Katsnelson et al [15] of the transmission probability T through a 100-nm-wide barrier as a function of the incident angle for single- (a) and bi-layer (b) graphene.

The electron concentration n outside the barrier is chosen as $0.5 \cdot 10^{12} \text{cm}^{-2}$ for all cases. Inside the barrier, hole concentrations p are $1 \cdot 10^{12} \text{cm}^{-2}$ and $3 \cdot 10^{12} \text{cm}^{-2}$ for red and blue curves, respectively (such concentrations are most typical in experiments with graphene). This corresponds to the Fermi energy E of incident electrons approximately 80 and 17 meV for single- and bi-layer graphene, respectively, and $\lambda \sim 50 \text{nm}$. The barrier heights V_0 are (a) 200 and (b) 50 meV (red curves) and (a) 285 and (b) 100 meV (blue curves).

In figure 1.13 a charge carrier arriving on a potential gap is represented. The system is at equilibrium so the Fermi level is constant everywhere, to represent the potential barrier we have to shift the Dirac cone.

When a charge carrier arrives on the shifted Dirac cone it can pass from conduction band to valance band. If the potential is smooth it must remain in the same valley. This implies that it will propagate in the same valley, but in a different band, with an opposite wave vector. The momentum is conserved, so in the valance band the momentum will be antiparallel to the wavevector [15].

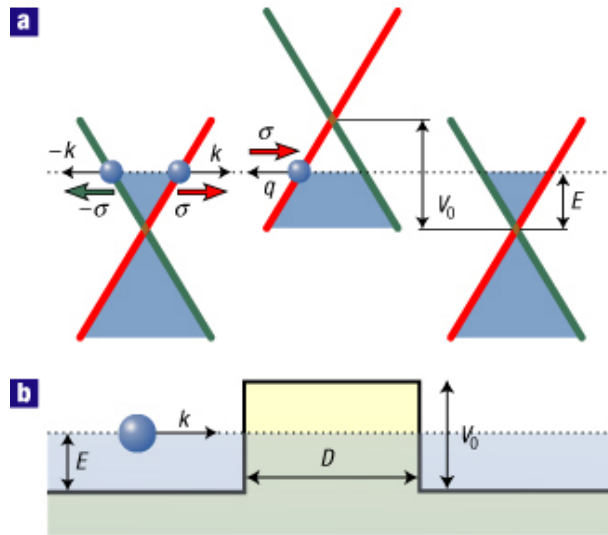


Figure 1.13: schematic diagram of the low energy bandstructure in graphene on top and potential barrier of high V_0 and width D at the bottom. extracted from [15].

This was seen experimentally in ref [16] and [17].

1.4 Bilayer graphene

Bilayer graphene is a very interesting 2DEG in that both its layers are vertically coupled, which induces a change in its bandstructure.

The bandstructure can be calculated by extending the tight-binding model developed for graphite to a finite number of graphene layers. Computation is based on ref. [18]

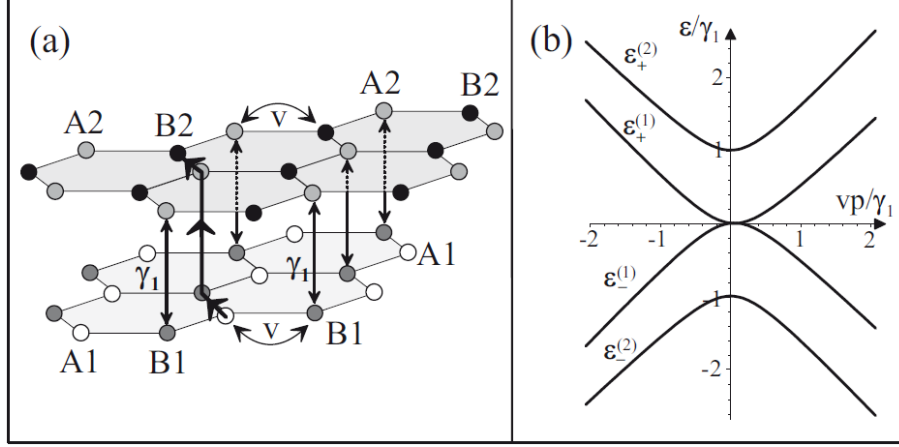


Figure 1.14: The bandstructure of bilayer graphene [18]

The detailed calculation for bilayers would be an unnecessary digression given the core subject of this work. However, an overview on the bandstructure of a bilayer could prove judicious at this point.

The calculation is similar to that for the monolayer, but a little more complicated, because there are 2 layers with 2 atoms per cell, which causes more hopping paths for the electrons.

We consider here bilayer graphene in an A2-B1 Bernal-stacking configuration. Fig. 1.14 shows that the A1 and B1 atoms are on the lower layer and the A2 and B2 atoms on the upper layer; every B1 atom is situated directly under an A2 atom, whereas A1 and B2 atoms are not aligned in the z direction.

This leads us to write the Hamiltonian in the following basis

$$\Psi_{\xi=+} = \begin{bmatrix} \Psi_{A1} \\ \Psi_{B2} \\ \Psi_{A2} \\ \Psi_{B1} \end{bmatrix}, \quad \Psi_{\xi=-} = \begin{bmatrix} \Psi_{B2} \\ \Psi_{A1} \\ \Psi_{B1} \\ \Psi_{A2} \end{bmatrix}$$

$$H = \xi \begin{pmatrix} -\frac{\Delta}{2} & v_3\pi & 0 & v\pi^\dagger \\ v_3\pi^\dagger & \frac{\Delta}{2} & v\pi & 0 \\ 0 & v\pi^\dagger & \frac{\Delta}{2} & \xi\gamma_1 \\ v\pi & 0 & \xi\gamma_1 & -\frac{\Delta}{2} \end{pmatrix} \quad (1.56)$$

Where γ_{12} is the hopping term between a site 1 and a site 2.

The dominant hopping term is between A and B atoms of the same layer:

$$\gamma_{A1B1} = \gamma_{A2B2} = \gamma_0$$

$$v_F = \frac{3}{2} \frac{a_0 \gamma_0}{\hbar}$$

Due to the Bernal stacking, the main hopping term between layers is

$$\gamma_{A_2B_1} = \gamma_1$$

The other term coupling both layers is

$$\gamma_{A_1B_2} = \gamma_3$$

$$v_3 = \frac{3}{2} \frac{a_0 \gamma_3}{\hbar}$$

where $v_3 \ll v_F$.

$$\Delta = \varepsilon_1 - \varepsilon_2$$

where ε_1 and ε_2 stand for the on-site energy of layers 1 and 2.

The Hamiltonian has four valley degenerate bands. Solving it gives us the energy eigenvalues E_{\pm}^{α} , ($\alpha = 1, 2$)

$$(E^{\alpha})^2 = \frac{\gamma_1^2}{2} + \frac{\Delta^2}{4} + \left(v^2 + \frac{v_3^2}{2}\right) p^2 + (-1)^{\alpha} \left(\frac{(\gamma_1^2 - v_3^2 p^2)^2}{4} + v^2 p^2 (\gamma_1^2 + \Delta^2 + v_3^2 p^2) + 2\xi \gamma_1 v_3 v^2 p^3 \cos 3\phi \right)^{1/2}$$

where $\mathbf{p} = p(\cos\phi, \sin\phi)$

As regards the lower-band energy

$$E_{\pm}^1 = \pm \frac{1}{2} \gamma_1 \left(\sqrt{1 + 4v^2 p^2 / \gamma_1^2} - 1 \right) \quad (1.57)$$

which leads to the definition of an effective mass

$$m_c = \frac{p}{\frac{\partial E^1}{\partial p}} = \frac{\gamma_1}{2v^2} \sqrt{1 + \frac{4\pi \hbar^2 v^2 n}{\gamma_1^2}} \quad (1.58)$$

A low-energy Taylor expansion of 1.57 leads to a quadratic energy spectrum $E_1 \approx p^2/2m_c$, where $m_c \approx \gamma_1/2v^2$, which experiment gives to be $m_c \approx 0,035m_e$; at high energy the energy, spectrum becomes linear $E_1 \approx vp$ and the crossover takes place at $p \approx \gamma_1/2v$. Computing experimental values for graphite showed that the crossover occurs at a density $n = 4,36.10^{16}m^{-2}$. The estimated density at which the higher-energy band begins to be filled is $n^{(2)} = 3,49.10^{17}m^{-2}$, which is not attainable by classical-transport experiments.

Remarkably, setting both layers at different potentials (i.e. $\Delta \neq 0$) makes it possible to open a gap at the Fermi level (see ref.[19]).

At low energy, in the quadratic regime, it is possible to write an effective Hamiltonian in a simple way

$$H = -\frac{1}{2m_c} \begin{pmatrix} 0 & (\pi^\dagger)^2 \\ \pi^2 & 0 \end{pmatrix} \quad (1.59)$$

where $\pi = p_x + ip_y$.

This Hamiltonian is applied to the following wavefunction, using the same notation as in graphene for the K and K' valleys:

$$\Psi_{\xi=+1} = \begin{pmatrix} \psi_{A1} \\ \psi_{B2} \end{pmatrix}, \quad \Psi_{\xi=-1} = \begin{pmatrix} \psi_{B2} \\ \psi_{A1} \end{pmatrix}$$

Chapter 2

Electronic Transport

2.1 Mesoscopic physics

Mesoscopic physics is a field of condensed-matter physics and describes materials at and below an intermediate lengthscale, defined as coherence length, which separates the quantum from the classical behavior of a conductor.

In order to provide an accurate picture of the transport properties of graphene, we will firstly introduce some concepts of mesoscopic physics, and then examine basic results concerning electronic transport. As a conclusion, we will see how these concepts apply to graphene.

Physics has two distinct approaches: the microscopic and macroscopic approaches. The microscopic phenomena are best described by the laws of quantum physics whereas, for the macroscopic phenomena, classical physics applies. Microscopic physics' first scope of study was centered on very small objects, typically of atomic size ($< 1\text{nm}$). For many years, the observation of quantum effects was confined to atomic-size objects or to the properties of light. Larger objects, by nature, made it very hard to observe let alone maintain coherence. During the past three decades, a vast series of advances have been made when it comes to building intermediate-size devices. Intermediate size ranges from objects comprised of a few molecules to objects of naked-eye visibility. Such progress, combined to low-temperature technology, made it possible to reach phase coherence for micron-size objects and to study decoherence processes, as well as the crossover from quantum to classical physics.

The following chapter will be centered on the transport of charge carriers in mesoscopic-size 2DEGs.

2.2 Two-dimensional electron gases

A 2-dimensional electron gas (2DEG) is a gas composed of electrons moving freely in two directions x and y and in a very confined sort of way in a third one z .

Up to 2004, all the 2DEG were made by means of heterojunctions of semiconductors with a different band gap, silicon oxide semiconductor interface (like in MOS-FETs), or at the surface of liquid helium.

Most 2DEGs are made with semiconductors, which we will thereafter call conventional 2DEG.

So far, the better-quality conventional 2DEG have been produced by means of the heterojunction of aluminum-gallium-arsenide (AlGaAs) and gallium-arsenide (GaAs). In the widegap AlGaAs, the conduction band is higher than in the narrowgap GaAs. As a consequence the electrons exit the n-doped AlGaAs leaving positively charged donors behind. In order to maintain the equilibrium with a flat Fermi level everywhere, the conduction and valence bands in the narrowgap GaAs side are bent downwards to form a quantum well. As a result, the electron motion perpendicular to the interface is frozen in the ground state and the electron density is sharply peaked near the GaAs-AlGaAs interface, as shown in fig.2.1.

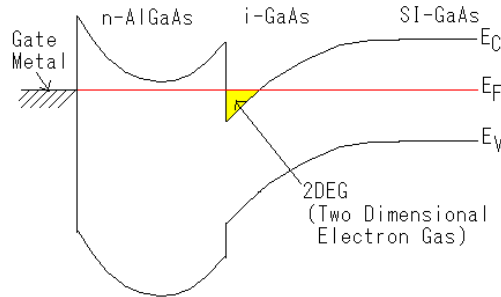


Figure 2.1: Schematic view of a 2DEG at the interface of 2 semiconductors

The carrier concentration in conventional 2DEGs typically ranges from $2 \cdot 10^{11} \text{ cm}^{-2}$ to $2 \cdot 10^{12} \text{ cm}^{-2}$. Therefore, a 2DEG is a very practical structure: its density can be controlled with metallic gates, which results in the possible engineering of constriction, quantum dots, tunnel barriers and many other useful probing devices for the study of electrons properties. The electronic mobility (define in eq. 2.2) is a good tool to compare the 2DEGs quality. Figure 2.2 shows the maximal mobility obtained in conventional 2DEG over the year.

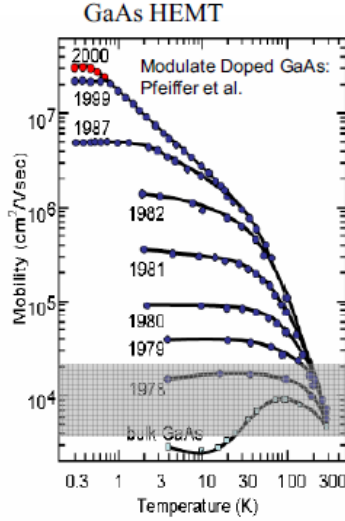


Figure 2.2: Mobility versus temperature in conventional 2DEGs over the years

Our interest in graphene has arisen from our long standing interest in electronic properties in conventional 2DEG.

2.3 Lengthscales

A series of length scales are central in characterizing the transport regime.

- λ_F is the Fermi wavelength, it is the wavelength of an electron at the Fermi level, i.e. electrons participating in transport. In most cases, the Fermi wavelength is the shortest length in our problem: it can vary from few of a nanometer tenths in metals to few tens of nanometers in graphene and conventional semiconductor heterojunctions.
- l_ϕ the phase coherence length. The phase of the wavefunction is always defined within this length scale, which is the most important length to consider when looking for quantum effects. It varies with temperature: below 1K it ranges from few tenths of a micron to few microns and decreases very quickly when temperature increases.
- l_e is the elastic mean free path between two collisions with impurities. An elastic collision maintains phase coherence but favors multiple interferences of the wavefunction with itself.

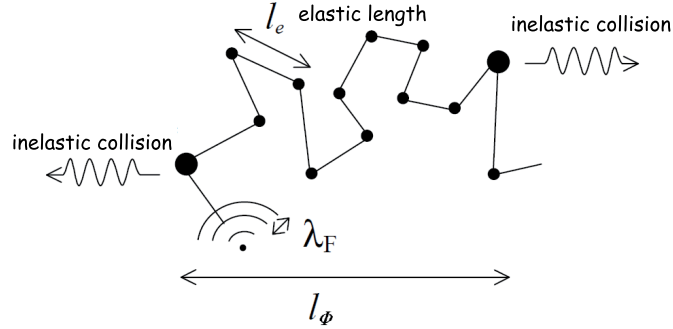


Figure 2.3: Various characteristic lengthscales

When we consider the relation between these lengthscales and the length l of the sample, then transport is said to diffusive when $l > l_e$ and ballistic when $l < l_e$.

2.4 Transport, from macro to micro via meso

In this section, we examine electronic transport from a macroscopic scale where classical physics is valid to a microscopic scale where quantum phenomena have to be taken into account.

2.4.1 Drude model

Electron transport in macroscopic devices is generally described using the classical Drude model. It is also valid for a mesoscopic system in which interferences effects average as is the case to first order in a diffusive conductor with many elastic impurities.

It is based on the classical description of free electrons with a charge $q = -e$ and a mass m .

Inspired by the kinetic theory of gas, Drude introduced this model in 1900. In this model the electron is free to move in response to an electric field in a conductor, with ions and impurities randomly distributed and considered as static. The electrons collide with these impurities, either elastically or inelastically. Also, electrons may collide with other electrons. We suppose here that the velocity of an electron is randomly redistributed after a collision, therefore we can write $\langle \vec{v} \rangle = \vec{0}$ when the system is not driven by an electric field.

This model is not aimed at describing the microscopic path of the electrons. Consequently, the drift velocity under an electric field E : $v_{drift} = \langle \vec{v} \rangle$ is now different from zero.

The drift velocity is defined as

$$\vec{v}_{drift} = -\frac{e\tau}{m}\vec{E} \quad (2.1)$$

and the mobility as

$$\mu = \frac{|\vec{v}_{drift}|}{|\vec{E}|} \quad (2.2)$$

where τ is the time between 2 collisions. Originally seen as the transport time τ_{tr} calculated using the Boltzmann equation, with two basic assumptions:

- between collisions, electrons move as classical particles, subject only to the external field;
- collisions are independent instantaneous events, which occur with a probability $1/\tau_{tr}$ per unit of time.

The current density which is defined by the density of charge crossing a conductor per unit of time is written

$$\vec{j} = \frac{ne^2\tau}{m} \vec{E} \quad (2.3)$$

from which we define the conductivity

$$\vec{j} = \sigma \vec{E}$$

$$\sigma_D = \frac{ne^2\tau_{tr}}{m} \quad (2.4)$$

This model explains Ohm's law.

Although the Drude model provides us with a valid result, it comes with reservations:

- in metals, the electric field vanishes due to electron screening; as a consequence the system is not fully described using a view of a motion related to an electrical field;
- the Coulomb interactions are not taken to account;
- a priori there is no reason to presuppose that electrons have a classical motion and that their collisions must be considered independent.

Also, τ can hide a multitude of collisions of various types.

2.4.1.1 Collision time τ

τ_{tr} is not easily computed.

At this point, it is important to draw the distinction between the transport time τ_{tr} and the lifetime τ_e of an electronic wavefunction: τ_e depends on the number of collisions; τ_{tr} depends on the number of collisions and the scattering angle and will not account for collisions with zero scattering angles. A large τ_{tr}/τ_e ratio indicates a predominance of scattering in the forward direction.

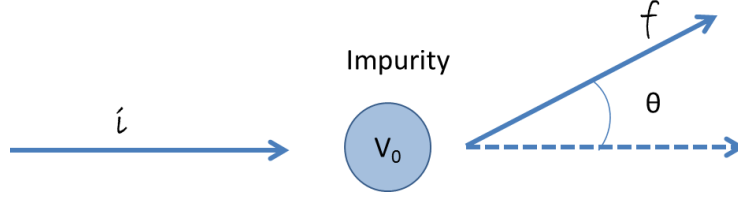


Figure 2.4: Schematic of scattering

The general expression for τ_{tr} as per the Boltzmann law is:

$$\frac{1}{\tau_{tr}} = n_{imp} v_F \int (1 - \cos\theta) |f(\theta)|^2 d\theta \quad (2.5)$$

while, for τ_e

$$\frac{1}{\tau_e} = n_{imp} v_F \int |f(\theta)|^2 d\theta \quad (2.6)$$

$f(\theta)$, the scattering amplitude at 2 dimensions, is has the dimension of a length, is a non trivial function correlated with the type of scatterers.

2.4.2 Coherent diffusive transport

The Drude law can be applied to this type of transport after a slight adaptation. Schrödinger electrons have a 2D density of

$$N = \frac{2S}{(2\pi)^2} \int d^2k = \frac{2S}{(2\pi)^2} \pi k_F^2$$

$$n = \frac{k_F^2}{2\pi}$$

We can now express the Drude conductivity

$$\sigma_D = \frac{k_F^2}{2\pi} \frac{e^2}{m} \tau_{tr} = \frac{e^2}{h} k_F l_{tr}$$

where $l_{tr} = v_F \tau_{tr}$ is the mean free path, $v_F = \hbar k_F / m$ is the Fermi velocity of particles with parabolic dispersion.

In coherent systems, conductance is meaningful, not conductivity. Therefore, we will describe transport properties in terms of conductance G

$$G = \sigma \frac{W}{L}$$

with sample width W and length L

The Drude conductance is:

$$G_D = \frac{e^2}{h} k_F l_{tr} \frac{W}{L}$$

At this point, we can introduce the number of electronic modes which the sample can contain, as for a waveguide, it is $M = \frac{W}{\lambda_F/2}$

$$G_D = M \frac{2e^2}{h} \frac{\tilde{l}_{tr}}{L}$$

where $\tilde{l}_{tr} = \frac{\pi}{2} l_{tr}$

We must now include the value of the contact resistance $R_c = h/2e^2M$ (calculated considering a ballistic conductor and assuming that the contact are reflectionless) in the value of the total resistance.

$$R_{classic} = \frac{h}{2e^2M} + \frac{1}{G_D} \quad (2.7)$$

As a result

$$G_{classic} = \frac{2e^2M}{h} \frac{\tilde{l}_{tr}}{L + \tilde{l}_{tr}} \quad (2.8)$$

The above applies to semi-classical diffusive conductance, when all interference effects are disregarded. When interference effects are taken into account, correction terms have to be applied to conductance

$$G_Q = G_{classic} + \Delta G_{wl} + \delta G_{ucf} \quad (2.9)$$

where ΔG_{wl} is the weak localization correction and δG_{ucf} the universal conductance fluctuation term, both terms will be described in the following two sections.

2.4.3 Weak localization

Weak localization was first calculated in ref. [20] after a publication [21], which offered a scaling theory for localization, as well as a method to compute quantum corrections. The weak localization correction consists of a correction of the order of $1/k_F l_{tr}$. Its origin lies to coherent backscattering of electrons with momenta k and $-k$, it leads to a decrease of the conductivity compared to its classical value. A series of simple arguments will help us fully appreciate this correction.

If an electron is backscattered, the reverse path is also possible. If the length of the electron's paths is less than the coherence length, they will interfere positively leading to an increase of the probability of return.

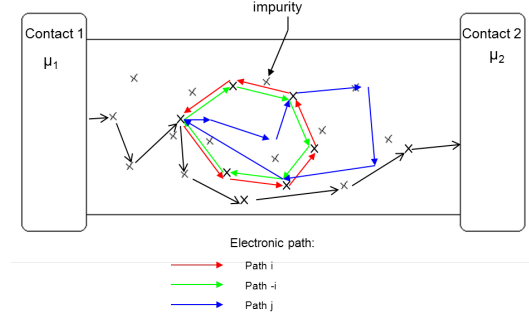


Figure 2.5: Schematic of different electronic paths. The colored arrows represent the electronic paths while the black crosses represent the scatterers; in a WL regime, the equal but opposite the red and green paths interfere constructively.

The classical probability of return is given by:

$$P = \left| \sum_i A_i \right|^2 = \sum_i |A_i|^2 + \sum_{j \neq i} A_j^* A_i + A_i^* A_j$$

Where i and j are all the return paths.

In the case of coherent transport, our model must take the inverse path into account.

$$P = \left| \sum_i A_i + A_{-i} \right|^2 \quad (2.10)$$

$$P = \sum_i (|A_i|^2 + 2 \sum_i A_i^* A_{-i} + A_{-i}^* A_i + \sum_{j \neq i, -i} A_j^* (A_i + A_{-i}) + A_i (A_j + A_{-j})^*) \quad (2.11)$$

The interference term $\sum_i A_i^* A_{-i} + A_{-i}^* A_i$ causes the probability of return to double, thus making it possible to calculate conductivity.

$$\Delta G_{wl} = \frac{2e^2}{\pi h} \ln \left(\frac{l_\phi}{l_e} \right) \quad (2.12)$$

A simple and detailed computation of the weak localization can be found in [22] or in [23].

It is interesting to note that the weak localization is suppressed by a magnetic field:

$$A_i \propto \exp \left(i \int \frac{\boldsymbol{\pi} \cdot d\mathbf{l}}{\hbar} \right)$$

where $\boldsymbol{\pi} = \mathbf{p} - e\mathbf{A}$

We can now easily demonstrate that

$$A_i(B) = A_i(0) \exp\left(i2\pi \frac{\phi_i}{\phi_0}\right)$$

and:

$$A_{-i}(B) = A_i(0) \exp\left(-i2\pi \frac{\phi_i}{\phi_0}\right)$$

Where ϕ_i is the magnetic flux in a closed backscattering path and ϕ_0 is the flux quantum, $\phi_0 = h/e$.

As a result, the interference term can be expressed as

$$A_i^* A_{-i} + A_{-i}^* A_i = |A_i(0)|^2 2 \cos\left(4\pi \frac{\phi_i}{\phi_0}\right)$$

A critical magnetic field B_c can be define, beyond which the weak localization effects are suppressed. Considering that the maximum closed path is given by the coherence length l_ϕ , the maximale surface (circle) is $l_\phi^2/4\pi$.

$$B_c \sim \frac{\phi_0}{l_\phi^2} \tag{2.13}$$

We needn't consider resonance when $\phi_i = n\phi_0$ because the closed interfering paths have sizes ranging from $l = 0$ to $l = l_\phi$.

In graphene, the interferences in the returning path can be destructive due to the Berry phase π , while they are constructive in a conventional 2DEG. This can result in an increase in conductance at zero field (manifestation of the weak antilocalization phenomenon). As per ref. [24], both weak localization and antilocalization were observed in graphene. The referenced article demonstrated that antilocalization takes place when dephasing time is small compared to elastic scattering time for intravalley scattering.

2.4.4 Universal conductance fluctuations (UCF)

The UCF are reproducible fluctuations in the conductance and are a function of the density or of the magnetic fields. These fluctuations are caused by quantum interferences between the many electronic paths which contribute to the conductance in the diffusive case. These fluctuations have an amplitude of the order of e^2/h for a sample smaller than l_ϕ .

$$\delta G \sim \frac{e^2}{h}$$

For a sample of length L larger than l_ϕ :

$$\delta G \sim \frac{e^2}{h} \frac{1}{N_{ucf}^{\frac{4-d}{2}}}$$

where $N_{ucf} = L/l_\phi$, d is the dimension.

Temperature limits the phase coherence length, thus leading to variations in the UCF amplitude. If $k_B T > \hbar/\tau_\phi$, then thermal energy can be viewed as N_{ucf} uncorrelated channels in parallel, having a width of \hbar/τ_ϕ each

$$N_{ucf} = \frac{k_B T}{\hbar \tau_\phi}$$

where $l_\phi^2 = D\tau_\phi$.

2.4.5 Einstein-Smoluchowski's diffusion approach

In 1905, Einstein and Smoluchowski proposed a diffusion relation based on the study of Brownian motion. This relation is a first instance of the fluctuation dissipation theorem (formulated later in 1928 by Nyquist and proved by Callen and Welton in 1951). Einstein's relation brings a new vision to electron transport. It introduces the fact that transport can happen not only with an electrical field but also due to chemical potential difference.

This general diffusion relation can be applied to charged particles motion, and expressed as

$$\sigma_E = e^2 \frac{\partial n}{\partial \mu} D \quad (2.14)$$

where D is the diffusion coefficient.

Here n is the density of charged particle and μ the chemical potential, the ratio $\partial n/\partial \mu$ can be viewed as a compressibility, and D is the diffusion coefficient

$$\mu = F_{N+1} - F_N$$

where N is the number of particles in the system.

$F = U - TS$ is the Helmholtz energy. It is a thermodynamic potential which measures the work obtainable from a closed system.

To take both in account:

$$j = \sigma E + eD\nabla n$$

The electrochemical potential can be used to take both contributions into account $\mu_{el} = \mu - e\phi$ where $E = -\nabla\phi$. μ_{el} is constant in space when the system is at thermodynamic equilibrium.

2.4.6 Landauer's description of quantum transport

If we consider smaller systems ($L \sim l_e < l_\phi$), Drude's and Einstein's law prove insufficient to explain transport phenomena such as conductance quantization or the fact that the conductance does not increase linearly with the width.

At this point, an introduction to the Landauer formalism will be useful to describe transport under the quantum Hall effect. This description is based on the diffusive approach.

The Landauer equation states that

$$G = \frac{2e^2}{h}MT \quad (2.15)$$

where T represents the average probability that an electron injected from the source contact transmits to the drain contact at the other end of the sample and M is the number of electronic transverse modes.

In this description, graphically represented in fig. 2.6, both contacts are considered as infinite electron reservoir. The conductor is connected to these contacts by 2 leads. Contact resistance is taken in account in this formula.

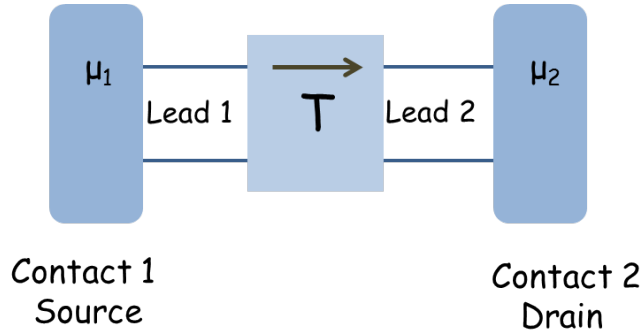


Figure 2.6

This approach is very useful to describe ballistic conductors when conduction through a small number of channel is achievable needing a full quantum description. Is also useful in the quantum Hall effect as we will see later. It is very well described in ref. [22]

However, we will not use this approach to describe transport in graphene at zero magnetic field, because all our experiments on graphene are in the diffusive regime. Until very recently the ballistic regime had not been observed in graphene. A regime approaching ballistic conditions was observed in suspended graphene in ref [25].

2.5 Transport in graphene

In most experiments with graphene, only diffusive transport was observed. Therefore, some theoretical calculations for this regime will be introduced in this section. Note that conductivity was computed using Drude's and Einstein's laws.

The nature of the scattering defect plays an essential role in the value of conductivity and has a major effect on the transport collision time τ_{tr} . There is still an ongoing debate to determine which impurity is the dominant scatterer.

2.5.1 Magnitudes

Monolayer Characteristic lengths:

$$50\text{\AA} \lesssim \lambda_F \lesssim 0.3\mu m$$

$$v_F \sim c/300$$

Fermi wave vector

$$n = g_s g_v \int \frac{d\vec{k}}{(2\pi)^2} \rightarrow k_F = \sqrt{\frac{4\pi n}{g_s g_v}}$$

where $g_s = 2$ is the spin degeneracy and $g_v = 2$ is the valley degeneracy.
Fermi Energy

$$E_F = \hbar v_F k_F = \hbar v_F \sqrt{\frac{4\pi n}{g_s g_v}}$$

Density is usually tuned using a back gate:
 $n = CV_g$ where $C \sim 7.2 \cdot 10^{10} \text{cm}^{-2}$

The typical energies that we can probe are:

$$0.05\text{eV} < E_F < 0.3\text{eV}$$

The maximal energy is limited by the maximum gate potential that we can apply without breaking the graphene (around $V_G = 100V$), the minimal energy is due to some residual doping at low density.

Bilayer In bilayer the energies reachable are of the same order as in monolayer. The important change here is given by the quadratic energy dispersion:

$$E_F = \frac{\hbar^2 k_F^2}{2m^*} = \frac{2\pi \hbar^2 n}{m^* g_s g_v}$$

with:

$$m^* = 0,035m_e$$

2.5.2 Incoherent diffusive transport

Two factors enter in the expression of conductivity:

- current flows due to external electric field (Drude law) $\overrightarrow{j}_{drift} = \sigma \overrightarrow{E}$
 - the other factor is diffusion; current is given by Fick's law: $\overrightarrow{j}_{diff} = -qD\overrightarrow{\nabla}n$
- where D is the Diffusion coefficient.

$$\vec{j} = \overrightarrow{j}_{drift} + \overrightarrow{j}_{diff} = -qD\overrightarrow{\nabla}n + \sigma\overrightarrow{E}$$

We can set \overrightarrow{E} in order that $\vec{j} = 0$

We consider the system at thermodynamic equilibrium, which implies that $\overrightarrow{\nabla}\mu=0$

$$\mu(\vec{r}) \simeq \mu_{homogeneous}(n(\vec{r})) + qV(\vec{r})$$

$$\frac{\partial\mu_{homogeneous}}{\partial n}\overrightarrow{\nabla}_r n + q\overrightarrow{\nabla}_r V = 0$$

$$\sigma = q^2 D \frac{\partial n}{\partial \mu_h}$$

In graphene, $D = \frac{v_F^2 \tau}{2}$

$$\sigma = \frac{e^2 v_F^2}{2} \tau_{tr} \frac{\partial n}{\partial \mu}$$

if $T \ll T_F$: $\frac{\partial n}{\partial \mu_h} = \rho(\varepsilon_F)$, $\rho(\varepsilon_F)$ is the density of states

$$\sigma = \frac{2e^2}{h} \frac{\tau_{tr}}{\hbar} |\varepsilon_F|$$

Now, if we have $T \gg T_F$ [26]

$$\mu = k_B T \ln(n \lambda_T^2)$$

$$\lambda_T \simeq \frac{\hbar v_F}{k_B T}$$

$$\frac{\partial \mu}{\partial n} = \frac{k_B T}{n}$$

$$\sigma = 4 \ln 2 \frac{e^2}{h} \frac{k_B T}{\hbar} \tau_{tr}$$

$$\boxed{\sigma(T, V_g) \simeq \frac{e^2}{h} \frac{\tau_{tr}}{\hbar} \max(k_B T, \hbar v_F \sqrt{\alpha V_g})} \quad (2.16)$$

2.5.3 Scattering processes

Here we will introduce some scattering processes which were found relevant for the electronic transport in graphene.

This part is largely inspired by the supplementary material of [27] and explanations of J.N. Fuchs.

Firstly, we should recall the definition of the transport time τ_{tr}

$$\frac{1}{\tau_{tr}} = n_{imp} v_F \int (1 - \cos\theta) |f(\theta)|^2 d\theta \quad (2.17)$$

where the transport cross-section is

$$A_{tr} = \int (1 - \cos\theta) |f(\theta)|^2 d\theta \quad (2.18)$$

The cross-section which accounts for τ_e is:

$$A = \int |f(\theta)|^2 d\theta \quad (2.19)$$

We remind that $f(\theta)$ is the scattering amplitude, a non trivial function which depends on the type of scatterers.

2.5.3.1 Resonant impurities

This section will focus on a specific type of resonance, called \ln^2 resonance, which is the result of electrons scattering on high potential impurities of a range R , shorter than the Fermi wavelength $R \ll \lambda_F$.

This result comes essentially from ref [28] explained by J.N. Fuchs in the supplementary material of ref. [27].

Considering as sketch on fig 2.7 a potential where $U(r) = V_o > 0$ for $r < R$ and $U(r) = 0$ for $r > R$ we have

$$f(\theta) = \frac{e^{i2\delta(k)} - 1}{i\sqrt{2\pi k}} [1 + e^{-i\theta}] = \frac{\sqrt{\pi/2k}}{\frac{J_0(\bar{k}R)}{kR J_1(kR)} + \ln(\frac{2}{\gamma_E k R}) + i\frac{\pi}{2}} [1 + e^{-i\theta}] \quad (2.20)$$

Here $\delta(k)$ is the s wave scattering phase shift, J_n are Bessel functions and $\gamma_E = e^\gamma \sim 1,78$. The wavevector $\bar{k} = |\varepsilon - V_0|/\hbar v_F$.

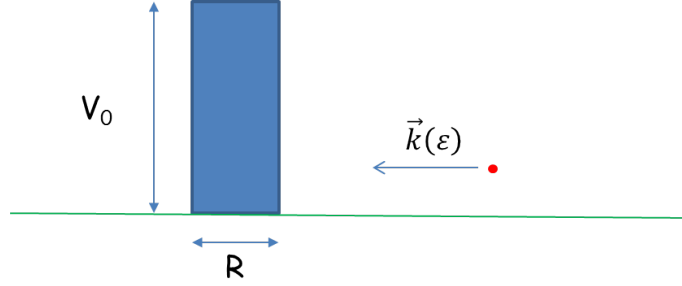


Figure 2.7

We can now compute A and A_{tr} :

$$A = \frac{8\sin^2\delta}{k} \quad (2.21)$$

$$A_{tr} = \frac{4\sin^2\delta}{k} = \frac{A}{2} \quad (2.22)$$

There are three resulting cases:

- The most probable case happens when the logarithmic term wins because $J_0(\tilde{k}R) \approx 0$. This is possible when $\varepsilon \ll V_0$ because $\tilde{k}R \approx V_0R/\hbar v_F$ can be larger than 1 and reach the zero of the Bessel function.

$$f(\theta) \approx \frac{-\sqrt{\pi/2k}}{\ln(\frac{2}{\gamma_E kR})} [1 + e^{-i\theta}] \approx \frac{\sqrt{\pi/2k}}{\ln(kR)} [1 + e^{-i\theta}] \quad (2.23)$$

This corresponds to a phase shift:

$$\delta(k) \approx -\frac{\pi}{2\ln(kR)} \rightarrow 0 \quad (2.24)$$

leading to a transport cross-section:

$$A_{tr} \approx \frac{4\delta^2}{k} \approx \frac{\pi^2}{k\ln^2(kR)} \quad (2.25)$$

and a transport time

$$\tau_{tr} \approx \frac{k\ln^2(kR)}{n_{imp}v_F\pi^2} \propto k\ln^2(kR) \quad (2.26)$$

As a result, conductivity is

$$\sigma \approx \frac{2}{\pi} \frac{e^2}{h} \frac{n_c \ln^2(R\sqrt{\pi n_c})}{n_{imp}} \quad (2.27)$$

where n_c is the density of charge carriers

- When the term J_0/J_1 wins,

$$\delta(k) \approx kR \frac{\pi J_1(\tilde{k}R)}{2J_0(\tilde{k}R)} \quad (2.28)$$

the resulting cross section is

$$A_{tr} \approx \frac{4\delta^2}{k} \approx \left(\frac{\pi J_1(\tilde{k}R)}{2J_0(\tilde{k}R)} \right)^2 kR^2 \quad (2.29)$$

which gives us

$$\sigma \approx \frac{e^2}{h} \frac{1}{n_{imp} R^2} \quad (2.30)$$

This result implies that constant conductivity would be reached, which has never been observed.

- When $\nu\pi/2$ wins, then $\frac{J_0(\tilde{k}R)}{kR J_1(\tilde{k}R)} + \ln\left(\frac{2}{\gamma_E kR}\right) = 0$. This implicates both $\tilde{k}R$ and kR ; this can happen at a given density, but there is no reason for it to happen throughout the range of density we can achieve. In this case $\sigma \approx \frac{\pi}{2} \frac{e^2}{h} \frac{n_c}{n_{imp}}$

2.5.3.2 Charged impurities

The following calculation was done by Nomura and MacDonald in ref. [29].

For charged impurities, we can use the Fermi golden rule to compute τ_{tr} .

$$\frac{1}{\tau_{tr}} = \frac{2\pi}{\hbar} n_{imp} |\overline{\tilde{V}(q)}|^2 \rho(\varepsilon_F) \quad (2.31)$$

$\tilde{V}(q) = \frac{2\pi e^2}{q}$, if the potential is not screened. As no intervalley scattering is allowed, q must link one edge to another at the Fermi level, implying that $q = k_F$, as shown in the figure below.

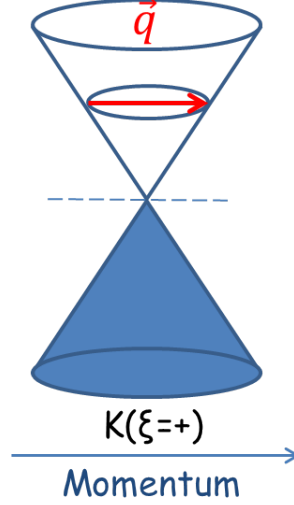


Figure 2.8: Intravalley scattering

As a consequence, we obtain

$$\frac{1}{\tau_{tr}} = \frac{2\pi}{\hbar} n_{imp} \left(\frac{2\pi e^2}{k_F} \right)^2 \rho(\varepsilon_F) \quad (2.32)$$

$$\frac{1}{\tau_{tr}} = n_{imp} \left(\frac{e^2}{\hbar v_F} \right)^2 \frac{v_F}{k_F} = n_{imp} r_s \frac{v_F}{k_F} \quad (2.33)$$

$$\boxed{\sigma(n_c) \sim \frac{e^2}{h} \frac{n_c}{n_{imp}}} \quad (2.34)$$

Adding electronic screening of the charged impurities like Thomas-Fermi screening $\tilde{V}(q) = \frac{2\pi e^2}{q+\kappa}$, will result in the addition of a numerical factor in the expression of σ without altering its dependency on n_c .

2.5.4 Experimental transport results

Many interesting experiments have been done on this subject and it seems that there is no clear consensus to the question of which scatterers limit the mobility. Both types of scatterers described before are present : Coulomb impurities leading to long range disorder and neutral impurities leading to short range disorder. Recent experiments tend to show that the short range neutral impurities are those which limit the mobility even though Coulomb scatterers are present.

An experiment done by M. Monteverde et al measured that transport is dominated by short-range impurities [27], this experiment will be detailed in chapter 7.

M. Fuhrer studied σ as a function of doping in [30] and claims that it is the long range Coulomb impurity scatterers which limit mobility.

In another article [31] M.Fuhrer showed that both short-range and long-range impurities are active. Long range are coulomb impurity leading to $\sigma \sim n$ while the short-range impurities led to $\sigma = cte$. For these measurements, the dielectric constant was changed (by adding ice) to screen the long-range impurities.

Experiments were carried out on different substrates and in different environments with different dielectric constants (between 1 and 80) by Geim's group [32]. If Coulomb impurities had been the major source of scattering they should have observed a large difference in the values of the mobility μ whereas they did not. M. Fuhrer's experiments showed that the major source of scattering was not the charges trapped in substrates, by using different substrates; also, the difference in kappas showed that the major scatterers were not the charges trapped underneath graphene.

2.5.5 Adsorption on Graphene

As is the case with graphite, graphene has an efficient atom-adsorbing surface. Interestingly, the electronic properties of graphene change when its surface adsorbs atoms. The adsorbed atoms cause a change in the electronic density of graphene, which results in a shift of the Fermi level from the Dirac point.

K. Novoselov et al showed that the adsorption or desorption of even a single atom can be observed by transport measurement, as shown in fig. 2.9 ref.[33].

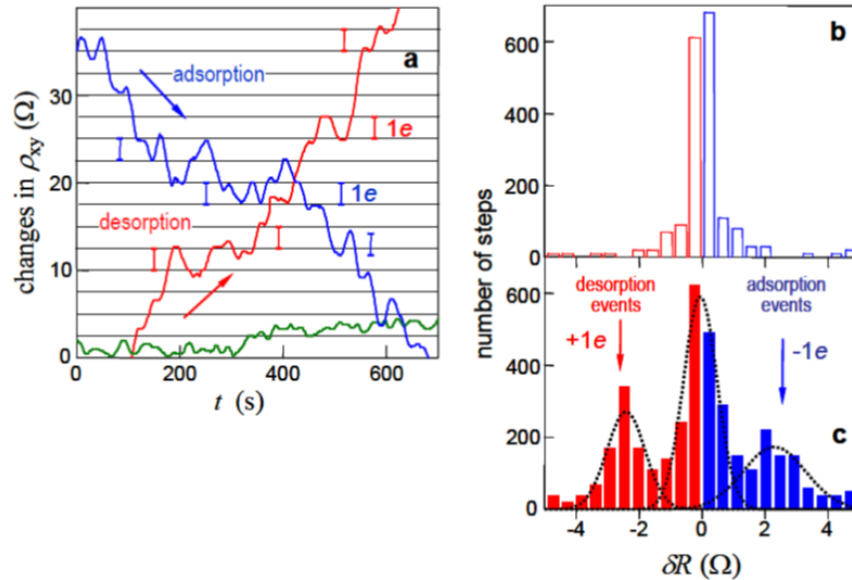


Figure 2.9: (a) measurement of Hall resistivity ρ_{xy} at 10 Tesla as a function of the time during adsorption of NO_2 (blue curve), during annealing at $50^\circ C$ (red curve), and reference (green curve). (b) statistical distribution of events with graphene in helium; (c) compared statistical distribution of events with graphene in helium and during adsorption and desorption of NO_2 [33].

Graphene-based electronic devices could make for very sensitive gas detectors. Graphene layers might become a powerful tool to study the adsorption properties of different atoms.

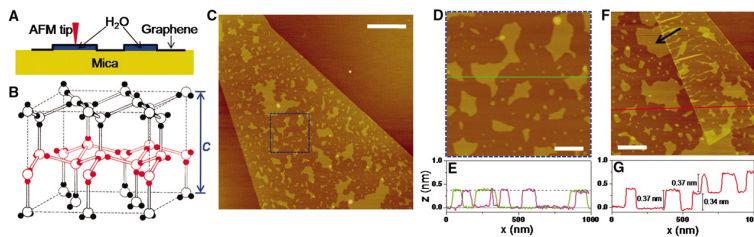


Figure 2.10: Imaging of the adsorbed water layer with AFM from ref. [34]

The adsorbates also have an effect on the electronic mobility: as shown in fig. 2.11 from ref [35], a larger amount adsorbed atoms lowers the electronic mobility. Atom adsorption provides us with a means to measure the electronic properties of graphene at a given electronic density but with different mobility values.

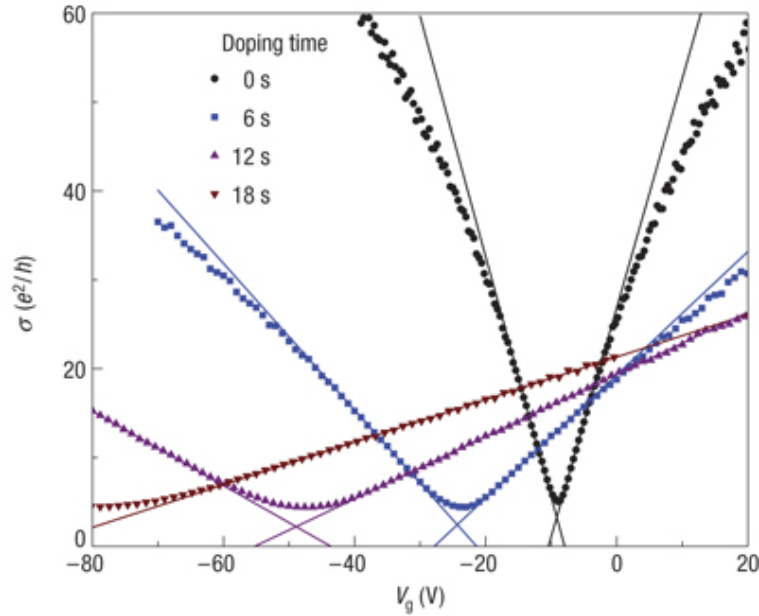


Figure 2.11: Conductivity as a function of backgate doping for different concentrations of adsorbate [35]

However, a new difficulty arises: these adsorbates must be removed under ultra high vacuum conditions just before measuring, so that a better mobility level is achieved.

2.5.6 Approaching the Dirac point

Theoretically speaking, the density of graphene can be tuned to zero. However, experiments showed that electron-hole puddles, generated by random doping by either charged impurities or adsorbed donor or acceptor molecules, make it difficult. According to ref. [36], typical fluctuations of the density of graphene on SiO_2 are $\Delta n = \pm 2, 3 \cdot 10^{11} cm^{-2}$ (corresponding to $\Delta V_g \sim \pm 3V$).

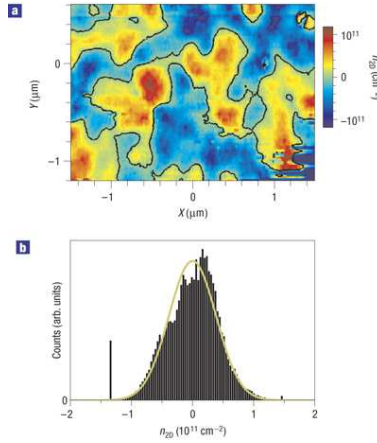


Figure 2.12: (a) Imaging of the density on the Dirac point with scanning tunneling spectroscopy, (b) histogram of the residual density [36]

Greater mobility levels were achieved on suspended graphene (after annealing to remove adsorbed molecules), revealing interaction effects. Bolotin et al reported that $\Delta n = \pm 2.10^{10} \text{ cm}^{-2}$ [37] on suspended graphene, which was a great improvement compared to experimentation on unsuspended graphene.

2.5.7 Quality of the graphene as a function of the substrate.

Silicon, with a top layer of insulating silicon oxide, is frequently used to measure the electronic properties of graphene. As will be detailed in section 6.2, this substrate enables the tuning of the density of graphene; this substrate was shown to limit mobility in graphene as silicon oxide is not free of defects and can trap charges. Typical mobility levels for graphene on this substrate is between $1000 \text{ cm}^2 \text{ V}^{-1} \text{ s}^{-1}$ and $15000 \text{ cm}^2 \text{ V}^{-1} \text{ s}^{-1}$.

P. Kim's and E. Andrei's groups considerably improved mobility by experimenting on suspended graphene, which generated mobility levels greater than $100000 \text{ cm}^2 \text{ V}^{-1} \text{ s}^{-1}$ with a residual density of about $\delta n \sim 2.10^{10} \text{ cm}^{-2}$ [37, 25].

Very recently, Kim's group reported high mobility $80000 \text{ cm}^2 \text{ V}^{-1} \text{ s}^{-1}$ and low residual density at $\delta n < 7.10^{10} \text{ cm}^{-2}$ after they used graphene on top of boron nitride, which is an isomorph of graphene [38].

Chapter 3

Quantum Hall effect

In 1879, eighteen years before Joseph J. Thomson discovered the electron, Edwin H. Hall discovered the eponymous Hall effect, while working on his doctorate. The Hall effect is the appearance of a potential difference perpendicular to the current in a conductor placed in a magnetic field. It is best observed in a thin metallic plate with the magnetic field set perpendicular to the thin plane. The Hall voltage varies linearly with the magnetic field according to $V_{Hall} = R_{Hall} I_{DS}$ where $R_H = \frac{B}{en_S}$ (B is the magnetic field, n_S the electron density per area) defining a Hall resistance.

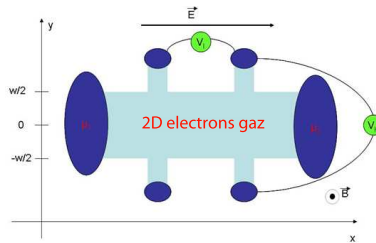


Figure 3.1: Hall bar

During the night between “the 4th to the 5th of February 1980 at around 2 a.m.”[39], K.V.Klitzling discovered plateaus in the Hall resistance[40] while measuring the transport properties of silicon field effect transistor. He found these plateaus to be quantized as a fraction of $\frac{h}{e^2}$ and independent on the sample characteristics like size or disorder. With these plateaus he found that the potential drop along an edge parallel to the current direction (we will call it longitudinal potential V_{xx} associated with a longitudinal resistance R_{xx}) goes to 0 when R_H shows a plateau. This was the birth of the Quantum Hall effect which led to a Nobel prize in 1985.

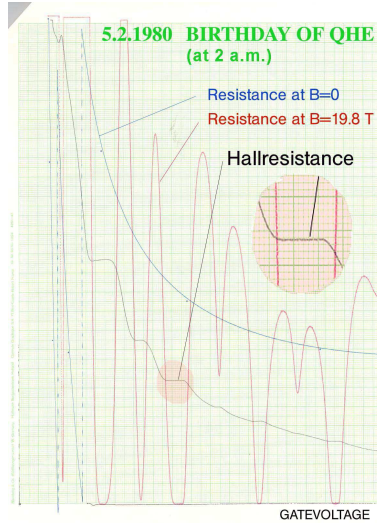


Figure 3.2: First quantum Hall measurement

For the description of Quantum Hall transport we will follow the same path as in the transport chapter (2). A description of the classical Hall transport will first be done using the Drude model, then a semi classical model will be used based on a quantum calculation of the energy spectrum and Einstein's diffusion equation to explain Shubnikov-De Haas effect. Finally a full quantum model will be used to describe the quantum Hall effect.

3.1 Motion of an electron in a magnetic field

We describe first the motion of an electron in an infinite plate in a perpendicular magnetic field B .

The x and y axes are chosen to lie in the plane with unit vectors, the two units vector are \vec{e}_x and \vec{e}_y , while the magnetic field is oriented perpendicularly to the plane:

$$\vec{B} = B\vec{e}_z$$

The vector potential A is defined by:

$$\vec{B} = \vec{\nabla} \wedge \vec{A}$$

It is important to notice that the magnetic field B is translation invariant whereas the magnetic potential A is not.

$$B = \partial_x A_y - \partial_y A_x$$

The symmetric gauge gives a vector potential A satisfying this equation

$$A = \frac{1}{2}(-By, Bx, 0)$$

The Hamiltonian for a free electron in 2 dimensions is

$$H = \frac{1}{2m}(p_x^2 + p_y^2)$$

Where $\mathbf{p} = m\dot{\mathbf{r}}$ is the momentum conjugated to \mathbf{r} .

In a magnetic field, the electron is subjected to the Lorentz force $\vec{F} = q\vec{v} \wedge \vec{B}$, proportional to the electron velocity, and can be taken into account by writing new expression for the kinetic momentum π in terms of the conjugate momentum p : $\vec{\pi} = \vec{p} - e\vec{A}$. This quantity is proportional to the velocity of an electron under a magnetic field.

$$\begin{cases} \pi_x = p_x + \frac{eB}{2}y \\ \pi_y = p_y - \frac{eB}{2}x \end{cases}$$

The Hamiltonian in magnetic field becomes

$$H = \frac{1}{2m}(\pi_x^2 + \pi_y^2) = \frac{1}{2}mv^2 \quad (3.1)$$

This Hamiltonian is the same as the one of a harmonic oscillator, indeed, by looking at the motion projected on the x or y axis, the harmonic oscillator motion can be recognized.

We can solve the equation of motion using the Hamiltonian formalism

$$\dot{\pi}_x = \sum_i \frac{\partial \pi_x}{\partial q_i} \dot{q}_i + \frac{\partial \pi_x}{\partial p_i} \dot{p}_i = \{\pi_x, H\} \quad (3.2)$$

$$\{\pi_x, \pi_y\} = eB \quad (3.3)$$

$$\{\pi_y^2, \pi_x\} = 2\pi_y \{\pi_y, \pi_x\} = -2eB\pi_y \quad (3.4)$$

$$\begin{cases} \dot{\pi}_x = -\frac{eB}{m}\pi_y \\ \dot{\pi}_y = \frac{eB}{m}\pi_x \end{cases} \quad (3.5)$$

The movement is cyclic and can therefore be written in the form $\pi(\omega) = e^{i\omega t}\chi$; as a result the derivative can be expressed as follow:

$$\begin{cases} i\omega\pi_x = -\frac{eB}{m}\pi_y \\ i\omega\pi_y = \frac{eB}{m}\pi_x \end{cases} \quad (3.6)$$

$$\omega^2 = \frac{e^2 B^2}{m^2}$$

To express the energy, it is convenient to use the action angle variable:

$$H(\pi_x, \pi_y) \rightarrow H(J, \theta)$$

where J is the area of the π_x, π_y circle.

$$J = \frac{1}{2\pi} \int \pi_y(\pi_x) d\pi_x$$

J and θ are conjugate variables

$$\begin{cases} \dot{\theta} = \frac{\partial H}{\partial J} = \omega(J) = cte \\ \dot{J} = \frac{\partial H}{\partial \theta} = 0 \end{cases}$$

hence

$$E = J\omega$$

ω is a constant at a given magnetic field, thus the energy does not depend on the position on the π_x, π_y circle.

Electronic motion can be described here by using the motion of the the cyclotron orbit centers, called the guiding center coordinates R_x and R_y .

$$\begin{cases} \dot{x} = \frac{\partial H}{\partial p_x} = \frac{1}{m}(p_x - \frac{eB}{2}y) = \frac{\pi_x}{m} = -\frac{eB}{m}(y - R_y) \\ \dot{y} = \frac{\partial H}{\partial p_y} = \frac{1}{m}(p_y + \frac{eB}{2}x) = \frac{\pi_y}{m} = \frac{eB}{m}(x - R_x) \end{cases}$$

R_x and R_y move along equipotential lines in the plane whereas x and y describe the cyclotron motion.

$$\begin{cases} R_x = \frac{1}{eB}(-p_y + \frac{eB}{2}x) \\ R_y = \frac{1}{eB}(p_x - \frac{eB}{2}x) \end{cases}$$

We can show that R_x and R_y are constant of motion:

$$\{R_x, \pi_x\} = \{R_x, \pi_y\} = \{R_y, \pi_x\} = \{R_y, \pi_y\} = 0$$

Thus R_x and R_y are translation generator, indeed these quantities are conserved through any space translation in the xy plane. So the motion can be described from the guiding center coordinates (this sketched on fig. 3.3).

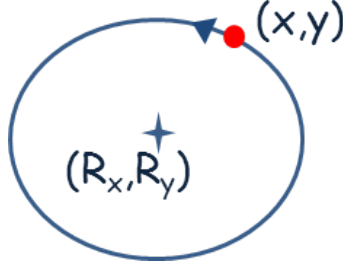


Figure 3.3

3.2 Classical Hall effect

First, we consider the motion of charge without magnetic field:

We recall here the Drude model

$$\vec{v}_d = -\frac{e\vec{E}\tau}{m} \quad (3.7)$$

where \vec{E} is the electric field and m the charge carrier mass. The density of the current is:

$$\vec{j} = -ne\vec{v}_d = \sigma_0\vec{E} \quad (3.8)$$

where:

$$\sigma_0 = \frac{ne^2\tau}{m} \quad (3.9)$$

is the conductivity and n is here the surface density of charge carriers.

For the two dimensional problem, electrons are free to move in the x and y direction and \vec{E} is assumed to be oriented in the x direction.

We apply a perpendicular magnetic field

$$\vec{B} = B\vec{e}_z$$

Under a magnetic field the Lorentz force has to be added to the electric force in order to compute the drift velocity:

3.7 :

$$\vec{v}_d = -e(\vec{E} + \vec{v}_d \wedge \vec{B})\frac{\tau}{m} \quad (3.10)$$

The conductivity and resistivity tensors are written

$$\boldsymbol{\sigma} = \begin{pmatrix} \sigma_{xx} & \sigma_{xy} \\ \sigma_{yx} & \sigma_{yy} \end{pmatrix}$$

and

$$\boldsymbol{\rho} = \begin{pmatrix} \rho_{xx} & \rho_{xy} \\ \rho_{yx} & \rho_{yy} \end{pmatrix}$$

with $\vec{j} = \sigma \vec{E}$ and $\vec{E} = \rho \vec{j}$
in the xy plan , we get

$$\sigma_0 E_x = \omega_c \tau j_y + j_x \quad (3.11)$$

$$\sigma_0 E_y = -\omega_c \tau j_x + j_y \quad (3.12)$$

with: $\omega_c = \frac{eB}{m}$

Eq. 3.11 and 3.12 result in

$$\rho_{xx} = \rho_{yy} = 1/\sigma_0 \quad (3.13)$$

$$\rho_{xy} = -\rho_{yx} = \frac{\omega_c \tau}{\sigma_0} \quad (3.14)$$

Combining eq. 3.14 and 3.9 we obtain

$$\boxed{\rho_{xy} = \frac{B}{ne} = R_H} \quad (3.15)$$

In 2 dimensions the resistivity has the same units as a resistance. Here the transverse resistivity does not depend on sample characteristics. It can be assimilated to the Hall resistance and increases linearly with the magnetic field.

The conductivity is

$$\sigma_{xx} = \sigma_{yy} = \frac{\sigma_0}{1 + (\omega_c \tau)^2} \quad (3.16)$$

$$\sigma_{xy} = -\sigma_{yx} = -\frac{\sigma_0 \omega_c \tau}{1 + (\omega_c \tau)^2} = -\frac{1}{R_H} \frac{1}{1 + (\omega_c \tau)^2} \quad (3.17)$$

leading directly to the relation between conductivity and resistivity

$$\sigma_{xx} = \frac{\rho_{xx}}{\rho_{xx}^2 + \rho_{xy}^2} \iff \rho_{xx} = \frac{\sigma_{xx}}{\sigma_{xx}^2 + \sigma_{xy}^2} \quad (3.18)$$

$$\sigma_{xy} = -\frac{\rho_{xy}}{\rho_{xx}^2 + \rho_{xy}^2} \iff \rho_{xy} = -\frac{\sigma_{xy}}{\sigma_{xx}^2 + \sigma_{xy}^2} \quad (3.19)$$

In accordance with the inversion of the equation 3.19 it is seen that when the longitudinal resistivity (ρ_{xx}) goes to zero so does the the longitudinal conductivity (σ_{xx}).

3.3 The Landau quantization

3.3.1 Bohr's semi-classical quantization

The Bohr's calculus gives an initial insight to the quantification of the energy in a magnetic field. For a Newtonian (finite mass) charge in an infinite 2 dimensional conductor, a magnetic fields leads that the trajectories of the electrons

become circle, the radius of which we can estimate classically by balancing the centripetal Lorentz force against the acceleration

$$m |\ddot{r}| = m \frac{\dot{r}^2}{a} = q |\dot{r}| B$$

The radius is $a = m\dot{r}/eB$.

Now we can take in account the wave nature of electrons with a wavefunction where the motion part is expressed by $\exp(i\mathbf{k}\cdot\mathbf{s})$ where \mathbf{s} is the trajectory. The probability of presence of a particle is proportional to the square of the wavefunction, this probability is maximum when there is a constructive interference of the wavefunction and evanescent if not. The condition of interference is that there is a phase shift of $2n\pi$ on one revolution (n is a integer):

$$2\pi k \cdot a = 2n\pi$$

We can now express energy:

$$E = \frac{\hbar^2 k^2}{2m} = \frac{\hbar^2}{2m} \frac{n^2}{a^2}$$

$$E = \hbar \frac{eB}{m} n = \hbar \omega_c n$$

Here, the energy is quantized due to the wave nature of electrons. We will see later with an appropriate quantum computation that the energy is in fact:

$$E = \hbar \omega_c \left(n + \frac{1}{2} \right)$$

where the $1/2$ term comes from an exact calculation (as usual Bohr-Sommerfeld calculation cannot give such extra term but only the leading term rising with the quantum number n)

3.3.2 Quantum mechanical computation

The motion of a particle in a magnetic field exhibits energies quantized into a series of levels named after Landau who was the first to solve this problem. In the following we will describe how the Landau equation is obtain from the Schrödinger equation.

The calculation is reproduced in numerous books , not least of all in Landau and Lifshitz "Quantum Mechanics". Nonetheless we will outline the reasoning to be able to extend it to the case of massless Dirac mechanics of graphene which is as yet less widespread.

In the quantum description there are major changes. The wave mechanics of the particle has to be taken into account so the equation of motion becomes a wave equation. Momentum is now an operator which acts on the wavefunctions:

$p_i \rightarrow -i\hbar\partial_{r_i}$. Poisson brackets which we used for the classical motion of the electron in a magnetic field are replaced by commutators with the relations:

$$[r_i, r_j] = 0; \quad [p_i, p_j] = 0; \quad [r_i, p_j] = i\hbar\delta_{ij}$$

These relations are reflected in the Heisenberg principle which is intimately related to the wave nature of the particle.

With these relations we can determine the commutator values of the quantities previously introduced in the harmonic oscillator calculus 3.1:

$$[\Pi_x, \Pi_y] = -i\hbar eB, \quad [R_x, R_y] = i\hbar \frac{1}{eB}, \quad [\Pi_x, R_y] = 0$$

The Schrödinger equation in an external magnetic field in the absence of any confining potential becomes:

$$\left(\frac{1}{2m}(\mathbf{p} - e\mathbf{A})^2\right)|\Psi\rangle = E|\Psi\rangle \quad (3.20)$$

Defining a and a^\dagger operators which describe the coordinates in a phase space circle:

$$a = \frac{1}{\sqrt{2\hbar eB}}(\pi_x + i\pi_y), \quad a^\dagger = \frac{1}{\sqrt{2\hbar eB}}(\pi_x - i\pi_y) \quad (3.21)$$

The commutator of a and a^\dagger is non zero:

$$[a, a^\dagger] = 1$$

As a result, the Hamiltonian can be simplified as

$$H = \hbar\omega_c\left(a^\dagger a + \frac{1}{2}\right) \quad (3.22)$$

This notation for the Hamiltonian is clearly reminiscent of the notation action angle that we set in the classical calculation of the harmonic oscillator (3.1). Here the energy at fixed magnetic fields does not vary with the position of the phase space circle (given by ω_c) but only with the radius of the phase space circle which is the operator

$$n = a^\dagger a$$

As we made very clear in the previous paragraph, this operator takes on quantized values, thus giving the eigenvalues of the Hamiltonian.

$$E = \hbar\omega_c\left(n + \frac{1}{2}\right) \quad (3.23)$$

The quantized energy is sketched on figure 3.4.

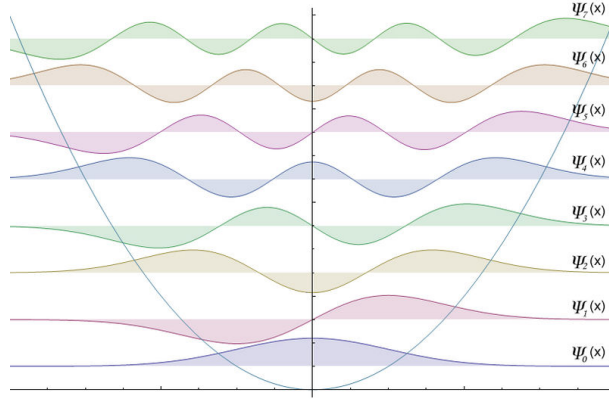


Figure 3.4: Harmonic potential of E versus k at different energy levels

Guiding center coordinate and Landau Level degeneracy An important aspect is contained in the commutation relation of the coordinates of guiding center. With the quantum treatment they do not commute. As a consequence dynamics of the guiding center coordinate is like that of a one-dimensional system (although R_x and R_y pertains to the real 2D plane) where R_x would play the role of 'X' coordinate and R_y the role of the conjugate momentum 'P' or vice versa. There is a quantum uncertainty $\Delta R_x \Delta R_y = \hbar/eB$ in determining the position of the guiding centers coordinates.

The magnetic length is usually expressed as

$$l_c = \sqrt{\frac{\hbar}{eB}}$$

Due to the uncertainty principle a quantum state of a LL has a size which is inversely proportional to the magnetic field. The size of the quantum state is equivalent to the size of a state of a one-dimensional system in the phase-space. The 2D plane is like a phase space. The physical plane can be described as divided into disjoint cells of area $2\pi l_c^2$, where only one electron can stay in each cell due to the Pauli principle. This area is equal to that of one magnetic flux quantum $\Phi_0 = h/e$.

With these considerations it is possible to count the number of energetically degenerate independent eigenstates on one level as equal to the surface divided by one cell, and in terms of flux it is

$$N = \frac{\Phi}{\Phi_0} \quad (3.24)$$

where $\Phi = B * S$ is the total magnetic flux threading the sample.

When a level is fully occupied, the Pauli principle implies that one additional electron must acquire an extra energy $\hbar\omega$ to put it into the next Landau level. We can introduce here the filling factor ν which corresponds to the number of levels occupied at a given density n_s .

$$\boxed{\nu = \frac{\hbar n_s}{e^2 N} = n_s \frac{\hbar}{eB}} \quad (3.25)$$

With this definition ν is a positive real number; however, usually only the integer part is considered to reflect the quantized nature of the energy and to indicate the last completely filled Landau level. It is important to keep in mind this notion of filling factors because it is very convenient to use it in the experimental description of the quantum Hall effect.

3.3.3 Eigenfunctions in the Landau gauge

It is interesting to look at the eigenfunctions of electrons in Landau Levels. For that we will use the Landau gauge where the results find simpler expressions:

$$\hat{A} = (0, -Bx, 0) \quad (3.26)$$

In this gauge the Schrödinger equation becomes

$$H = \frac{\hat{p}_x^2}{2m} + \frac{(\hat{p}_y - eB\hat{x})^2}{2m} \quad (3.27)$$

We can do a similar computation as previously stated

$$\begin{cases} \pi_x = p_x \\ \pi_y = p_y + eBx \end{cases}$$

We can see easily that $[\hat{H}, \hat{P}_y] = 0$, So we can write the wave functions as follows

$$\psi(x, y) = e^{-ik_y y} \phi_n(x + x_k) \quad (3.28)$$

$$\phi_{k0}(x) = \exp\left(-\frac{(x - x_k)^2}{2l_c^2}\right)$$

$$\phi_{kn}(x) = H_n\left(\frac{x - x_k}{l_c}\right) \exp\left(-\frac{(x - x_k)^2}{2l_c^2}\right)$$

where H_n is an Hermite polynomial solution of the harmonic oscillator problem.

As $E_{n,k}$ does not depend on k , the degeneracy is given by the number of "k" possible.

The periodic boundary condition imposes $k_y = m * \frac{2\pi}{L_y}$, where m is an integer. This implies $\Delta k_y = \frac{2\pi}{L_y}$, therefore

$$\Delta x = x_{k=(m+1)\frac{\pi}{L}} - x_{k=m\frac{\pi}{L}} = \frac{\hbar}{eB} \Delta k_y = \frac{\hbar}{eBL_y}$$

Again we find the result of eq.3.24 for the number of states:

$$N = \frac{L_x}{\Delta x} = \frac{BL_x L_y}{h/e} = \frac{\Phi}{\Phi_0}$$

3.4 Zeeman splitting

So far spin has been disregarded. It plays an important role under high magnetic field. To take account of it we have to add a Zeeman term to the energy expression. In order to introduce this term we will use the Pauli Hamiltonian which is a simplified version of the Dirac Hamiltonian, this will allow to understand easily the spin effect.

$$H = \frac{1}{2m} (\vec{\sigma} \cdot (\vec{P} - e\vec{A}))^2 \quad (3.29)$$

with the relation: $(\vec{\sigma}\vec{a})(\vec{\sigma}\vec{b}) = \vec{a}\vec{b} + i\vec{\sigma}(\vec{a} \times \vec{b})$

$$H = \frac{(\vec{P} - e\vec{A})^2}{2m} + i \frac{\vec{\sigma}(\vec{P} - e\vec{A}) \times (\vec{P} - e\vec{A})}{2m} \quad (3.30)$$

$$(\vec{P} - e\vec{A}) \times (\vec{P} - e\vec{A}) = e(\vec{P} \times \vec{A}) + (\vec{A} \times \vec{P}) = \frac{e\hbar}{i} (\vec{\nabla} \times \vec{A}) \quad (3.31)$$

$$H = \frac{(\vec{P} - e\vec{A})^2}{2m} + i\vec{\sigma}(-i\hbar\vec{B}) \quad (3.32)$$

$\hbar\vec{\sigma}\vec{B}$ has for eigenvalue BS_z .

We can now determine the eigenvalues of the Hamiltonian :

$$E_n = (n + \frac{1}{2} + \gamma\frac{1}{2})\hbar\omega_C \text{ with } \omega_C = eB/m \quad (3.33)$$

where $\gamma = \pm 1$ corresponds to the spin-up and spin-down states.

In fact quantum electrodynamics and interactions impose to add a gyromagnetic factor g :

$$E_n = (n + 1/2)\hbar\omega_C + \frac{1}{2}g\mu_B B \quad (3.34)$$

where $\mu_B = e\hbar/2m_e$ is the Bohr magneton.

In the QHE regime it can be shown, and this is consistent with observations, that the g -factor is enhanced by the exchange interactions (calculated in ref [41]):

$$g = g_z + \alpha \frac{n_{s\uparrow} - n_{s\downarrow}}{n_{s\uparrow} + n_{s\downarrow}}$$

where $n_{s\uparrow}$, $n_{s\downarrow}$ are the density of spin up and spin down electron.

In QHE regime, interactions can eventually strengthen this factor g by an exchange term which linearly depend of the population difference between spin up and down. Here the terms $\frac{n_{s\uparrow} - n_{s\downarrow}}{n_{s\uparrow} + n_{s\downarrow}}$ is proportional to $1/\nu$ for odd filling factor and 0 for even filling factors. As a consequence high filling factors show less interaction effect and very weak Zeeman splitting is remaining.

This explains why at high magnetic field spin splitting in conventional 2DEGs is observed only at low filling factors (high field). As manifestation of interactions require low disorder, it is more easily seen in high mobility samples. In standard Graphene samples as those used here, we will not observe spin splitting as disorder is too high.

3.5 Landau Levels in graphene

3.5.1 Monolayer graphene

In graphene the Landau levels spectrum is following the zero field case quite different as in conventional 2DEG. Here its computation is shown with the help of [42, 43].

The Dirac Hamiltonian under a magnetic field can be expressed as:

$$H = \hbar v_F \boldsymbol{\alpha} \cdot \boldsymbol{\pi} \quad (3.35)$$

Where:

$$\boldsymbol{\pi} = -i\hbar\nabla + e\mathbf{A}$$

$$H = \hbar v_F \begin{pmatrix} 0 & \boldsymbol{\sigma} \cdot \boldsymbol{\pi} \\ \boldsymbol{\sigma} \cdot \boldsymbol{\pi} & 0 \end{pmatrix} = \begin{pmatrix} 0 & Q \\ Q & 0 \end{pmatrix} \quad (3.36)$$

This matrix applies to four component wavefunctions of the type seen in section 1.3.2.3:

$$\Psi = \begin{pmatrix} \psi_+^A \\ \psi_+^B \\ \psi_-^B \\ \psi_-^A \end{pmatrix} = \begin{pmatrix} 1 \\ \lambda e^{i\theta_{\mathbf{k}}} \\ 1 \\ -\lambda e^{i\theta_{\mathbf{k}}} \end{pmatrix} \varphi$$

As in the previous chapter we will use the notation :

$$a = \frac{l_B}{\hbar\sqrt{2}}(\pi_x + i\pi_y), \quad a^\dagger = \frac{l_B}{\hbar\sqrt{2}}(\pi_x - i\pi_y) \quad (3.37)$$

Here $l_c = \sqrt{\hbar/eB}$ is the magnetic length. Also we can set $A = \hbar\omega_c a$ with $\omega_c = v_F\sqrt{2eB/\hbar}$

With these notations we have:

$$Q = \hbar v_F \boldsymbol{\sigma} \cdot \boldsymbol{\pi} = \hbar v_F \begin{pmatrix} 0 & \pi_x - i\pi_y \\ \pi_x + i\pi_y & 0 \end{pmatrix} = \begin{pmatrix} 0 & A^\dagger \\ A & 0 \end{pmatrix} \quad (3.38)$$

Linearizing the Hamiltonian is pretty easy and gives:

$$H = \begin{pmatrix} \sqrt{QQ} & 0 \\ 0 & -\sqrt{QQ} \end{pmatrix} \quad (3.39)$$

Nicely the multiplication of two off diagonal matrices gives a diagonal matrix:

$$QQ = \begin{pmatrix} A^\dagger A & 0 \\ 0 & AA^\dagger \end{pmatrix} = (\hbar\omega_c)^2 \begin{pmatrix} a^\dagger a & 0 \\ 0 & aa^\dagger \end{pmatrix} \quad (3.40)$$

In The K valley the Hamiltonian can be written:

$$E_N^{\xi=+} = \hbar\omega \begin{pmatrix} \sqrt{N} & 0 & 0 & 0 \\ 0 & \sqrt{N+1} & 0 & 0 \\ 0 & 0 & -\sqrt{N} & 0 \\ 0 & 0 & 0 & -\sqrt{N+1} \end{pmatrix} \quad (3.41)$$

And in the K' valley:

$$E_N^{\xi=-} = \hbar\omega \begin{pmatrix} \sqrt{N+1} & 0 & 0 & 0 \\ 0 & \sqrt{N} & 0 & 0 \\ 0 & 0 & -\sqrt{N+1} & 0 \\ 0 & 0 & 0 & -\sqrt{N} \end{pmatrix} \quad (3.42)$$

Associated with the wave function:

$$\Psi = \begin{pmatrix} \psi_{\xi=\pm}^{A,\lambda=+} \\ \psi_{\xi=\pm}^{B,\lambda=+} \\ \psi_{\xi=\pm}^{B,\lambda=-} \\ \psi_{\xi=\pm}^{A,\lambda=-} \end{pmatrix}$$

To remind, subscript are defined in section 1.3.2, λ correspond to the band, ξ to the valley, A and B to the 2 sublattices.

Here the diagonalized Hamiltonian is very instructive because it shows the different eigenvalues of the energy for each sublattice and each band. All the eigenvalues elements are 2 times degenerate due to valley degeneracy (K and K'). We can see that each value of the energy will be composed of 2 different energy levels coming from the 2 sublattices, for example the levels $E = 2 * E_0$ will be composed by the $N = 4$ level for an electron of the A sublattice in the conduction band and by the $N = 3$ level for an electron of a B sublattice also in the conduction band.

Something remarkable is the fact that the zero Energy level is shared by electrons and holes.

As a result all the energy levels are four fold degenerated, 2 for the real spin and 2 for the valley except the $E = 0$ as we can discriminate electron and hole (in Quantum Hall effect this discrimination is done by the direction of their motion).

$$E_{N,\xi=\pm}^\lambda = \lambda \hbar v_F \sqrt{2eBN} \quad (3.43)$$

Here two remarkable things: Compared to Schrödinger electrons the energy has a square root dependence on the magnetic field and there is a zero energy Landau Level.

Also an other important fact for graphene is that the characteristic cyclotron energy $\frac{\hbar v_F}{\sqrt{\hbar/2eB}} \approx 420K/\sqrt{T}$ (for the 2 first Landau levels), is much larger than in a conventional 2DEG. For example in an heterojunction of GaAs/AlGaAs $\hbar\omega_c \approx 20K/T$. This high cyclotron gap allows observation of quantum hall effect at room temperature ([44]).

Infrared spectroscopy provided to measure the gap between Landau levels in graphene in ref. [45]

3.5.2 Bilayer Graphene

For the case of the Bilayer we will consider only the lower energy bands of a Bernal configuration (see 1.4).

The effective low energy Hamiltonian can be written under the form of:

$$H_D = \begin{pmatrix} \sqrt{Q_\pm Q_\pm} & 0 \\ 0 & -\sqrt{Q_\pm Q_\pm} \end{pmatrix} \quad (3.44)$$

applied to the wavefunctions:

$$\Psi = \begin{pmatrix} \psi_+^{A1} \\ \psi_+^{B2} \\ \psi_-^{B2} \\ \psi_-^{A1} \end{pmatrix}$$

where:

$$Q_+ = \hbar\omega_c \begin{pmatrix} 0 & (\pi_x + i\pi_y)^2 \\ (\pi_x - i\pi_y)^2 & 0 \end{pmatrix} = \begin{pmatrix} 0 & A^\dagger \\ A & 0 \end{pmatrix} \quad (3.45)$$

and

$$Q_- = \begin{pmatrix} 0 & A \\ A^\dagger & 0 \end{pmatrix} \quad (3.46)$$

Here $A = \hbar\omega a^2$ and $A^\dagger = \hbar\omega a^{\dagger 2}$

Here we assume the same wave functions that we use for the monolayer graphene, the Hamiltonian is now expressed as

$$(H_D^{\xi=+})^2 = \hbar\omega \begin{pmatrix} a^{2\dagger}a^2 & 0 & 0 & 0 \\ 0 & a^2a^{2\dagger} & 0 & 0 \\ 0 & 0 & -a^{2\dagger}a^2 & 0 \\ 0 & 0 & 0 & -a^2a^{2\dagger} \end{pmatrix} \quad (3.47)$$

$$(H_D^{\xi=-})^2 = \hbar\omega \begin{pmatrix} a^2a^{2\dagger} & 0 & 0 & 0 \\ 0 & a^{2\dagger}a^2 & 0 & 0 \\ 0 & 0 & -a^{2\dagger}a^2 & 0 \\ 0 & 0 & 0 & -a^{2\dagger}a^2 \end{pmatrix} \quad (3.48)$$

By using the relation $a^{2\dagger}a^2 = a^\dagger a(a^\dagger a - 1)$ the energy spectrum can be found. The eigenvalues of the energy are:

$$\boxed{E_N^{A,\xi=+} = E_N^{B,\xi=-} = \hbar\omega_c \sqrt{N(N-1)}} \quad (3.49)$$

$$\boxed{E_N^{B,\xi=+} = E_N^{A,\xi=-} = \hbar\omega_c \sqrt{(N+2)(N+1)}} \quad (3.50)$$

As in monolayer there is a zero energy state, however here 2 Landau levels give rise to this state, thus this state has the same degeneracy as the other energy states.

Another difference with a monolayer is that here the space between Landau levels is quasi constant at fixed magnetic fields and the variation is linear with the magnetic field.

The estimated mass in bilayer graphene is $m^* \sim 0.035m_e$, thus the cyclotron energy is $\sim 40K/T$ is about twice as much as in AlGaAs.

3.6 Landau levels comparison

We can conclude these description of Landau levels by showing a plot of the different cyclotron energies on fig. 3.5. This graph makes very clear the interest of studying the quantum Hall effect in graphene.

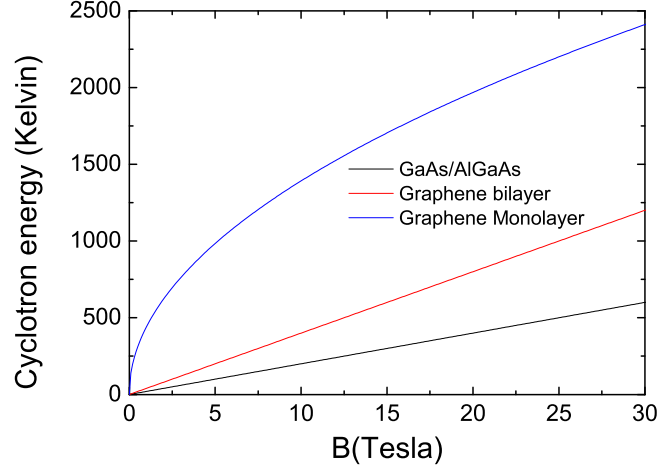


Figure 3.5: Comparison of cyclotron energies for graphene and typical 2DEG

3.7 Shubnikov-De Haas (SDH) oscillations, a first observation of Landau quantization

Shubnikov and De Haas[46] discovered oscillations in the field dependence of the magneto-resistance of a metal. It is a consequence of the Landau quantization that we saw before in 3.3 and which first gives rise to a modulation of the density of states before displaying well resolved Landau levels with higher magnetic field.

SDH oscillations arise when the coherence length exceeds the cyclotron length and when the cyclotron frequency ω_c is such that electrons have a high probability of making an elastic collision with an impurity before completing one revolution

$$\omega_c \sim \frac{1}{\tau_e}$$

$$l_\phi > l_e \sim l_c$$

To describe electronic transport in such conditions we have to take into account the quantized density of states.

The Einstein relation relating mobility and diffusion constant can be used here (presented in 2.4.5):

$$\sigma_l = e^2 D g(E_F) \quad (3.51)$$

Where $g(E_F)$ is the density of states at the Fermi level.

As the energy is quantized the density of states will oscillate as sketched on figure 3.6

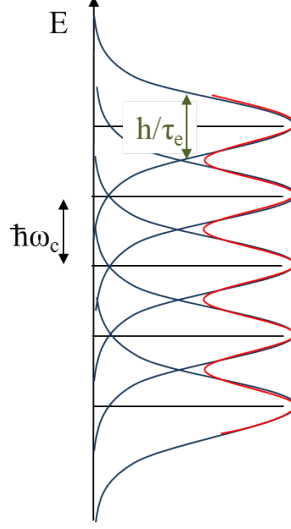


Figure 3.6: Schematic view of the density of states (blue curves) as a function of the energy. The red curve represents the harmonic approximation

The density of states in conventional 2DEG can be calculated using the harmonic approximation of the broadened Landau levels, as is done in ref [47, 48]:

$$\frac{\Delta g(\varepsilon)}{g_0} = 2 \sum_{s=1}^{\infty} \exp\left(-\frac{\pi s}{\omega_c \tau_e}\right) \cos\left(\frac{2\pi s \varepsilon}{\hbar \omega_c} - s\pi\right) \quad (3.52)$$

Here the cosine term represents the harmonic approximation of the density of states (represented by the curve in red on fig.3.6).

The exponential represents the amplitude of the oscillations, assuming lorentzian broadening of the Landau levels of a width Γ independent of the energy and magnetic field such as $\tau_e = \hbar/2\Gamma$.

The expression for the resistivity tensor of graphene is then [27]:

$$\frac{\delta \rho_{xx}(B)}{\rho_0} = 4D_T \exp\left(-\frac{\pi}{\omega_c \tau_e}\right) \cos\left(\frac{j\pi E_F}{\hbar \omega_c} - j\pi\right) \quad (3.53)$$

$$\rho_{xy}(B) = \rho_0 \omega_c \tau_{tr} - \frac{\delta \rho_{xx}(B)}{2\omega \tau_{tr}} \quad (3.54)$$

Where ρ_0 is the zero field resistivity.

This formula is valid for both monolayer and bilayer with slight changes:

$\omega_c = eB/m^*$ where $m^* = \hbar k_F/v_F$ for a monolayer and m^* about equal to $m_{eff} \sim 0.035m_e$ at low energy for a bilayer. j is equal to 1 in the case of monolayer and 2 in the case of bilayer.

Thermal damping of the oscillations is expressed in: $D_T = \gamma/\sinh \gamma$ where $\gamma = 2\pi^2 k_B T/\hbar\omega_c$.

For a monolayer we can write the expression as follows to make appear explicitly the quadratic dependence of the oscillation on the energy

$$\frac{\delta\rho_{xx}(B)}{\rho_0} = 4D_T \exp\left(-\frac{\pi}{\omega_c\tau_e}\right) \cos\left(\frac{\pi E_F^2}{v_F^2} - \pi\right) \quad (3.55)$$

These expressions have been used for the determination of the elastic time τ_e and the transport time τ_{tr} at low magnetic field in graphene (see chapter 7).

3.8 Transport in the regime of Integer Quantum Hall effect

In this section we will describe the transport at higher magnetic field, in the integer quantum Hall effect regime. Here the two striking phenomena are that the Hall resistance reaches quantized plateaus as a function of the field or density while at the same time the longitudinal resistance vanishes. This effect occurs when the energy scale given by $k_B T$ is significantly smaller than the energy gap between Landau levels $\hbar\omega_c$.

3.8.1 Hall bar geometry

The so called Hall bar probe geometry is the usual geometry used to observe the quantum Hall effect.

The Hall and the longitudinal resistance can be simultaneously recorded with four potential probes.

3.8.1.1 Four probe measurement

With the 2 probe method, the device resistance is measured in series with the wire and the contact resistance. It is accurate only when the resistance of the device is much higher than the wire and contact resistance.

A four point measurements avoids this problem. A current is applied through two probes that we call the source and the drain, and the two other probes are used to measure a potential drop. This way no current passes through the two measuring probes allowing one to measure only the resistance of the sample.

3.8.1.2 Hall bar, a 6 probe geometry to measure separately Hall and longitudinal resistance

It is interesting to separate the Hall and the longitudinal contributions to the resistance. The idea of the Hall bar is to have two contacts as a drain and a

source at the ends of the sample and 3 potential probes to measure separately the 4 point resistance along one edge and between the two opposite edges. This is sketched in figure 3.1.

3.8.2 Landau level in presence of an external edge confinement potential

We have seen that under a magnetic field the charge carriers are subject to Landau quantization. The energy spectrum is discrete and takes the following values for Schrödinger electrons

$$E_n = (n + 1/2)\hbar\omega_C \quad (3.56)$$

Transport occurs if there is some free state at the Fermi level. Here if the Fermi level is between two Landau levels there should not be any transport. We have to add an important ingredient which is the confinement potential. Thanks to this confinement there is a continuum of energy on the edge, this confinement enables to have some states at the Fermi level to carry the current.

We can see it in a classical way with figure 3.7. Charge carriers in the bulk perform circular trajectories around a fixed point (the guiding center coordinate R_x, R_y) due to the Lorentz force, so they cannot participate in the transport. However, on the edges, assuming a hard wall for simplicity, they bounce and move forward along the edge and backward along the opposite edge. Then there is a permanent current circulating along the edges while no current occurs in the bulk.

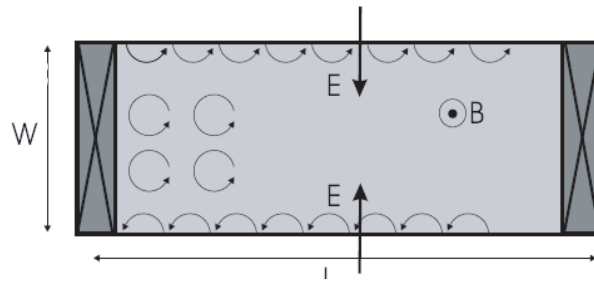


Figure 3.7: 2DEG with a perpendicular magnetic field applied, electron trajectories are represented by the black arrows.

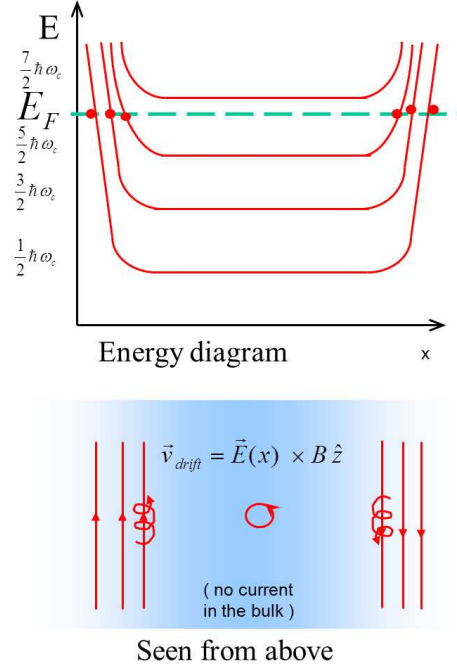


Figure 3.8: Diagram of energy levels as a function position across the sample and representation of electronic trajectories

For a confinement potential $V_c(y)$, independent of x for simplicity, the energy can be expressed (neglecting mixing between LLs):

$$E_n = (n + 1/2)\hbar\omega_C + V_c(y_k) \quad (3.57)$$

From this equation we can compute the drift velocity of the electrons:

$$v_d(n, k) = \frac{1}{\hbar} \frac{\partial E(n, k)}{\partial k} = \frac{1}{\hbar} \frac{\partial V_c(y_k)}{\partial k} = \frac{1}{\hbar} \frac{\partial V_c(y_k)}{\partial y_k} \frac{\partial y_k}{k} = \frac{1}{eB} \frac{\partial V_c(y_k)}{\partial y_k} \quad (3.58)$$

as $\partial U / \partial y = -eE_y$ it comes:

$$\boxed{v_d = -\frac{1}{B} E_y} \quad (3.59)$$

Leading to a current:

$$I = 2e \sum_n \int_{\mu_d}^{\mu_g} \frac{1}{2\pi} v(n, k) dk \quad (3.60)$$

$$I = 2e \sum_n \int_{\mu_d}^{\mu_g} \frac{1}{2\pi} \frac{1}{\hbar} \frac{\partial E(n, k)}{\partial k} dk \quad (3.61)$$

$$I = \frac{2e}{\hbar} \sum_n \int_{\mu_d}^{\mu_g} dE \quad (3.62)$$

$$I = \frac{2e}{\hbar} M(\mu_g - \mu_d) \quad (3.63)$$

The Hall resistance is then:

$$R_H = \frac{V_H}{I} = \frac{h}{2e^2 M} \quad (3.64)$$

$$R_H = \frac{25,8128k\Omega}{2M} \quad (3.65)$$

Where M is the number of filled Landau levels.

In the case of graphene, confinement is abrupt (on an atomic scale) and a full quantum mechanical treatment is needed leading qualitatively to the same picture.

3.8.3 Edge states

As we saw above, the transport in QHE takes place at the edges of the sample. On the plateau these states behave as perfect channels of conduction with no scattering. As mentioned earlier in 2.4.6 the conductance (excluding degeneracy) of such a channel is $\sigma = e^2/h$ due to Pauli principle and does not depend on its length.

These edge states are chiral (this is not linked to Dirac equation), a drift velocity $V_D = \frac{E \times B}{B^2}$ is imposed on the electrons due to the potential and the magnetic field, the sign of V_D depending on the edge, so along one edge the transport is unidirectional. Therefore all the electrons on the same edge regardless of the Landau Level have the same chirality. If an electron is scattered from a channel to another on the same edge it will not change direction and the transmission of the edges will not change. The only way the transmission can differ from $T = 1$ is to scatter an electron onto the opposite edge. This phenomena is strongly suppressed in QHE because the edges are separated by a large distance w (from μm to mm) with respect to the typical extension of the wavefunction under magnetic field l_B which is of the order of nm at high field.

The consequence of this absence of back scattering is that there is no potential drop along an edge, thus $\rho_{xx} = 0$. However we will see in the following back scattering can occur more easily as the energy is increased.

3.8.4 Buttiker equation for transport

A simple view of transport in quantum Hall effect with the edge states picture can be given using the Buttiker formula [49]:

$$I_i = \frac{e}{h} \left((M - r_{ii}) \mu_i - \sum_j t_{ij} \mu_j \right) \quad (3.66)$$

describing the current flowing between two contacts, i and j .

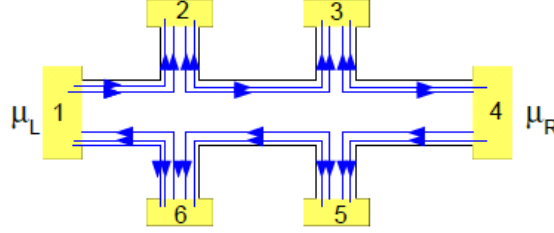


Figure 3.9: Schematic of Buttiker's formula application in a Hall bar

Here we assume that the channels are perfect 1D channels with no back scattering. Then it is easy to know the conductivity, we just have to count the M channels present between two contacts assuming a channel to have a conductance of $G = 2e/h$ (x2 if we count the spin). If we note p the contact from which the channel starts and q the contact at the end, then the conductivity matrix between the 6 contacts can be expressed by:

| G_{pq} | $q = 1$ | $q = 2$ | $q = 3$ | $q = 4$ | $q = 5$ | $q = 6$ |
|----------|---------|---------|---------|---------|---------|---------|
| $p = 1$ | 0 | 0 | 0 | 0 | 0 | G_c |
| $p = 2$ | G_c | 0 | 0 | 0 | 0 | 0 |
| $p = 3$ | 0 | G_c | 0 | 0 | 0 | 0 |
| $p = 4$ | 0 | 0 | G_c | 0 | 0 | 0 |
| $p = 5$ | 0 | 0 | 0 | G_c | 0 | 0 |
| $p = 6$ | 0 | 0 | 0 | 0 | G_c | 0 |

Where $G_C = \frac{2e^2 M}{h}$

$$I_p = \sum_q G_{pq} (V_p - V_q) \quad (3.67)$$

$$\begin{pmatrix} I_1 \\ I_2 \\ I_3 \\ I_4 \\ I_5 \\ I_6 \end{pmatrix} = \begin{pmatrix} G_c & 0 & 0 & 0 & 0 & -G_c \\ -G_c & G_c & 0 & 0 & 0 & 0 \\ 0 & -G_c & G_c & 0 & 0 & 0 \\ 0 & 0 & -G_c & G_c & 0 & 0 \\ 0 & 0 & 0 & -G_c & G_c & 0 \\ 0 & 0 & 0 & 0 & -G_c & G_c \end{pmatrix} \begin{pmatrix} V_1 \\ V_2 \\ V_3 \\ V_4 \\ V_5 \\ V_6 \end{pmatrix}$$

V_4 is usually the drain of the circuit so it is set to be zero. Also a bias current is imposed on the circuit via the source contact which is here the contact 1, so we set $I_1 = I$

Here we can easily see that a same edge remains always at the same potential thus the potential drop is zero:

$$V_1 = V_2 = V_3 = \frac{I}{G_c}, \quad V_4 = V_5 = V_6 = \frac{-I}{G_c}$$

The longitudinal resistance is:

$$R_L = \frac{V_2 - V_3}{I} = \frac{V_6 - V_5}{I} = 0$$

and the Hall resistance is:

$$R_H = \frac{V_2 - V_6}{I} = \frac{V_3 - V_5}{I} = \frac{1}{G_c}$$

This is a simple and powerful tool to know the potential on each contact and to understand different geometries like 3 point measurements.

3.8.5 Quantum Hall transport in graphene

3.8.5.1 Monolayer

QHE in graphene is special due to the Dirac nature of its charge carrier. Geim's group and Kim's group were able to measure this effect in graphene for the first time in 2005 ([50, 14]). The results are different from the conventional QHE. They measure that the indexing of quantum Hall plateaus is $\sigma_{xy} = \pm(4e^2/h)(N + 1/2)$ (where N is an integer) whereas in conventional 2DEG $\sigma_{xy} = (2e^2/h)N$. For this reason QHE in graphene is often called a half integer quantum Hall effect.

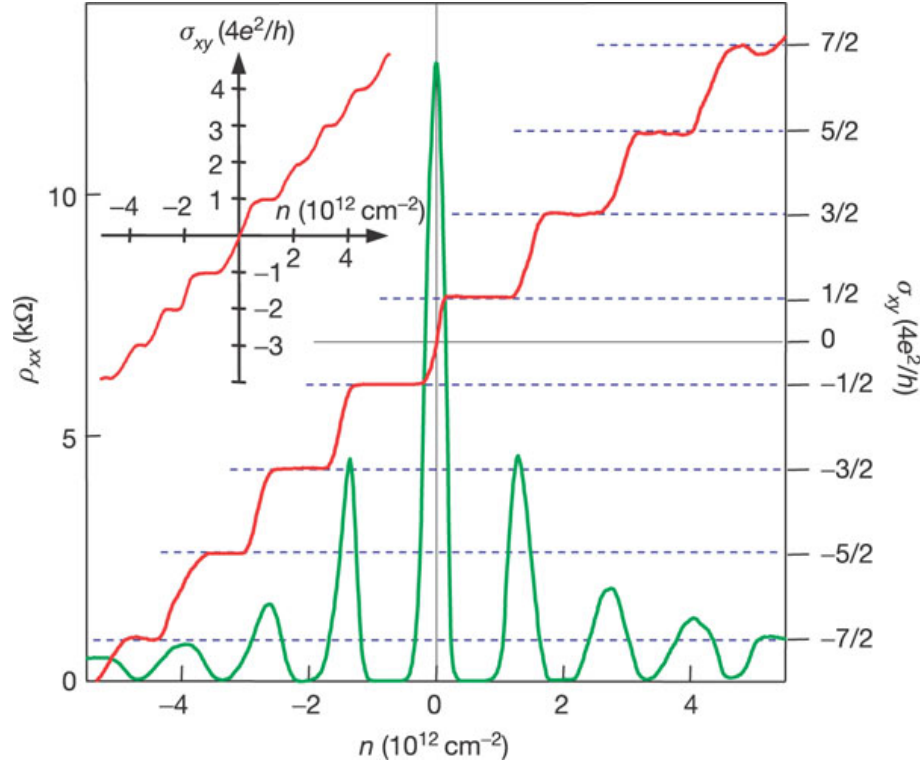


Figure 3.10: Hall conductivity σ_{xy} and longitudinal resistivity ρ_{xx} of graphene as a function of their concentration at $B = 14 \text{ T}$ and $T = 4 \text{ K}$. Inset shows σ_{xy} for a bilayer graphene from [50]

Each channel contributes a quantum of conductance $\sigma = \frac{e^2}{h}$. All Landau levels have degeneracy 4 (2 for the valley and 2 for the spin) except the zero energy Landau level which is shared by electrons and holes thus the conductance for this level is $\sigma = 2\frac{e^2}{h}$ and for the other levels it is $\sigma = 4\frac{e^2}{h}$. As the resistance is the inverse of the conductance (on the Hall plateaus) we can see easily that

$$R_H = \frac{h}{e^2(4n + 2)}$$

On figure 3.11 we show a diagram of the Landau levels in graphene as a function of the distance in the y direction (transverse to the current). At the edge the A and B lattice become inequivalent due to an asymmetry A and B (except on a perfect armchair edge) leading to a splitting of the valley degeneracy.

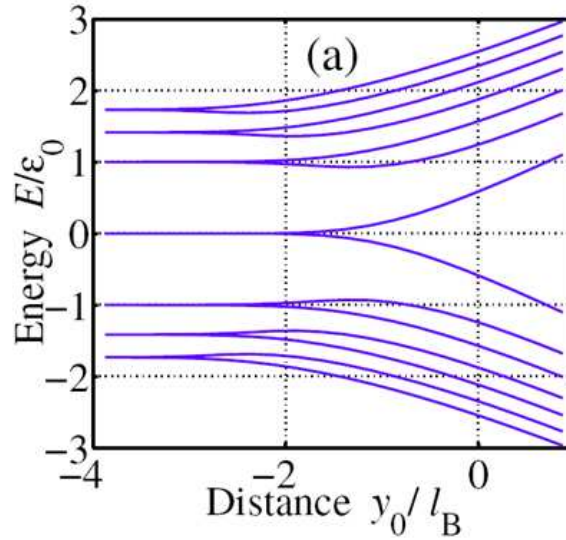


Figure 3.11: Landau Level of graphene.

Since the first observation many group have done experiments to measure graphene's properties in quantum Hall regime.

P.Kim's group was able to observe some degeneracy splitting leading to the apparition of plateau at $\nu = 1$ (spin and valley splitting) and $\nu = 4$ (spin splitting) in ref.[51].

The fractional quantum Hall effect has been observed in 2-probe geometry suspended samples [52, 53]. It has also been observed very recently with multi-probe geometry on suspended graphene [54] and graphene deposited on top of boron nitride [55].

Intriguing quantum Hall state at $\nu = 0$

The zero energy level addressed many questions. A lifting of a degeneracy allowing to observe $\nu = 0$ was mentioned in several experiments [56, 57, ?, 58]. In particular the question whereas when the degeneracy is lifted, it is a quantum Hall insulator or not (the 2 possibilities are sketched on figure 3.12) was very discussed.

The lifting of $\nu = 0$ can be observed only in the conductivities σ_{xx} and σ_{xy} : here both conductivities vanish when the degeneracy is lifted.

Several different behaviors for the longitudinal resistivity ρ_{xx} at the charge neutrality point were reported, some groups observed at low temperature $\rho_{xx} < h/e^2$ [59, 14, 56, 60, 61] whereas other observed $\rho_{xx} \gg h/e^2$ [57, 62, 58]. The observation of $\rho_{xx} \gg h/e^2$ was coupled with decreasing values along with increasing temperature, this indicates an insulating state; whereas observation $\rho_{xx} < h/e^2$ was often coupled with increasing values of ρ_{xx} along with the tem-

perature. From previous references the lifting of degeneracy at $\nu = 0$ seem to be associated with $\rho_{xx} \gg h/e^2$ and an insulator state, whereas, the degeneracy seem to be unlifted in the case of $\rho_{xx} < h/e^2$; however we can note the interesting case of ref [60] which measure a degeneracy lifting on $\nu = 1$ surely associated with a one at $\nu = 0$ (the geometry did not allow to compute σ_{xx} and σ_{xy}) coupled with $\rho_{xx} < h/e^2$ increasing with the temperature.

Corbino measurement on good mobility samples could help to answer this question.

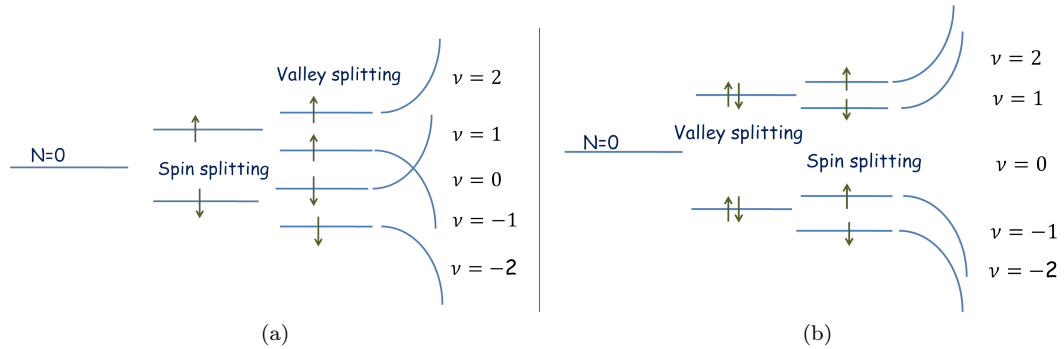


Figure 3.12: schematic of 2 possibilities in spin and valley splitting

3.8.5.2 Bilayer

Quantum Hall effect in bilayer graphene was also measured (it is shown on the inset of figure 3.10). The plateau sequence is different from both monolayers and conventional 2DEG. The indexing is now $\sigma_{xy} = \pm(4e^2/h)N$. This is due to the four fold degeneracy of the Landau levels, and as we saw in 3.5.2 contrary to graphene the zero energy Landau level has the same degeneracy than the other Landau levels, thus the $1/2$ factor disappears.

An observation of quantum Hall effect in bilayer graphene associated with a 2π berry's phase was done in ref.[63].

3.8.6 Corbino geometry

Quantum Hall effect can be seen in other than the four probe geometry we have studied. One interesting variant is the Corbino geometry which allows direct measurement of the longitudinal conductivity σ_{xx} , although the Hall conductivity σ_{xy} in this configuration requires a delicate inductive method. This is of considerable interest because the physics of the transport is contained in the conductivity ($\vec{j} = \sigma \vec{E}$) as the information comes from the way the current is established under an electric field. Also as in Corbino geometry there is no edge one can probe the physics of the bulk. We saw that in four probe measurements QHE edges play an important role, so it is interesting to be able to look only at what happens in the bulk.

The Corbino geometry was introduced by Orso Mario Corbino in 1912 [64]. It is composed of 2 contacts, one external which has the form of a ring surrounding the sample and the other has the form of a circle at the center of the sample, it is attached to the electric circuit by a bridge over the sample.

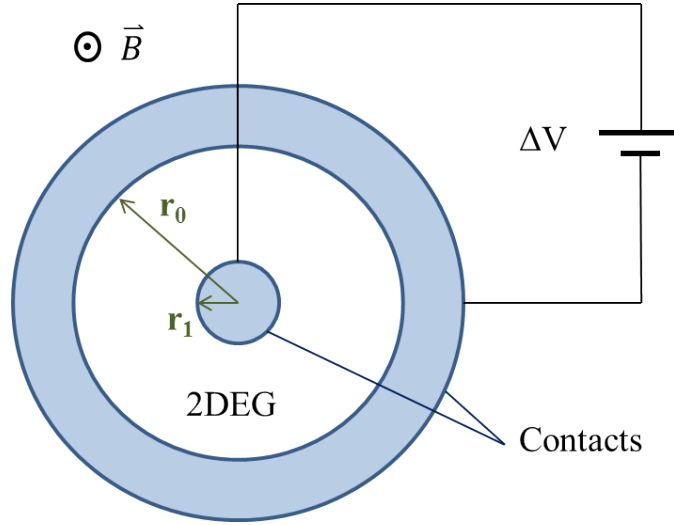


Figure 3.13: Corbino geometry

In the four probe geometry a potential drop is measured, knowing the bias current the values of the Hall resistance R_H and the longitudinal resistance R_{xx} can easily be calculated. However for the resistivity it is not so simple. In 2D, resistivity is defined as a resistance per square. The calculation at $B \neq 0$ requires solving the current density distribution and the electric field everywhere in the sample and has no straightforward expression except in simple geometries.

In practice the aspect ratio of the sample is not easy to determine. It is not a problem for R_H because it is independent of the aspect ratio thus $R_H = \rho_H$. But for ρ_{xx} one needs to know the exact aspect ratio to determine it. And as we saw in eqs. 3.18 and 3.19, to determine the conductivities in the quantum Hall effect one needs to know ρ_{xx} .

This problem is eliminated with Corbino geometry (the calculation is paraphrasing ref [65]):

We consider a time dependent magnetic field

$$B(t) = B_0 + B_1 \sin(\omega t) \quad (3.68)$$

A current $J(J_r, J_\phi)$ is applied, the angular electric field is given by

$$E_\phi = \rho_{\phi\phi} J_\phi + \rho_{\phi r} J_r = \frac{1}{2} r \frac{dB}{dt} \quad (3.69)$$

and The radial electric field is given by

$$E_r = -\rho_{\varphi r} J_\varphi + \rho_{\varphi\varphi} J_r \quad (3.70)$$

$$E_r = J_r \frac{(\rho_{xx}^2 + \rho_{xy}^2)}{\rho_{xx}} - \frac{1}{2} r \frac{dB}{dt} \quad (3.71)$$

The potential drop in between the contact is

$$V = -\frac{I}{2\pi\sigma_{xx}} \ln\left(\frac{r_0}{r_1}\right) + \frac{\rho_{xy}}{4\rho_{xx}} (r_0^2 - r_1^2) \frac{dB}{dt} \quad (3.72)$$

At constant magnetic field the expression is :

$$V = -\frac{I}{2\pi\sigma_{xx}} \ln\left(\frac{r_0}{r_1}\right) \quad (3.73)$$

The longitudinal conductivity is directly accessible by measuring the current as a function of the applied potential. The Hall conductivity can also be measured with an oscillating magnetic field but it is more delicate.

One can find an example of Corbino measurement in conventional 2DEG in ref [66].

3.8.7 Compressibility

Compressibility is an important ingredient for understanding some properties of the quantum Hall effect.

The compressibility κ is defined by:

$$\kappa = -\frac{1}{V} \frac{\partial V}{\partial P} \quad (3.74)$$

Where P is the pressure and V is the volume.

This expression can be linked with the Energy E considering an adiabatic transformation where $\delta E = P\delta V$:

$$\frac{1}{\kappa} = -V \frac{\partial P}{\partial V} = V \frac{\partial^2 E}{\partial V^2} \quad (3.75)$$

We can link this expression to the chemical potential. For a systems with $N \gg 1$ particles with a density $n = N/V$. The chemical potential is $\mu = \partial E / \partial N$

$$\frac{1}{\kappa} = n^2 \frac{d\mu}{dn} \quad (3.76)$$

In QHE when the Fermi level lies between two Landau levels the density does not vary with the potential ie $dn/d\mu = 0$ implying that $\kappa = 0$ which means that the system is incompressible.

This view doesn't yield anything really new but it is interesting to explain the fact that there is no screening when the Fermi level lies between 2 Landau

Levels meaning that the Hall resistance is on a Hall plateau. Because the liquid of electrons is not compressible, it can not be rearranged to screen an external field or Coulomb interactions.

3.8.8 Disorder and localization

From the very beginning we have not considered disorder to explain the QHE. Samples are always disordered and one astonishing fact is that this disorder does not change any of the QHE properties we discussed before, the Hall resistance always takes the same quantized values with metrological accuracy regardless of the amount and type of disorder at zero temperature. More than that, the disorder which leads to localization was shown to improve the quality of the quantum Hall effect and allows its observation in macroscopic samples (typically mm size).

The effect of disorder is to add hills and valleys of potential with random size and distribution.

To take the example of Newtonian dynamics (usual 2DEGs), the Landau level energies become:

$$E_n = (n + 1/2)\hbar\omega_C + V_c(y) + V_l(x, y) \quad (3.77)$$

As a result there will be states available at the Fermi level for electrons in the bulk of the sample, these states are localized and they have small spatial extension compared to the size of the sample.

When the Fermi level lies between two Landau levels, these random hills or valleys of potential provide local crossing between the Fermi level and the Landau level allowing electrons to circle the hills and valleys with a speed $V_D = \frac{E \times B}{B^2}$, enclosing an area $A = i \cdot \phi_0$ where i is an integer and $\phi_0 = h/e$ is the quantum of flux.

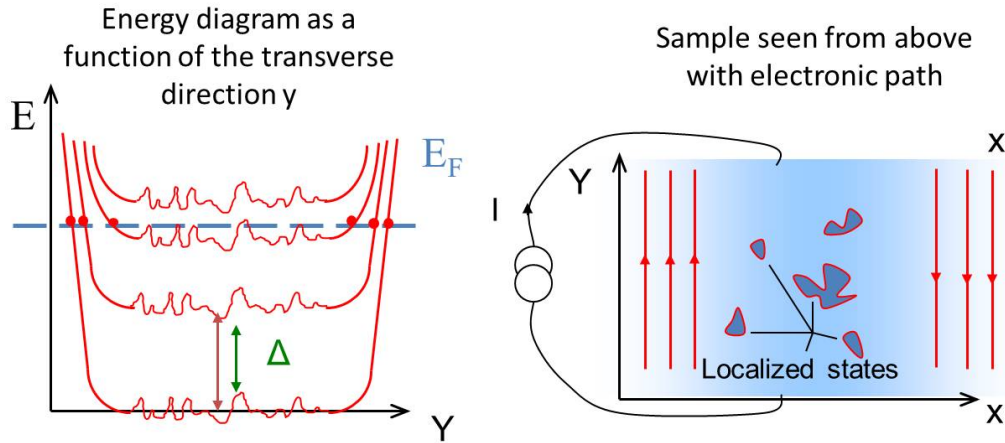


Figure 3.14: Schematic representation of disorder and localized states

This potential is disordered and breaks the symmetry along x and y direction. We can distinguish two types of impurity

- Charged impurities which change locally the density of states and make a smooth potential shift
- Defects (like missing atoms, or dislocations) which make sharp potential shifts like on the edge of the sample.

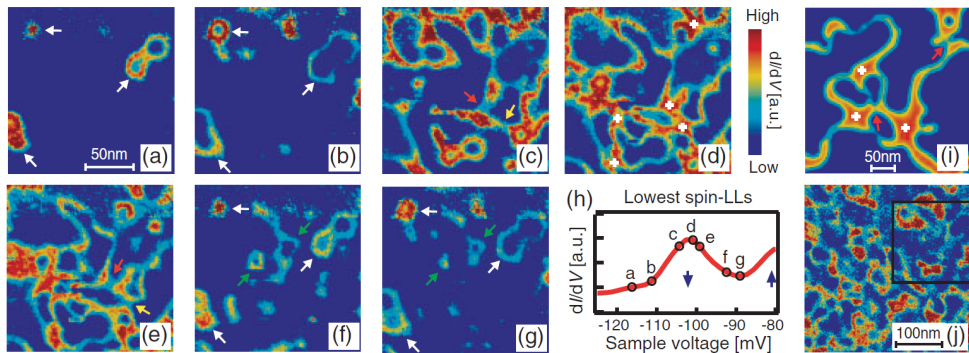


Figure 3.15: Image of localized state by probing the LDOS with scanning tunneling spectroscopy for different energies around a Landau Level.[67]

Figure 3.15 shows experimental image of the localized states realized with scanning tunneling spectroscopy at different energy. Far from a Landau level, localized states can be viewed as small islands at the Fermi level. When the Fermi level approaches a Landau level, these localized states increase in size

until they percolate opening channel at the Fermi levels. The metal-insulator transition in QHE arises when continuous channels are open between sample edges. When the system is insulating the localized state will play an important role in the variable range hopping conduction (detailed in section 3.10.2).

In graphene, images of localized state were achieved using scanning single-electron transistor by Yacobi et al [68].

3.8.9 Broadening of the Landau levels

Disorder leads to broadening of the Landau Levels. If the potential is perfectly flat there is no broadening but if there is some disorder making some hills and valleys, there are regions of energy around the Landau levels that electrons can occupy. This is shown schematically on figure 3.16.

3.9 Metal insulator transition

The quantum Hall effect offers an interesting example of a quantum phase transition in the plateau to plateau transition. Indeed when this transition occurs the longitudinal resistance is non zero and at one single point the system is metallic.

In 2 dimensions in zero magnetic field it is thought that no metallic system can exist because of localization.

3.9.1 Localization length

The localization length ξ which is very near to the size of the localized states provides a good understanding of what happens at the metal insulator transition in QHE. At a critical energy E_C which corresponds to a critical filling factor ν_C , ξ diverges leading to the percolation of the localized state.

For an infinite sample at zero temperature the localization diverges and the system becomes metallic at a single point $E_C = E_n$ where E_n is the unperturbed energy of a Landau level. For finite temperature the system behaves like a metal when the localization length is longer than the sample width allowing electronic backscattering.

This divergence is explained in percolation theory. When the filling factor ν is moved from the middle of a plateau in the direction of an unperturbed Landau level energy the size of localized states extends to open channels of the size of the width of the sample. This is the percolation transition illustrated in fig 3.16.

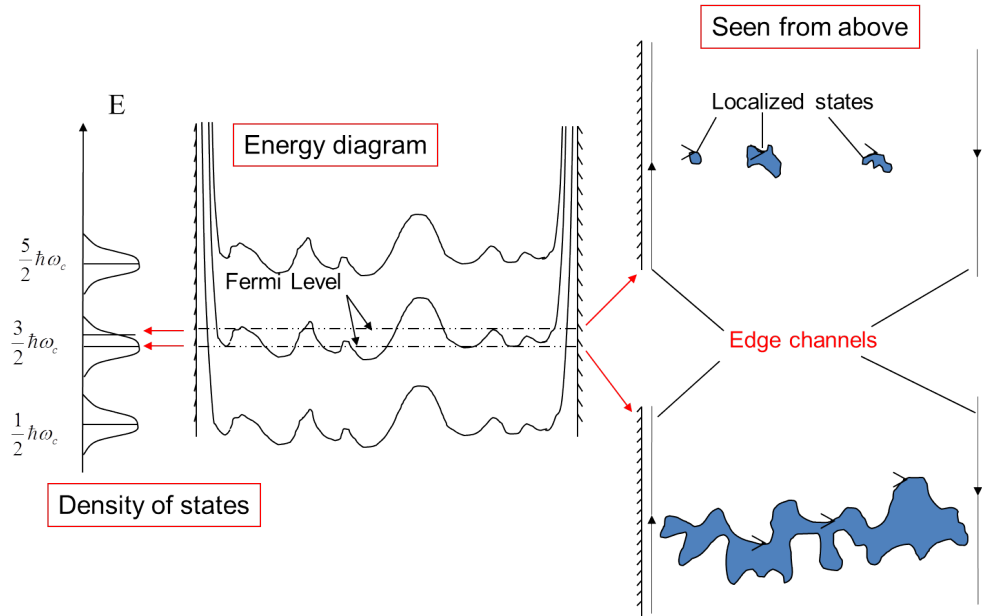


Figure 3.16

From this percolation theory we can express ξ as:

$$\xi(\nu) = \xi(\nu - \nu_c)^{-\gamma}$$

For 2 dimensions classical percolation theory gives $\gamma = 4/3$ ref [69]

In the quantum Hall effect γ was measured several times to be $\gamma \sim 7/3$ which is in apparent contradiction with the percolation theory. However when quantum tunneling between states is included it was found that $\gamma = 7/3$

Numerical calculation confirms this exponent [70, 71, 72]

$$\xi \propto |E - E_C|^{-\gamma}$$

Direct measurement of γ is possible deducing the localization length from VRH theory, as done in ref [73, 74].

Such measurements have also been done in graphene in ref [75]. The results are shown in fig 3.17, but the localization lengths shown are strange because the localization length should mimic the magnetic length and decrease with increasing magnetic field and this is not what is observed.

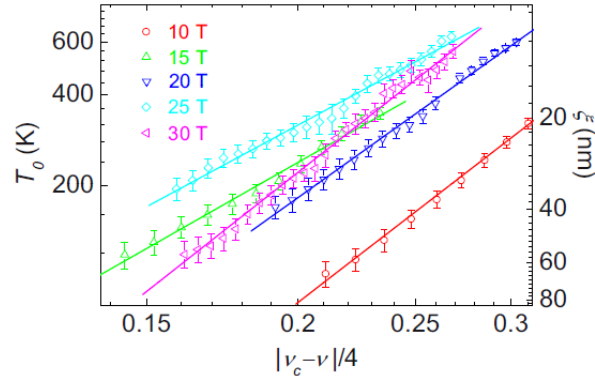


Figure 3.17: Measurement of the localization length in ref [75], The authors took $C=1$ (which will be define later in equation 3.90)

3.10 Finite energy Quantum Hall effect

In the previous section all the physics was at zero temperature, the study of which offers a very powerful tool to understand the physics of the quantum Hall effect.

Also this zero temperature study is justified at low temperature where the value of the longitudinal resistance can be as low as $\rho_{xx} \sim 10^{-16}\Omega$ [76].

It is also very interesting to probe the quantum Hall effect at finite temperature. As we see on the figure 3.18, the Hall and longitudinal resistance vary dramatically with temperature and with bias current. Measuring the quantum Hall effects as a function of the temperature or of the bias current provides much interesting physical information. We will see that at low energy this provides information about the localization defined in the previous section. When the energy is sufficiently high activation energies appear, which indicate of the energy gap between Landau levels.

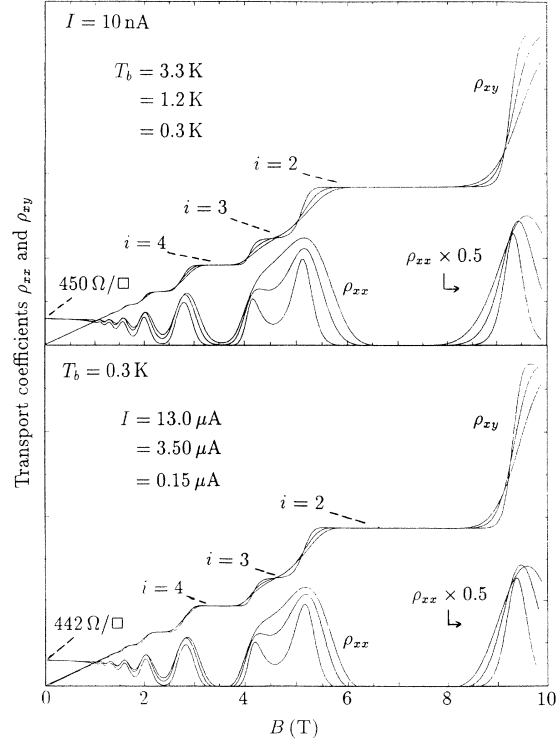


Figure 3.18: Measurement of ρ_{xx} and ρ_{xy} has a function of the magnetic field for different temperatures at fixed bias current (top figure) and for different bias current at fixed temperature (bottom figure)[77]

3.10.1 Thermal activation

Thermal activation usually follows an Arrhenius law which is an empirical law that appeared in the measurement of chemical reactions. In this law the rate of a chemical reaction k is expressed as follow:

$$k = Ae^{-E_a/RT}$$

R is the gas constant. The dominant parameter here is the activation energy E_a . The statistical mechanism was later explained by Eyring [78].

The probability for an electron to jump onto a higher Landau level is also given by an Arrhenius law. The expression of the conductivity as a function of the temperature is thus expressed as follows:

$$\sigma_{xx} = \sigma_{xx}^0 \exp\left(-\frac{E_a}{k_B T}\right)$$

Theoretical calculations for the conductivity in the activated regime can be

found in ref. [79, 80, 81], the universality of the prefactor σ_{xx}^0 was addressed in ref [82] and found to be $\sigma_{xx}^0 = 2e^2/h$.

The energy gap Δ between Landau levels can be deduced from the activation energy when the Fermi levels lies in the middle of 2 Landau levels, there $\Delta = 2E_a$.

The Activation law has been demonstrated both in conventional 2DEG [83, 84] and in graphene [61]. For both it is usual to get lower values of the activation gap than those predicted by the theory because of the broadening of the Landau levels by the disorder (as mentioned in 3.8.9).

A measurement of the prefactor finding the value of $2e^2/h$ is done in ref. [85].

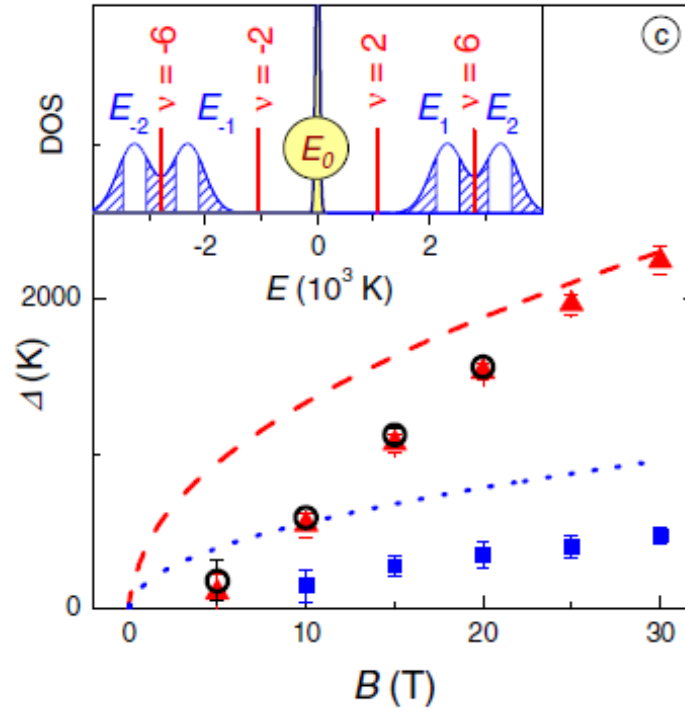


Figure 3.19: Energy gap 2Δ for $\nu = 2$ and $\nu = 6$ graphene QHE plotted as a function of the magnetic fields. These gaps are deduced from the Arrhenius plots of ρ_{xx} . The dashed (red) and dotted (blue) lines are the theoretically expected energy gaps for sharp Landau levels. The inset shows schematically the density of states for a sharp zeroth Landau level and broadened higher Landau levels for electrons and holes at 30 T. figure from [61]

The values of the activation gap were determined for both monolayers (see figure 3.19) and bilayers [19].

3.10.2 Transport through localized states.

3.10.2.1 Variable Range Hopping (VRH)

Mott VRH

The variable range hopping law was originally derived by Mott to describe a conduction process at finite energy in some insulators.

Here I would like to introduce a calculation of this process which is amenable to a good physical interpretation.

A complete and rigorous computation is not easy, but a good example can be found in ref [86]

To derive this law we emphasize that there are some states occupied by charge carriers and other states which are empty but can be occupied and which are separated by a distance R and by an energy w (as shown on the figure 3.20). The probability of hopping from an occupied to an empty state is given by

$$P = e^{-R/\xi} \cdot e^{-w/k_B T} \quad (3.78)$$

where ξ is the spatial extension of the wavefunction. An electron is able to hop if there is an empty state within the radius considered. This condition takes the form:

$$\alpha \rho w R^d = 1 \quad (3.79)$$

where α is a constant, ρ is the density of states and d the dimensionality. With this expression we can express w as a function of R , then replace it in the expression 3.78.

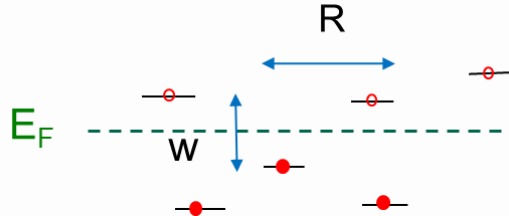


Figure 3.20: representation of occupied and empty states

The next step is to maximize the probability of a hopping as a function of the distance.

Here we consider a small energy interval w near the Fermi level. Assuming density of states is constant over this interval we can write the probability for N hopping as follows:

$$P = e^{-\left(\frac{R}{\xi} + \frac{T_0 R^d}{R^d T}\right) \cdot N} \quad (3.80)$$

where $T_0 R_0^d = \frac{1}{\rho \alpha k_B}$. Maximizing this probability we get the most probable hopping distance R :

$$\frac{d}{dR} \left(\frac{R}{\xi} + \frac{T_0 R^d}{R^d T} \right) = 0 \quad (3.81)$$

$$R = \beta.T^{-1/(d+1)} \quad (3.82)$$

where $\beta = (\xi d R_0^d T_0)^{1/(d+1)}$

Putting this expression for R in equation 3.78 and assuming the conductivity is proportional to the probability of hopping we get Mott's law:

$$\sigma \approx e^{-(T_0/T)^{1/(d+1)}} \quad (3.83)$$

Efros-Shklovskii VRH

Efros and Shklovskii re-derived this law for electrons with Coulomb interactions [87]. The effect of the Coulomb interaction is to empty the density of states near the Fermi energy. In the Mott law the density of states was assumed constant, but when one includes the Coulomb interaction it varies with energy below a critical energy E_c from the Fermi level and vanishes at the Fermi level.

We take into account Coulomb interactions to express the energy that an electron needs to hop from an empty state j to an occupied one i :

$$\Delta E_{ij} = E_j - E_i - \frac{U}{2r_{ij}} \quad (3.84)$$

where $U = e^2/4\pi\epsilon$ is the interaction parameter.
This energy needs to be positive, thus

$$\Delta E_{ij} > 0 \quad (3.85)$$

We consider a small energy interval $\varepsilon = E_i - E_j$ centred at the Fermi surface. With the assumption that $\varepsilon < E_c$, E_c is the size in energy of the coulomb gap. As a result of the inequality 3.85: $U/2r_{ij} < \varepsilon$.

Assuming that the $N(\varepsilon)$ states are homogeneously distributed in a volume L^d we have $N(\varepsilon) \sim (L/r_{ij})^d$.

The density of states is:

$$\rho(\varepsilon) = \frac{1}{L^d} \frac{N(\varepsilon)}{\varepsilon} < A \frac{\varepsilon^{d-1}}{U^d} \quad (3.86)$$

Where A is a constant. It can be shown that this inequality is in fact an equality.

Indeed, if $g(\varepsilon) \propto \varepsilon^\nu$, at 2 dimensions, $\nu < 1$ would contradict the inequality 3.85 and if $\nu > 1$ the mean distance between the states in the energy interval ε would be so large that the interactions may be neglected.

This equality remains valid when the density $g(\varepsilon)$ is small compared to the density g_0 at the Fermi level, so the width of the gap can be given by the equation $g(E_c) = g_0$.

Thus the density of state for 2 dimensions is:

$$\begin{cases} g(\varepsilon) = \frac{2}{\pi} \frac{\varepsilon^2}{e^4} |\varepsilon - \varepsilon_F| & \varepsilon < E_C \\ g(\varepsilon) = cte & \varepsilon > E_C \end{cases} \quad (3.87)$$

The derivation of the hopping probability with this density of states leads to a conductivity independent of the space dimension:

$$\boxed{\sigma \approx e^{-(T_0/T)^{1/2}}} \quad (3.88)$$

The crossover from ES VRH to Mott VRH has been measured in several different materials at zero magnetic field [88, 89].

A detailed calculation of Mott and ES VRH can be found in ref. [86].

3.10.2.2 Variable range hopping and quantum hall effect

Variable range Hopping with Efros-Shklovskii law

Poliakov and Shklovskii proposed [90] that VRH explain transport through localized states in the Quantum Hall system.

$$\sigma_{xx} = \sigma_0 \exp(-(T_0/T)^{1/2}) \quad (3.89)$$

where :

$$k_B T_0 = \frac{C e^2}{4\pi\varepsilon\varepsilon_0\xi(\nu)} \quad (3.90)$$

Here ξ is the localization length which represents the typical size of localized states. C is a constant; for 2 dimensions it was found that $C = 6.2$ [91].

It is interesting to express the E-S formula in terms of the characteristic length ξ :

$$\sigma_{xx} \propto \sigma_0 \exp(-(L_{E-S}/\xi)^{1/2}) \quad (3.91)$$

where $L_{E-S}(T) = 4\pi\varepsilon_0\varepsilon k_B T / C e^2$.

This law was measured many times in conventional 2DEG [73, 74, 92, 93, 94]

VRH Prefactor

The VRH prefactor rises the question of its possible temperature dependence. Most experiments which had observed VRH behavior (cited just before) found that $\sigma_{xx}^0 \propto 1/T$.

In Ono's theory the prefactor found is in agreement with most of the observation::

$$\sigma_{xx}^0 = \frac{e^2 \gamma_0}{k_B T}$$

Where γ_0 is an electron-phonon coupling constant.

Poliakov and Shklovskii found in their derivation of ES VRH for quantum Hall effect:

$$\sigma_{xx}^0 = \frac{e^2}{h} f\left(\frac{T}{T_3}\right)$$

Here f is a dimensionless function. Experimentally it was observed that $f \propto 1/T$. To my knowledge no precise calculation of f has been done, P-S argue that it cannot be derived in the framework of a conventional theory of phonon-assisted hopping and suggest doing the calculation from the starting point of electron electron scattering.

Pepper and Shlimak use this argument to derive the prefactor based on electron-electron scattering [95]: they found a universal temperature independent value:

$$\sigma_{xx}^0 = \frac{e^2}{h}$$

Experimentally such a prefactor has been measured in ref.[96, 97].

However they argue that under a high magnetic field phonon assisted hopping is restored and $\sigma_{xx}^0 \propto 1/T$.

Variable range Hopping with Mott law

Aleiner and Shklovskii [98] predicted that there should be a cross over between E-S VRH and Mott VRH when interactions are screened as for example in the case of a gated Hall bar.

The Mott formula:

$$\sigma_{xx} \propto \frac{1}{T} \exp(-(T_M/T)^{1/3}) \quad (3.92)$$

can be written as a function of the characteristic length which gives a better physical image as in this problem we are looking at typical hopping distances:

$$\sigma_{xx} \propto \left(\frac{1}{L_M(T)}\right)^2 \exp(-(\frac{L_M(T)}{\xi})^{2/3}) \quad (3.93)$$

Where $L_M(T) = \sqrt{1/\pi g(E_F)k_B T}$, here $g(E_F)$ is the energy independent density of states at the Fermi energy.

The prefactor of the Mott law in the quantum Hall effect has not been investigated theoretically but there is no reason that it differ from the $1/T$ prefactor in ES-VRH as this prefactor is due to the electron-phonon coupling.

This crossover was observed for the first time in the QHE regime in our experiments (see chapter 8).

Variable range hopping with bias current

Variable range hopping has also been derived as a function of the Hall field which is proportional to the bias current. It is based on the fact that there exists a quasi-Fermi level tilted by the electric field E_H . Zero temperature hopping with phonon emission then becomes possible. The local Fermi distribution takes on an effective temperature of $\sim eE_H\xi$ where ξ is the localization length. The exponent of the current voltage characteristic can then be obtained by replacing the temperature as follows: $T \rightarrow eE_H\xi/2$. The VRH conductivity can then be expressed by replacing the temperature in 3.89:

$$\sigma_{xx} = \sigma_0 \exp\left(-\left(\frac{2T_0}{eE_H\xi}\right)^{1/2}\right) \quad (3.94)$$

Comparing this equation to 3.89 we can easily extract an effective temperature

$$k_B T_{eff} = \left(\frac{ce^3}{2k_B^2 \epsilon \epsilon_0} E_H\right)^{1/2}$$

The effective temperature can be expressed in terms of the bias current using the fact that on the center of a Hall plateau where $\rho_{xx} = 0$ there is a relation between bias current J and the Hall field E_H : $J = \rho_{xy} E_H$

$$k_B T_{eff}(I) = e\xi \frac{\rho_{xy} I}{2\alpha L_y} \quad (3.95)$$

where α is a coefficient depending on the way of decrease of Hall potential in the sample and L_y is the sample width. (see section 3.10.4)

In this expression we see that bias current plays the role of a temperature with a linear power law.

The prefactor σ_0 with bias current should be similar as in the temperature VRH and proportional to $1/I$.

3.10.3 Breakdown of the QHE

Usually the longitudinal resistivity ρ_{xx} and the deviation of the Hall plateau in ρ_{xy} from the quantized values increases in a smooth monotonic way with temperature. In contrast, with increasing bias current, a sudden increase of ρ_{xx} (by several orders of magnitude) was reported when the current exceeded a certain value. This was reported as the breakdown of the quantum Hall effect. Here we will only give a short introduction and a few references to this vast subject. A good introduction to can be found in ref. [99] and a detailed review in ref.[100]

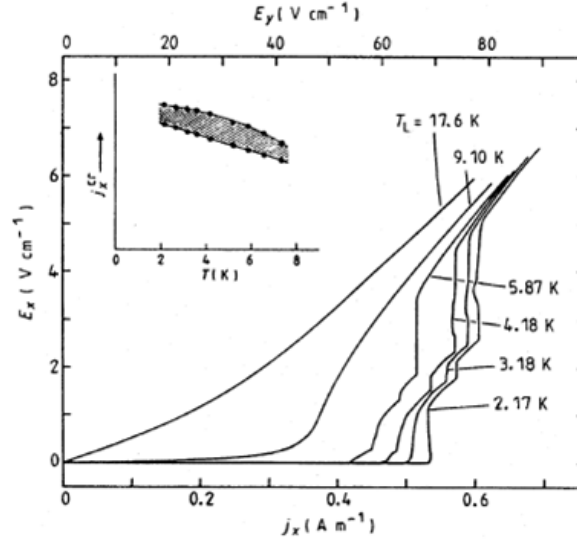


Figure 3.21: Longitudinal potential V_{xx} as a function of the bias current for different temperature on $\nu = 2$ at 6 Tesla for a $380\mu\text{m}$ wide sample. The sharp increase of V_{xx} at low temperature is a typical example of breakdown [101].

The critical breakdown current was found to increase linearly with the sample size in most experiments (references can be found in ref.[99]) but sublinearly in high mobility samples[102]. Also several experiments report a $B^{3/2}$ dependence of the critical current with the magnetic field [99].

Several models have been proposed to explain this breakdown which are well described in [100]. One which can explain both the linear dependence on the critical current with the size of the sample and the $B^{3/2}$ dependence has been introduced by Kominaya and Kawagashi [103]; they propose an avalanche type electron-hole pair multiplication when the Hall field exceeds a critical value. As shown on figure 3.22, the Landau levels are tilted due to the Hall field and when the total tilt becomes of the same order as the Landau level spacing, it becomes energetically advantageous for charge carriers to hop into a higher index empty Landau level leading to backscattering. This gives rise to an avalanche effect which explain the sharpness of the ρ_{xx} increase. This process was found to need a minimal distance L_M for developing the electron-hole pair creation cascade. Measurement of cyclotron emission spatially resolved by Y. Kawano and S. Komiyama [104] confirmed this idea of avalanche. They also measured cyclotron emission as a function of the width [105] and found that above $w \sim 100\mu\text{m}$ the breakdown was preceded by a local breakdown near the drain and source contacts whereas for smaller values it was not.

Note that Y. Kawaguchi et al observed the disappearance of the breakdown in short devices (less than $30\mu\text{m}$) [106]. As we will see, graphene samples studied in our work do not show sharp breakdown and this may be due to too narrow

samples.

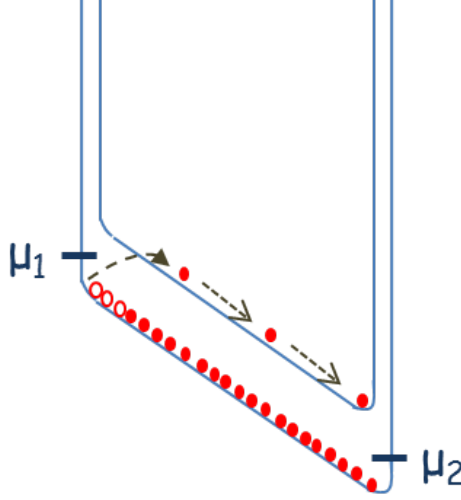


Figure 3.22: schematic of the breakdown of QHE

3.10.4 Hall Field distribution

In the previous section we represented the Hall potential as decreasing linearly across the sample. A more realistic view is given in figure 3.23 where the decrease of potential on the Hall plateaus take place mostly within a short distance of the sample edges, whereas in the insulating bulk where screening is very low the potential decreases more slowly. This can be explained by the fact that the electron liquid in the bulk of the sample is nearly incompressible, charges cannot rearrange to screen the potential whereas at the edges they can, thus an important part of the potential is screened on the edges. Several experiments measured this non-homogeneity of the Hall field distribution on a plateau by placing contacts in the bulk of the Hall bar [107, 108, 109]. Also, it was measured optically on very large sample by Fountein et al [110], the results are presented in fig. 3.23, for a 2mm wide Hall bar they measured that the Hall potential decreases to 80% at a distance of $70\mu\text{m}$ from the edges; here the $70\mu\text{m}$ represents the spatial resolution of the experiment and therefore represents an upper bound on the length. This length depends on the shape of the confinement potential: if it is abrupt, Buttiker's model [111] predicts that it is approximately equal to the cyclotron length l_c whereas other approaches consider a length of the order of the Bohr radius a [112]; Mac Donald et al. calculated it using the Hartree approximation for slowly varying potentials and found a length of the order of $l_c^2/\pi a$ which is of the order of λ_F in graphene[113]. Here the important result is that on a Hall plateau the Hall field decrease is distributed near the edges on a lengthscale which is very small compared to the size of the sample.

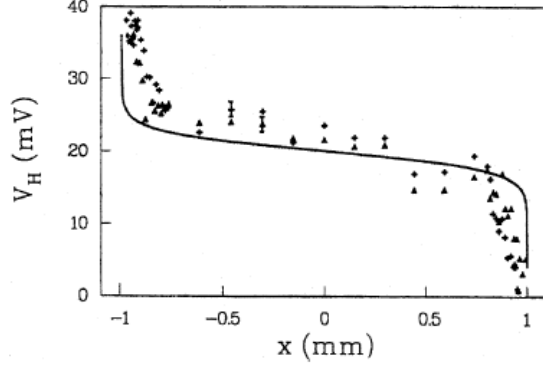


Figure 3.23: Hall potential measured electro-optically across a 2mm wide Hall bar in a conventional 2DEG, at a current of 5 A. The scans were taken within the 4th QH plateau, at $B=5,0\text{T}$ (\blacktriangle) and $5,25\text{T}$ ($+$). Full line: calculated profile. Data from Fontein et al. [110]

3.10.5 Width of the ρ_{xx} peak

An interesting and widely studied aspect of the QHE is the transition from plateau to plateau which gives rise to a non zero longitudinal conductivity. In many experiments the width $\Delta\nu$ of the resistivity peak was found to shrink as $T \rightarrow 0$ according to a power law $\Delta\nu \propto T^\mu$.

Two main theories explain this fact and up to now there has been no clear experimental evidence for choosing between them.

3.10.5.1 Pruisken theory, Anderson Transition

Pruisken [114] was the first to give an explanation for the width of the ρ_{xx} peak, in terms of a metal-insulator transition. He argued that at finite temperature the phase coherence length L_ϕ is inversely proportional to the temperature T . If $L_\phi \ll \xi(\varepsilon_F)$ the localization is destroyed and the electron system exhibits metallic behavior.

In this theory, the effective sample length is taken as $L = (D\tau_\phi)^{1/2}$ where D is a diffusion constant and $\tau_\phi \propto T^{-p}$ a phase coherence time which follows a non-universal power law, $p = 2$ usually. As a consequence the FWHM $\Delta\nu$ of the conductance peaks obeys the temperature power law

$$\Delta\nu = (T/T_1)^\mu \quad (3.96)$$

with

$$\mu = p/2\gamma \quad (3.97)$$

Also considering that the quantized plateau occurs when $\rho_{xx} = 0$, we can easily understand that the slope of the Hall resistance R_H is related to the width of the peak of ρ_{xx} , indeed it was shown that [114]:

$$\left(\frac{\partial \rho_{xy}}{\partial B}\right)^{max} \propto T^\mu$$

This scaling was also verified with bias current measurements by Wei [115, 77] which led to:

$$\Delta\nu = (J/J_1)^{\mu'} \quad (3.98)$$

$$\boxed{\mu' = p/4\gamma} \quad (3.99)$$

Many experiments were carried out to measure μ . Historically it was the first method for the determination of γ but it is not direct as it involves p . This was originally observed by Wei et al [116]

The first extensive measurement of μ was done by Wei and Tsui in ref [117] who found the classical values of $\mu = 0.42$ and $\gamma = 2.3$. The experimental results are shown in fig 3.24.

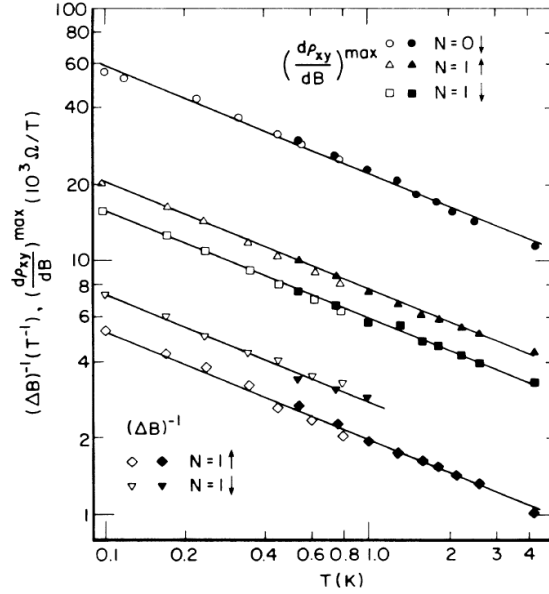


Figure 3.24: The upper portion shows the temperature dependence of $(\partial \rho_{xy}/\partial B)^{max}$ for $N=0$ and $N=1$. The lower part shows the temperature dependence of the width of the ρ_{xx} peak ($1/\Delta B$). Figure from ref. [117].

In an experiment performed by Koch et al [118] shown in figure 3.25, the μ exponent was measured as a function of the sample width. It is shown to be independent of the sample width except at low temperature, where the ρ_{xx} peak width saturates when the localization length attain the size of the sample.

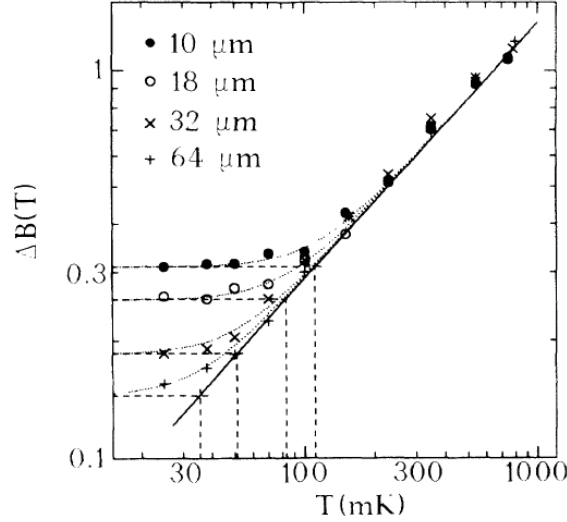


Figure 3.25: The width of ρ_{xx} as a function of the temperature in the Landau level $N = 1 \uparrow$, data from ref. [118]

Much measurements and debates have been centred around on the value and universality of μ as a function of different parameters such as spin [119] or the type of disorder [120, 121]. A good review exists in ref. [122].

3.10.5.2 VRH

E-S VRH: PS argument The argument of Poliakov and Shklovskii to explain the width of the ρ_{xx} peak is that it should be proportional to the value of T_0 as when $T = T_0$ in eq 3.89, the value of the conductivity σ is not vanishing any more. This theory doesn't involve the coherence length for the metal insulator transition.

From the equation 3.90 we can express a universal behavior with T_0 :

$$T_0(\nu) = \alpha(\nu - \nu_c)^\gamma \quad (3.100)$$

Where α is a constant.

With the argument of P-S we can easily compute the width of the peak which is linked to the metal-insulator transition:

$$\Delta\nu = \left(\frac{T}{T_1}\right)^\mu \quad (3.101)$$

with:

$$\mu = 1/\gamma$$

and

$$T_1 = A \frac{1}{k_B} \frac{e^2}{\varepsilon \xi_0}$$

where A is a numerical coefficient.

The same argument for the width of ρ_{xx} peak with increasing bias current leads to:

$$\Delta\nu = \left(\frac{J}{J_1}\right)^{\mu'} \quad (3.102)$$

$$\boxed{\mu' = 1/2\gamma}$$

The same factor was found from Pruisken's argument with $p = 2$ in agreement with Wei's experimental values, so a priori it is impossible to distinguish which is the better adapted. Except, as we shall see, if there is a metallic gate which can screen the interactions beyond a certain length scale.

Mott: Aleiner and Shklovskii argument Aleiner and Shklovskii use the same argument as P-S to compute μ and μ' but in the Mott VRH regime.

For the behavior of $\Delta\nu$ with the temperature, they found:

$$\Delta\nu = \left(\frac{T}{T_2}\right)^\mu \quad (3.103)$$

$$\boxed{\mu = 1/2\gamma}$$

where

$$T_2 = B \frac{1}{k_B} \frac{e^2 d}{\epsilon \xi_0^2}$$

$B \sim 140$ is a constant.

The same argument for bias current leads to:

$$\Delta\nu = \left(\frac{J}{J_1}\right)^{\mu'} \quad (3.104)$$

$$\boxed{\mu' = 1/3\gamma}$$

Pruisken's theory predicts no change in the $\Delta\nu$ exponent if the interactions are screened.

Thus, a good way to distinguish between the PS argument and Pruisken's is provided by measuring the universal exponent in the Mott VRH regime.

To our knowledge, VRH in the QHE has been always observed in the ES regime and no transition from ES to Mott has been observed in QHE before our own experiments.

3.10.5.3 To summarize:

| Theory | Pruisken | P-S | |
|------------------|-------------|-------------|-------------|
| Transport regime | all | E-S VRH | Mott's VRH |
| μ | $p/2\gamma$ | $1/\gamma$ | $1/2\gamma$ |
| μ' | $p/4\gamma$ | $1/2\gamma$ | $1/3\gamma$ |

3.11 Metrology

Since the discovery of the quantum Hall effect it became evident that the very precise quantized value of the Hall resistance could be used for metrological purposes. Indeed K. Von Klitzing cites in ref [39] “discussions with Prof. Kose at the PTB about this new quantum phenomenon started already one day after the discovery of the quantized Hall resistance”. Only 10 years after its discovery the CIPM (conférence internationale des poids et mesures) recommended using QHE for ohm metrology.

The quantum Hall resistance gives access to the value of $h/e^2 = 25812.807\dots\Omega$. This measured value is universal: it does not depend on the shape, disorder or microscopic details of the sample. This universality makes it a very interesting candidate for the metrologist.

The international system of units is based on the “second”, the “meter”, the “kilogram” and the “Ampere”. The first three are well defined with very good accuracy, in contrast to the Ampere which has a relative uncertainty of 10^{-6} . The Ampere is that constant current which, if maintained in two straight parallel conductors of infinite length, of negligible circular cross-section, and placed 1 meter apart in vacuum, would produce between these conductors a force equal to 2.10^{-7} newton per meter of length [123]. The ohm is derived from the Ampere: $1\Omega = 1s^{-3}.m^2.kg.A^{-2}$, so it should have a larger uncertainty than the Ampere. This is not the case, with the measurement of A.C. impedance $R = \frac{1}{\omega C}$ of a capacitor C [124], 10^{-7} uncertainty is achievable. Knowing the Ω value in SI it was thought to use the QHE for a better accuracy in the fine structure constant measurement (max 10^{-7}).

The precision and accuracy of the quantum Hall resistance is better than any A.C. resistor, so metrologists have sought instead to use this resistance as a standard for the Ω . The Comité Consultatif d’Electricité recommended “that exactly 25 812.807 Ohm should be adopted as a conventional value, denoted by R_{K-90} , for the Von Klitzing constant RK” and that this value should be used starting on 1.1.1990 to form laboratory reference standards of resistances all over the world[124].

We collaborated with the Laboratoire National de Métrologie et d’Essais (LNE) on the fabrication of graphene samples for metrology.

Graphene is very promising for metrology due to its high cyclotron energy (excited state energies). For fundamental metrology it is important to demonstrate the universality of QHE by comparing it in several materials with different bandstructures. Also, because it accepts a higher bias current than in conventional 2DEGs without change in the Hall resistance, it affords better accuracy.

For applications it opens the possibility of making commercial devices to compare resistances based on the quantum Hall effect which work at nitrogen temperature with magnetic field of the order of 1 Tesla (achievable with a simple magnet).

J.Guignard et al at the LNE made quantitative tests on an exfoliated graphene sample made in CEA (with the same technique as described in 4), by comparison of a 100Ω resistor previously calibrated with the QHE of an AlGaAs/GaAs

(Hall-) Resistance $R_H = U/I$

| | |
|-------------------|---|
| PRL 45,494 (1980) | 25 812.68 (8) Ω |
| BIPM (PARIS) | 25 812.809 (3) Ω |
| PTB (D) | 25 812.802 (3) Ω |
| ETL (JAPAN) | 25 812.804 (8) Ω |
| VSL (NL) | 25 812.802 (5) Ω |
| NRC (Can) | 25 812.814 (6) Ω |
| EAM (CH) | 25 812.809 (4) Ω |
| NBS (USA) | 25 812.810 (2) Ω |
| NPL (GB) | 25 812.811 (2) Ω |
| 1.1.1990 | 25 812.80700 Ω |

Figure 3.26

heterostructure.

They found $\Delta R_H/R_H = 3.10^{-7}$ on the plateau $\nu = 2$ with a monolayer at 12 Tesla, for a temperature of 1,3K .

On a bilayer they measured $\Delta R_H/R_H = 5.10^{-7}$. (to be published soon)

Part II

Experimental

Chapter 4

Graphene Fabrication

In this chapter the fabrication of electronic device centered on graphene will be described from the exfoliation of the graphene to the deposition of metal contacts.

4.1 Obtaining graphene

The method used during my PhD was the graphene exfoliation. I will first introduce briefly the other method found for graphene deposition, then I will focus on the exfoliation method.

4.1.1 Epitaxy

Epitaxy is a depositing method using chemical reaction. This technique allows deposition of a monocrystalline film on a monocrystalline substrate. The term epitaxy comes from the Greek, epi, meaning "above", and taxis, meaning "in ordered manner".

Epitaxial films may be grown from gaseous or liquid precursors. Because the substrate acts as a seed crystal, the deposited film takes on a lattice structure and orientation identical to those of the substrate. If a film is deposited on a substrate of the same composition, the process is called homoepitaxy; otherwise it is called hetero-epitaxy.

This process is widely used for the fabrication of conventional 2DEGs (Heterojunction of AsGaAs/AlGaAs). It allows high purity in the growth crystal resulting in a very high mobility.

4.1.1.1 Epitaxy on SiC

Graphene can be grown by the thermal decomposition of SiC. This method leads to a few layers of graphene decoupled one from the other: wafer size graphene should be possible via this method [125]. Electronic properties of graphene including the half integer quantum Hall effect have already been observed.[126]

Several methods had been tried, on different kind of SiC on both faces. Heating first with argon seems to generate large domains.

4.1.1.2 Epitaxy on Ruthenium

Epitaxy growth of graphene was also achieved on ruthenium. This technique allows a controlled graphene manufacturing layer by layer [127].

4.1.2 Liquid phase exfoliation

An other method than the conventional scotch tape for exfoliate graphite is the dispersion of graphite in organic solvent. This method was shown to allow the production of graphene monolayers in [128] but do not seem to be very used.

4.1.3 Chemical Vapor Deposition (CVD)

CVD is a process often used in the semiconductor industry to produce high purity solids. In a typical CVD process the substrate is exposed to a heated vapor precursor to allow activated chemical reaction with the substrate. The chemical reaction can either be decomposition or combination. For graphene the usual precursor is CH₄. Nickel and copper substrates have been used in CVD process with good results, indeed this method allows the production of good mobility graphene comparable to those obtained with the Exfoliation technique. [129, 130]. This technique seems to be the most promising for future graphene development in industry and some applications such as a touchscreen have already been achieved.

4.1.4 Exfoliation

This is the method I used for the fabrication of the devices. This was the first method to obtain graphene discovered by Geim and Novoselov[7]. When I begun my PhD it was the only known method to make a sample in which QHE was observable. This method consists of peeling graphite with tape, and depositing it on a Silicon wafer.

I will describe here in details all the manufacturing processes as it was the one I developed thanks to K.Novoselov's advice.

4.1.4.1 Preparation of the substrate.

An array of gold marks to avoid being lost

Before depositing Graphene it is important to prepare the SiO₂ substrate.

The first step is to put an array of gold crosses on the sample. For that I used optical lithography to put an array of crosses with numbers, so that when a graphene is located its position on the substrate can be saved. Also these crosses are essential for alignment in manufacturing devices. We evaporate 3/70nm Cr/Au for these crosses. Chromium is an interesting adhesive layer because unlike titanium it is resistant to the cleaning process. Gold which has

a higher density allows it to be seen with E-beam microscope under a PMMA resist (see lithography 4.3.2).

Cleaning, a critical step for graphene adhesion

The next step is to divide the 2-inch wafer into four parts (it is more convenient to deposit graphene on one fourth of a wafer).

Then, a very important step is the cleaning. As van der Waals forces enable graphene to stick to the substrate, the cleaner it is the more graphene will stick. If some dust or other small things remains on the substrate the surface of adherence for graphene will decrease resulting a lower probability of gripping.

We must therefore be extremely careful during this step. First we clean the substrate with acetone and isopropyl alcohol then with a Piranha solution.

Piranha solution is a mixture of hydrogen peroxide (H_2O_2) and sulfuric acid (H_2SO_4) in ratio of 1:3. This mixture is a strong oxidizer and removes most of the organic matter. It reacts with heat release and the temperature typically rises to around 100°C , then slowly decreases. We leave the wafer in this solution for 1 hour with a heater at 90°C to maintain the temperature during all the process.

This process is done in a clean room in an extractor hood which is specifically used for acids.

4.1.4.2 Graphite exfoliation

At this point graphite is exfoliated with tape. As explained before graphite is composed by graphene layers bonded by van der Waals forces. It is possible to separate graphite by pulling on both sides. Doing that the graphite will randomly split at the interface of two graphene layers.

The process is as follows:

- A few graphite flakes are put on the adhesive tape.
- The tape is folded and unfolded to obtain a homogeneous distribution of graphite all over the tape (see photo 4.1)
- A new piece of tape is put on the tape with graphite in order to have the homogeneous distribution on a tape with good adhesive (sticking) properties (this is important for good deposition)
- The tape is folded on itself, so when it is unfolded (just before putting on the substrate) we have a fresh surface of graphite.

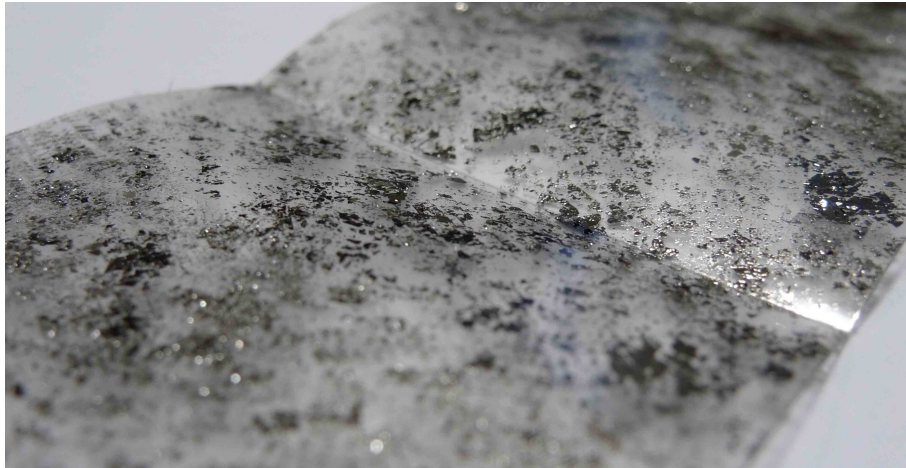


Figure 4.1: photography of tape with exfoliated graphite

4.1.5 Deposition

When this is done and the wafer spent an hour in the piranha solution it is taken out of the acid solution, rinsed with deionized water, and then dried with clean nitrogen. Finally we open the tape with graphite and press it onto the wafer.

The deposition is done.

The last step is to put the wafer with the tape under a press for a few days. This step was found to enhance the graphene deposition.



Figure 4.2: graphene exfoliation

4.1.6 Removing the tape

The final step is to remove the tape in a clean room. The tape is removed very slowly with tweezers ($\sim 1\text{cm}/\text{mn}$).

Then the sample is put in acetone for 1 mn and in isopropyl alcohol for another mn in order to remove adhesive residues and overly fragile layers of graphene (if graphene layers don't go through this treatment, they will never survive the lithography processes). Here we avoid ultrasound, because it is deleterious for graphene: indeed we have observed that with ultrasound the larger flakes detach very easily from the substrate.

4.2 Location of the graphene

Locating the small (a few micrometers) graphene flakes is not easy as a monolayer of graphene is only 3 Angstrom thick.

A priori an optical microscope would be unable to image graphene but a matter of luck led K. Novoselov [7] to deposit graphitic layers on silicon with a 300nm thick oxide layer.

The light interfering through the silicon oxide and graphene makes a phase shift in these interferences as it is shown schematically on fig.4.3, in such a way that the contrast of monolayers is enhanced. This allows direct observation of graphene with an optical microscope, which is very convenient. Indeed with optical microscopy it is reasonably fast to scan a large area compared to other imaging techniques. Furthermore it is totally non destructive and very accessible.

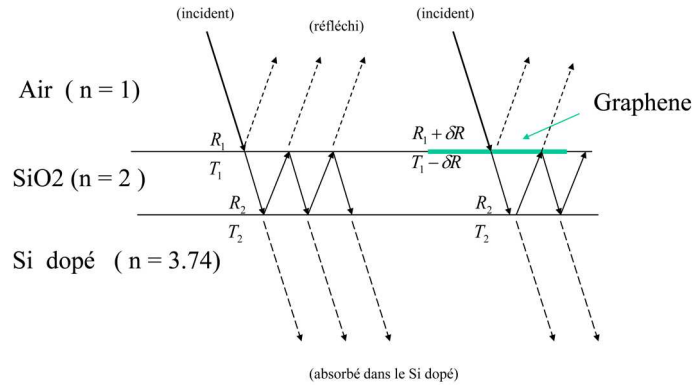


Figure 4.3: schema of light interfering in the silicon oxide. The graphene is represented in green.

A computation of the visibility of the graphene enhanced by the interference has been done in ref.[131]. The computation may not be of great fundamental interest and can be viewed in the paper, but the result as it is shown on fig.4.4 is very useful for the experimentalist researcher when choosing a silicon oxide thickness.

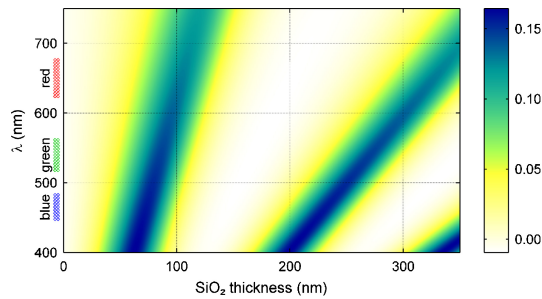


Figure 4.4: Visibility of a graphene monolayer as a function of the oxide thickness for different color from ref.[131].

Despite the fact that the contrast is enhanced, it remains very low. And to observe monolayers by eye in the microscope remains a challenge especially at the beginning.

It took me a long time at the beginning of my PhD to manage and find some graphene layers and to have good images. I should however say that

the thickness of the oxide layer of our silicon wafers (sold to be 300nm) was 340nm (we measured it many months after beginning working with them). As a consequence graphene was almost invisible and therefore it was very hard to obtain good images in order to design our electronic circuit.

Another challenge at the beginning of my PhD was to discriminate between monolayers and multilayers, as no reproducible method available set to do so before measuring the electronic properties of the sample (which requires making the electronic circuit on graphene, and as we will see, that it is not immediate), we will see in sec 5.1 that this problem can be solve with a Raman spectrometer.

4.2.1 Optical microscope and CCD imagery

The microscope used to locate graphene is a Zeiss AX10 equipped with Scion Corporation CFW-1308C CCD device.

At the start I spent hours and hours straining my eyes scanning with the microscope to locate and observe monolayers. But without knowing what a monolayers looked like at the beginning of my work, it was not very easy. Nevertheless soon I got used to locating tenuous thin films of graphite.

A microscope alone cannot discriminate between monolayers and multilayers, but for a given wafer, a given number of layers always has the same contrast. So once a monolayer is unambiguously identified by another characterization technique, the search for monolayers can be done with an optical microscope.

Making a good image of the graphene flake is essential for the sample design. At the beginning imaging graphene was not easy. Classical microscope CCDs do not give good results on a 340nm thick oxide layer, so we had to stack many pictures to increase the signal to noise ratio to be able to distinguish the graphene with classical image processing. A technique found to do rapid stacking is inspired by techniques used by amateur astronomers for imaging planets. It is the use of a web cam which is a fast imaging CCD: a web cam was mounted on the microscope and a video of graphene was acquired. Adapted softwares select automatically the sharpest images and stack them. An example is shown on figure 5.11 right image.

Then with the arrival of new 300nm oxide thick wafer and a new microscope it became easier to image it, by playing with RGB parameters and contrast, it became possible to acquire directly our images with the CCD. However sometimes this stacking method was still useful to see clearly a defect on a small region ($\sim 1\mu m$).

Finally after training it took me around 3 hours to scan 1/4 of a 2 inches wafer.

The images I took during my PhD represent 4,2Go for more than 1500 files

There are a few instruments able to image such a thin object like scanning electronic microscope or atomic force microscope, but they make the scanning for graphene very long and they may damage it. And as monolayer exfoliated graphene flakes are small and not very numerous on a substrate we can guess that it would never have been discovered with such imaging techniques.

4.3 Lithography

The lithography processes were mostly done in a class 10000 clean room to avoid contaminant.



Figure 4.5

4.3.1 UV lithography

UV lithography allows one to imprint large patterns on a substrate with better than $1\mu m$ resolution. It is essentially a stencil technique. The principle is to illuminate a UV sensitive resist through a mask. The non-shadowed parts are removed with a developer and a metal is evaporated onto the substrate through the removed pattern.

The masker I mainly used is a Karl Suss MJB4 which was delivered during my PhD. This machine disposes of a sample holder and a mask holder. A vacuum is established between the sample and the mask to ensure good contact which is extremely important to achieve homogeneous lithography on a full wafer. I found the MJB4 fairly good for achieving very homogeneous and reproducible lithography without taking special precautions.

The mask is a 3 inches quartz plate with a chromium pattern. I designed it with Auto-cad and the manufacturing was done by Toppan Photomasks.

The resist I used is Microposit S1813 with exposure time of 3s at 300 watt. It was developed in Shipley MF319 for 60 seconds.

4.3.2 E-beam Lithography

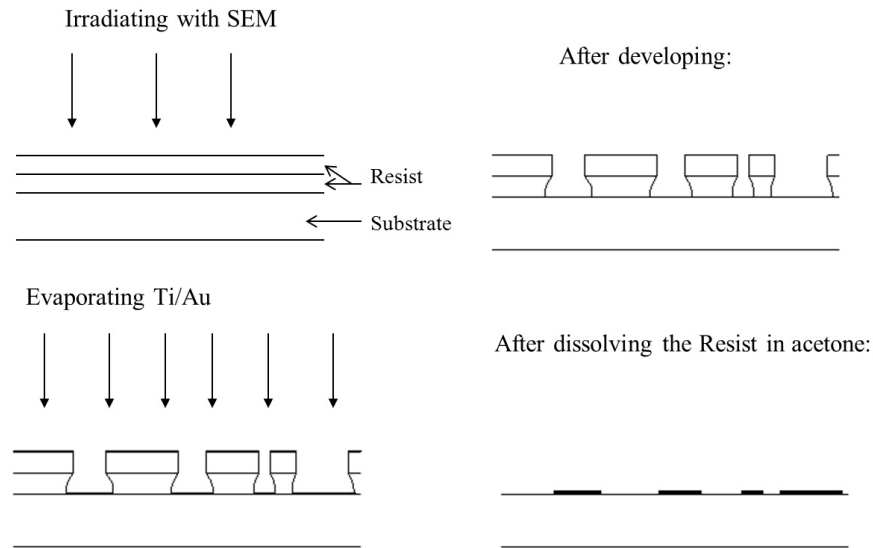


Figure 4.6: lithography process

This lithography technique uses an electronic microscope coupled with an electro-sensitive resist. The parts of the resist which are irradiated by electrons is removed with a developer (see fig 4.6). This technique achieves 50nm resolution and 100nm precision on the alignment. And it is very convenient because we can adapt the pattern to the graphene shape.

Usually I used a PMMA-A8 resist, spun at 4000 rpm, resulting in a thickness of $1\mu m$. I also used a bi-layer resist with MAA and PMMA, that technique allow to make an undercut: the bottom resist is more sensitive than the top one, thus bottom resist is more develop allowing to avoid contact between the deposited metal on top of the resist (which will be remove) and the one on the developed part. This technique avoid lift off problems such as resist which doest leave every well, but is a little bit less precise than using one layer resist. I found that with one thick layer of PMMA, lift off problems are rare.

For the E-beam lithography: I used a Phillips Scanning Electron beam Microscope (SEM) type XL30 with 25kV energy , and irradiated the smaller parts with 20 % less dose than the larger ones to avoid proximity effect with the electrons. I developed the resist in MIBK.

The E-beam microscop disposes of different fields (from $96\mu m^2$ to $3mm^2$) coupled with different spots which deliver a current from 10pA to 100nA, these fields and spots allow to draw patterns very precisely on small scales and rapidly on large scales.

4.4 Metal deposition: Physical vapor deposition

For deposition of the alignment mark or the metallic track I used two types of Physical Vapor deposition: E-beam Vapor deposition (EBPVD) and joule vapor deposition (JPVD).

4.4.1 E-beam Vapor deposition (EBPVD)

The EBPVD is a form of physical vapor deposition allowing the deposition of high quality thin film of many types of metals.

A target is bombarded with an electron beam given off by a tungsten filament allowing the transformation of the target's atoms into a gas phase. This e-beam bombing is done under deep vacuum (typically below $10^{-5}mbar$) which enables vapor atoms to go directly on the sample without any collision with stray gas molecules. This process allows deposition of nm size films at a very well controlled rate (the minimum rate is $0.2nm/s$).

4.4.2 Joule evaporator (JPVD)

The JPVD is an other kind physical vapor deposition with typically the same characteristics as the EBPVD except that the metal is heated by joule effect passing a high current ($\sim 250A$) through a resistive plate that holds it. This technique allows to deposit the magnetic materials such as chromium. As in the JPVD machine of the lab a lower vacuum is achievable than in the EBPVD machine, I used mainly the EBPVD except for the chromium deposition.

4.5 plasma etching

In order to cut the graphene at the shape we used a plasma etcher (shown in figure 4.7). Our plasma oven is a simple machine dedicated to graphene. It is composed of a vacuum chamber where oxygen can be injected and a radiofrequency source which cause the ionization of oxygen. In this machine the ionized gas is not accelerated.

As oxygen is a reactive gas, it will combine with organic materials to form ash which are removed by the vacuum pump.

It is a very efficient solution to etch graphene: first we achieve a E-beam lithography to let uncover by the resist the graphene part we want to etch. The the sample is put around 30s per layer in oxygen plasma. The plasma also removes the resist at a rate of around $100nm/mn$, so we have to be careful not to let graphene in plasma too much time.



Figure 4.7: Plasma etcher

Oxygen plasma is also useful to make suspended devices (see section 4.8). We could measure that in silicon wafer with silicon oxide on top which was exposed to oxygen plasma, the etching of silicon oxide with hydrofluoric acid was not isotropic. For 1nm etched vertically around 5nm were etched horizontally.

4.6 Device Fabrication

When a suitable layer of graphene is found, we can build a device with it.

The first step is to take many pictures of the graphene layer and its surroundings in order to design the device.

To make the design which will be used for E-beam irradiation I used Autocad, a very powerful software for drawing. The design made with this software can be converted to a file readable by the E-beam control software.

To design a sample we need to:

- Draw contacts adapted to the shape of the graphene flake with a 10nm resolution (E-Beam resolution) taking into account possible alignment errors of 100nm
- Draw 500 square micron pads which for connecting the circuit to the measurement system
- Draw tracks between pads and contact, avoiding interconnection with graphite flakes

- Take care of avoiding large exposure time (which results on misalignment) by making different layers of appropriate size for the different spots.

The first step in the design is to combine some pictures done with an optical microscope with different magnification.

Next step is the metal deposition

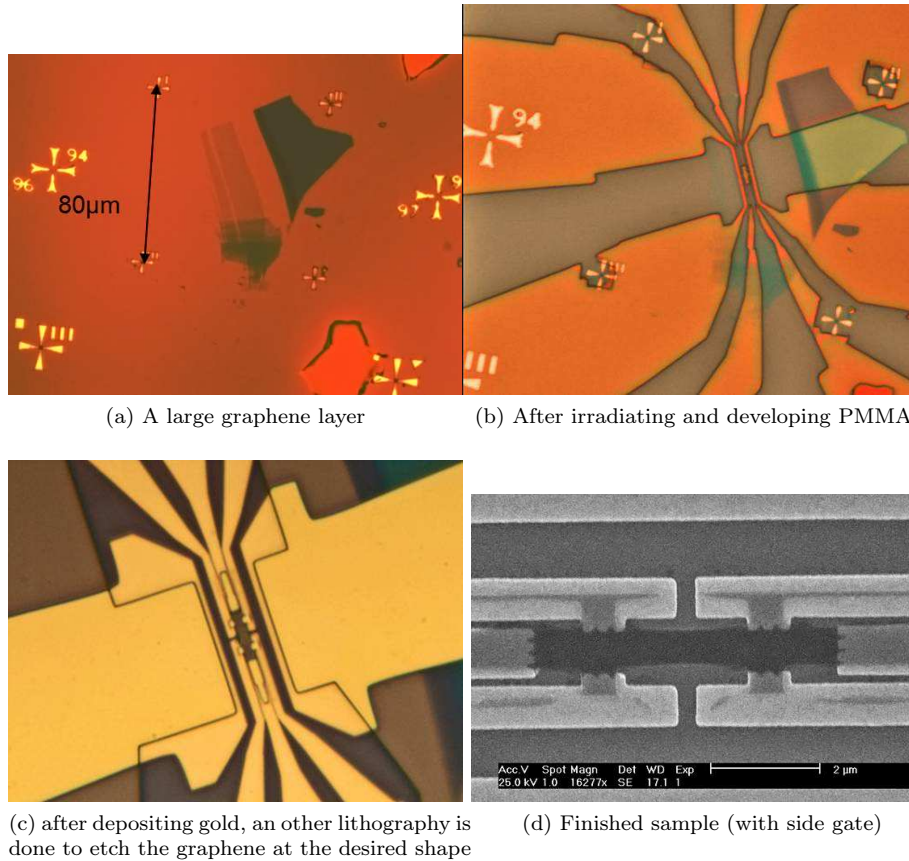


Figure 4.8

After that we put an electro-sensitive resist for the lithography

For the measurement I did three types of device:

- Hall bar with back gate
- Hall bar with side gate
- Corbino sample

4.7 Corbino

4.7.1 Metallic air bridges

To make a Corbino sample, the most difficult part is building an insulated golden air bridge to connect to the inner contact.

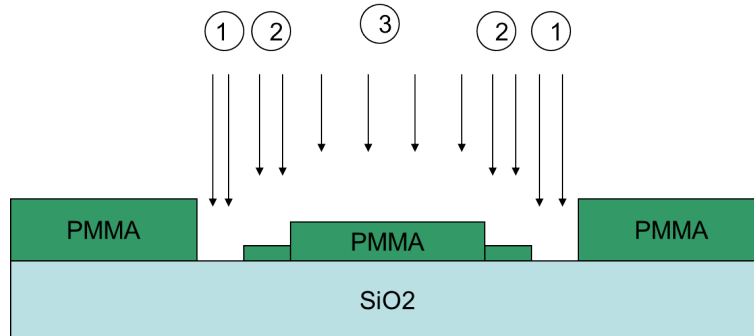


Figure 4.9: schema of how the insulated resist

As represented in fig.4.9, in order to build a bridge we can play with different irradiation of resist, resulting in different thicknesses after development. This manufacturing needed many tests and many hours behind the E-beam microscope.

Spinning resist To make the step as represented on fig 4.9 I used 3 layers of electro sensitive resist. The idea was that the first layer will define the height of the bridge, so it needed to be exposed for the starting points of the bridge but not for the suspended part. This layer is done with PMMA. The second layer is to make an undercut for the suspended part, achieved with MAA resist which is much more sensitive than PMMA. This way it is possible to expose it without exposing the first layer of PMMA. The top layer is PMMA, similar to the bottom layer. This layer provides a well defined suspended part of the bridge.

This sandwich with 1 more sensitive layer in the middle enables one to expose only the top and the middle layers or all the layers.

The recipe is:

- 1 layer of PMMA-A6 spun at 2000 rpm (leading to a 600nm thickness) and dried 3mn at 170° C
- 1 layer of MAA-EL10 spun at 2000 rpm (500nm) and dry 1mn at 170° C
- 1 layer of PMMA-A6 spun at 2000 rpm.

E-Beam irradiation We insulate the different part of the bridge with different relative doses.

The dose were 0.64 for the suspended part, 0,9 and 1,6 for the basement of the bridge $210mC.m^{-2}$.

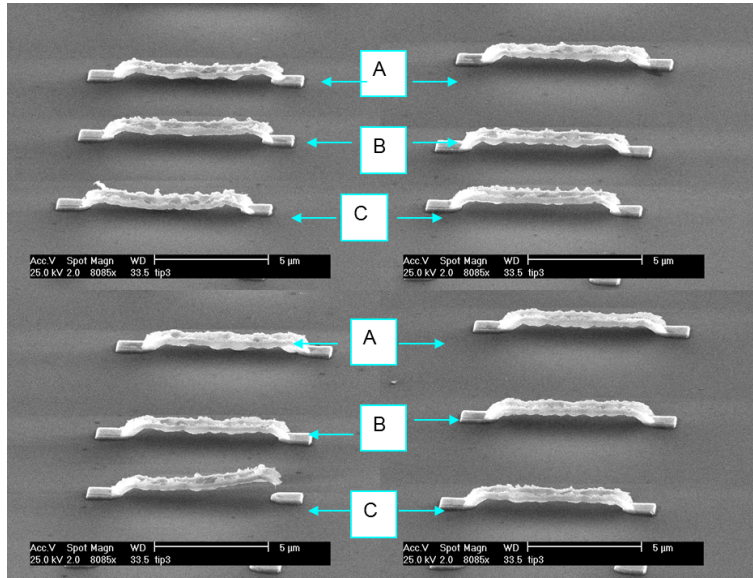


Figure 4.10: Tilted (50°) E-Beam picture of some test of metallic air bridges

Metal deposition The metal deposition is also an important step to have a bridge. For that I used the E-Beam evaporator which facilitates angle deposition. In order to join the foundation to the suspended part of the bridge a step was done with the resist but it was not sufficient due to proximity effects with the E-Beam irradiation. It was nearly impossible to realize a $1\mu m$ large step in the resist. Tilting the sample at 45° provide a good way to make this link. And indeed experiment has proved to me that it helps.

The recipe for the metallic evaporation:

- 5nm of Titanium for adhesion
- 160nm of gold at 0 tilt
- 50nm of gold at tilted at $+45^\circ$
- 50nm of gold at tilted at -45°

Obviously the tilting direction is the same as the bridge direction.

Corbino fabrication For the corbino fabrication a first step lithography is done to make the inner and outer contacts, tracks and pads. A second step is to

make the bridge. A E-beam picture of a Corbino is presented on figure 4.11. One can notice that the bridge looks fragile, I emphasize that due to backscattering by the gold on the outer ring the doses are somewhat shifted.

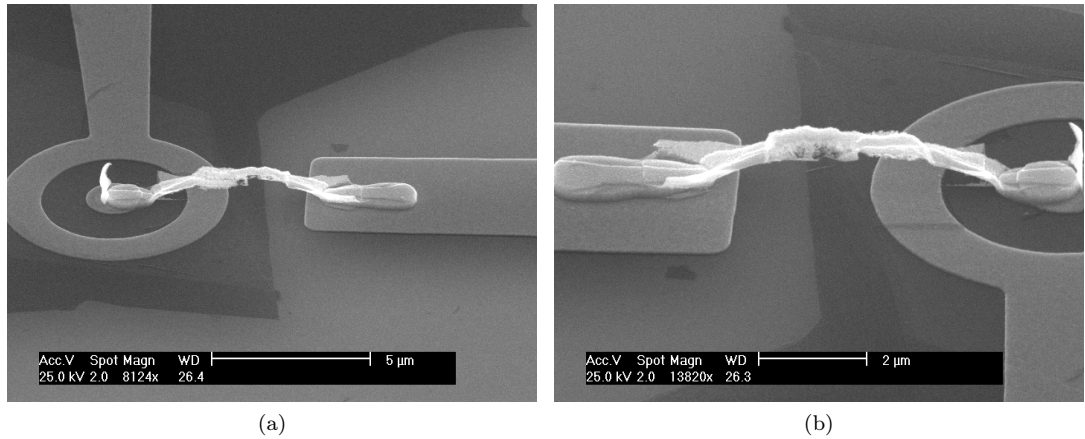


Figure 4.11: E-beam picture of a Corbino sample

4.8 Suspended Sample

Suspended Graphene shows a better mobility and possibility of attaining lower density. Two techniques are mainly used, the first consists of depositing graphene and etching the silicon oxide under the graphene with hydrofluoric acid, as was done in ref [37, 25].

The second technique consists in etching an array of holes and then depositing the graphene as was done in ref. [132].

Neither of these techniques is straightforward, the first may provoke graphene collapse, and for the second one needs to be lucky or to make a lot of graphene deposition.

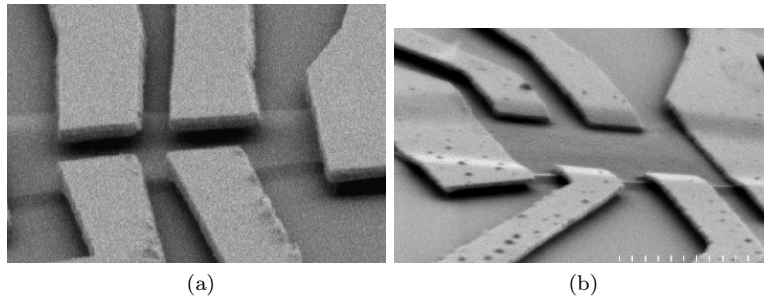


Figure 4.12: Suspended Hall bar from Kim's group. On the left the Hall bar collapsed due to electrostatic forces exerted by the back gate (at $V_g \sim 5V$)

I tried to build Corbino suspended samples with the second technique. Here the first method is not possible because there is no edge from which the hydrofluoric acid can attack the underside of the graphene.

I designed a mask for making the pattern of holes with optical lithography. The holes are rings where the external diameter is $5\mu m$ and the internal diameter is $1\mu m$, separated by $7\mu m$.

The ring geometry is to avoid collapsing caused by the gate. Indeed the electrostatic force exerted by the back gate is very strong; in Kim's experiment he observed a typical collapsing gate voltage of 5 Volts.

As the graphene sticks to the substrate thanks to Van de Waals forces it is important to have some surface on silicon oxide for the graphene to stick to. Also it is necessary to put the trenches close enough together in order to have a chance to see a graphene layer on a hole. The density of structures ($7\mu m$ between holes) was set to provide 70% of the substrate not drilled for the graphene to stick to.

4.9 Contacting the sample

To connect the sample with the measurement setup we have to connect the $500\mu m$ contact pad to the sample holder (see 10.3.6 with a $25\mu m$ width gold wire).

Normally a commercial ultrasonic bonding machine is used for this purpose. I stopped using such a machine for two reasons:

- The principle reason is that the probability of drilling a hole in the silicon oxide was high leading to backgate leakage
- The sample Holder is in Vespel (a polyimide of plastic) and the ultrasonic bonding is not efficient.

The solution I found to solve this problem is to use silver epoxy glue (Epotek H20E) which conducts at low temperature and is very resistant. This glue takes

15mn at 170°C to stick. So the trick was to put the sample holder with the sample on a hot plate. The wire was put into the epoxy glue to make a small ball of glue at an extremity which was then put on the contact pad during 15mn with a micro-manipulator.

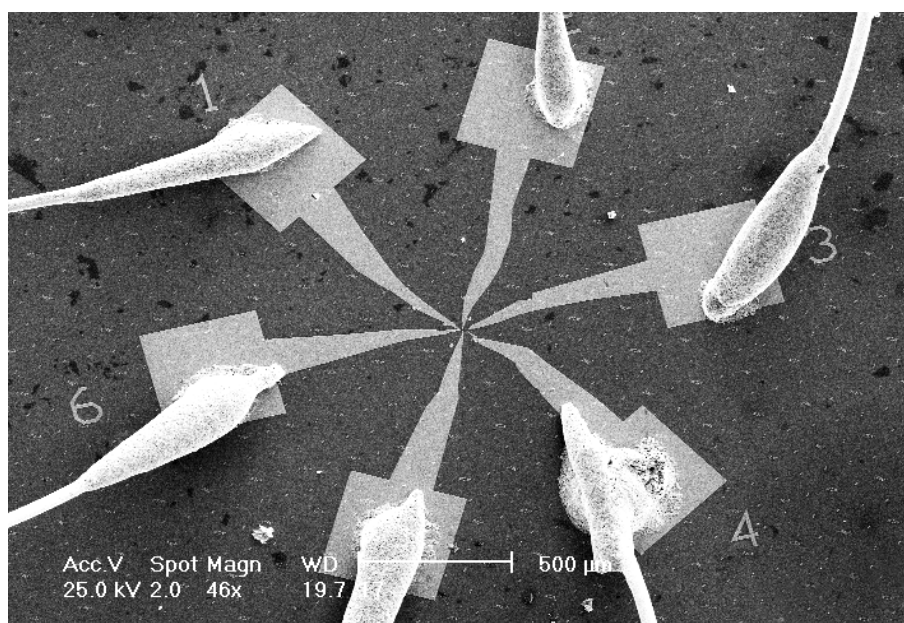


Figure 4.13: Picture of a contacted sample

4.10 Cause of death during the fabrication

I think it is important to dedicate a paragraph on the causes of death during the manufacturing process as most of the samples never reached the fridge.

- back gate leakage is the biggest cause of invalidity of cooled down samples. I used mainly two types of highly doped silicon wafers which came from NEYCO and SILTRONIX. I found that on the first I had more than 50 % probability of boring a hole in the oxide doing the wire bonding (I used a conventional Karl Suss machine with the smallest possible force parameter). In the second the probability of piercing the oxide was lower but still too high!
- lithography problem: it happened often that there was a hidden problem in the drawing or a bogue of the machine... that damage the lithography.
- dust on the sample: occasionally a large dust particle would fall onto the sample with no way to remove it (example on image 4.14)

- lift off problems; especially for the annular part of the Corbino samples as shows picture 4.15a. We think the annular part was removed and stuck there by Van der Waals force.
- graphene disappearance, as the picture 4.14 shows it happend often that graphene was torn or disappeared during lithography process, even but rarely when the contact deposition was done.
- exploding due to electrostatic choc. Here the picture 4.15b of a Corbino sample after a probable electrostatic choc speaks from itself (picture 4.11 show it before the blast).
- graphene torn. As shows the picture 6.4, many contacts were lost due to a graphene tear (see section 6.1.3).

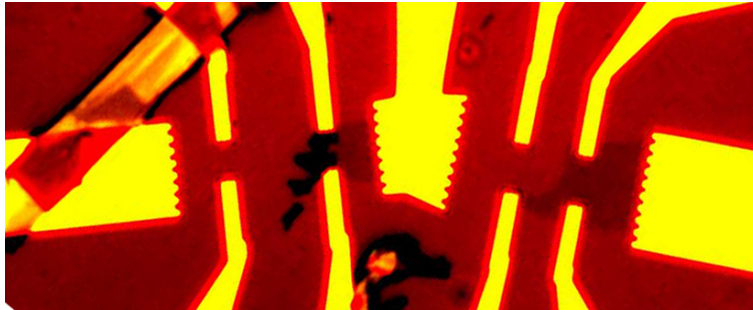
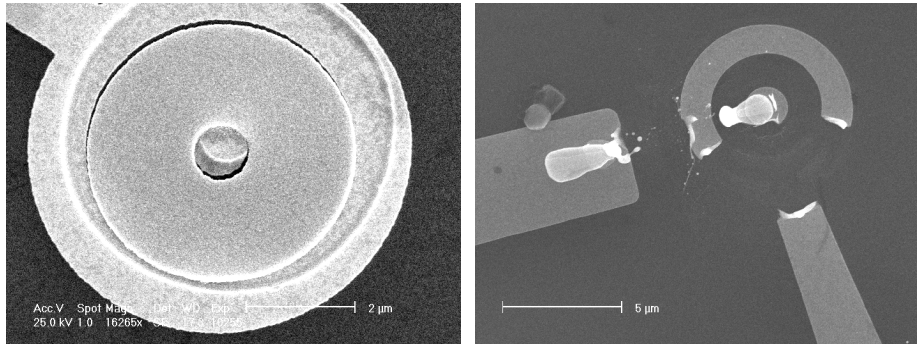


Figure 4.14: Optical microscope picture of torn graphene. Here a dust came between 2 contacts during lithography process.



(a) Lift off problem on a suspended corbino sample (e-beam picture) (b) Explosion of a Corbino sample probably due to an electrostatic choc (e-beam picture)

Figure 4.15

Chapter 5

Phonons and Raman spectroscopy in Graphene

The study of the phonons in graphene turned out to be very important for the characterization of graphene monolayer. As it will be describe here it allow to discriminate between one and few layers graphene.

5.0.1 Different phonon modes in graphene

As graphene has 2 atoms per unit cell, there are optical (O) and acoustical (A) phonon modes. Thus with longitudinal (L) and transverse (T) modes there are four combinations of in plane phonon modes : LA, TA, LO, TO. Also there are two transverse out of plane phonon modes which are called ZA, ZO.

A schematic illustration of LA, LO, TO phonons is given in figure 5.1 and 5.2.

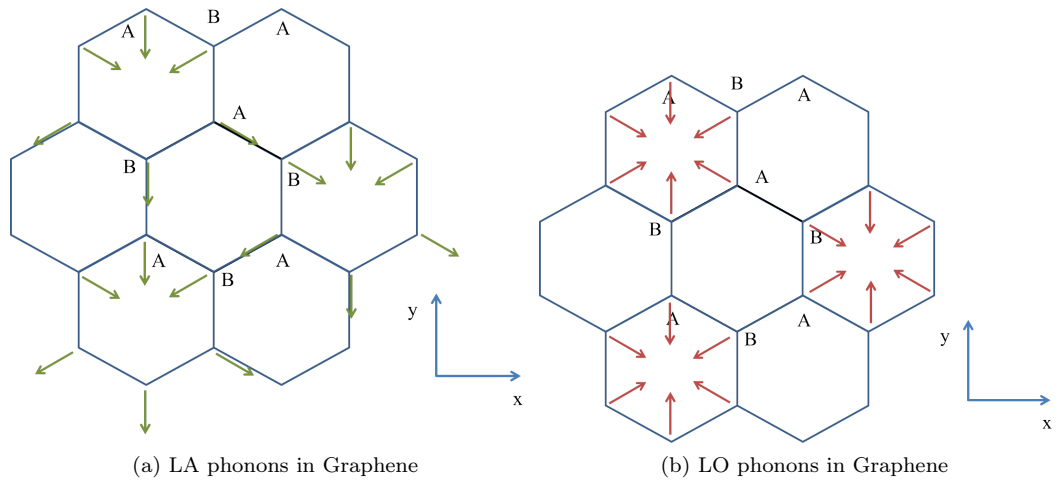


Figure 5.1

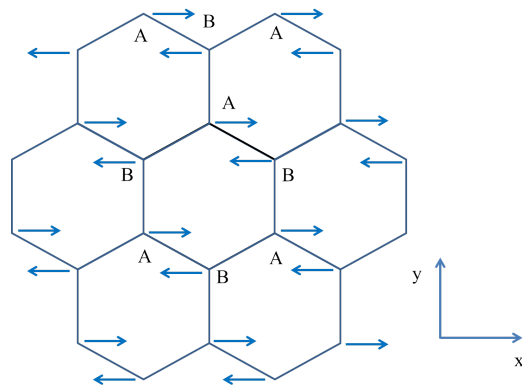


Figure 5.2: TO phonons in graphene

The calculation of phonon bandstructure in graphene was done in several ways, a review can be found in ref.[133]. An example done by ab-initio calculation [133] is shown on figure 5.3.

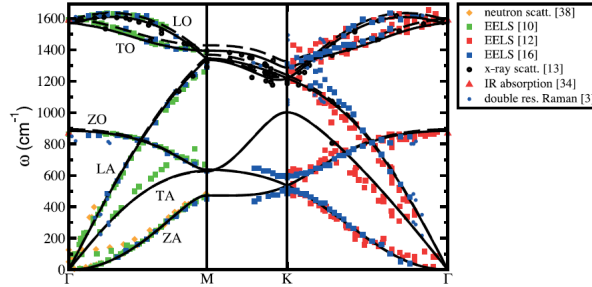


Figure 5.3: (Color online): Experimental data points for the phonon dispersion relation of graphite. Diamonds: neutron scattering, squares: EELS, circles: X-ray scattering, triangles: IR absorption, asterisks: data of various double resonant Raman scattering experiments. These data are compared with ab initio calculations from Ludger Wirtz and Angel Rubio: dashed line: local-density approximation, solid line: generalized-gradient approximation.

5.1 Raman Spectroscopy, a way to ensure that we have monolayers

The contrast of monolayers for a given thickness of silicon oxide is always the same. Optical microscope alone can be used to look for graphene once we have identified the contrast of a monolayer. We tried several methods to determine the numbers of layers: SEM, AFM, Raman spectroscopy.

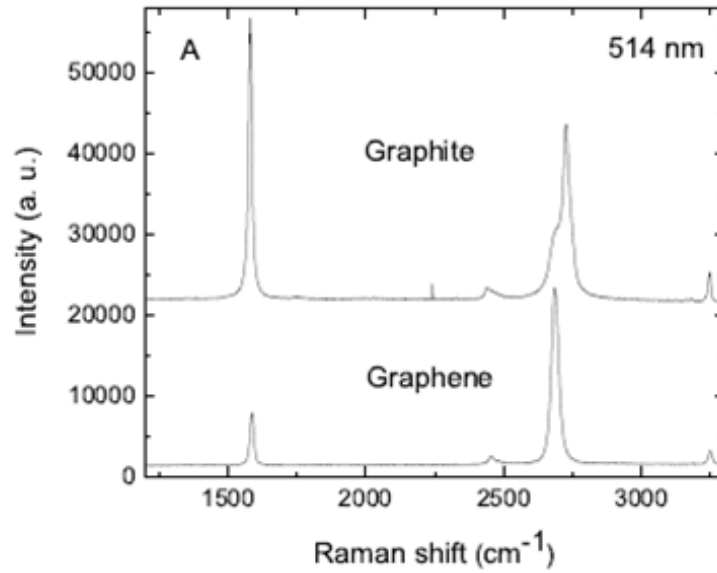
SEM gives a better contrast than optical microscopes but gives no information on the thickness of the sheet.

AFM could be a good way to distinguish a monolayer from few layer because we can theoretically know the thickness of one layer. Notwithstanding, the height of the first layer of graphene is not well resolved with AFM: it appears to be between 6 and 12 Angstrom whereas a graphene layer is 3 angstrom thick. Two possible causes for this are:

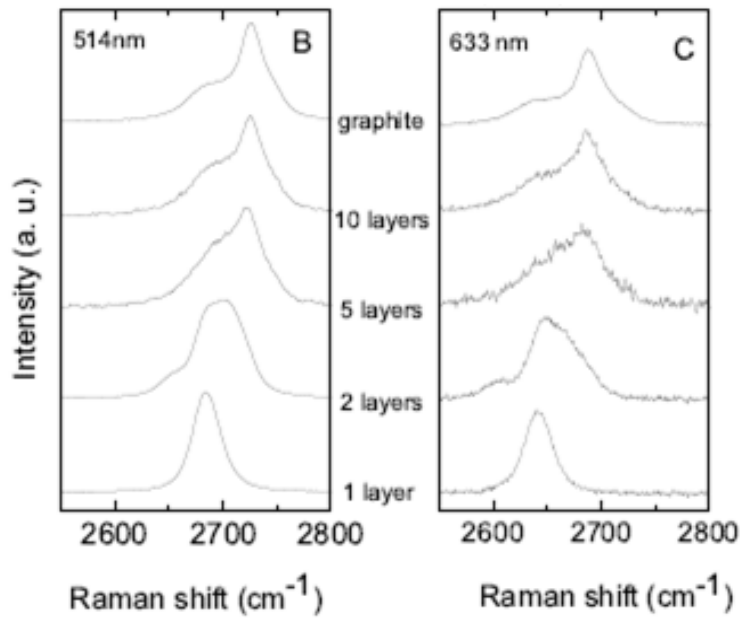
- water adsorbed underneath
- the interaction between the tip and the sample may be different than between the tip and the silicon oxide[134].

Raman spectroscopy seems to be the best option to distinguish monolayers before contacting the sample. It is fast, sure and nondestructive.

On figure 5.4 is shown an example of Raman spectrum of graphene and graphite obtained by Ferrari et al [135] who first put in evidence the interest of Raman spectroscopy for graphene characterization. We can see on these figure that the shape of the peak at 2700cm^{-1} is very different from graphene to graphite.



(a) D and G peak of graphene and graphite



(b) G peak for different number of graphene layers and for different excitation wavelength

Figure 5.4: This figure are extracted from ref.[135]

5.1.1 Raman principle

Raman spectroscopy is a very powerful tool for probing vibrational properties of a molecule or an atom in a crystal.

There are several types of scattering processes when light hits an object. The most probable process is Rayleigh scattering which is an elastic scattering on objects much smaller than the wavelength (typically atoms or molecules). Raman scattering is another process, but which is inelastic. As this is a higher order process involving in addition a phonon, it is weaker than the Rayleigh scattering. Classically, it depends on the modulation of the polarizability by the vibration.

The light thus interacts with a vibration mode resulting in an energy shift of the re-emitted light. From this energy shift we can know the frequency of the phonon.

There are two possible processes for Raman scattering: Stokes (emission of a phonon) and anti-Stokes (absorption of a phonon).

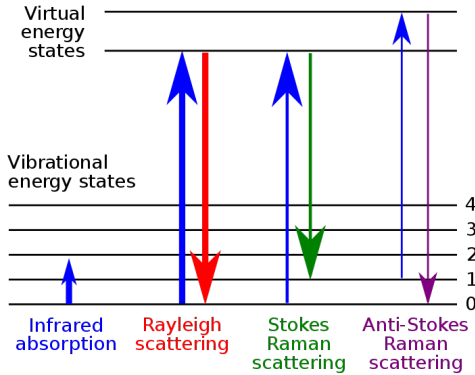


Figure 5.5: Energy levels involved in Raman scattering.

A Raman spectrometer based on this principle measures the re-emission frequency and thereby the frequency shift corresponding to the frequency of the Raman active mode. By means of a confocal microscope with very low depth of field, the sample is illuminated intensely on the focal plane with monochromatic laser light. The backscattered light from a very thin space is then collected by the microscope. A notch filter at the frequency of the light source is used to remove the Rayleigh scattered light. Then the signal passes through a spectrometer which measures precisely the frequency shift.

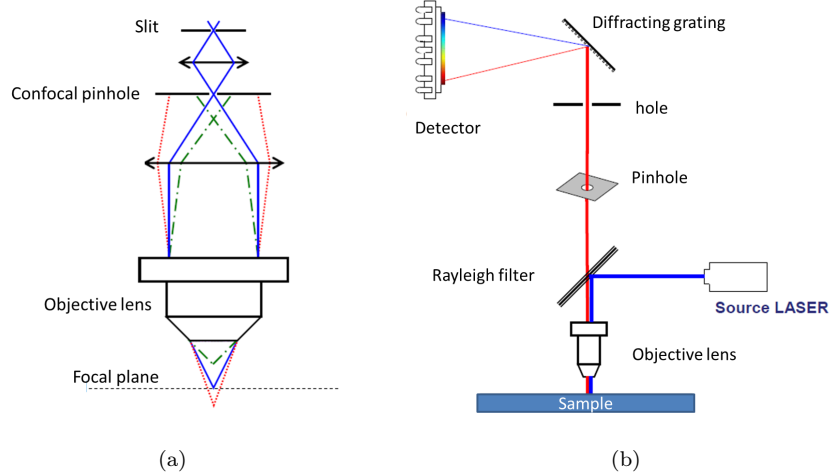


Figure 5.6

5.1.2 Raman spectroscopy of graphene

It is based on the electron-optical phonon coupling: electron-photon coupling drives the absorption of an incident photon to mix a virtual excited state (photoelectron with respect to the Fermi level in our case) which by absorption (or emission) of a phonon is mixed with another virtual excited state by electron-phonon coupling before returning to the original energy by emission of an energy conserving photon $\omega_{Stokes(anti-Stokes)} = \omega_{incident} \pm \omega_{phonon}$. Raman spectrometer probes the gain or the loss of energy due to absorption or emission of a phonon.

A simple interpretation of electron-phonon coupling for electron described using tight binding approximation is given assuming that the vibrating ions carry the electron orbitals when vibrating. As a consequence, the tight binding parameter t is shifted. A simple description of the t shift is given by Harrison law (see ref.[43] and references therein)

$$t' = t + \delta t = t + \frac{\partial t}{\partial a} \delta a$$

$$\frac{\partial t}{\partial a} \simeq -2 \frac{t}{a} \sim 4, 3eV.A$$

Here we will describe the possible processes of de-excitation of a photoelectron. There are 5 important peaks in the Raman spectrum of graphene:

- The G peak is the graphite-like peak. The single phonon mode Raman peak corresponding to the emission of an in plane optical mode phonon (E_{2g}) with zero wave vector, i.e close to Γ point. This peak is located at

about 1582cm^{-1} from the incident energy and is the first order allowed. With the 2D peak, it is the most prominent peak in graphene.

- The D and D' peaks, called D for disorder and arising from a double resonant Raman scattering, are located at around 1350cm^{-1} shift for D and 1620cm^{-1} for D'. They are also due to optical phonons, here with a wavevector near K or K' for D inter-valley mode and very small of about ϵ/v for D' for the intra-valley mode. D peak is observable essentially at the edge of graphene and is weak in the bulk where there is low concentration of disorder. This is sketched on fig. 5.8 and 5.7.
- The 2D peak, Raman shift around 2700cm^{-1} , corresponds to the emission of two phonons with opposite wavevectors at K(K') and -K(K'). This peak is particularly interesting as it changes shape, width and position as a function of the number of graphene layers allowing to discern between mono, bi, and few layers graphene. The change in the shape is due to the fact that in multilayer graphene the 2D peak has several components whereas in monolayer it has only one component. The multiple component is attributed to a splitting in phonon branch. (see ref.[135] and references therein). This is sketched on fig. 5.9.
- The 2G peak corresponds to the emission of two phonons with opposite wavevectors near the Γ point.

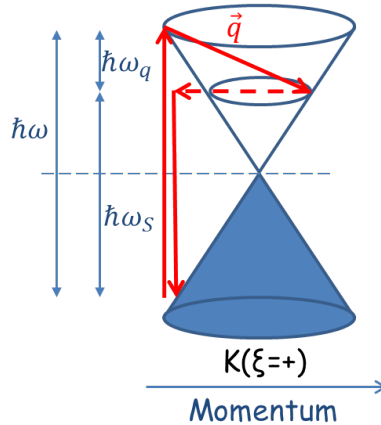


Figure 5.7: Intravalley double resonant process, explaining the origin of the D' band

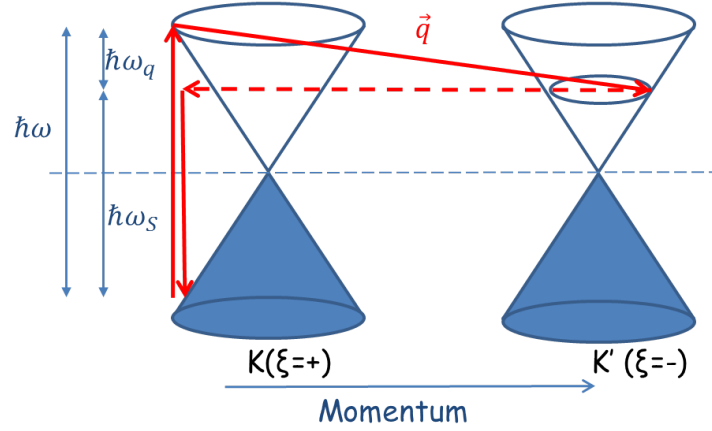


Figure 5.8: intervalley double resonant process explaining the origin of the D band

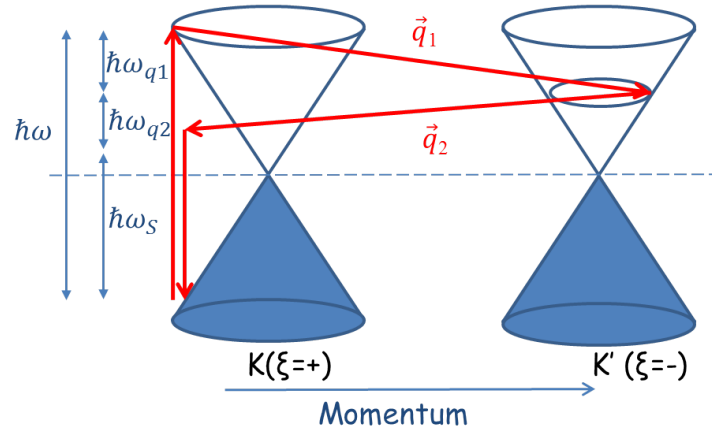


Figure 5.9: Intervalley two phonon mode, responsible for the 2D band.

5.1.3 Measurement of Raman on graphene

We often used Raman spectroscopy to probe graphene. First measurement were done thanks to Y.Dewilde in ESPCI and to A.Filoramo in CEA. In 2009 the group acquired a Raman spectrometer (Jobin-Yvon Labraham Aramis shown on fig.5.10). This spectrometer was specially designed for making high speed large cartography.

This spectrometer is equipped of an Electron Multiplying Charge Coupled Device (EMCCD), this CCD amplifies signal before readout, thus the readout noise is negligible, also this CCD is back-illuminated allowing to use the full

CHAPTER 5. PHONONS AND RAMAN SPECTROSCOPY IN GRAPHENE

surface of the sensor to collect light. As a result this type of CCD introduced by Andor technology is single photon sensitive.

This detector coupled to a 100mW laser source allows to have a signal over noise ratio higher than 3 for the 2D peak after a 10ms exposure. This very low exposure time coupled with a fast scanning mode (technology from Jobin-Yvon called SWIFT) allows high speed mapping. This high speed cartography adaptation of Labram Aramis spectrometer was the first done, designed for graphene mapping and searching application.



Figure 5.10: The Raman spectrometer, model Jobin-Yvon Labraham Aramis

Figure 5.11 shows the 2D band of 1,2,3 layer(s) and bulk graphene.

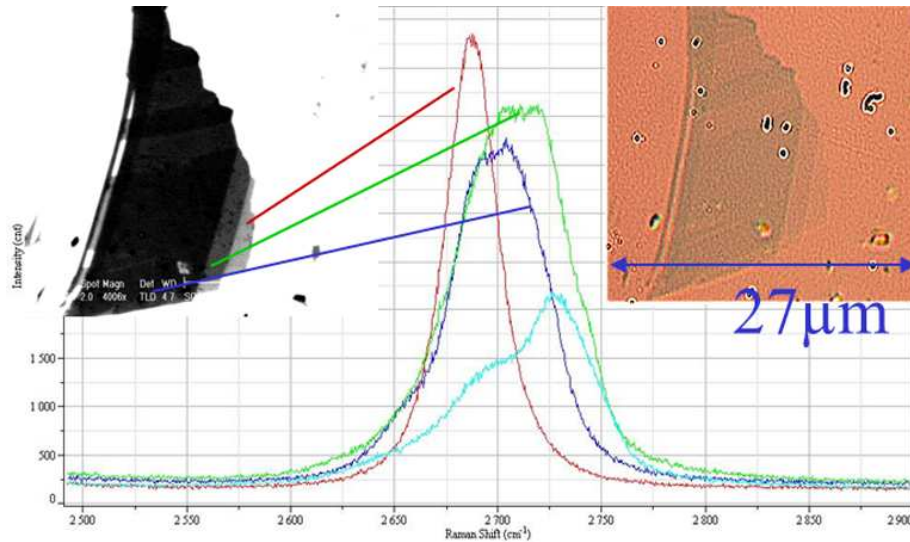


Figure 5.11: spectra from a monolayer (red), a bilayer (green) a trilayer (blue) and multilayers of graphene (light blue). Measurement made in Y.Dewilde's lab at ESPCI. On left is an E-beam picture and right optical picture (using the stacking method described in section 4.2.1) of the graphene flake used for this spectroscopy.

Figure 5.12 shows the result of a small size cartography. The red part on this figure represents the area of the G peak.



Figure 5.12: Image of sample 3 (monolayer): superposition of an optical and a false colour Raman image (the represents the area of the G peak)

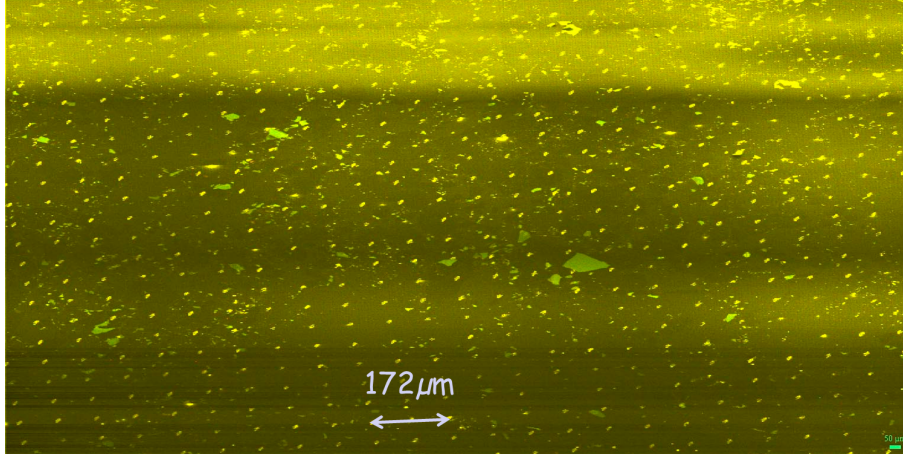


Figure 5.13: Large Raman cartography of graphene flakes.

Raman spectrum image of graphene and graphite flakes on a Si/SiO₂ substrate is shown on fig. 5.13. The scanned area is 4mm², with a resolution of 5μm. This mapping last approximately 3h. The colors represent the area under the curve given by one spectrum of the intensity versus the wavelength between 2650cm⁻¹ and 2750cm⁻¹. On this map thick flakes of graphene appears in green and thin (between 1 and 3 layers) appears in orange. The software provides to view each spectrum by clicking on a location on this map. The gold cross makes a shift in all the spectrum, as a result they appears in yellow.

As a conclusion, Raman spectrometer is the ultimate tool to probe graphene, it is fast, sure and non destructive, also Raman mapping allows the deposition of graphene on other substrates than SiO₂, where graphene would not be visible with optical microscope.

Chapter 6

Setup and basic electronic Measurements

In this chapter we will show a description of the samples and of their preparation followed by a presentation of basic electronic measurements which are very important for the characterization of graphene and for the comparison with results obtained by other group.

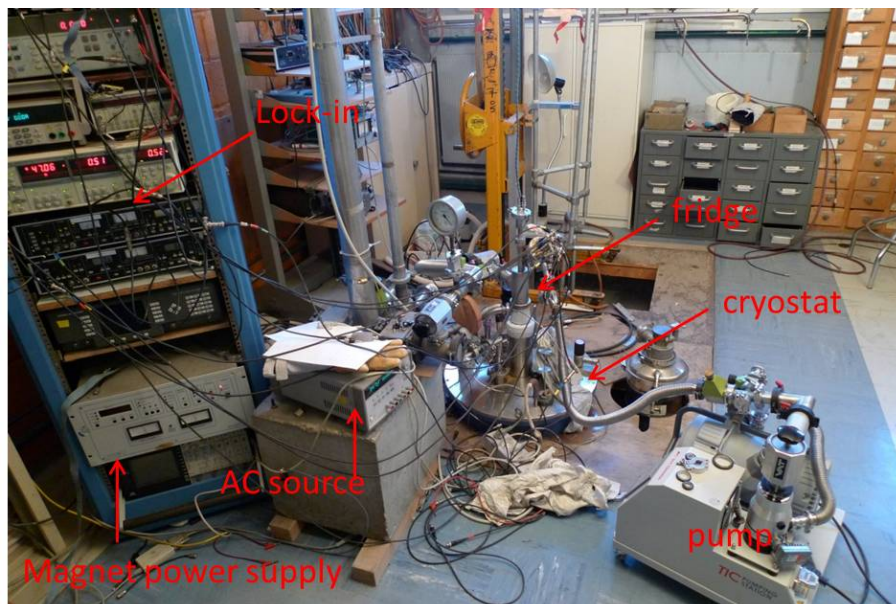


Figure 6.1: Experiment room

6.1 Cleaning the graphene

For our measurements, it is very important to have good mobility, one of the keys to which is good sample cleaning.

Graphene, like graphite, can adsorb many things, in particular water as discussed in 2.5.5. These adsorbates dope the graphene and shift the Dirac point away from 0 gate voltage[33]. Also their random spatial distribution on the graphene surface introduces density inhomogeneity. It has been shown that doped graphene has always lower mobility. Indeed we can easily imagine that the adsorbates are randomly located, as a result the doping is not homogeneous giving rise to electron scattering[136, 137].

Another source of graphene pollution is residues of photoresist which is used in the processing of the sample.

In order to remove these we have different techniques at our disposal.

6.1.1 Annealing the sample in Situ:

The easiest way to remove adsorbates is to heat the graphene under vacuum for several hours. To avoid new adsorbates we have to heat the sample in the fridge under cryogenic vacuum, before measuring. The temperature at which the adsorbates begin to desorb is around 400K. As said in chapter 10, heating the graphene at more than 400K when the fridge is immersed in 4.2K liquid helium, may be difficult and requires some care and a good thermal design of the fridge and the sample mount.

We typically heat the sample at 450K for several hours. During this operation we monitor the 4-probe or 2-probe resistance. As molecules desorb, graphene is less doped, implying that the resistance measured increases. Note that in 2-point measurements which probe the contact resistance in series there is a competition between the decrease of the contact resistance (contact may improve while heating) and the increase of the sample resistance. The monitoring allows us to determine at which temperature molecules desorb and also a way to find the right moment to stop heating: we heat until the value of the resistance remains stable.

6.1.2 Current annealing:

Another method discovered by J.Moser to clean graphene is to send a high current through it[138].

Here a high current is injected in the sample typically of the order of mA (which is really huge for a monolayer). The method is to increase very slowly the voltage on the sample while measuring the current until the value of the current decreases for a fixed voltage. This means that the resistance is rising. This method is hazardous because it doesn't give reproducible results (sometime graphene's density become smaller, other times it doesn't). It is also a bit

dangerous because it can damage the sample. Too much current tears Graphene [139] till breaking it, and that occurs very quickly.

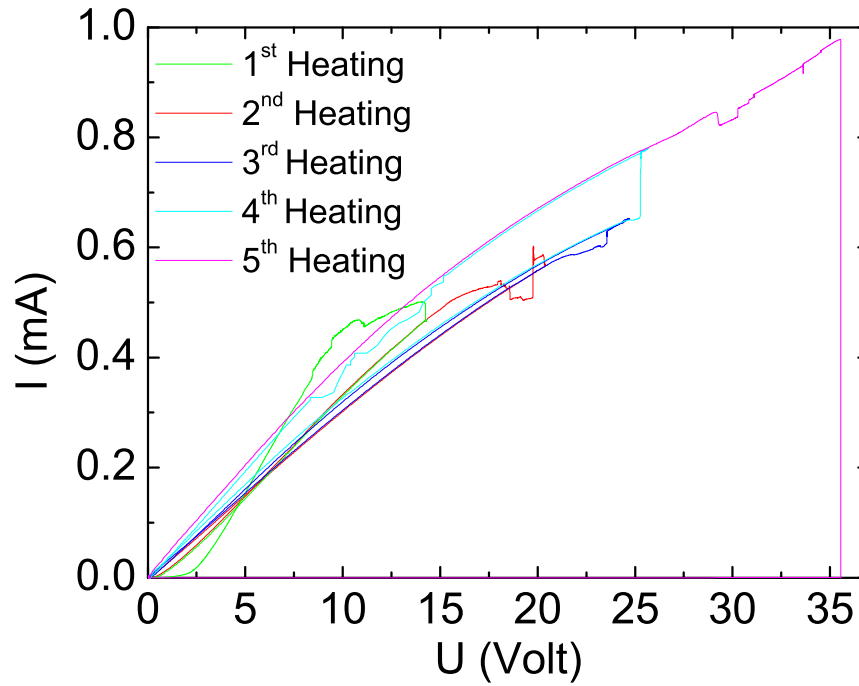


Figure 6.2: Plot of different current annealing on a sample. It died after the 5th at a current near 1mA which is unbelievably high. The surface of the sample was around $5\mu\text{m}^2$, so the density of current was of 4.10^7A.m^{-2} and the power dissipated was around $1,4\text{GWatt.m}^{-2}$, in a one single atom thick layer.

6.1.3 AR/ H_2 HeatingFigure 6.3: tubular oven for AR/ H_2 heating

After the lithography process some resist residues remain on the graphene. One way to remove them was found by Fuhrer [140]. It consists in heating the graphene in a Hydrogen and Argon mixture at temperatures above 600K. This way it is possible to heat graphene to relatively high temperature without oxidizing it. This technique was shown to remove resist residues.

I tried to set up this technique but I encountered several problems. A tubular oven was bought. Also a mixture of Ar/H_2 with ratio 9:1 was used.

The oven is composed of a quartz tube and 2 caps, one with an entry for the gas and the other with 2 entries, one to provide an exit for the gas and the other for a nacelle. The nacelle allows us to introduce the sample. It looks like a shovel for a pizza oven: a long tube of quartz allows us to put it in the middle of the oven and a 2 inch quartz plate supports the sample. A leak proof joint lets us remove a part of our shovel from the oven tube.

Several heating cycles were done on 5 samples. The temperatures were set between 550K and 650K with low ramping rate (1K/hours). The sample remained about two hours at the highest temperature.

The major problem that I encounter is the loss of contacts. Most of contacts were lost after heating. This was due to graphene break after heating or when cooled down after heating as it is possible to see on fig 6.4.

A possible explanation comes from C.N.Lau results about thermal expansion coefficient of graphene[132] which is negative below 350K. There is a strong differential thermal stress between graphene and the substrate. As the monolayer is glued at some points in Ti/Au contacts, when it is heated its strong contraction opposed to the substrate expansion induces strong stress and even-

tually tears graphene near the contact region. Also when cooling down the revers thermal expansion process may lead to favor ripples which degrade the Graphene mobility.

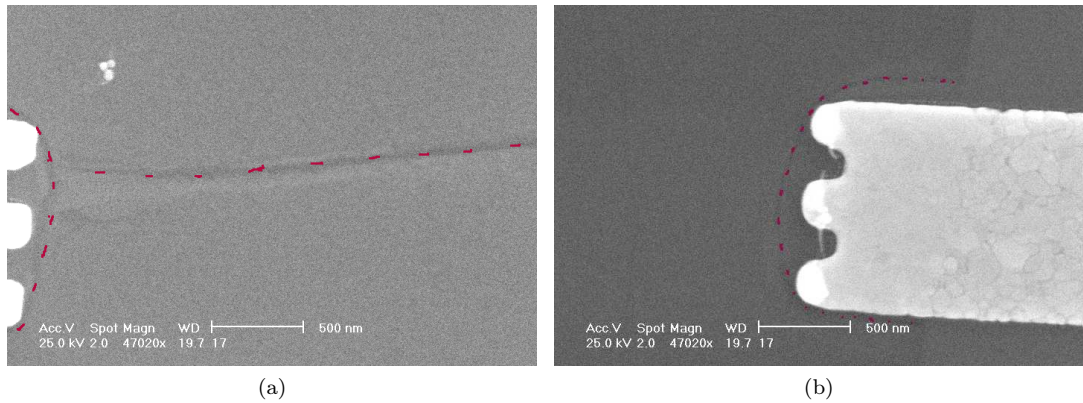


Figure 6.4: E-beam picture of tearing in the graphene near the contacts.

An other consequence of this heating is that the gold of the contacts becomes very soft and do not offer the possibility to be bonded anymore.

Thermal properties Graphene also has rather special thermal properties, in that its thermal expansion coefficient changes sign at around 350K.[132]

6.2 Doping graphene using gates

6.2.1 Back gate

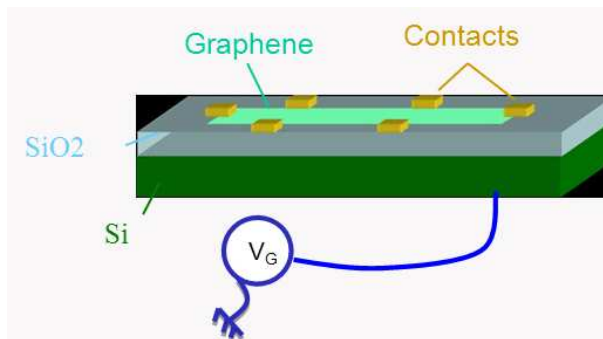


Figure 6.5: schematic of back gated graphene

A so-called back gate is the more commonly way to tune the density in graphene.

To make a back gate, graphene is deposited on top of an insulating silica layer deposited on a conducting highly doped silicon substrate. The graphene then plays the role of one electrode of a parallel plate capacitor with the conducting silicon and applying a potential puts a controlled charge on the graphene. The value of the capacitor is:

$$C = \frac{Q}{V_G} = \varepsilon_0 \varepsilon \frac{A}{d}$$

the density is then

$$n = \frac{C.V_G}{A} = 7,4.10^{10} cm^{-2}.V^{-1}$$

for a 300nm silicon oxide layer.

This provides a simple tool to tune the density .

Back gate is a very useful and simple way to vary the density in a sample, but the doping is not homogeneous and charges tend to accumulate on the edges of the sample on a lengthscale of the order of the SiO₂ thickness. A simple explanation for this is that the field lines are not perpendicular to the sample on the edges due to a sharp potential drop. A calculation is done in ref [141]. This can alter the quantum Hall effect because in Hall bar geometry it is very sensitive to what happens at the edges.

6.2.2 The side Gate

In order to be free from the homogeneity problems we first left some graphene just near the edge of the sample by patterning a Hall bar in a large flake of graphene and cutting a trench of 300nm. This was done for sample 1.

Then we tried to make samples with a side gate and no back gate. Here one can guess that near the edge the electric fields should be stronger. In order to avoid that, we used a strip line geometry.

A conformal transformation which allows to make the correspondence between the upper half plane and a rectangle provides a way to calculate the electrostatic problem of parallel plate capacitor. The density is:

$$n_s(x) = n_s \frac{1}{\sqrt{1-u^2}\sqrt{1-k^2u^2}} \quad (6.1)$$

where $u = \frac{2x}{w}$ and k is linked to the gate distance.(see fig 6.6),

$$n_s = \frac{Q}{eLwK(k)}$$

K is an elliptic integral. The charge $Q = CV$ can be calculated using a software (for example AppCad) to compute the value of the capacitance. Equation 6.1 shows that the density varies rapidly on the edge. By putting metal lines along

the graphene at its potential we can avoid that problem and choose the homogeneity we want inside the graphene by varying the distance between the gates and the line's width. So in our sample these line were contacting the graphene on the edges and were used to measure the potential (a picture is in 6.8). The counterpart is that the gate is less efficient especially if we want a very good homogeneity, and this limits the width of the sample.

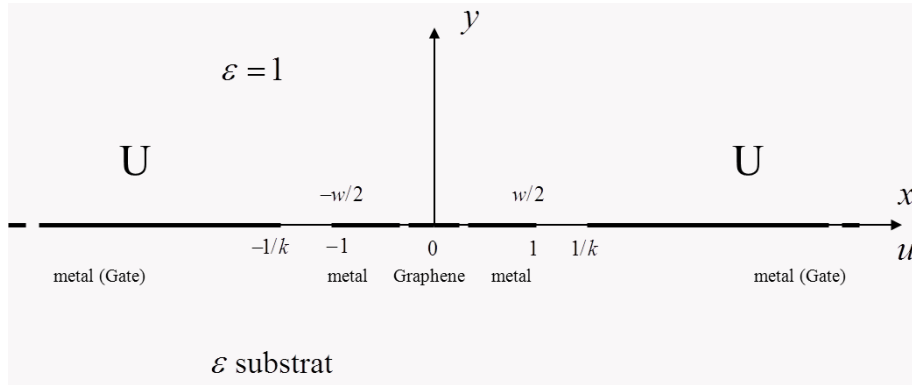


Figure 6.6

6.3 Transport measurement

6.3.1 Devices

15 devices were cooled down, 14 monolayers and 1 bilayer.

4 monolayers and 1 bilayer had good electronic properties: meaning that the gate was efficient, the Dirac point was not too shifted and the Quantum Hall effect was observable.

For these studies we measured four Hall bars made with monolayer graphene with different properties. The Aspect ratio R_{asp} was estimated using a numerical electrostatic calculation.

Sample 1: It was the 3rd cooled down and the first sample in which we were able to observe quantum Hall effect. It was covered with PMMA resist. As it is possible to see on the picture the Hall bar was designed in a larger graphene layer allowing to let some graphene spaced by a gap of 300nm connected to the voltage probes to have a better homogeneity at the edge. Four contacts were available on this sample (those numbered on the picture 6.7).

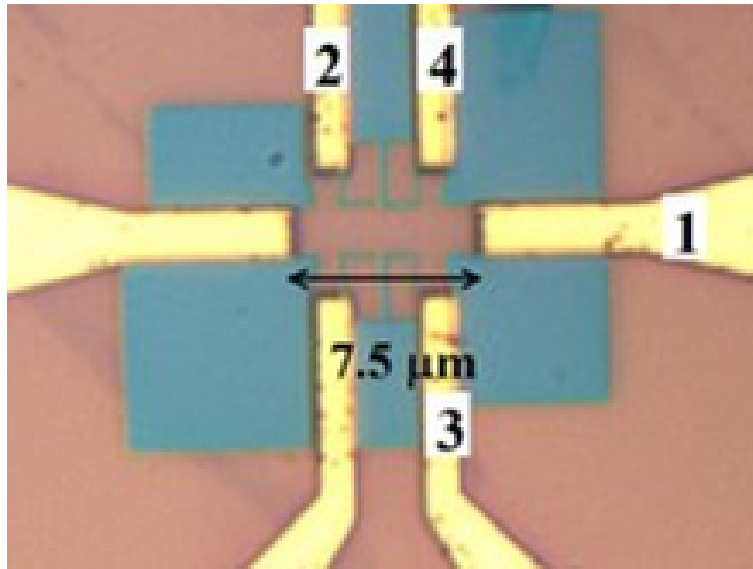


Figure 6.7: Optical image of sample 1

Sample 2: This sample was side gated. This side gate was less efficient than back gate by approximately a factor of 5. It was also covered with PMMA.

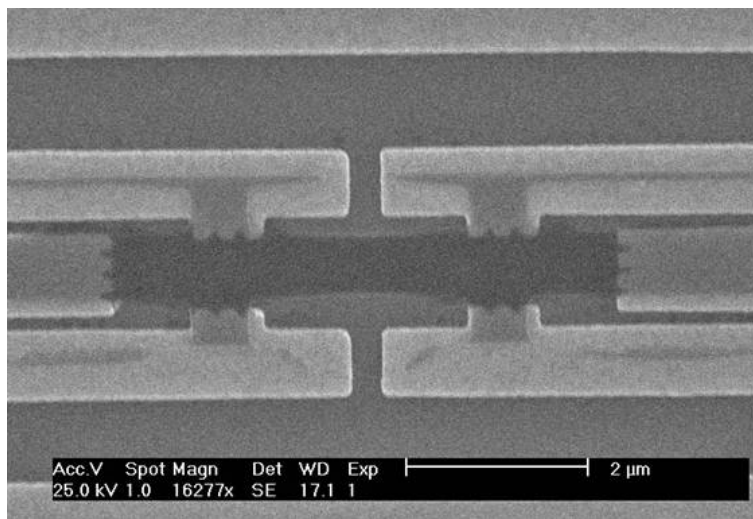


Figure 6.8: E-beam picture of sample 2

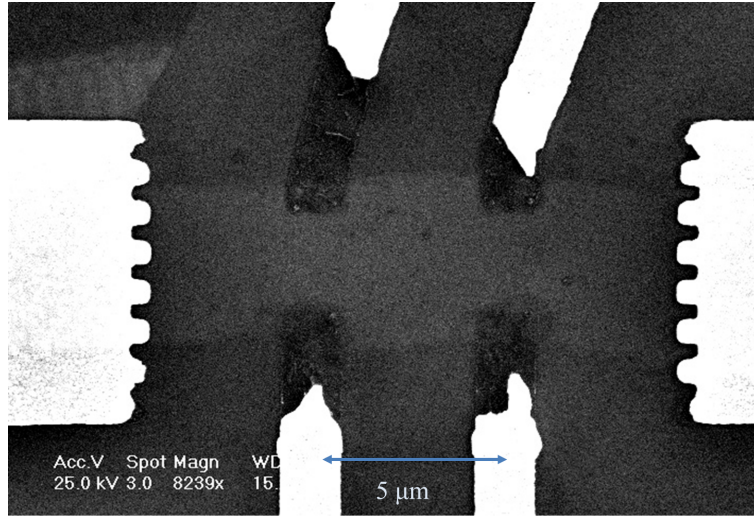


Figure 6.9: E-beam picture of S3, here some contacts had been destroyed by Ar/H₂ heating

Sample 3: Sample 3 was a simple Hall bar of graphene with a backgate to control the charge density. 4 contacts were available on this sample which allowed four point measurement of the longitudinal resistance. The aspect ratio used for ρ_{xx} is $R_{asp} = 1, 29$.

Sample 4: Samples show the QHE of a monolayer but the doping with the back gate was around twice less efficient than it should be with a 300nm thickness of silicon oxide. All the contacts were available allowing the measurement of Hall and longitudinal resistance. The aspect ratio used for ρ_{xx} is $R_{asp} = 4, 94$.

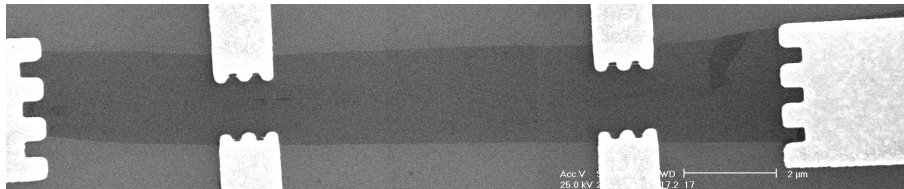


Figure 6.10: E-beam picture of S4

To summarize:

| sample | 1 | 2 | 3 | 4 |
|--|-----------|-----------|-----------|-----------|
| gate | back gate | side gate | back gate | back gate |
| cover | PMMA | PMMA | no | no |
| Mobility $cm^2.V^{-1}.s^{-1}$ at $n = 1.10^{12}cm^{-2}$ | 2900 | 2000 | 6400 | 10000 |

Sample 5: Corbino sample A bilayer with a corbino geometry was also measured. A photograph of it can be found in fig. 4.11

The first two samples were measured with the old setup: they were immersed in liquid helium in a tube with the measurement wires going upwards. We were unable to heat them, so we found that putting PMMA on top protected them from too much residual doping. The three other samples were measured in the new fridge after in situ heating. The electronic measurements were done using a classical low frequency Lock-in method applying a bias current of 10nA.

6.3.2 Conductance and mobility

6.3.2.1 Monolayers

Electronic measurement at zero magnetic field provides a lot of useful information on the sample. We mainly measure the 2 point and 4 point resistance as a function of the density. The first information we can have is the position of the Dirac point. which tells us if the residual doping is high or low. With the four point measurements, the aspect ratio, and the density we can calculate the mobility, providing a very useful comparison with results from other groups. By comparing 2 and 4 probe measurements we can have some information on the quality of the contacts.

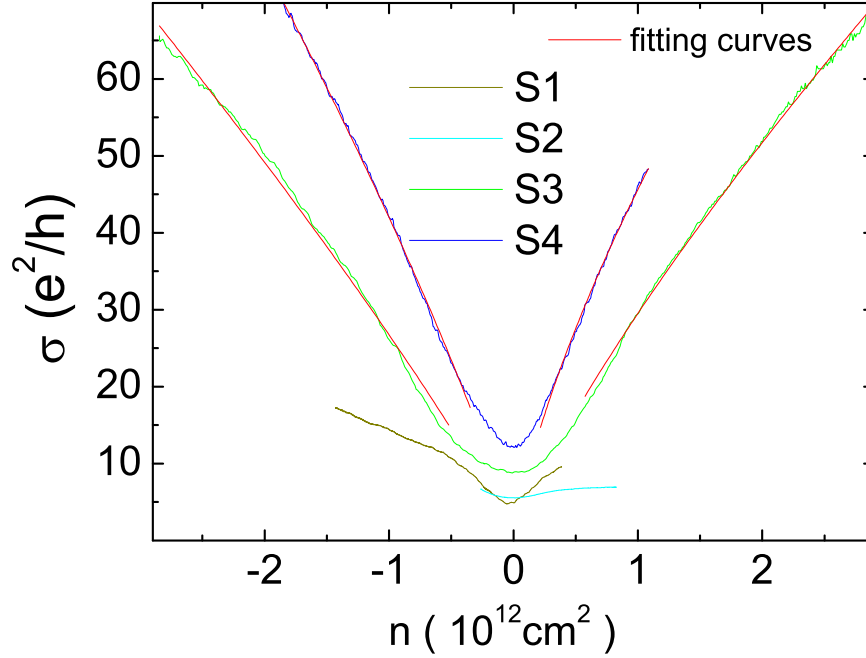


Figure 6.11: Conductivity as a function of the density for the different samples at 4,2 Kelvin and fitting curve for the resonant impurities model.

Also as mentioned in 2.5 measuring $\sigma(n_c)$ gives us information on the origin of scatterers limiting the mobility.

In sample S3 and S4 the dominant scatterers seem to be resonant impurities (explanation in 2.5.3.1), the conductivity is well described by (eq.2.27):

$$\sigma \approx \frac{2 e^2}{\pi h} \frac{n_c \ln^2(R\sqrt{\pi n_c})}{n_{imp}}$$

The results of the fit are:

| Sample | S3 | S4 |
|------------------|-------------------------------------|--------------------------------------|
| n_{imp}^{hole} | $5,7 \pm 0,5 \cdot 10^{12} cm^{-2}$ | $3,4 \pm 0,5 \cdot 10^{12} cm^{-2}$ |
| R^{hole} | $9 \pm 5 \cdot 10^{-12} m$ | $1,3 \pm 0,5 \cdot 10^{-11} m$ |
| $n_{imp}^{e^-}$ | $2,2 \pm 0,5 \cdot 10^{12} cm^{-2}$ | $1,72 \pm 0,5 \cdot 10^{12} cm^{-2}$ |
| R^{e^-} | $8 \pm 2 \cdot 10^{-11} m$ | $1,1 \pm 0,2 \cdot 10^{-10} m$ |

These fitting parameters show a density of impurities which is different for electrons and for holes

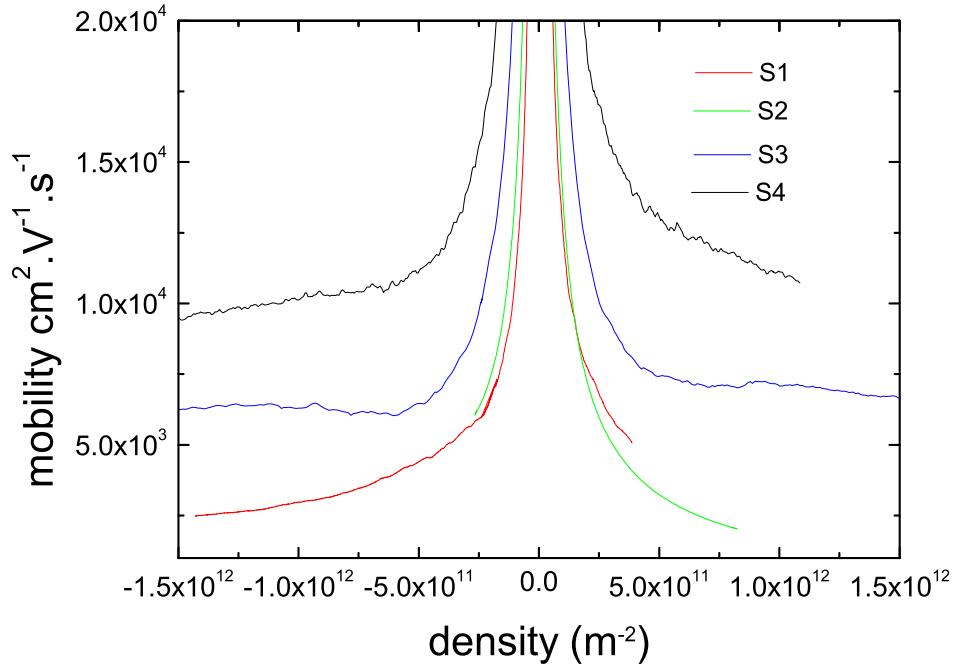


Figure 6.12

Also the size of the impurities is in agreement with the assumption that $R < \lambda_F$ and is different from electron to hole. On the hole side it seems to be very small, this let open the question wether there is an other mechanism that have a significant contribution. To give an example if a mechanism such as weak scattering contributes to a constant conductivity of $5e^2/h$, R would be 2 orders of magnitude higher.

On samples S1 and S2 which was covered by PMMA resist the conductivity does not seem be govern by the same law and it is harder to draw a conclusion on the dominant scatterers.

6.3.2.2 Bilayer

The bilayer measured shows a lower mobility. Transport was also found to be limited by resonant scattering impurities.

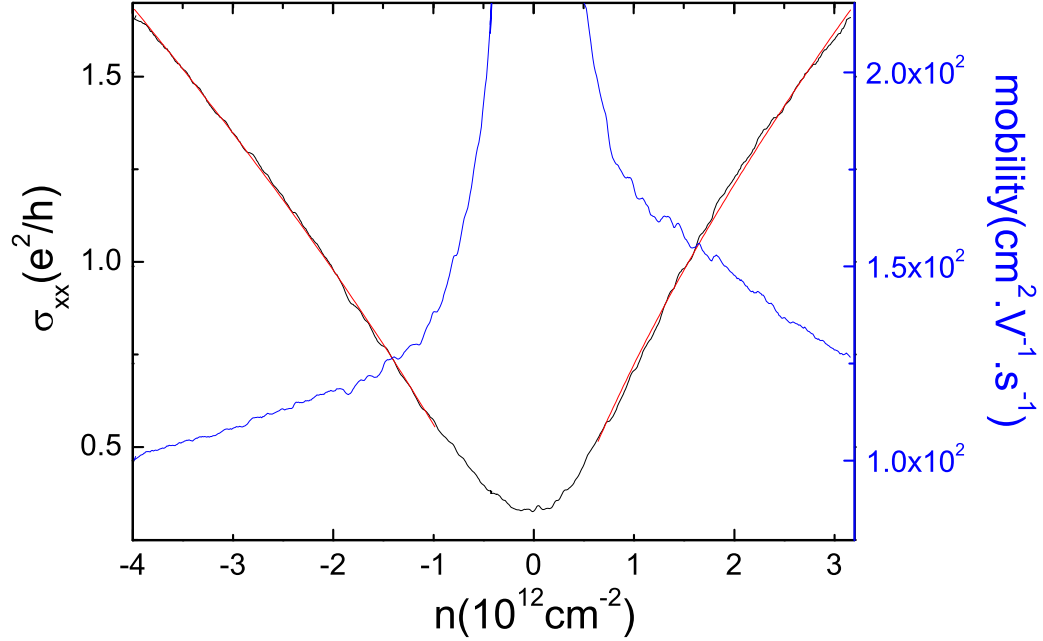


Figure 6.13: Measurement of the conductivity and mobility on the Corbino at 1.6K

The same law than for monolayers is applicable in case of resonant impurities for bilayer. From the fit of conductivity we get these parameters:

| Sample | Corbino |
|------------------|-------------------------------------|
| n_{imp}^{hole} | $1,9 \cdot 10^{14} \text{ cm}^{-2}$ |
| R^{hole} | $3,0 \cdot 10^{-11} \text{ m}$ |
| $n_{imp}^{e^-}$ | $8,8 \cdot 10^{13} \text{ cm}^{-2}$ |
| R^{e^-} | $1,0 \cdot 10^{-10} \text{ m}$ |

These values have to be taken carefully because it was not possible to extract the contact resistance and subtract it in the value of the conductivity. From results in monolayer we emphasise it to be low but with no certainty.

The fitting parameters and the value of the mobility seem to be quite lower than in our monolayers indicating more disorder. This was confirmed by quantum Hall measurements.

6.3.3 Universal Conductance Fluctuations

Universal Conductance Fluctuations (UCF) were usually seen on sample with typical value of $\sim e^2/h$. On our sample we observed some reproducible fluctuation attributed to UCF. The reproducibility was checked by sweeping the magnetic field in both directions.

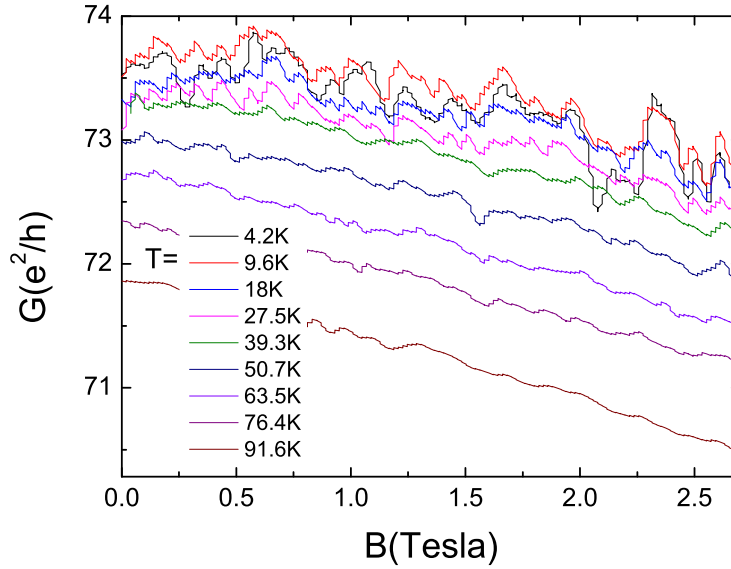


Figure 6.14: 4 point measurement of the conductance G on S3 at $n \sim 4,5 \cdot 10^{12} \text{cm}^{-2}$ as a function of the magnetic field for temperature ranging from 4.2K to 90K

Figure 6.14 shows an evolution of the UCF as a function of the temperature, here we can see the UCF disappeared around 40K and saturate around 10K with a value of $\delta G_{ucf} \sim \frac{1}{2} \frac{e^2}{h}$, which are the typical value expected for UCF.

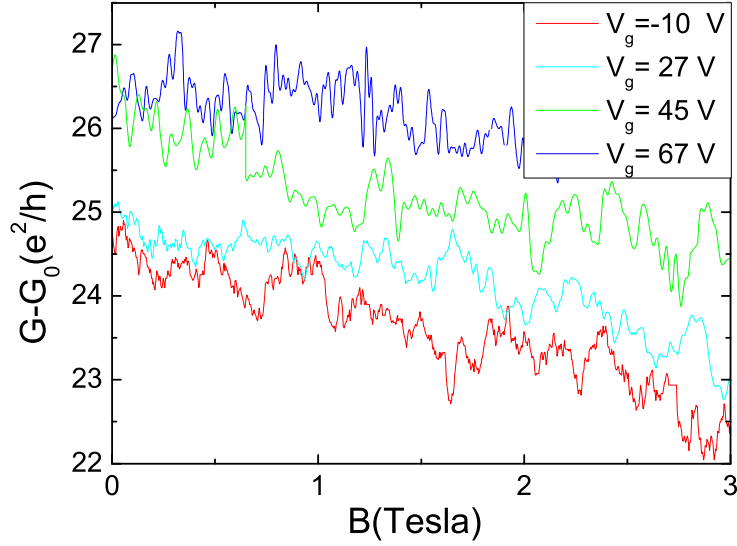


Figure 6.15: 4 points measurement of the conductance $G - G_0$ on S3 as a function of the magnetic field for different values of the density at $T=4.2\text{K}$. G_0 is a subtracted constant.

Figure 6.15 shows the UCF at different values of the density. We can see here that there is no substantial difference in the amplitude of the UCF near and far from the Dirac point.

Here these measurements are more qualitative than quantitative, they allow to confirm that the electronic transport was in the coherent diffusive regime.

More complete measurement of UCF in graphene can be found in ref. [142, 143], also imaging of UCF with scanning probe microscope can be found in ref.[144].

6.4 Quantum Hall measurements

To observe quantum Hall effect in graphene we can sweep the magnetic field at fixed density or sweep the density using the gate at a fixed magnetic field, while measuring the 4-probe resistance.

6.4.0.1 3-point measurements

For sample 1, as we had only four contacts available, we were able to measure R_{xy} with a four probe measurement and R_{xx} with a three point measurement.

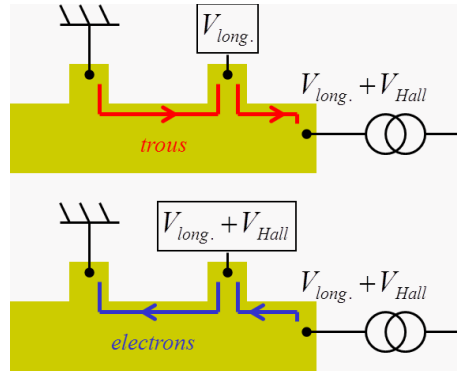


Figure 6.16

These measurements are particularly interesting because they show special features of the graphene. We were able to see R_{xx} for hole doping and $R_{xy} + R_{xx}$ for electron doping, showing that electron and hole propagate in opposite directions.

Indeed in QHE plateaus, an edge channel remains always at the potential of the lead from which the current originates. As shown on Fig. 6.16, in our 3-point measurements one probe was the drain (connected to the ground), another is the source and the third is a voltage probe (no current passes through this contact). The potential drop was always measured between the grounded contact and the voltage probe.

When the Fermi level lies in the valence band, the charge carriers are holes. As it is shown on the upper of figure 6.16, the channel leaves from the grounded contact implying that the entire edge is at the ground potential. The potential difference measured is just V_{xx} , which is the potential drop along a channel in the quantum Hall regime, giving R_{xx} + a contact resistance (here less than 10Ω , so it can be neglected). In contrast when the Fermi level lies in the conduction band, the charge carriers are electrons. In that case the channel leaves from the source contact which is at the Hall potential. The potential drop measured is now $V_{Hall} + V_{xx}$. These results are particularly clear, it is plotted on 6.17 where the red dots are the Hall resistance and the black dots are the 3 points resistance.

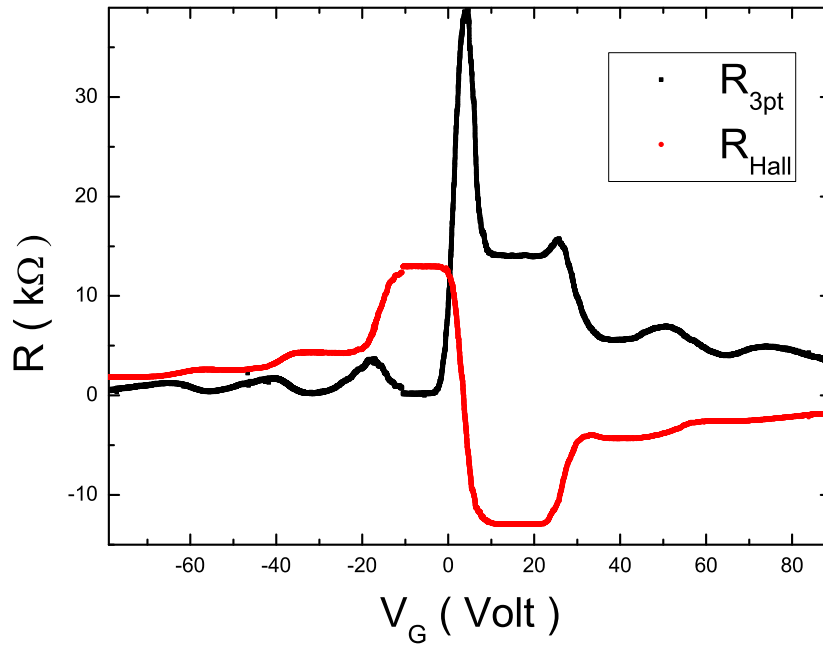


Figure 6.17: Hall and 3 point resistance as a function of gate voltage for $B=16.5$ Tesla at 4.2 Kelvin

6.4.0.2 Measurements on other samples.

Figure 6.18 shows measurement of the longitudinal resistivity versus the magnetic field for different value of the gate voltage. SDH oscillations arise here around 6 Tesla, which is a typical value for our samples.

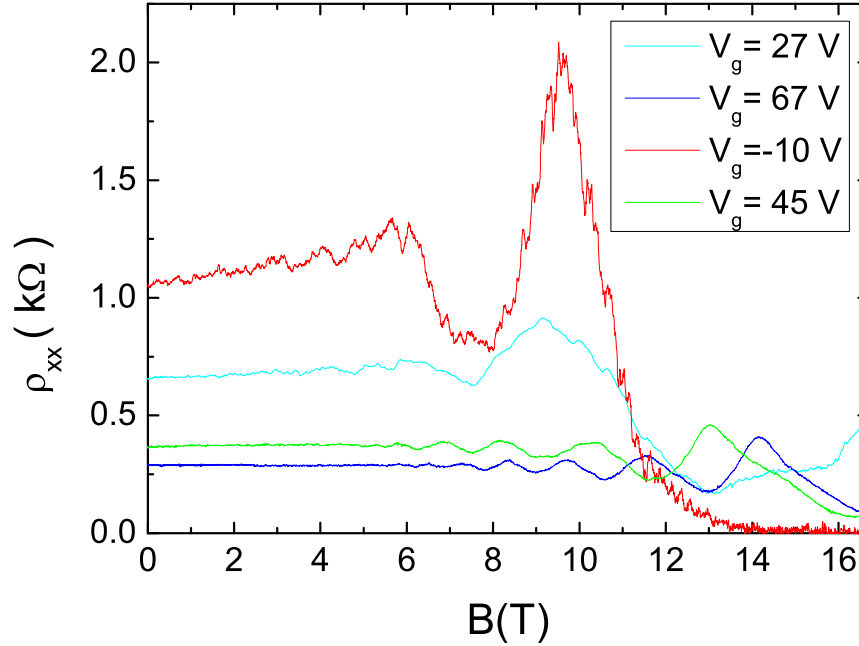


Figure 6.18: Magnetic field sweeps for different gate voltages on S3 at 4.2 Kelvin

On sample S4, it was possible to measure ρ_{xx} and ρ_{xy} thus it was possible to extract σ_{xx} and σ_{xy} . Figure 6.19 shows a flow diagram i.e σ_{xx} versus σ_{xy} on the sample S4 at a fixed magnetic field ($B=16.5\text{T}$). The inset is an enlargement of the transition from $\nu = -2$ to $\nu = -6$. The striking features here is the large circle representing the Dirac point which means that it can be possible to describe σ_{xx} and σ_{xy} with only one variable parameter. Similar figure than the half ellipse representing the transition between $\nu = -2$ and $\nu = -6$ was already observed in conventional 2DEGs in [115] and used as an argument for a behavior governed by an universal law in ref. [114].

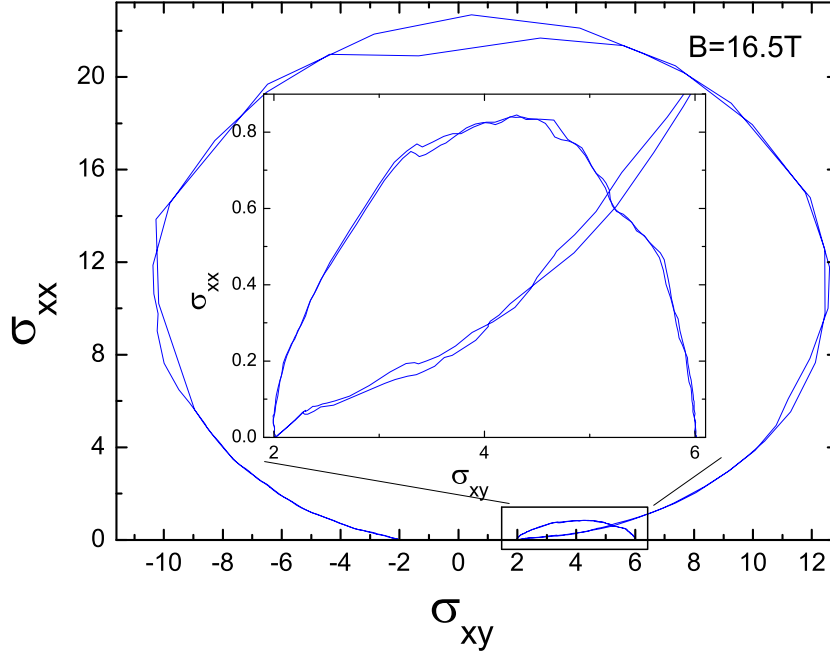


Figure 6.19: Flow diagram for sample S4, the circle of the main figure represents the flow around the Dirac point at 1.6K. Inset is a zoom on the transition between $\nu = -2$ and $\nu = -6$

6.4.1 The effect of the contacts

The usual contact resistance on good contacts was of the order of 10Ω which is quite low. We did not systematically measure the resistance of the contacts as we were usually measuring in a 4-point configuration. However the 2-point (fig.6.20) and 3-point (fig. 6.17) measurements we did in QHE regime gives accurate informations on the contacts resistances. Indeed on the Hall plateaus at low temperature the resistance of the sample is 0 on one edge and R_{Hall} between edges, thus we can determinate the contact resistance. As can be seen on figure 6.20 the 3-point resistance vanishes for hole transport and on 6.17 the 2-point resistance shows values very close to the quantized plateaus indicating a very low contact resistance.

Another important aspect to notice is that our 2-probe measurements in QHE show a clear asymmetry between electrons and holes. Electron doping by the contact can explain this fact: a right shift (electron side) of the 2-point resistance can explain why we see a peak around $-20V$ (on $\nu = -2$) and no

peak at 20V (on $\nu = 2$). Due to this doping the ρ_{xx} peak appears on the Hall plateau on one side and in the Hall plateau transition on the other side.

The doping by the contact has been measured in ref:[145, 146].

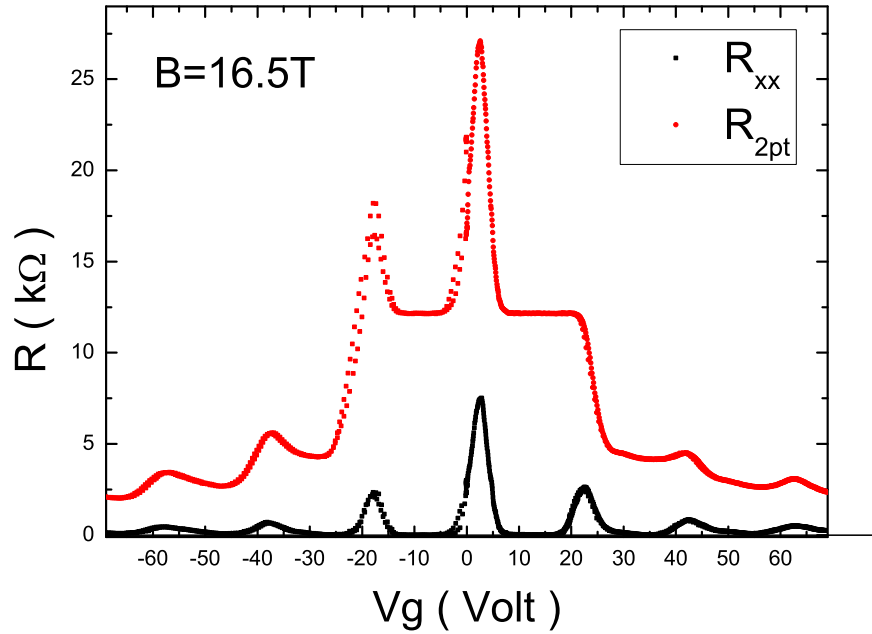


Figure 6.20: Four probe (R_{xx}) and 2 probe resistance as a function of gate voltage on S3 for B=16.5 Tesla at 4.2 Kelvin

6.5 Corbino measurements on a bilayer

Figure 6.21 shows measurement of the Quantum Hall effect in the Corbino sample done at various temperature. The interpretation of these measurements is not yet fully achieved and will not be presented in this thesis.

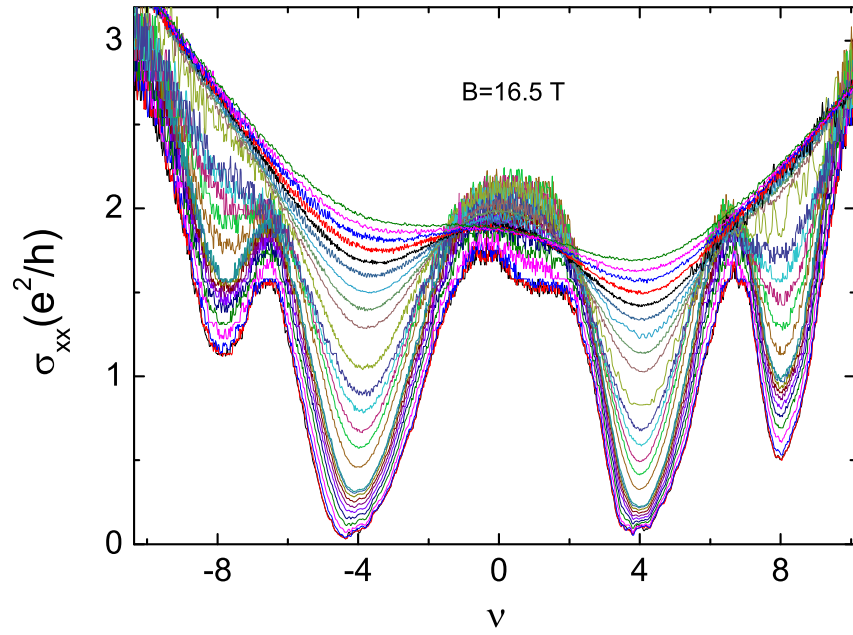


Figure 6.21: σ_{xx} on a corbino at $B=16.5$ Tesla for temperature ranging from 1.6K to 300K

Chapter 7

Measurement of the transport and elastic scattering time

The goal of this study was to measure the transport time τ_{tr} and the scattering time τ_e in graphene. From the ratio τ_{tr}/τ_e interesting physical properties of the scattering mechanisms can be extracted. Here we recall the discussion in section 2.4.1.1: τ_{tr} is the transport time entering the Drude conductivity and τ_e is the life time of an electronic wavefunction. τ_e is sensitive to the number of collisions whereas τ_{tr} depends on the number of collisions and the scattering angle. A large ratio τ_{tr}/τ_e indicates that the scattering is predominant in the forward direction as in 2DEG made at the interface of GaAs/AlGaAs heterojunctions where this ratio was found to be larger than 10.

This study was mainly done in the LPS Orsay, led by M.Monteverde in H.Bouchiat's team, it is published in ref [27].

The study was done on 5 samples. It is mostly focused on two samples manufactured and measured by C.Ojeda in Orsay, one monolayer (sample A) and one bilayer (sample B). Both have 2 contacts made with 40nm thick palladium. The samples were manufactured by the same procedure as described in chapter 4 except for metal deposition which was made with a sputtering technique. 4-probe measurements were made on 2 of our samples (S2, S3) to confirm the results of the two probe experiment.

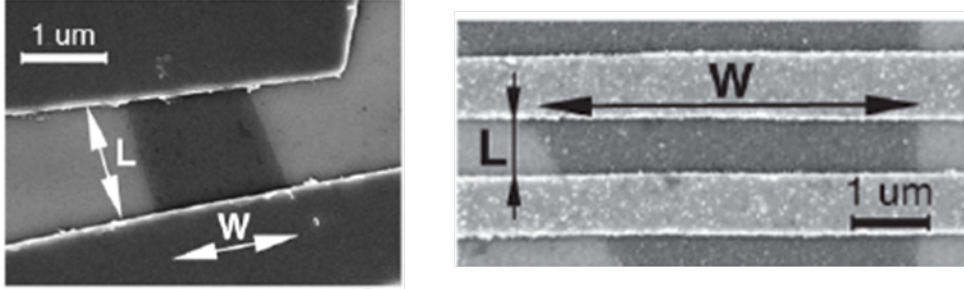


Figure 7.1: E-beam picture of sample A (left) and sample B (right)

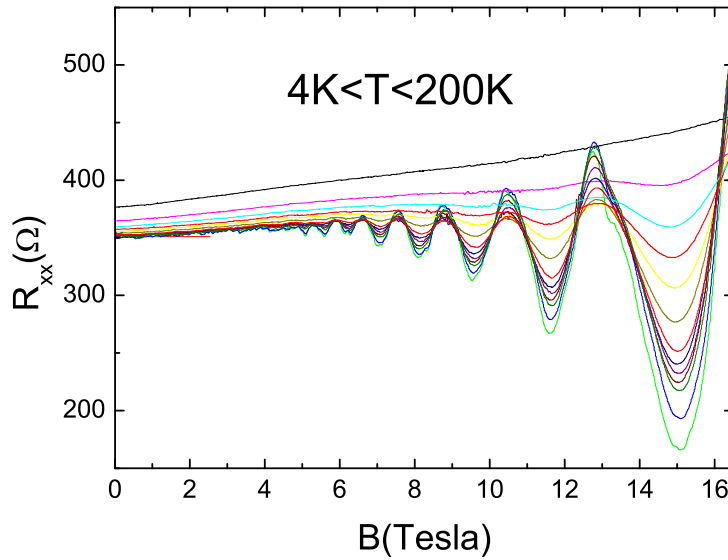


Figure 7.2: Example of our 4 point SDH measurement as function of the temperature from 4K to 200K on sample S3

We saw in 3.7 that both τ_e and τ_{tr} enter in the formula of the low field Shubnikov de Haas resistivity:

$$\frac{\delta\rho_{xx}(B)}{\rho_0} = 4D_T \exp\left(-\frac{\pi}{\omega_c\tau_e}\right) \cos\left(\frac{s\pi E_F}{\hbar\omega_c} - s\pi\right) \quad (7.1)$$

$$\rho_{xy}(B) = \rho_0\omega_c\tau_{tr} - \frac{\delta\rho_{xx}(B)}{2\omega\tau_{tr}} \quad (7.2)$$

Thus simultaneous measurements of $\rho_{xx}(B)$ and $\rho_{xy}(B)$ allow the extraction τ_e and τ_{tr} separately.

On two point samples $\rho_{xx}(B)$ and $\rho_{xy}(B)$ can be extracted from the two point resistance with the following formula involving the Hall and longitudinal resistances $R(B) - R_c = [\rho_{xx}^2 + \rho_{xy}^2]^{1/2}$ for a square geometry and $R(B) - R_c = (L/W) [\rho_{xx}^2 + \rho_{xy}^2] / \rho_{xx}$ for short and wide samples. R_c is the contact and wire resistance, and is not well known.

In 2-probe samples τ_{tr} was extracted from the low field magnetoresistance measurement. Using eq.7.1 and the considerations about the magnetoresistance in 2-probe samples we have at low magnetic field:

$$R(B) - R(0) = \frac{\hbar}{2e^2} \frac{L}{W} \frac{1}{k_F v_F \tau_{tr}} \alpha_g (\omega_c \tau_{tr})^2$$

Where $\rho_0 = 1/\sigma$ comes from the Drude conductivity, and α_g is a numerical coefficient depending on the aspect ratio of the sample. This method removes the dependence on contact resistances.

k_F was extracted from the periodicity of the SDH oscillations which is much more reliable than using the capacitance model to compute the density from the gate voltage especially near the Dirac point where electron-hole puddles induce a residual density.

For 4-probe measurements, τ_{tr} can be extracted directly from the Drude conductivity at zero field $\sigma = (2e^2/h) k_F v_F \tau_{tr}$ as the contact resistance does not contribute in the measurement of σ . The density n_c was extracted from tabulating the values of the density as a function of the gate voltage with the quantum Hall effect ($n_c = k_F^2/\pi$).

Figure 7.3 shows results of τ_{tr} measurements on sample A and Sample S3.

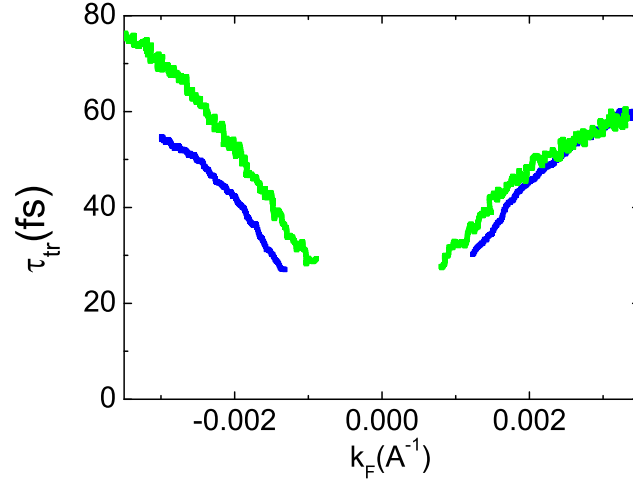


Figure 7.3: Transport time. The green curves are extracted from SDH oscillation on a 2-probe monolayer measured in LPS, the blue curves from the zero field conductivity on sample S3 at Saclay.

τ_e was extracted from the SDH oscillations on all samples by measuring their amplitude and fitting them with an exponential law (as shown in fig. 7.4 and 7.5).

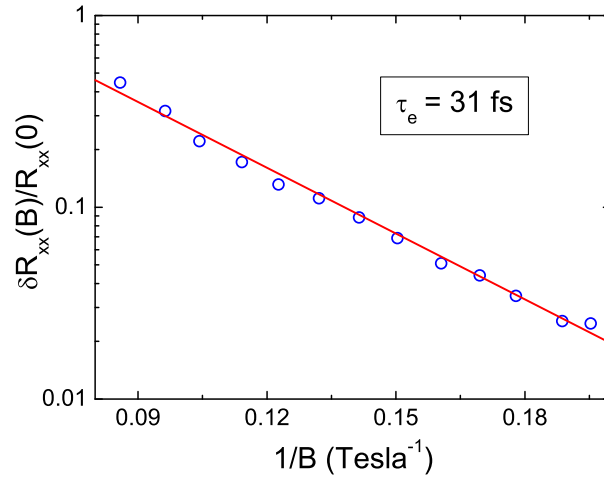


Figure 7.4: $\delta R_{xx}(B)/R_{xx}(0)$ as a function of $1/B$ on S3 at $n = 5, 2 \cdot 10^{12} \text{ cm}^{-2}$. The fit of this curve gives $\tau_e = 31 \text{ fs}$. Fit done by M.Monterverde.

CHAPTER 7. MEASUREMENT OF THE TRANSPORT AND ELASTIC SCATTERING TIME

The data acquired in Orsay are extensive, τ_e and τ_{tr} were measured for nearly all the accessible densities. For our samples, 3 points for τ_e in S3 and 1 point for S2 were measured.

The values of τ_{tr} and τ_e (extracted by M.Monteverde) for our samples are:

| $n(cm^{-2})$ | $k_F(m^{-1})$ | τ_{tr} (fs) | τ_e (fs) | τ_{tr}/τ_e |
|----------------------|--------------------|------------------|---------------|--------------------|
| S3 | | | | |
| $5, 2 \cdot 10^{12}$ | $-4, 1 \cdot 10^8$ | 59 | 31 | $1, 9 \pm 0, 3$ |
| $4, 1 \cdot 10^{12}$ | $3, 6 \cdot 10^8$ | 63 | 24 | $2, 6 \pm 0, 4$ |
| $5, 9 \cdot 10^{12}$ | $4, 3 \cdot 10^8$ | 68 | 26 | $2, 6 \pm 0, 4$ |
| S2 | | | | |
| $5, 1 \cdot 10^{12}$ | $4, 0 \cdot 10^8$ | 21 | 16 | $1, 3 \pm 0, 2$ |

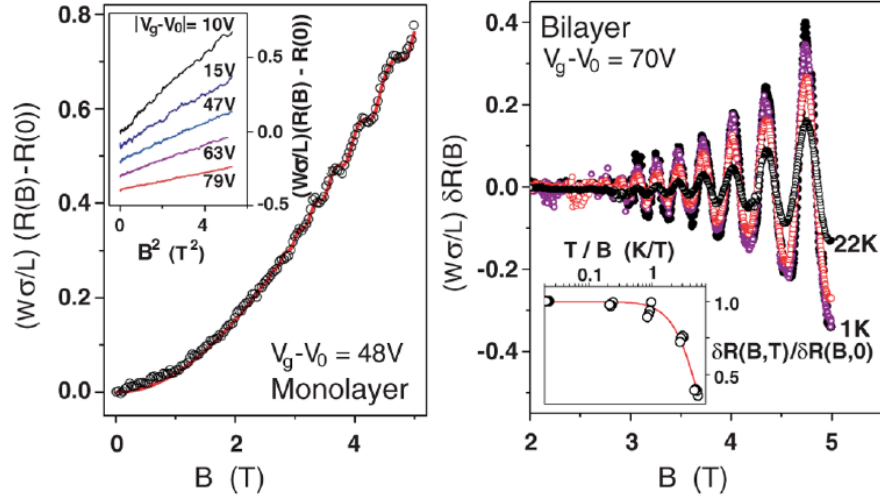


Figure 7.5: left panel shows magnetoresistance for monolayer sample A at 1K (dots) and the red line is the fitting curve according to eq. 7.1 and 7.2. Inset shows the same measurement for different values of the gate voltage. Right panel shows $\delta R(B)$ for a bilayer after subtraction of the quadratic background as a function of B for temperatures ranging from 1K to 22K. Inset shows a fit of the temperature dependence of SDH oscillations, from this fit it was possible to extract $m_{eff} = 0,035 \pm 0,2m_e$. (figure from M.Monteverde)

Figure 7.6 shows the measured values of the ratio τ_{tr}/τ_e as a function of k_F . For all samples $r = \tau_{tr}/\tau_e$ was found to be nearly independent of k_F . It is equal to $r = 1,7 \pm 0,3$ in samples A,C and S2 and $r = 1,8 \pm 0,2$ in sample B (bilayer) whereas sample S3 exhibits slightly higher ratio $r \simeq 2,4$ at high electron doping.

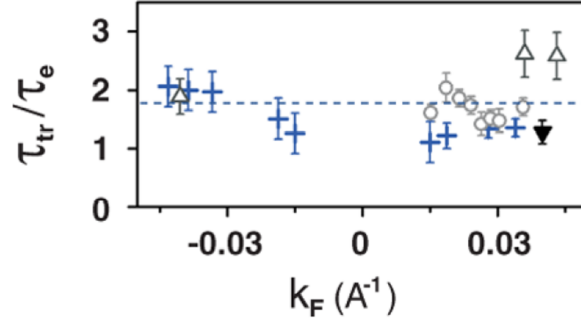


Figure 7.6: Value of τ_{tr}/τ_e for the four monolayers measured as a function of k_F

These measurements give an indication of the type of dominant scatterers at zero magnetic field in graphene. A computation made by Hwang and Das Sarma [147] predicts that the ratio τ_{tr}/τ_e for graphene is slightly less than 2 for short range neutral impurities and around 8 for charged impurities. As a consequence, charged impurities appear not to dominate the scattering. Further evidence for that is the dependence of the zero field conductivity σ on the density that is sublinear in our sample, and should be linear in the case of charged impurity scattering.

Neutral resonant impurities as described in section 2.5.3.1 appear to be a good candidate as the major source of scattering. The ratio τ_{tr}/τ_e is below 2 for all the samples except S3 (which is slightly higher but far from the ratio predicted for charged impurities). The sublinear variation of σ too is well fitted by a resonant neutral impurity model (results are shown in section 6.3.2).

To conclude we can say that strong resonant neutral defects with range shorter than the Fermi wavelength are the major source of scattering in our samples. Candidates for this type of scattering are vacancies, adatoms or short-range ripples. This does not exclude other types of scattering, especially for large samples like S3 where as we saw in 6.3.2 and from the value of τ_{tr}/τ_e , the electronic transport is probably limited by several different types of impurity.

Chapter 8

Mechanism of the disappearance of the QHE at finite energy

This chapter addresses the central part of the PhD thesis and concerns the disappearance of the Quantum Hall effect.

We will show that graphene mono-layers combined with 300nm close Si-doped backgate allow the first time observation of a cross-over from Efros-Shklovskii to Mott variable range hopping transport in the quantum Hall regime.

Since its recent discovery [50, 14], the anomalous Quantum Hall Effect (QHE) displayed by the relativistic like electrons of Graphene monolayers has been most closely investigated in the search for quantum Hall ferromagnetism [148] and the Fractional Quantum Hall effect [52, 53] in very low disorder samples to favor interaction effects. Here we address the opposite regime where disorder is strong enough to overcome electron interactions, as it is the case for standard exfoliated Graphene monolayers deposited on the oxide layer of a silicon substrate. Graphene offers a new set of parameters to revisit the quantum phase transition of localization in the Quantum Hall regime. In particular, we show that the screening of interactions by the 300 nm distant back-gate provided by highly doped silicon allows one to observe for the first time the transition from Efros-Shklovskii (E-S) to Mott Variable Range Hopping (VRH) in QHE for large localization length. The universal scaling exponents of quantum localization at Hall plateau transitions deduced from our entire set of temperature and bias current data, together with the E-S to Mott VRH transition, definitively validate the Polyakov-Shklovskii (P-S) suggestion that VRH transport is sufficient to describe the quantum Hall electrical transport [90].

In this chapter we present a complete set of data in temperature and bias current on the QHE regime performed on Graphene monolayers. The silicon back-gate at set back distance of $d = 300\text{nm}$ gives first time access to the cross-over from Mott to ES VRH regime on conductivity peaks for the highest filling

factors where ξ is large. All the scaling exponents agree with the P-S and A-S predictions in the screened and unscreened regime. This provides a definitive confirmation of these models. The scaling exponent found to be $\gamma \simeq 2.3$ is the same for first two $n = \pm 1, \pm 2$ LLs and the $n = 0$ LL where no anomalous behavior is observed as found in Ref.[75].

8.1 Transport measurement procedure and overview of the transport data.

8.1.1 Temperature measurements

Observing the variation of the conductivity (or resistivity) as a function of temperature for different magnetic fields is the first step in determining the basic transport mechanisms at work in the QH regime.

We have performed very extensive measurements on 2 samples, samples 3 and 4 (described in section 6.3.1). We will concentrate mostly on the measurements done on sample 3.

Longitudinal resistance R_{xx} was recorded on varying the electron density for about 50 fixed temperature values ranging from 1.6K to 300K and similar runs were repeated for different fixed high magnetic fields from 6 to 17 Tesla. The bias current was fixed at 10nA for all temperature measurements. Longitudinal resistivity ρ_{xx} was calculated from the R_{xx} values knowing the aspect ratio of the sample. Fig. 8.1 displays the whole set of data of ρ_{xx} at different temperatures for $B = 16,5$ Tesla.

For these measurements we varied the density slowly (less than 2 volts per minute) in order to avoid hysteresis effects due to trapped charges in the silicon oxide. The gate was swept in both directions, but in order to get rid of the weak remaining hysteresis for a given sample we always considered data for the same direction of gate voltage sweeping. The typical range of gate to sample potential at fixed temperature was -70V to +70V. During each sweep around 3000 data points were acquired.

Data acquisition was piloted automatically by computer using Labview software.

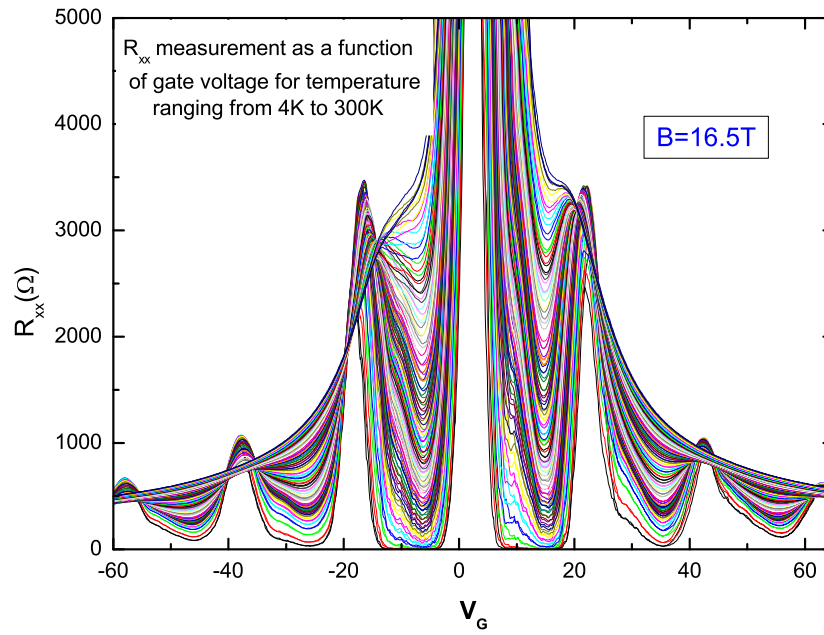


Figure 8.1: Longitudinal resistance ρ_{xx} versus filling factor at $B=16,5$ Tesla for temperature ranging from 4.2K to 300K on S3 in steps of around 5K at bias current of 10nA.

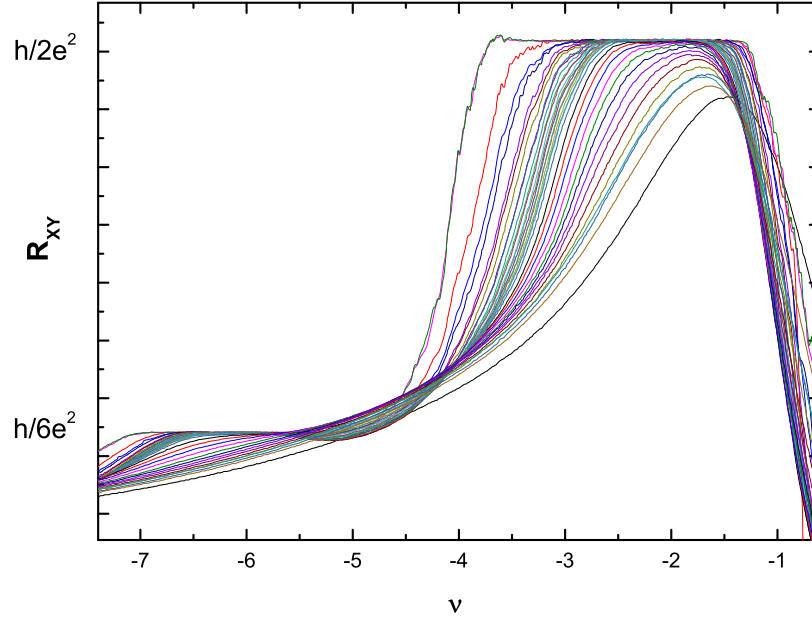


Figure 8.2: Hall resistance R_{Hall} versus filling factor at $B=16,5$ Tesla for temperatures ranging from 1.6K to 300K on S4

On sample 4 we were able to measure both ρ_{xx} and ρ_{xy} . Figure 8.2 shows the evolution of the Hall resistance as function of the filling factor (or gate voltage) at fixed magnetic field $B=16.5$ T for different temperatures.

Figure 8.3 shows a color plot of the Hall resistance as a function of the temperature for different fixed high magnetic fields. The part in red is the Hall plateau at $\nu = -2$, this figure provides to have a visualization of how the width of the plateau decreases with the temperature at different magnetic fields. At 16,5 Tesla, the Hall resistance on $\nu = -2$ deviates from the quantized value of $h/2e^2$ above a temperature of ~ 100 K and on $\nu = -6$ it deviates from the value of $h/6e^2$ above ~ 40 K. These temperatures vary strongly with magnetic field.

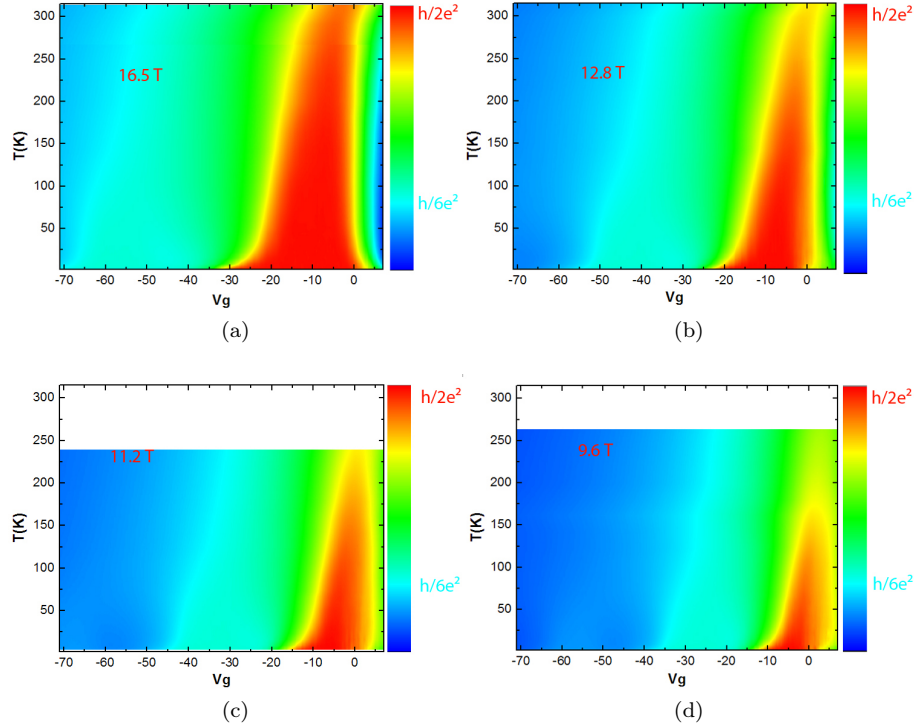


Figure 8.3: Color plot of R_{Hall} versus temperature and gate voltage for different magnetic fields. Red corresponds to the $\nu = -2$ Hall plateau

Both figures show that QHE effect is maintained at very high temperature compared to conventional 2DEGs, and even at room temperature some remaining oscillations can be seen in the longitudinal resistance as in ref [44].

8.1.2 Bias Current measurements

Studying the quantum Hall effect as a function of the bias current is also very interesting as it gives information about eventual breakdown. If no trivial heating accompanies the large currents, it can also confirm a hopping law or probe the Hall field profile in the sample which, up to now, has not been done with graphene.

For these measurements we fix temperature and magnetic field, and vary the bias current. As for the temperature measurements, the gate was swept for fixed bias current ranging from 10nA to 100 μ A in non equal steps. Some 50 curves were acquired for each magnetic field from 6 Tesla to 16,5 Tesla. The size of the steps was set to vary linearly between 10nA and 10 μ A and to give the wanted number of curves.

The bias current was injected from a constant voltage source in series with a

large resistor. Several resistors were used ranging from $20\text{M}\Omega$ to $100\text{k}\Omega$ to access all the bias current range. As for high bias current the graphene resistance is non negligible compared to the $100\text{k}\Omega$ source resistor and vary from around $2\text{k}\Omega$ to more than $12\text{k}\Omega$, 2 points measurement of graphene was recorded to access all the values of the bias current. This is important for the analysis; as we measure the 4-probe potential drop, a precise value of the current is needed to compute the resistivity ρ_{xx} and it is also needed to determine the evolution of ρ_{xx} with bias current. For the analysis, each value of ρ_{xx} was associated with the precise value of the bias current at this point.

These measurements were done for all four samples, but the most complete set of measurements was done on sample 3.

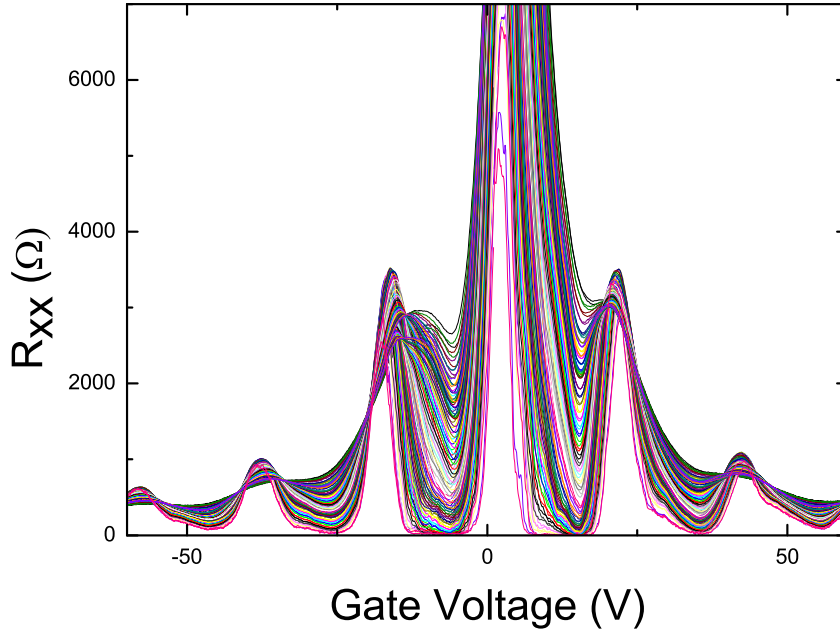


Figure 8.4: Longitudinal resistance ρ_{xx} versus filling factor at $B=16,5$ Tesla for bias current ranging from 10 nA to $100\text{ }\mu\text{A}$ with variable step ranging from 10nA to $10\mu\text{A}$ on sample S3 at $T=4\text{K}$

Note that additional bias current measurements on samples S1 and S2 are presented in the appendix (chapter 11).

8.1.3 Analysis of the data

Our measurement of ρ_{xx} versus temperature or bias current clearly showed 2 distinct behaviors. We attributed the non zero values of ρ_{xx} to variable range hopping at low energy and to activation at higher energy. This has been confirmed by a long series of function fits through nearly all the filling factor range. In this paragraph we will detail our fitting method and the way we extract relevant physical parameters such as the VRH temperature leading to the localization length or the activation energy, giving us the energy gap between Landau levels.

An example of the 2 distinct regions is given by figure 8.5 which shows the typical evolution of ρ_{xx} with temperature on a plateau (here on the minimum of ρ_{xx} at $\nu = -2$, which we will call $\rho_{xx}(-2)$ in the following); here we have plotted $T\rho_{xx}(-2)$ on a logarithmic scale versus $1/T^{1/2}$. This corresponds to the Efros-Shklovskii (E-S) VRH law, which fits well from 1.6K to $\simeq 80$ K. Above 100K however the departure from the E-S VRH law signals the onset of an activated law.

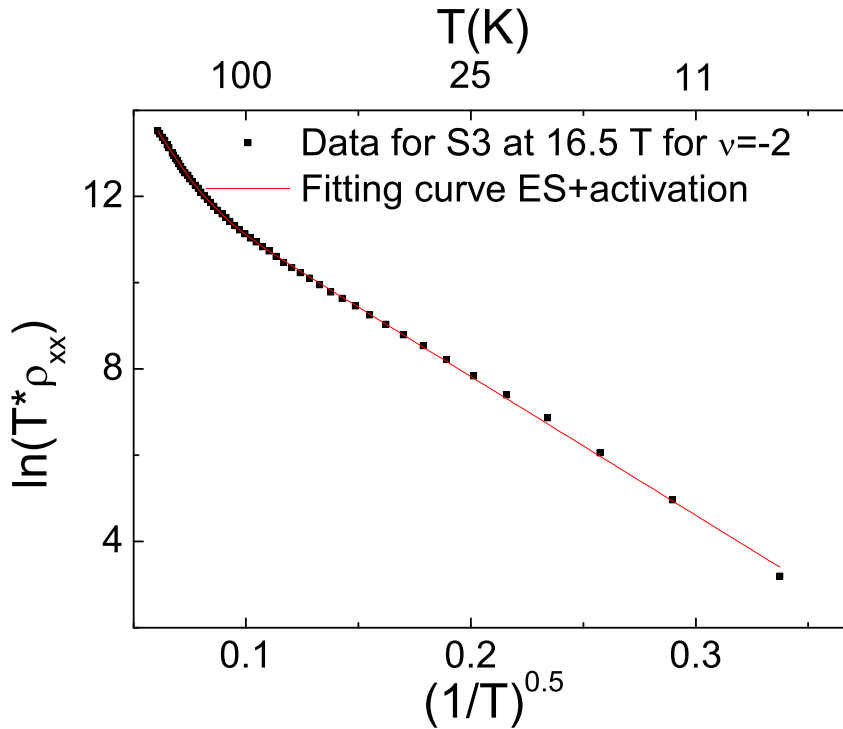


Figure 8.5: Example of a plot $T \cdot \rho_{xx}$ as a function of $\sqrt{1/T}$ on the center of the plateau $\nu = -2$ at 16.5 Tesla and fitted by VRH and activated laws. This plot clearly supports the ES-VRH picture for $T < 100$ K. (here for $\sqrt{1/T} > 0,1$).

Here we show in more detail how our fitting function based on a combination of activated and E-S VRH law allows us to extract the characteristic energies. As shown in chapter 3.10 it is very informative to know the parameter T_0 which is proportional to the inverse of the localization length over all the filling factor range to check the universal laws of the QHE.

$$\xi(\nu) = \frac{Ce^2}{4\pi\epsilon\epsilon_0 k_B T_0(\nu)}$$

In this study we focus mostly on the analysis of ρ_{xx} and not σ_{xx} which, although it has the most physical sense, is not strictly speaking available for sample S3 because ρ_{xy} could not be measured.

Recalling the relation between ρ_{xx} and σ_{xx} :

$$\sigma_{xx} = \frac{\rho_{xx}}{\rho_{xx}^2 + \rho_{xy}^2}$$

We see that on the Hall plateaus when ρ_{xx} values are very low $\rho_{xx} = k\sigma_{xx}$ where $k = 1/R_H^2$ is a constant, so fitting ρ_{xx} or σ_{xx} leads to the same results. On the edge of the plateau ρ_{xx} increases but is still low compared to ρ_{xy} (at the transition between $\nu = 2$ and $\nu = 6$, $\rho_{xx}^{max} \sim 2k\Omega$ when $4k\Omega < \rho_{xy} < 13k\Omega$) as the contributions are squared, fitting ρ_{xx} or σ_{xx} should not change much. To make sure of that we fitted both ρ_{xx} and σ_{xx} over the entire range of filling factors for sample S4 where ρ_{xy} data was available leading to very similar results.

Because of the huge amount of data (about 3000 data points per voltage bias sweep) we have had to construct reliable tools to fit the data as a sum of VRH and activated laws.

The first step was to build a temperature-gate voltage matrix of the data. This was done with the help of a 2000 point extrapolation of each set of data at fixed temperature. As there are around 50 temperatures, at the end of this process we have a matrix including 2000 curves of around 50 points of ρ_{xx} as a function of the temperature (for each magnetic field).

Another challenge was to generate automatically fitting curves representing two different behaviors (activated and VRH) with exponential dependence on the fitting parameters (the energy) and to ensure that the minimization occurs properly and reliably such that the values extracted are not meaningless. The transition between those 2 behaviors happens at different temperatures for different filling factors; the simpler alternative strategy of fitting separately the two laws for two different temperature ranges was not applicable here. Also in the transition region which can extend over about 20K, both contributions are present.

The total longitudinal conductance σ_{xx} sums the VRH and activated contributions, and as the ρ_{xx} is proportional to σ_{xx} , the best solution found to make these automatic fits was to use a function adding the two contributions:

$$\rho_{xx} = \frac{A}{T} \exp\left(-\left(\frac{T_0}{T}\right)^{1/2}\right) + B \exp\left(-\frac{E_a}{k_B T}\right) \quad (8.1)$$

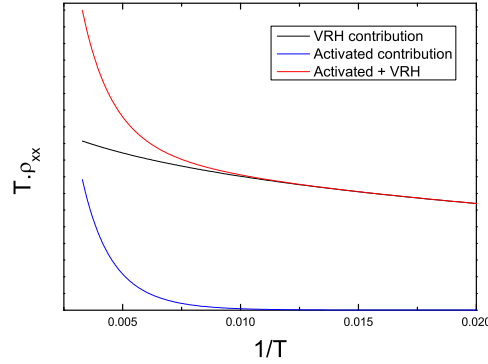


Figure 8.6: Activated (blue) and VRH (black) contribution to the resistivity (red), the functions of equation 8.1 are plotted with typical fitting parameters on $\nu = 2$.

This gives four fitting parameters (A, B, T_0, E_a).

Non sensible fitting parameter results can be avoided by making a careful choice of the initialization and bounds of the fit parameters. As shown on figure 8.6, below $\sim 100K$ the activated part is vanishing and the VRH part $A/T \cdot \exp(-\sqrt{T_0/T})$ is the sole fitting function. Above $100K$ the activated contribution starts to dominate, and grows exponentially whereas the VRH part can be viewed as a nearly constant contribution. In order to find good bounds for the parameters many curves were fitted manually before the automation. Also, to avoid that the activated part which is orders of magnitude higher than the VRH part, taking all the weight in the least square minimization, we fitted the logarithmic values of the data.

Figure 8.7 shows a color plot of the ratio of the experimental data over the data generated by the fit. A ratio equal to one indicates a perfect fit. As mentioned above, the fitting law contains both activated and E-S VRH. We can clearly see when the E-S law fits well. At high temperature, the activated part leads to good fits almost everywhere. At low temperature fits are not good everywhere. Particularly around $\nu = \pm 2$ the fits are not good below $20K$. This is due to a saturation of the variation of ρ_{xx} at low temperature arising when the hopping distance is longer than the sample width.

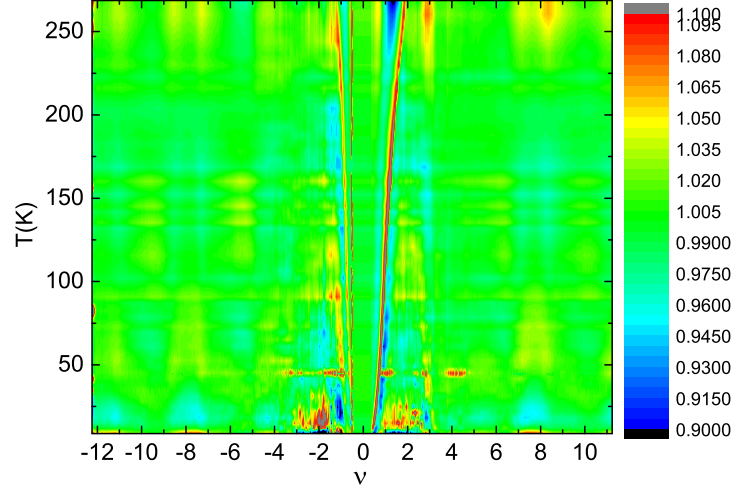


Figure 8.7: Comparison between fit and data

For the value of ρ_{xx} as a function of the bias current we followed the same procedure and use a law combining an activated part and a variable range hopping part.

$$\rho_{xx} = \frac{A}{T} \exp\left(-\left(\frac{I_0}{I}\right)^{1/2}\right) + B \exp\left(-\frac{I_a}{I}\right) \quad (8.2)$$

As we saw in section 3.10.2.2, and will be recalled in section 8.4, the bias current in VRH is proportional to the temperature but in the activated part there is no particular reason that it should be the case. Thus we do not expect to find a meaningful parameter in the activated part, but maintaining this part facilitates automatic fitting. Here these fittings were more difficult to make because the longitudinal resistance saturates below a certain bias current which depends on the filling factor; in fact the true parameter here is $V_{Hall} = I \cdot R_{Hall}$ which varies with the filling factor. At high magnetic field, however, it was possible to get meaningful values of I_0 .

8.2 High energy transport: thermal Activation energy

The activation process involves two contributions, if the Fermi level is somewhere in between two Landau levels (LL), an electron can jump from the Fermi level to the next LL or from the LL below to the Fermi level. Here we will not consider the higher order process, ie electrons jumping on LL higher than the nearest one.

If we set $\mu = 0$ in the middle of two LL (and corresponding ideally to the middle of a Hall plateau) we can write

$$\rho_{xx} \sim \left[\exp\left(-\frac{\Delta - \mu}{k_B T}\right) + \exp\left(-\frac{\Delta + \mu}{k_B T}\right) \right]$$

where $\mu(\nu)$ depends on the filling factor ν .

So at the center of two LL this expression becomes:

$$\rho_{xx} \sim \exp\left(-\frac{\Delta}{k_B T}\right)$$

This tells us the spacing between LL which is equal to $2 * \Delta$.

When the Fermi level is moved, one of the exponentials becomes rapidly dominant, thus we can fit ρ_{xx} by a single exponential which is the second term in equation 8.1

$$\rho_{xx} = \rho_{xx}^0 \exp\left(-\frac{E_a}{k_B T}\right) \quad (8.3)$$

where the prefactor will double upon approaching the midpoint between LL.

The theoretical maximum activation energy separating the N^{th} and $(N+1)^{th}$ LL obtained from the Dirac equation in magnetic field is

$$\Delta = \frac{1}{2}(E_{N+1} - E_N) = \frac{1}{2}(\sqrt{N+1} - \sqrt{N})\sqrt{2e\hbar v_F^2 B} \quad (8.4)$$

The probability for an electron to occupy the next LL follows an Arrhenius law $P \sim \exp(-E_a/k_B T)$, which is thus directly reflected in the conductivity (resistivity). When an electron occupies a higher empty LL it can backscatter to the opposite edge. As a consequence the conductance is proportional to the probability of occupation of the higher LL. At low energy it is not the dominant effect (from the gap values ρ_{xx} would show extremely small values) and the intra LL mechanism called VRH (see next paragraph) dominates. Our measurements show that this effect dominates only beyond 100K.

Activation energies were extracted from our automatic fitting procedure and are plotted on fig 8.8 as a function of filling factor for different magnetic fields.

As we do not know exactly where the midpoint between two LL lies, we take for values of the gap Δ the maximum of the activation energy E_a for each Hall plateau; these values are plotted as a function of the magnetic field on fig.8.9 for S3 and S4.

It is expected that the gaps Δ measured should be smaller than those predicted by LL separation because of disorder broadening of the levels. By comparing the experimental gap and the theoretical gap we can estimate the LL broadening by disorder. On the first sample we find a broadening of 200K at 17T and in the second sample 70K.

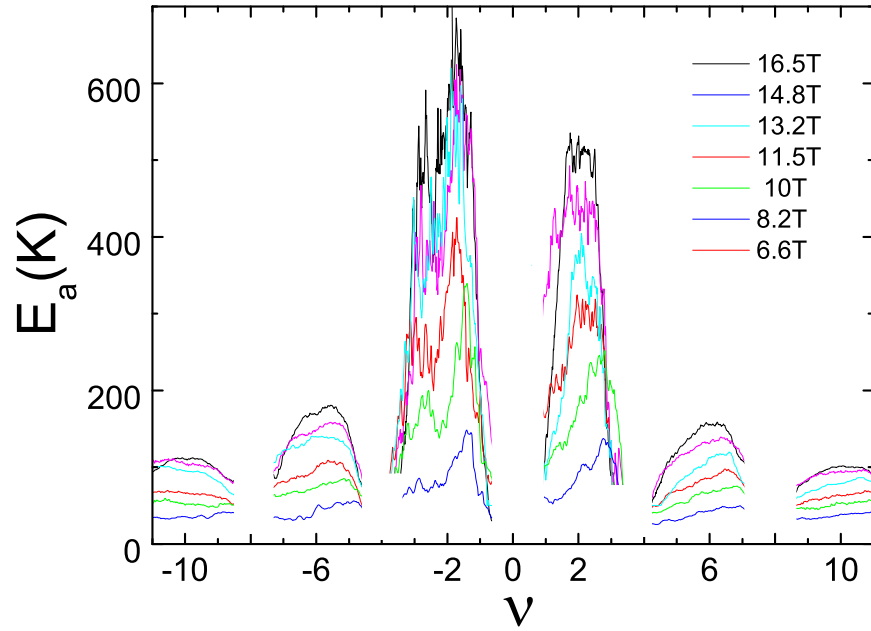


Figure 8.8: Activation energy as a function of filling factors for different magnetic fields ranging from 8,2T to 16,5T on S3.

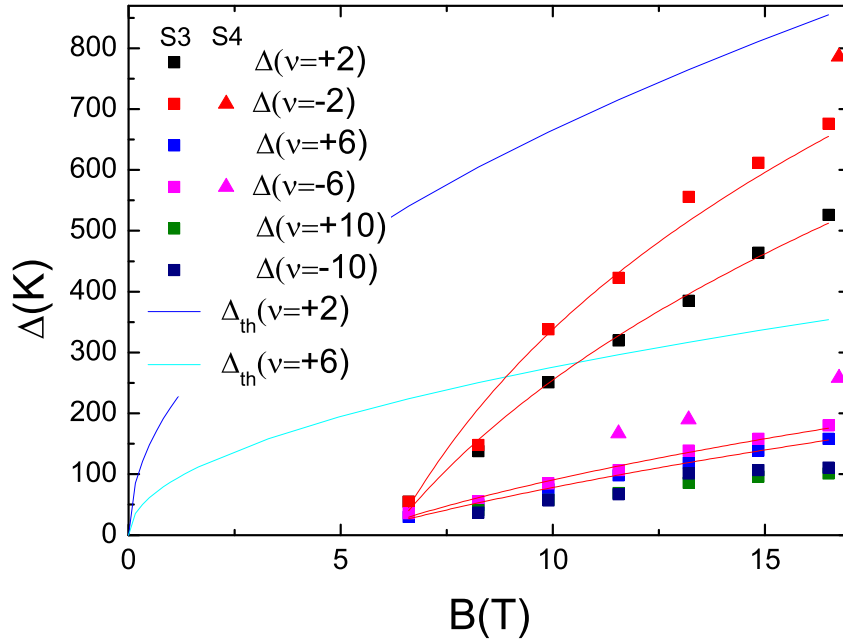


Figure 8.9: Activation gap for S3 and S4 at different magnetic fields for $\nu = \pm 2, \pm 6, \pm 10$. Squares are for sample S3 and triangles for S4. Solid lines are the theoretical gaps given by the Dirac equation, blue line for $\nu = \pm 2$ and light blue line is for $\nu = \pm 6$. The red lines are the fitting curve with Δn and ΔV contributions (see below).

The values of the activation gaps measured for sample 3 are very close to those measured in ref.[61] (see figure 3.19). In sample S4 the values of the measured gaps are higher, in agreement with expectations as this sample shows a higher mobility.

These values should vary with the square root of the magnetic field. Here our values are clearly lower than theoretical gaps, in transport measurement the fact that values of the extracted gap are lower than the theoretical values can be explained by two phenomena:

- Density fluctuations which are responsible for the fact that the chemical potential is not clearly defined. To compute these density fluctuations we can write:

$$\frac{\Delta\nu}{\nu} = \frac{\Delta n}{n}$$

$$\Delta\nu = \Delta n \frac{h}{eB}$$

Thus a variation Δn should lead to a variation in $\Delta\nu$ proportional to $1/B$. These variations are due to rearrangement of the charge to screen fluctuations of potential: on a Hall plateau the screening is weak but still present.

As we measure an energy gap we cannot extract an exact value of the density fluctuation since the variation of ν with the energy is not known but we can extract a maximum value using the derivative of the energy, as sketched on figure 8.10.

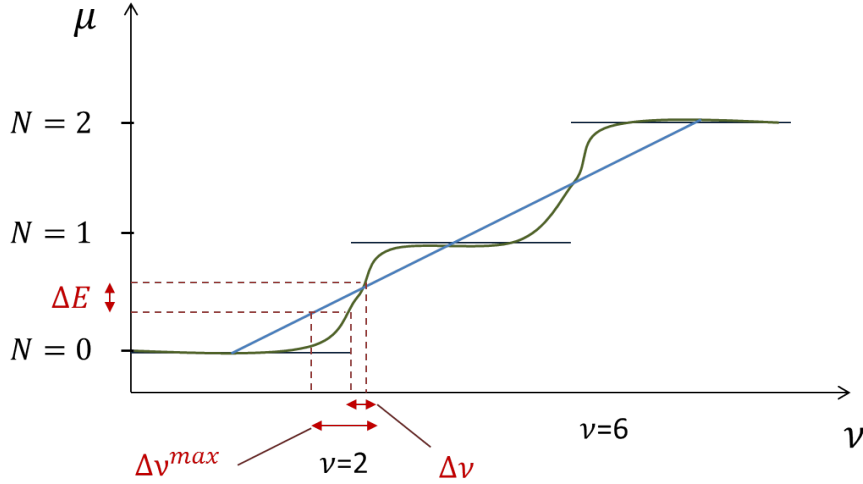


Figure 8.10: Filling factor as a function of the potential. The green curve sketches a realistic variation of ν with μ whereas the blue curve shows the linear variation used to compute an upper bound for Δn .

- As mentioned in section 3.8.9, the potential fluctuations broaden the Landau levels: these fluctuations make a constant contribution ΔU to the lowering of the gap.

By fitting the gap values on S3 with both contributions

$$\Delta(B) = \frac{1}{2}(\sqrt{N+1} - \sqrt{N})\sqrt{2e\hbar v_F^2 B - \Delta U - \Delta n/B}$$

(represented by red curves on figure 8.9) we can extract ΔU and Δn_{max}

| | ΔU | Δn_{max} |
|------------|-----------------|----------------------|
| $\nu = 2$ | $2, 0.10^{-2}V$ | $1, 9.10^{15}m^{-2}$ |
| $\nu = -2$ | $0V$ | $3, 5.10^{15}m^{-2}$ |
| $\nu = 6$ | $1, 6.10^{-2}V$ | $2, 4.10^{12}m^{-2}$ |
| $\nu = -6$ | $1, 4.10^{-2}V$ | $8, 6.10^{13}m^{-2}$ |

It is interesting that these results show a clear difference between electrons and holes doping. On the electron side the screening seems to be weaker, resulting in a lower Δn and higher ΔU fluctuations. The fluctuations of density are larger on $\nu = 2$ than on $\nu = 6$, a result which can be understood in view of the results of ref. [146] which clearly show that the density fluctuations are higher at low density around the Dirac point than at high density. The asymmetry between electrons and holes could be due to charged impurities affecting more one side than the other. This may seem in contradiction with results of chapter 7 but it is not; it is important to recall that the impurities limiting the zero field mobility are different from those limiting the quantum Hall effect. Trapped charges in the silica may result in large and smooth fluctuations which do not much affect the zero field conductivity, whereas these fluctuations may provide large localized states at the Fermi level limiting the QHE and also contribute to density fluctuations.

Prefactor of the conductivity for the activated law

It is interesting to look at the prefactor as it was predicted to have an universal value of $\sigma_{xx}^0 = 2e^2/h$ (see 3.10.1). On sample 3 and sample 4 following values were found at B=16,5 Tesla:

| sample | S3 | S4 |
|--------------------|------|------|
| $\nu = 2 (e^2/h)$ | 2,9 | - |
| $\nu = -2 (e^2/h)$ | 3,7 | 2,8 |
| $\nu = 6 (e^2/h)$ | 0,24 | - |
| $\nu = -6 (e^2/h)$ | 0,26 | 0,15 |

The values on the $\nu = \pm 2$ plateaus are close to the theoretical prediction of a universal value for σ_{xx}^0 and measured values in 2 DEG: $\sigma_{xx}^0 \sim 2e^2/h$ for $\nu = 2, 3, 4$ in ref [85]; whereas for the $\nu = \pm 6$ they are around 10 times lower.

8.3 Breakdown of QHE at high bias current?

We have also investigated the current dependence of the longitudinal resistance.

From the smooth evolution of the longitudinal resistance shown in Fig. 8.4, it is clear that in our sample we do not observe a sharp breakdown of the QHE (as observed in large conventional 2DEGs), but rather a smooth increase of R_{xx} . Plotting R_{xx} directly versus bias current leads us to define a characteristic current I_c above which R_{xx} starts to grow significantly as shown in figure 8.11.

Breakdown is related to transport through a higher Landau level. It varies with the size of the sample and is an avalanche effect resulting in a sharp increase in the longitudinal resistance. A smooth increase of the longitudinal resistance may be related to intra Landau levels transport via localized states. In this case the characteristic current I_c is related to the quality of the sample.

I_c was found to be of the same order for samples 1,2 and 3: a few μA on $\nu = \pm 2$. It was considerably higher in sample 4: $I_c \sim 40\mu A$. Note that compared with (real) current breakdown in conventional samples, this corresponds to a similar and even higher current density of several A/m. It is however difficult to make a direct comparison without a precise criterion.

We emphasize that the sharp breakdown in 2DEGs will be more difficult to observe in graphene than in conventional 2DEGs because the mechanism involves a transition between LLs and the gaps in Graphene are much higher. On the other hand, for a mechanism involving only intra Landau level process, the size of the Landau states, localized or not, is much the same so that one might expect the transport within the Landau level should be similar. Also, as was mentioned in section 3.10.3, the small size of our sample may also explain the fact that breakdown was not observable.

In sample 4 the critical current was around 10 times higher than in the others, a difference that we can attribute to a better mobility. We shall see in what follows that the localized states in this sample are around 10 times smaller than in sample 3 which confirms the better quality of sample 4.

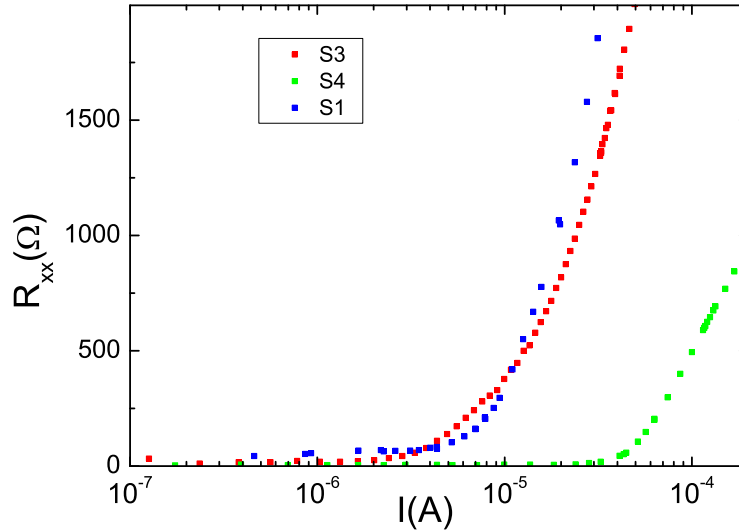


Figure 8.11: R_{xx} as a function of the bias current at the center of the $\nu = -2$ plateau at 16,5 Tesla for sample 1 and 3 at 4,2K and for sample 4 at 1,6K

8.4 Low energy transport, Mott or Efros-Shklovskii variable range hopping?

It is generally accepted that transport occurs via phonon assisted inelastic transitions between localized states, the so-called variable range hopping mechanism. For non-interacting electrons in two dimensions, the VRH Mott law gives

$$\sigma_{xx} \propto \frac{T_M}{T} \exp(-(T_M/T)^{1/3}) \quad (8.5)$$

or equivalently $\sigma_{xx} \propto (\frac{\xi}{L_M(T)})^2 \exp(-(L_M(T)/\xi)^{2/3})$, which defines the characteristic length $L(T)$ labeled as $L_M(T) = \sqrt{1/\pi g(\varepsilon_F) k_B T}$, where $g(\varepsilon)$ is the energy independent density of states at the Fermi energy. However, in the QHE regime screening is poor and Coulomb repulsion must be included. One thus enters the Efros-Shklovskii (E-S) VRH regime, where the density of states $g(E) \propto |E - E_F|$ yields

$$\sigma_{xx} \propto \frac{T_0}{T} \exp(-(T_0/T)^{1/2}) \quad (8.6)$$

or $\sigma_{xx} \propto (\frac{\xi}{L_{E-S}}) \exp(-(L_{E-S}/\xi)^{1/2})$ [87], with both the length $L_{E-S}(T) = 4\pi\varepsilon_0\varepsilon k_B T / C e^2$ and the energy $k_B T_0 = C e^2 / 4\pi\varepsilon_0\xi$ given by the Coulomb energy. $C \simeq 6.2$ is a numerical constant [149]. Measuring T_0 thus allows one to determine ξ and to probe the scaling law far from the conductance peaks. Still in the same regime, passing a current I through the sample while keeping a fixed low temperature gives an E-S VRH like law for σ_{xx} where the current plays the role of the temperature. This is the P-S model [90] which uses the effective electronic temperature $k_B T \rightarrow e E_H \xi / 2$ where the local Hall electric field E_H is proportional to the current I . This leads to

$$\sigma_{xx} \propto \exp(-((E_0/E_H)^{1/2})) \quad (8.7)$$

and

$$\sigma_{xx} \propto \exp(-((E_1/E_H)^{1/3})) \quad (8.8)$$

for E-S and Mott's VRH respectively.

8.4.1 Variable range hopping with temperature

So far, according to the literature on quantum Hall effect in 2DEGs, only E-S VRH has been observed. In graphene it is also expected as the leading mechanism for backscattering at low energy.

$$\rho_{xx} = \frac{A}{T} \exp\left(-\left(\frac{T_0}{T}\right)^{1/2}\right) \quad (8.9)$$

Indeed we observed that the evolution of ρ_{xx} with temperature is well described by E-S VRH law on the Hall plateaus at high magnetic field.

Figure 8.5 illustrates that fact. One can clearly see that below 100K ($\sqrt{1/T} > 0.1K^{-1/2}$), $\rho_{xx} \propto 1/T \exp(-\sqrt{T_0/T})$. The same type of behavior is found on other plateaus ($\nu = +2, \pm 6, \pm 10$).

From these fits we can extract T_0 which is related to the localization length via

$$\xi(\nu) = \frac{C e^2}{4\pi\epsilon\epsilon_0 k_B T_0(\nu)} \quad (8.10)$$

$T_0^{1/2}$ is plotted as a function of the filling factor on fig 8.12 for different magnetic fields.

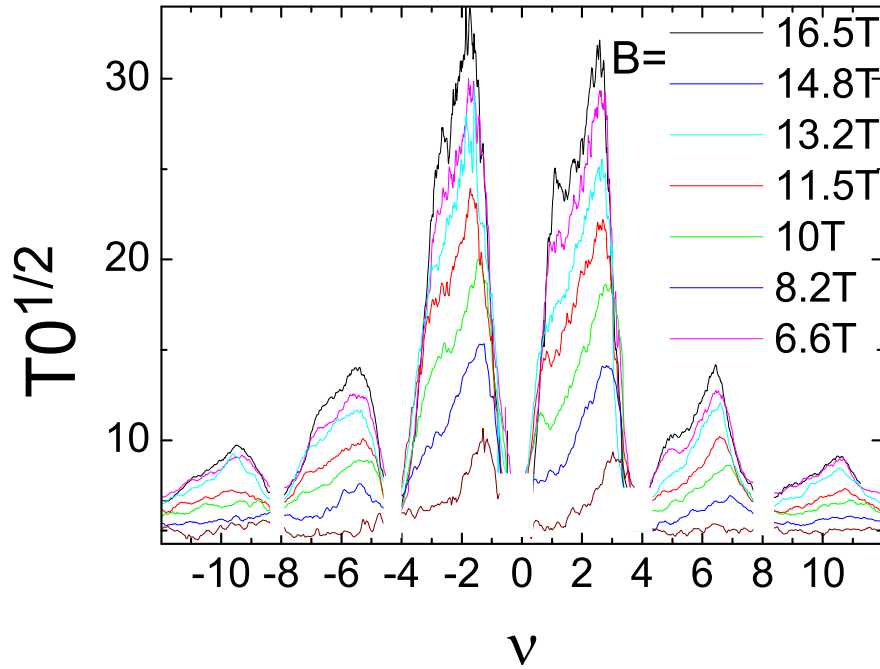


Figure 8.12: Square root of E-S VRH temperature T_0 versus filling factor for sample S3 at different magnetic fields ranging from 6.6T to 16.5T.

The extracted localization length ξ is plotted on figure 8.13.

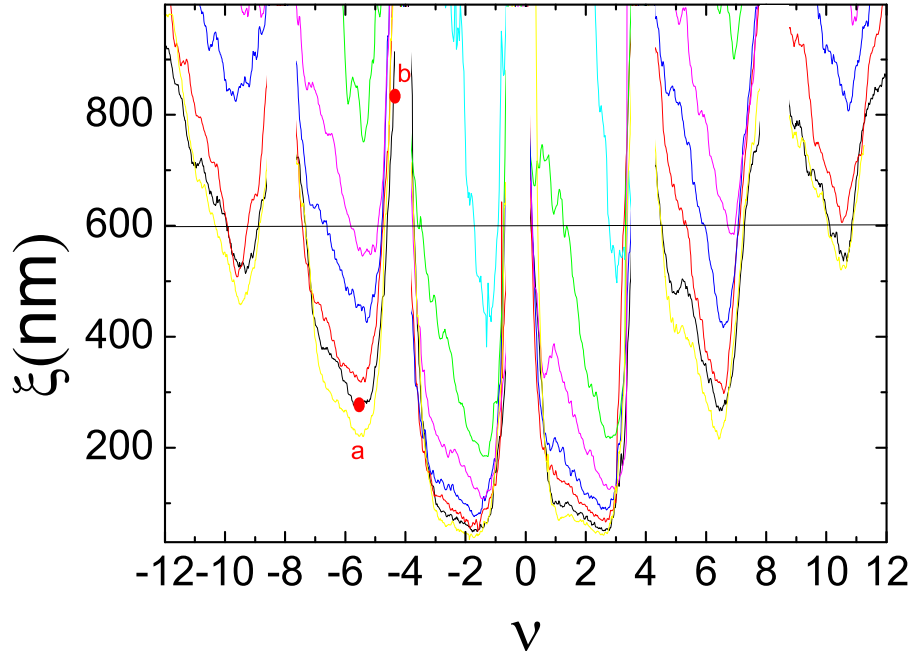


Figure 8.13: Localization length versus filling factor for S3 for different magnetic fields. The horizontal solid line $\xi = 600\text{nm}$ shows the limit above which the screening of interactions by the gate begins to play a role. (a and b points are the location of curves extracted in fig 8.15)

We see that there are maxima on the filling factor $\nu = \pm 2, \pm 6, \pm 10$. The maxima of T_0 correspond to minima of localization length ξ , we will call it ξ_{min} .

Figure 8.14 represents ξ_{min} as a function of the filling factor for different magnetic fields. The solid line curves correspond to the magnetic length, we can see that with the sample 3 we get $\xi_{min} \sim 40\text{nm}$ for $\nu = \pm 2$ which is around seven times larger than the magnetic length l_B whereas in sample 4 we find a smaller value for ξ_{min} which was of the order of l_B indicating a smaller size of localized states due to a higher sample quality.

Data measured on sample S3 are found to be very close to the value of ξ measured by tunneling spectroscopy measurement in ref [68] but are quite smaller than those of ref [75].

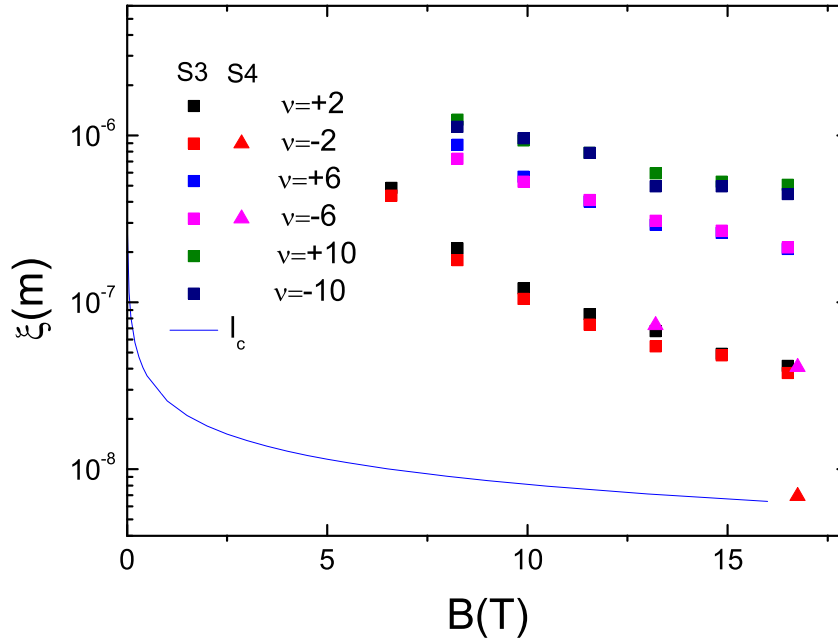


Figure 8.14: ξ_{min} as a function of the magnetic field. Squares are for sample S3 and triangles S4. The solid curve is for the magnetic length l_c .

Far from the center of the plateau or at lower magnetic fields the E-S law does not fit ρ_{xx} so well, as shown on fig 8.15. Indeed, as we saw in 3.10.2.2, Aleiner and Shklovskii have predicted that in gated 2DEG, due to the gate screening of the electronic interaction (as described in section 3.10.2.2) Mott's VRH is observable when ξ is larger than the screening distance. As the gate is $d = 300nm$ distant from the graphene the electronic interactions are screened for $\xi \gg 2d = 600nm$ ($2d$ represents the distance of image charges).

On fig 8.13, the horizontal line at $\xi = 600nm$ denotes the E-S to Mott VRH cross over. On fig 8.15 ρ_{xx} is plotted as a function of the temperature for different filling factors around $\nu = 6$, the curves corresponding to filling factors away from $\nu = 6$ and corresponding to $\xi \sim 800nm$ do not exhibit E-S VRH behavior (i.e. a linear variation when plotted in log scale as a function of $\sqrt{1/T}$) but they are well fitted by Mott's law. An example of Mott VRH fitting is displayed for the $\nu = -4.32$ curve.

This is the first evidence for the existence of a cross-over from the E-S to the Mott VRH regime in a system showing the Quantum Hall effect. But this is not sufficient to show it unambiguously. One other clear sign of Mott's VRH can be found by the dependence of the width of the ρ_{xx} peak on temperature and on bias current, according to the scaling laws of quantum localization as

will be shown below.

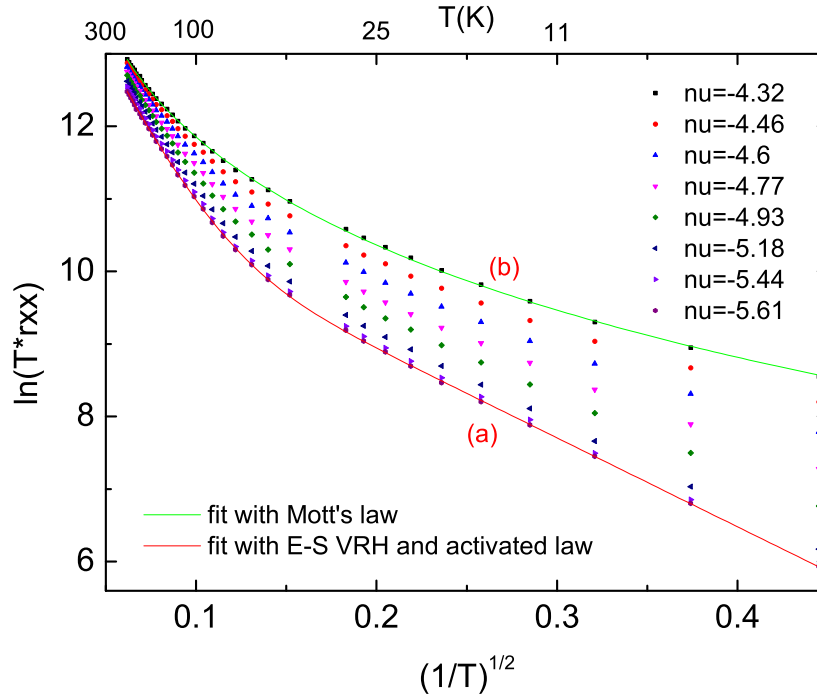


Figure 8.15: Different curves of ρ_{xx} as a function of the temperature around $\nu = -6$. The lower curves show the E-S VRH law, the upper curves clearly fit a Mott VRH law, i.e. the Coulomb interaction is screened. The localization of a and b curves can be visualized on fig. 8.13.

8.4.1.1 VRH observation under large bias currents

Poliakov and Shklovskii predict that in the VRH regime a bias current should act as an effective temperature T_{eff} (see 3.10.2.2) by tilting the Hall potential across the sample.

$$k_B T_{eff}(I) = e\xi \frac{\rho_{xy} I}{2\alpha L_y} \quad (8.11)$$

where I is the current L_y the width of the sample and α a numerical coefficient depending on the profile of the potential decrease in the sample.

Thus the longitudinal transport should obey the same VRH law with the real temperature replaced by this effective temperature. The VRH result may then be rewritten in the form:

$$\rho_{xx} = \rho_0 \exp\left(-\left(\frac{I_0}{I}\right)^{1/2}\right) \quad (8.12)$$

Where: $I_0 = \frac{2k_B T_0 \alpha L_y}{e \xi \rho_{xy}}$

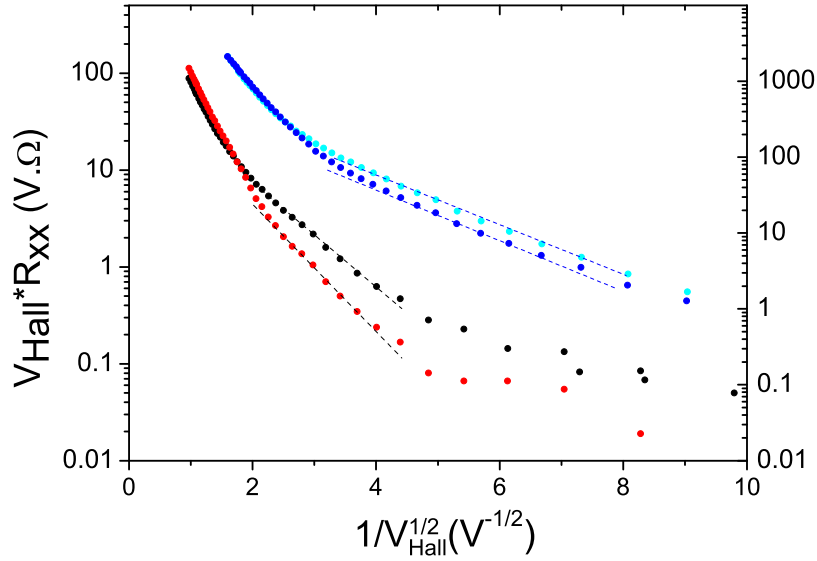


Figure 8.16: $V_{Hall} * R_{xx}$ as a function of $\sqrt{1/V_{Hall}}$ on sample 3 for $B=16,5$ Tesla at 4,2K. Black and red curves are for $\nu = 2$ and $\nu = -2$ (the y scale for these curves is on the right). Blue curves are for $\nu = \pm 6$ (corresponding scale on the left). Here, as for the figure in temperature (8.5), we can clearly see the ES-VRH behavior of these curves. For $\nu = 2$, ρ_{xx} saturates at the lower bias current. Dashed lines are straight lines showing VRH part.

Figure 8.16 shows plot of $V_{Hall} \cdot R_{xx}$ as a function of $1/V_{Hall}^{1/2}$ on $\nu = -2$ at 16.5 Tesla for sample 3 at 4.2K. On this plot, as for the temperature plot, we can see a linear part on the curves with bias current which is a sign of ES VRH. On the $\nu = \pm 6$ curves, however, we can distinguish 2 parts: the VRH part and the activated one, whereas on $\nu = \pm 2$ there are 3 parts, the first one at low bias current corresponds to the saturation of the variation of ρ_{xx} with bias current and the two others are the same as for $\nu = \pm 6$. This saturation can be due to the higher probability of a hopping due to temperature at 4.2K or to hopping distance longer than the sample width.

Compared with the similar previous study of VRH transport where the temperature was varied, it is more difficult to make automatic fits to the data. Here the longitudinal resistance saturates below a certain bias current which depends

on filling factor because the true parameter here is $V_{Hall} = I.R_{Hall}$ which varies with filling factor. At high magnetic field, however, it was possible to get some meaningful fit parameters like those shown on figure 8.17.

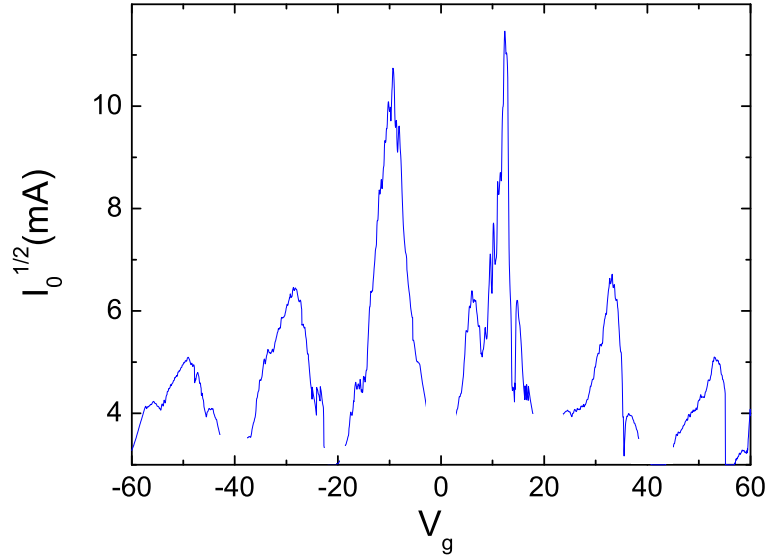


Figure 8.17: I_0 resulting from the fitting of ρ_{xx} as a function of bias current on S3.

Comparing Eq.8.9 and 8.12 we can write $(\frac{E_{H0}}{E_H})^{\beta_1} = (\frac{T_0}{T})^{\beta_2} + k$ where $k = \ln(\rho_0^I/\rho_0^T)$ is a constant and E_H is the Hall field. If E-S VRH law is obeyed for bias current one should see $\beta_1 = \beta_2 = 1/2$. In order to check this, we define the effective temperature $T_{eff}(I)$ such that $\rho_{xx}(I) = \rho_{xx}(T_{eff})$. On Fig.8.18, T_{eff} is shown as a function of the bias current on a log-log plot for $\nu = \pm 2, \pm 6$. It is clear that below 100K (no thermal activation) $T_{eff} \propto I$ showing that $\beta_1 = \beta_2$ and a VRH like law for current is well obeyed by σ_{xx} . Normally T_{eff} should start at 4K, however this effective temperature is possible to extract only when ρ_{xx} varies with the temperature and at the center of the plateau, we saw previously that the variation of ρ_{xx} saturates for the lower temperature curves.

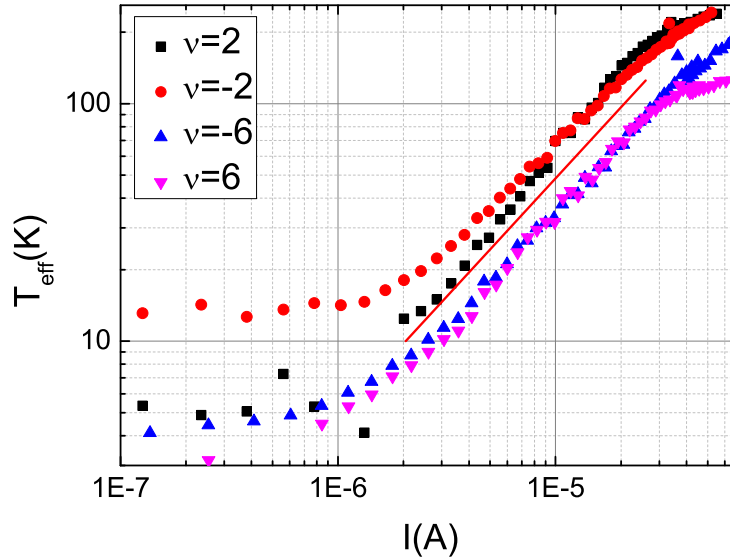


Figure 8.18: Effective temperature for sample S3 at $B=16,5$ Tesla for different integer filling factors. The red line shows a power 1 slope.

Here, we emphasize that bias current is not inducing thermal heating by joule effect in the VRH part, but it tilts the Hall plateaus inducing hopping in the Landau level. The power law of T_{eff} as a function of the current I is different on the resistivity peak or in activated part where homogeneous joule heating is more likely to appear in the sample due to a higher ρ_{xx} . An example of these different power laws is shown on fig. 8.19 which is a plot similar those in fig. 8.18 but not at the center of the plateau when activated temperature is a bit lower, allowing us to see clearly both regions.

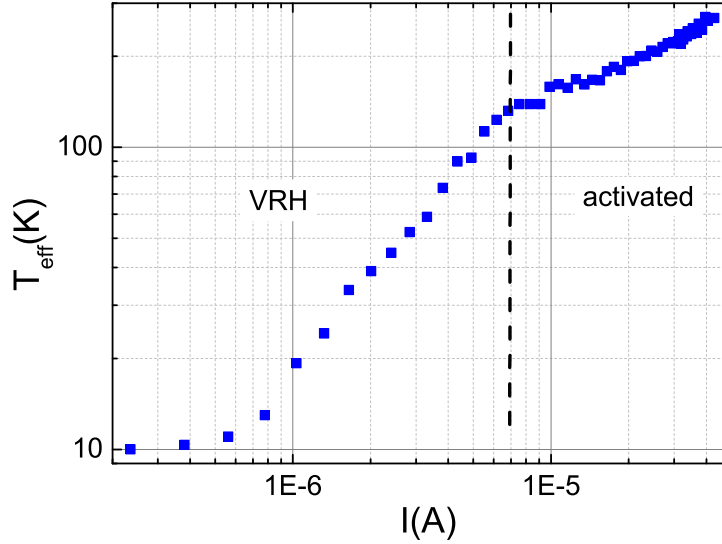


Figure 8.19: Effective temperature for sample S3 at $B=16,5$ Tesla on the plateau $\nu = -2$ away from the center. The VRH part shows a power 1 slope whereas the activated part shows a power 0.4 slope.

Recalling

$$k_B T_{eff}(I) = e\xi \frac{\rho_{xy} I}{2\alpha L_y} \quad (8.13)$$

it is interesting to compare the value of α obtained from the value of T_{eff} and from the values of the fitting parameters I_0 and T_0 where the same relation can be applied:

| | $\nu = 2$ | $\nu = -2$ | $\nu = 6$ | $\nu = -6$ |
|---------------------------------------|-----------|------------|-----------|------------|
| α from ES-VRH fitting | 6,1 | 8,45 | 2,1 | 2,2 |
| α from T_{eff} extrapolation | 5,6 | 5,1 | 1,5 | 1,5 |

The results of the extrapolation and the comparison between the value of I_0 and T_0 (which are the fitting parameters of VRH with bias current and temperature) lead to $5 < \alpha < 9$ for $\nu = \pm 2$ and $1,5 < \alpha < 2,2$ for $\nu = \pm 6$. We can interpret this result by recalling the discussion of section 3.10.4 about the Hall field distribution. This distribution is not uniform across the sample: as sketched on figure 8.20, the variation of the Hall field is fast on the edges of the sample and slower in between. The region limiting the conductivity is that of the hopping conductivity, i.e. at the center of the sample where Hall field is small. Thus the VRH energy is given by an effective energy proportional to the potential $V_{eff} = V_H/\alpha$.

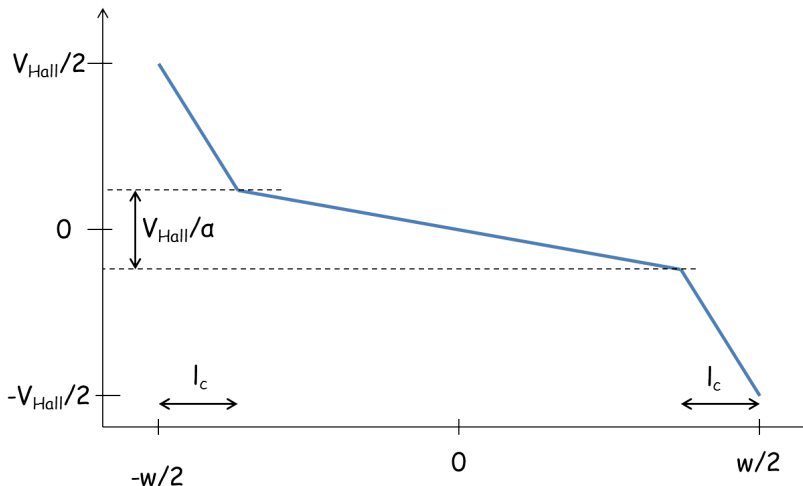


Figure 8.20: schematic of the Hall potential decrease across the sample

8.5 Universal laws in QHE

Probing the localization scaling law for large localization length requires understanding the conduction mechanism close to the conductance peaks, in the plateau transition region where the Fermi level approaches an unperturbed LL. Historically, the first conduction mechanism proposed for conductance peaks was a metallic regime. The Pruisken model [114] sets the characteristic length $L(T)$ as the phase coherence length $L_\phi(T) = (D\tau_\phi)^{1/2}$. Here D is a diffusion constant and the phase coherence time $\tau_\phi \propto T^{-p}$ follows a non-universal power law with T ($p = 2$ accounts for most observations). The localization scaling exponent γ can be indirectly accessed by the temperature dependence of the Full Width at Half Maximum (FWHM) $\Delta\nu$ of the conductance peaks. The latter is obtained when $\xi(\Delta\nu/2) \simeq L_\phi(T)$ giving $\Delta\nu = (T/T_1)^\kappa$ with the non universal exponent $\kappa = p/2\gamma$. However Polyakov and Shklovskii proposed that the VRH regime should last in the plateau transition region and the FWHM obtained from $\xi(\Delta\nu/2) \simeq L_{E-S}(T)$ (or $T \simeq T_0$) giving $\Delta\nu = (T/T_1)^\kappa$ and the now universal $\kappa = 1/\gamma$. Here $k_B T_1 = Ae^2/4\pi\epsilon\epsilon_0\xi$ with A a numerical constant. Similarly, the dependence of the FWHM with bias current using P-S model is $\Delta\nu = (I/I_1)^\mu$ with $\mu = 1/2\gamma = \kappa/2$ while using the phase coherence length approach $\mu = p/4\gamma$. As we saw in chapter 3, $p = 2$ is a reasonable exponent for τ_ϕ , thus the scaling law of the FWHM with temperature cannot discriminate between the two scenarii nor that with bias current.

A further criterion is thus needed to discriminate between the two scenarios, and that is addressed experimentally here. The idea originates from the Aleiner Shklovskii (A-S) [98] prediction that a cross-over from E-S to Mott VRH occurs when interactions are screened, for example by a gate parallel to the 2DEG at a

distance d . This requires $\xi > 2d$ which is likely to occur on conductance peaks for sample size $\gg 2d$. In the Mott VRH regime the FWHM conductance peak now becomes $\Delta\nu \propto (T/T_2)^\kappa$ with $\kappa = 1/2\gamma$ and $\Delta\nu \propto (I/I_1)^\mu$ with $\mu = 1/3\gamma$. On the contrary in the Pruisken scenario screening is not expected to impact the temperature dependence of the FWHM. This yet never observed E-S to Mott cross-over in the QH regime would definitely establish the P-S scenario, that VRH describes transport almost everywhere in the QHE regime even close to the maximum of the conductance peaks and that the phase coherence length approach is not appropriate.

Previous measurements performed in conventional 2DEGs, including Si-MOSFETs, and InAs/InGAAs or GaAs/AlGAAs heterojunctions have been able to probe the localization length scaling exponent of ξ (described in section 3.9.1). Experiments using direct determination of ξ from the E-S VRH [73] and even more directly by geometrical comparison with sample width [118] have given $\gamma \simeq 2.3$. Probing the scaling law using the conductance peak width is less direct and showed a dispersion in the extracted values of κ . Works combining temperature and bias current have shown excellent agreement with the P-S model [74, 73, 77, 118]. Recently the scaling law has been studied in Graphene using temperature, but no current bias study was done [75]. Except on the $n = 0$ LL level the results were found compatible with $\gamma = 2.3$.

8.5.1 Universal localization length scaling exponents

As discussed in section 3.9.1, the transition between two Hall plateaus occurs when the Fermi level lies in the middle of a disorder energy broadened LL. For an infinite size sample, the localized state size ξ diverges at a single energy $E_c \approx E_n$ resulting in backscattering and a longitudinal conductance peak. According to the quantum localization theory [122] $\xi \sim |E - E_c|^{-\gamma} \sim |\nu - \nu_c|^{-\gamma}$ with $\gamma \simeq 7/3$, a value confirmed in many experiments on conventional 2DEGs [116, 73]. The better agreement was obtained when extracting $\xi(\nu)$ from $T_0(\nu)$ or with direct geometrical comparison of ξ with the sample width.

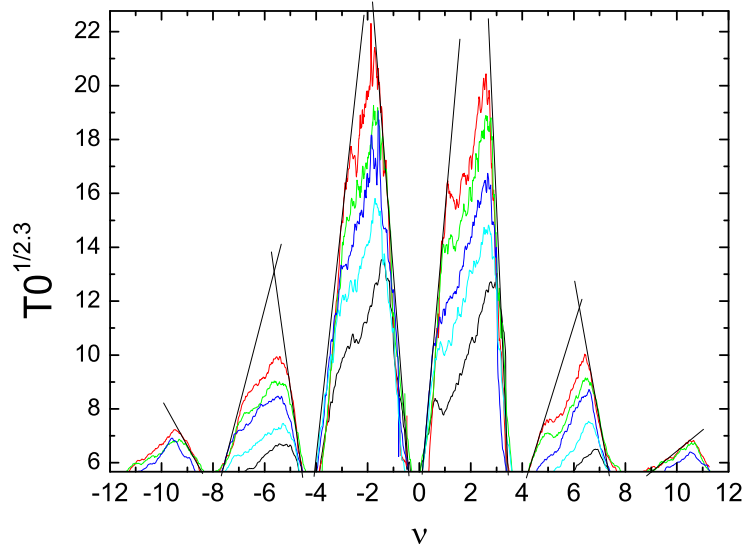


Figure 8.21: Efros-Shklovskii temperature T_0 to the power $1/2,3$ plotted as a function of the filling factor for magnetic fields ranging from 10 to 16,5 Tesla. Lines have been added to show that the expected universal exponent $\gamma = 2.3$ is qualitatively observed here.

The plot of Figure 8.21 shows that our results are in good agreement with a universal behavior of the localization length exponent $\gamma = 2.3$ for transition between $\nu = \pm 2$ and $\nu = \pm 4$, $\nu = 0$ and $\nu = \pm 2$ and also between $\nu = \pm 4$ and $\nu = \pm 6$. On this figure, the scale in $T_0^{1/2.3}$ begins at 5.7, which correspond to $\xi = 600nm$, thus only the data for ES-VRH regime appears here.

Figure 8.22, shows a plot of the ES-VRH temperature T_o (which is inversely proportional to ξ) to the power $1/2.3$ versus the deviation of filling factor from the filling factor ν_c of the metal-insulator transition. Most of the data plots seems to be linear in ν within a range of between 0,5 and 1 ν .

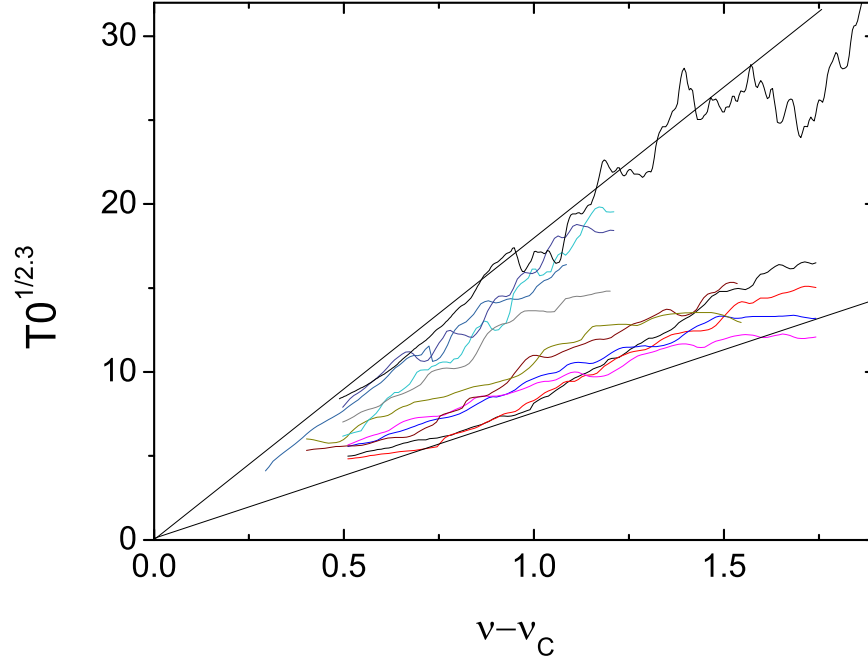


Figure 8.22: $T_0^{1/2.3}$ plotted as a function of $\nu - \nu_C$ for $\nu = [\pm 2, \pm 4]$ and $\nu = [\pm 2, 0]$ at different magnetic field, the black curve is for S4 while the other are for S3.

The transition between $\nu = \pm 6$ and $\nu = \pm 10$ shows also this universal behavior as shown in figure 8.21 at high magnetic fields, albeit a little bit less clearly.

8.6 Transition between Hall plateaus: Evidence for a Universal Regime driven by VRH

As we saw in 3.10.5 the full width at half maximum (FWHM) of the ρ_{xx} peak is also predicted to follow a universal law such as:

$$\Delta\nu = (T/T_1)^\mu \quad (8.14)$$

$$\Delta\nu = (J/J_1)^{\mu'} \quad (8.15)$$

Two theories describe the metal insulator transition: the Pruisken and the Poliakov-Shklovskii theories, Although it is not possible to discriminate between

CHAPTER 8. MECHANISM OF THE DISAPPEARANCE OF THE QHE
AT FINITE ENERGY

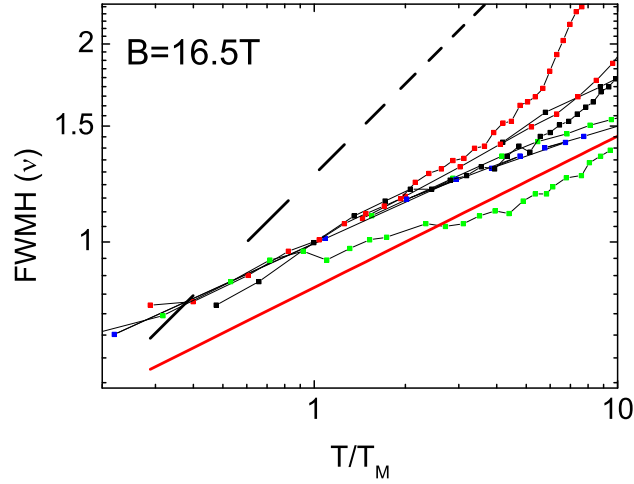
them for ES-VRH transport, it becomes possible for Mott VRH for which the two theories predict different universal laws.

We recall the exponents predicted by the two scenarios:

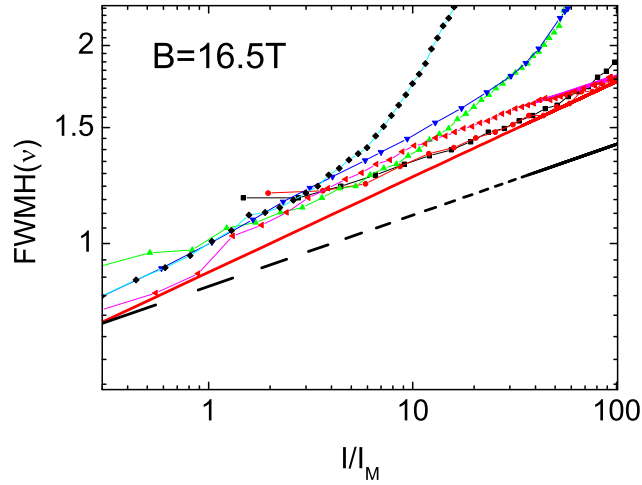
| Theory | Pruisken | P-S | |
|------------------|-------------|-------------|-------------|
| Transport regime | all | E-S VRH | Mott' VRH |
| μ | $p/2\gamma$ | $1/\gamma$ | $1/2\gamma$ |
| μ' | $p/4\gamma$ | $1/2\gamma$ | $1/3\gamma$ |

Where p is non universal and equal to 2 in most of the experiments.

Our data on figure 8.23 on S3 and S4 show clearly that the widths of the ρ_{xx} peaks follow universal laws. The FWHM of ρ_{xx} as a function of the temperature is plotted in figure 8.23a and the width is plotted as a function of bias current in figure 8.23b .



(a) Log-log plot of FWHM of ρ_{xx} as a function of the temperature at B=16,5 Tesla



(b) Log-log plot of FWHM of ρ_{xx} as a function of the bias current at B=16,5 Tesla

Figure 8.23: On both figures blue curves are for the peaks between $\nu = \pm 10$ and ± 6 , denoted $[\pm 10, \pm 6]$, green curves are for $\nu = [\pm 6, \pm 2]$ and red are for $\nu = [-2, +2]$ (Dirac point). Squares are for S3 and triangles are for S4. The black straight lines correspond to the expected exponents for E-S or Pruisken's (with $p=2$) law, the red lines correspond to the one for Mott law.

The exponents found from our analysis are $\mu = 0.21 \pm 0.02$ and $\mu' = 0.13 \pm 0.01$, these are in good agreement with Mott's VRH. This is consistent with Aleiner and Shklovskii prediction and with our supposition in 8.4. Also it is a supplementary proof of the validity of the VRH theory and it allows us to discriminate between two much debated scenarios.

Here it is important to mention that we do not observe any substantial difference between the plateau transitions on the electron and hole sides and passing the Dirac point itself. As it is possible to see on figure 6.19, the degeneracy was not lifted in our samples and it was not possible to observe the quantum Hall state at $\nu = 0$. Also as shown on figure 8.1, we do not observe any insulating behavior at the Dirac point for all our samples as was observed by some groups (references and description in section 3.8.5.1).

It would have been interesting to check if only the E-S VRH law was followed in sample 2 which was side gated (implying no screening by the back gate). Unfortunately only data near the center of the $\nu = 6$ plateau was taken on this sample and we cannot conclude anything on the non-observation of a crossover from ES to Mott VRH.

8.7 Conclusion

We have revisited quantum localization in the quantum Hall effect using graphene. Graphene brings several new features: first of all it is a different system than conventional 2DEGs where the preceding studies of localization took place thus it is very interesting to observe if the universal laws observed in conventional 2DEGs will pertain. The main difference between graphene and conventional 2DEGs are the energy scales, the VRH hopping is similar in both system whereas the Dirac nature of the charge carriers leads to a much higher cyclotron energy in graphene. Thus a larger range in energy is available for measuring localization effects. Also, most of the time graphene is backgated allowing the screening of the electronic interactions.

In our study, the standard localization length scaling was found for all studied Landau levels including the Dirac point, confirming the universality of the previous observation in 2DEGs.

The most important result is the observation of the cross-over between Mott and E-S Variable range hopping in the study of ρ_{xx} with temperature for all filling factors from $\nu = -10$ to $\nu = 10$ and the width of the ρ_{xx} peak. This cross-over is provided by the back gate which screens the Coulomb interactions. These observations allow one to discriminate between two scenarii for the plateau to plateau transition, the Poliakov Shklovskii scenario based on the variable range hopping and the Pruisken one based on a metal-insulator transition.

Chapter 9

Conclusion

9.1 Conclusion

In this manuscript is presented an experimental study of electronic transport in graphene. It describes all the steps from the fabrication of graphene samples to electronic transport measurement. The transport in quantum Hall regime was particularly studied in this work.

As study of graphene was a starting project in the group, fabrication of graphene and some adapted tools had to be adapted in our laboratory.

Fabrication of graphene samples with a mobility between 1000 and 10000 $cm^2.V^{-1}.s^{-1}$ has been done using conventional exfoliation method set by K.Novoselov with scotch tape.

A cryogenic insert was design and built with adapted capacity for graphene measurement such as the possibility of varying the temperature from 1K to 450K when the insert is in liquid helium.

Basic electronic transport measurement such as zero field conductivity or quantum Hall effect have been done to confirm the results of other groups, they allowed the observation of graphene particular properties and confirmation of good samples quality.

Transport time τ_e and the scattering time τ_{tr} had been measured in collaboration with H.Bouchiat's group. The ratio τ_{tr}/τ_e was found to be on the order of 2 and independent of k_F , indicating that the dominant scatterers at 0 magnetic field are small neutral impurities. These results are confirmed by the fitting of the zero field conductivity with a resonant neutral impurity model.

The main work of this thesis has been to study of transport in the quantum Hall effect using graphene. For a temperature inducing an energy comparable

to Landau level spacing, activated law was found to drive the values of ρ_{xx} . The comparison between cyclotron gaps predicts by Dirac's equation and measured gaps gave us information about the density and potential fluctuations. The ratio of the density fluctuations over the potential fluctuations linked to the screening of electrons in Landau levels, which is supposed to be low when Fermi levels lies between Landau levels, was found to be larger on the $\nu = \pm 2$ plateaus than in other plateaus. This ratio was also found to differ from electrons to holes, indicating that charged impurities played a relevant role here. However this interpretation is done with results of one sample and would need other measurement to be claimed with certainty.

At lower temperature, the transport across the sample limiting the QHE was found to obey Efros-Shklovskii Variable range hopping law on large domains of filling factors around the center of the Hall plateaus, fitting data with this law allows us to extract the localization length; this length was found to diverge near the transition plateau to plateau, following the universal exponent of quantum percolation as it was previously observed in conventional 2DEGs: $\xi(\nu) = \xi(\nu - \nu_c)^{-\gamma}$ with $\gamma = 2, .3$. The large size of localized states compared to the size of defects limiting the zero field mobility and the asymmetry between electrons and holes seem to point the charged impurities as responsible of localized states in QHE.

ES VRH law was also found to govern the values of ρ_{xx} with increasing bias current confirming Poliakov-Shklovskii prediction describing the bias current as an effective temperature. The comparison of the characteristic values of the current to the one of temperature leads to suppose that the Hall potential variation was around 5 times larger near the edge than is the bulk of the sample on the plateaus at $\nu = \pm 2$.

Finally the major result of this work is the observation of the cross-over between Mott and E-S Variable range hopping conduction when the localization length exceed 2 times the distance from graphene to the screening gate. The width of the ρ_{xx} peak where ξ is the larger was found to be well described by Mott's law. These observations allow to discriminate between two scenarii for the plateau to plateau transition, the Poliakov-Shklovskii scenario based on the variable range hopping and the Pruisken one based on a metal-insulator transition.

Part III
Appendix

Chapter 10

Variable temperature insert

In order to make the electronic measurements we built a variable temperature insert for placing the sample in the bore of the liquid helium cooled 20 Tesla superconducting magnet. The construction was largely carried out by Patrice Jacques, the technician of our group.

The insert is made to control sample temperature between 1.6 K and room temperature. intermediate between helium bath at 4.2K in a cryostat (describe later in this chapter) and the room. The temperatures from 4.2K to 1.6K are attained by evaporation of a stream of liquid helium drawn from the magnet Dewar bath.

The requirements needed for the graphene measurements are:

- lowest temperature of 1.6K with He^4 from the Dewar Helium liquid bath. For quantum Hall effect in graphene we do not need very low temperatures.
- upper temperature of 450K when the fridge is in liquid helium to be able to clean the sample in a cryogenic vacuum (see 6.1).
- ultra high (cryogenic) vacuum.
- restricted outer diameter to fit 30 mm magnet bore.
- at least 14 measurement and control wires thermalized to the lowest temperature
- ability to implement for high frequency measurement.

10.1 Remarks on thermal exchanges in a solid

Here the main mechanisms providing heat exchange will be presented. This was a very important point for the conception of the insert.

The heat transfer is expressed by the Fourier relation:

$$\dot{Q} = \frac{A}{L} \int_{T_2}^{T_1} \kappa(T) dT$$

κ is the thermal conductivity.

There are two main mechanisms contributing to the thermal conductivity in solids:

- the phonons (vibrating mode of the lattice)
- the electrons

In metals, electronic contribution is 2 to 3 magnitudes higher, so we can consider solely this contribution whereas in insulating materials phonons are the only mechanism of heat transport.

10.1.1 Phonons

A general expression for the thermal conductivity due to phonons is similar to that of a perfect gas:

$$\kappa(T) = \frac{1}{3} C_v c l = \frac{1}{3} C_v c^2 \tau$$

This is an approximation for monoatomic Bravais lattice, where the phonon spectrum is uniquely constituted by acoustic branch. c is the phonon's velocity using the Debye approximation $\omega = ck$. C_v is the specific heat in the Debye approximation (for acoustic branch) $C_v = \frac{12\pi^4}{5} n k_B (\frac{T}{\Theta_D})^3$ where n is the atom number density and Θ_D is the Debye temperature treated as an empirical parameter.

l is the mean free path and τ is the time between two collisions.

Here τ is not easy to determine and the question whether it is temperature dependent or not is subtle.

We can distinguish two cases:

- High temperature when $T \gg \Theta_D$

At high temperature the number of phonons is proportional to the temperature $n_s(k) \approx \frac{k_B T}{\hbar \omega_s(k)}$. As a consequence there are more probabilities for a phonon to be scattered and τ to decrease with the temperature. Also at high temperature C_v is given by the Dulong and Petit's law and is independent of temperature. As a consequence $\kappa = \frac{1}{T^x}$ where x has a value between 1 and 2.

- low temperature when $T \ll \Theta_D$

Here $\tau \sim e^{T_0/T}$, below a certain temperature τ become exponentially long and the mean free path has to be replaced by a length linked to impurities of the lattice which is not temperature dependent. The latter leads to $\kappa \sim C_v \sim T^3$.

10.1.2 Electrons

In metals, the electronic contribution plays a major role in the thermal conductivity. The ratio for the electronic contribution to thermal conductivity (κ) to electrical conductivity (σ) is proportional to temperature T . This is expressed by the Wiedemann-Franz law (1853): $\frac{\kappa}{\sigma} = LT$ where L is a constant. $L = \frac{\pi^2}{3} \left(\frac{k_B}{e}\right)^2 = 2,44 \cdot 10^{-8} W\Omega K^{-2}$.

The electronic role in κ was supposed by Drude in order to explain originally this empirical law. Observation of much better thermal conductivity in metals than in insulators led him to speculate that the ionic contribution is less important than the electronic one in metals.

The thermal conductivity in an electron gas is expressed similarly to a perfect gas obeying Fermi-Dirac statistics: $\kappa(T) = \frac{1}{3}C_v v_F l = \frac{1}{3}C_v v_F^2 \tau$ where $v_F^2 = 2\varepsilon_F/m$ and $C_v = \frac{\pi^2}{2} \left(\frac{k_B T}{\varepsilon_F}\right) n k_B$

From Drude law: $\sigma = \frac{ne^2\tau}{m}$. L arises from the ratio $\frac{\kappa}{\sigma}$.

10.2 The cryostat

The magnet cryostat is a standard stainless steel Dewar with a superinsulated liquid nitrogen radiation shield. It is designed to hold about 40 l of liquid helium which can be cooled to the lambda point (2.2K) on pumping with a $50 m^3 h^{-1}$ vacuum pump. The helium boil-off rate is about 10 l per day. The helium constitutes the cooling bath for the 20 Tesla, 30mm bore Nb-Sn superconducting coil. The cryostat and magnet were supplied by Oxford Instruments in 1992. The variable temperature cryogenic insert containing the sample and measurement probes is introduced into the liquid helium in the magnet bore as sketched in figure 10.1

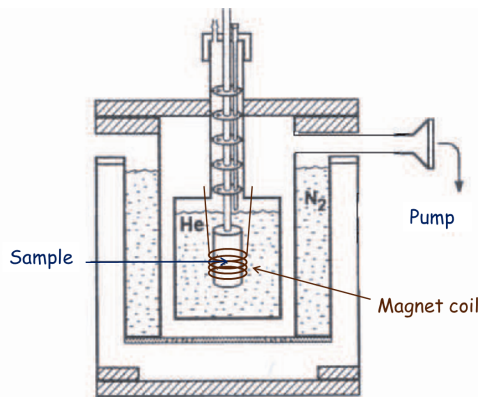


Figure 10.1: scheme of a cryostat

10.3 The insert assembly

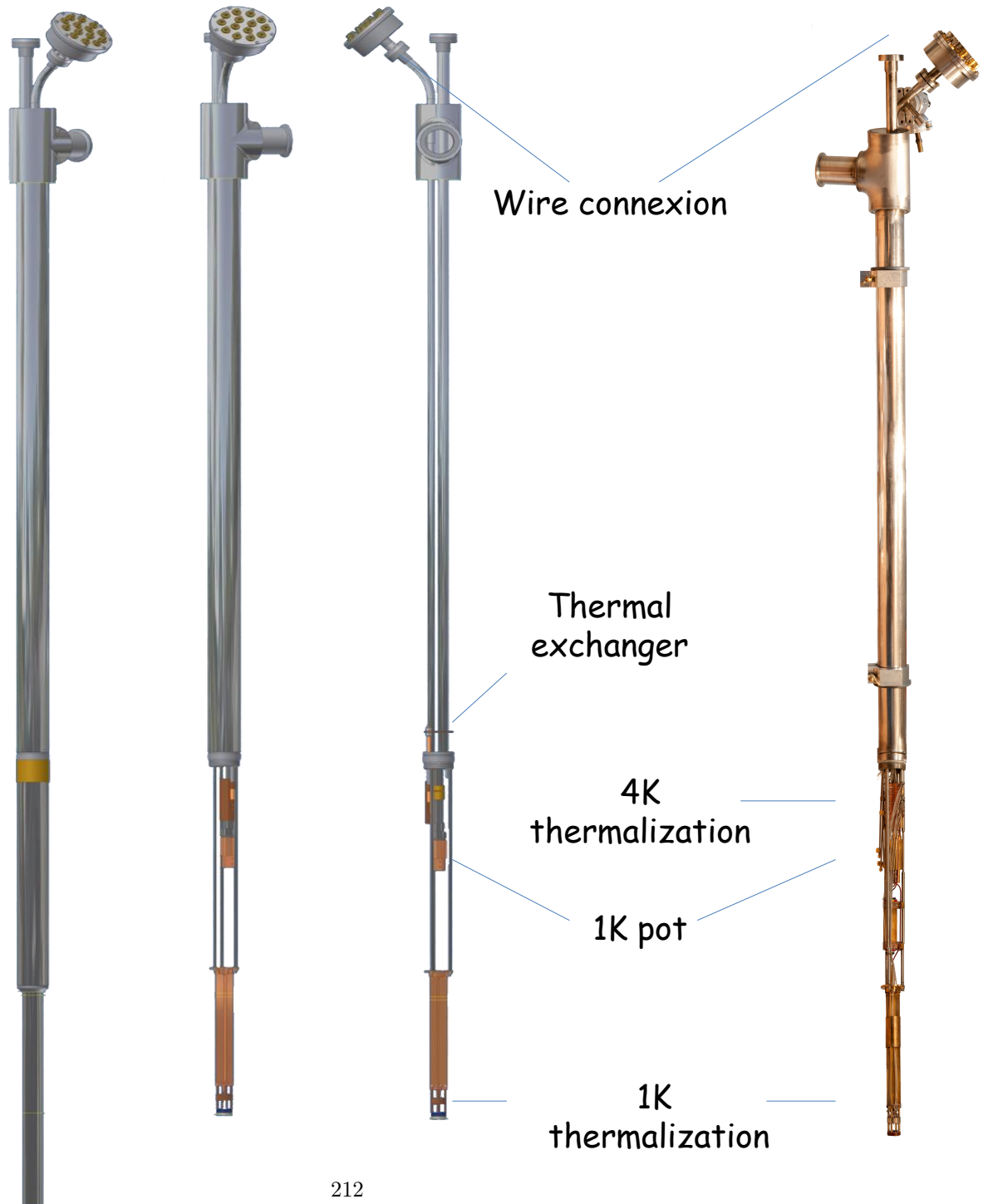


Figure 10.2: Successive unveiling of the cryogenic insert. 3D sketch of the fridge on the left, and photography of it on the last right image.

10.3.1 Bonding techniques

Metal-metal bonding is assured by TIG (Tungsten Inert Gas) electric arc welding where possible. Bonds between different metals are usually hard brased with Ag-Cu alloy in an oxy-acetylene flame. Certain joints which have to be periodically dismantled are sealed with soft Pb_Sn solder. Plastics such as Kel-F are glued to metallic substrates with epoxy (Araldite or Stycast).

10.3.2 The body

The essential constraints on the body of the insert are:

- low heat conductivity: the insert is partially immersed in liquid helium but its top part remains at room temperature . It is then wires important that the head be thermally insulated from the lower immersed part to avoid excessive evaporation of the liquid helium.
- leak tightness to be able to maintain cryogenic vacuum (10^{-10} mbar)
- robustness

Stainless steel was chosen for its low thermal conductivity, its availability in thin walled tubing, its non magnetic composition and its amenity to good TIG welds.

The main body consists of an exterior 45 mm diameter tube to fit the mouth of the magnet Dewar enveloping two smaller diameter tubes which carry the measurement and control cables. The outer tube doubles as a pumping tube for a 1K evaporation refrigerator used to cool the sample.

10.3.3 Connection head tulip

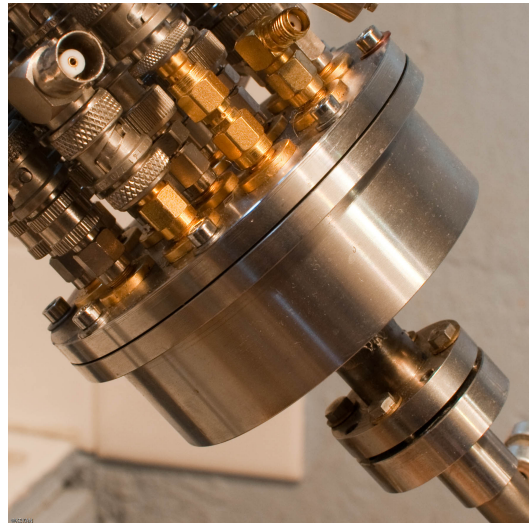


Figure 10.3: The connection head "tulip" with its 14 hermetic coaxial feed through connectors.

The tulip is made of a stainless steel cup with a hole at the bottom to allow a path for the wires and a cover with the 14 connectors. The parts are joined with indium, a heavy metal which has the particularity of being very soft. When the two parts are tighten indium vacuum seals to assure optimum electromagnetic shielding.

10.3.4 1K Pot

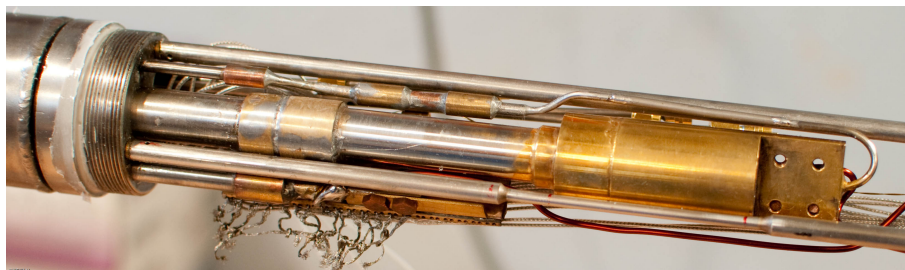


Figure 10.4: 1K Pot

The "1 K pot" is a small volume of a few cm^3 supplied with liquid helium from the magnet bath through a flow impedance and pumped by a vacuum pump for evaporative cooling. The flow impedance (compressed alumina powder

giving $20\text{ l}\cdot\text{s}^{-1}$ STP He flow with 1 bar differential) determines the maximum cooling rate while the pressure maintained by the vacuum pump determines the temperature according to the pressure-temperature characteristic of liquid helium. In our case, 1.6 K is achieved with a cooling power of 20mW.



Figure 10.5

10.3.5 thermalization of measurement wires

There are two thermalizations for this fridge, one at the helium bath temperature and the other at the 1K pot temperature.

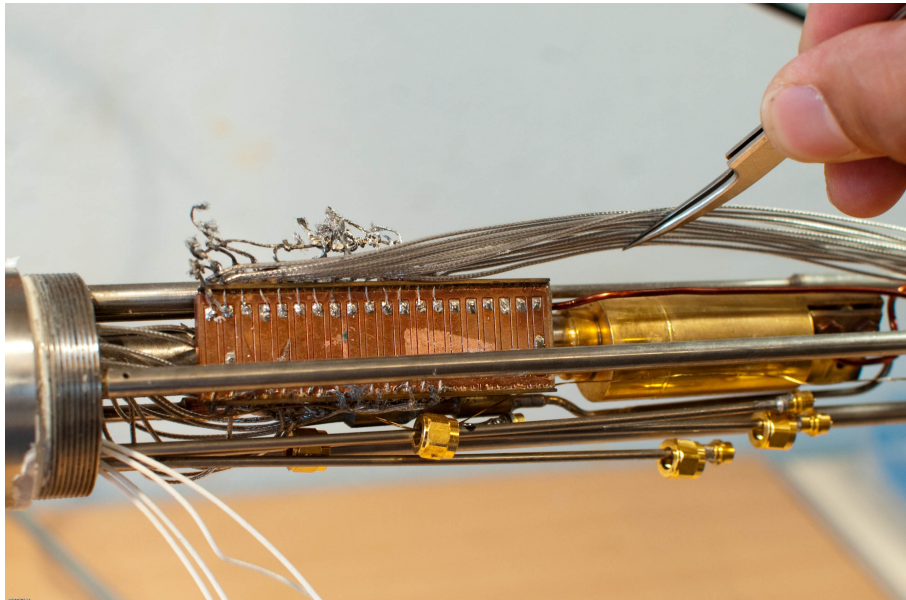


Figure 10.6: 4K thermalization

4K thermalization

the first thermalizer at 4K is composed of a copper heat exchanger in copper which is in the cold helium vapor pumped from the 1K pot. This exchanger is linked to a copper plate (see figure 10.6) where there are 16 copper tracks separated from the plate by a thin Kapton film ($50\mu m$). These tracks are 1 cm long and 2mm large, they provide a good thermalization at 4K.

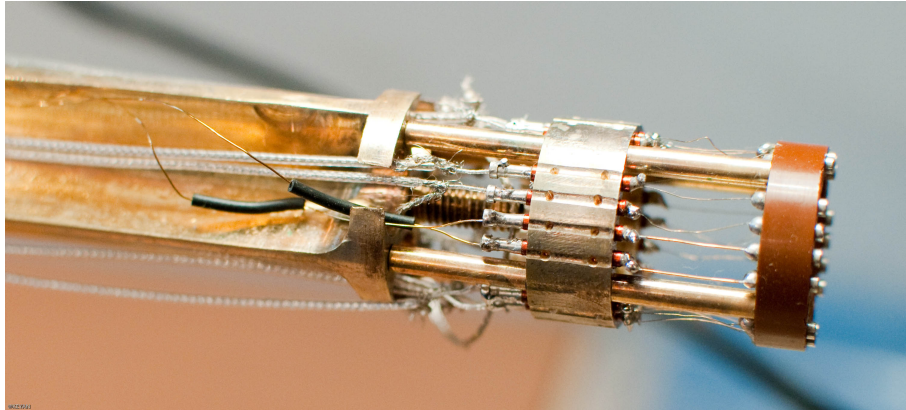


Figure 10.7: 1K thermalization

1K thermalization The second thermalization is at the bottom of the fridge, near the sample. It is a copper ring which is thermally linked to the 1K pot. 2mm copper wires pass through the material of the ring electrically insulated from it by a varnish.

Wires For the wires between the tulip and 4K thermalization and between 2 thermalizations we used lakeshore coaxial wires with a resistivity of $50\Omega.m^{-1}$

10.3.6 The sample Holder

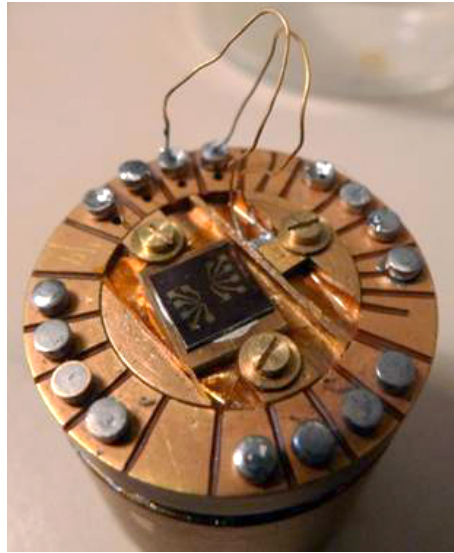


Figure 10.8: The sample holder.

The sample holder is specially adapted for our procedure for cleaning and measuring graphene in situ. graphene measurement. The constraint is to be able to heat graphene to 450K under cryogenic vacuum, imposing low thermal exchange at high temperature. At low temperature however, good thermalization is needed to ensure that the sample is at 1.6K.

It is composed of two parts: an inner piece of copper with a cylinder at the back in order to wind resistive wire for the heater. The other part is an outer ring in Kel_F.

The Kel_F ring provides insulation to the rest of the fridge when the sample is heated to 450K. The thermal contact at low temperatures is provided by the 50 μ m cold wires thermalized with the 1K pot.

10.3.7 Thermometer

The thermometer is a lakeshore model CX-1050-SD-HT-1.4M made with a Cernox resistor . This thermometer has a temperature range going from 1.4K to 420K which is perfect for our experiments.

Chapter 11

Additional measurements

We show here some measurement done on samples S1 and S2 confirming variable range hopping in our samples.

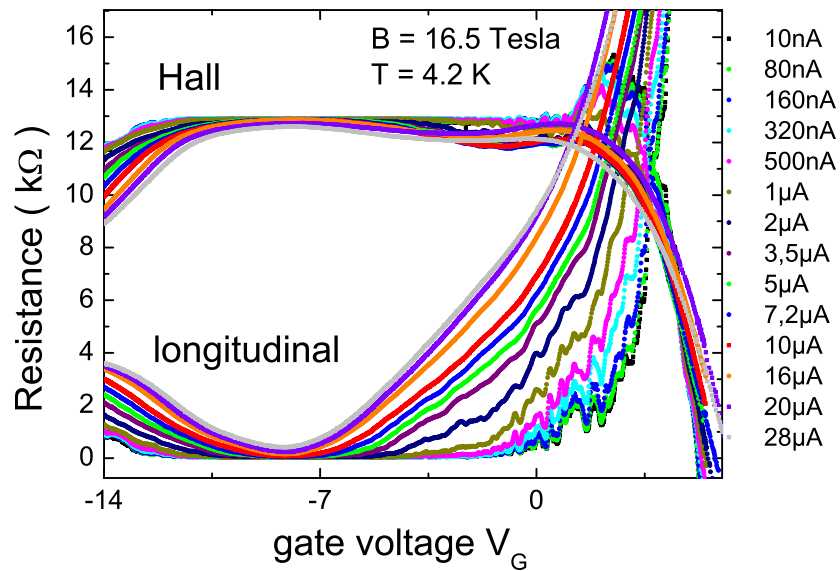


Figure 11.1: R_{xx} and R_{Hall} around $\nu = -2$ is sample S1 at $B=16,5$ Tesla, $T=4.2K$, for different bias current ranging from $10nA$ to $28\mu A$.

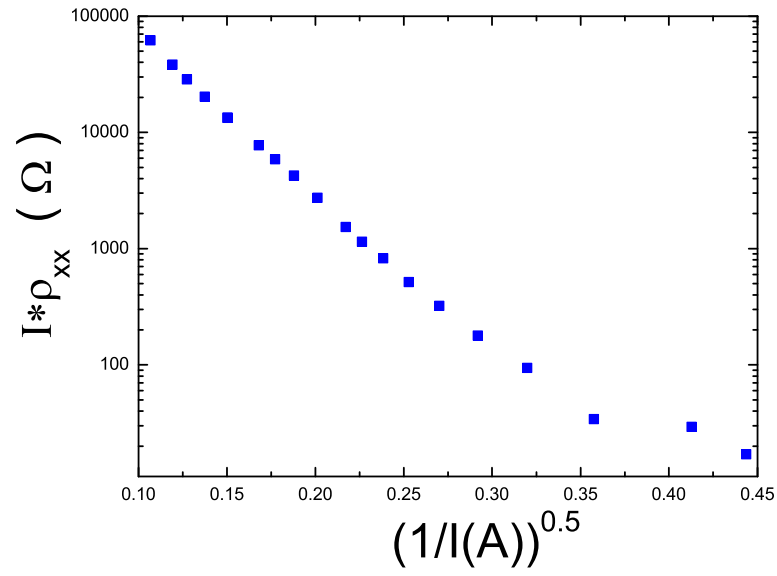


Figure 11.2: $I * \rho_{xx}$ as a function of $\sqrt{1/I}$ on the center of the plateau $\nu = -2$ on sample S1 at B=16.5 Tesla and T=4.2K. The linear behavior confirms E-S VRH law

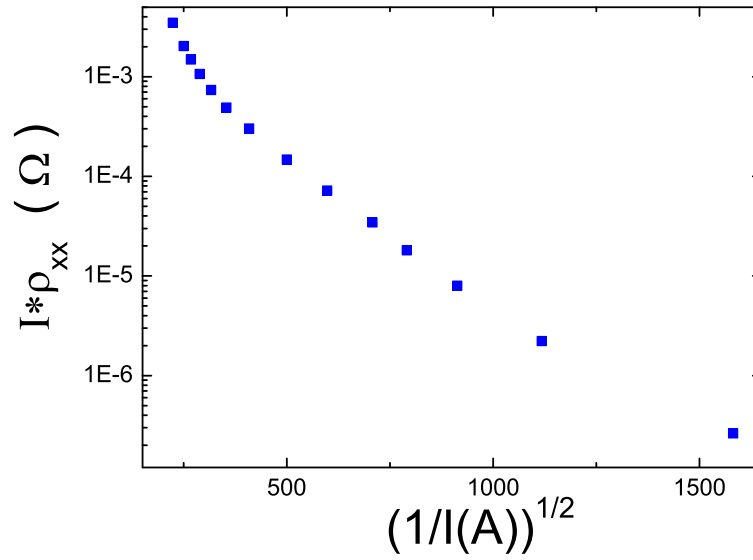


Figure 11.3: $I * \rho_{xx}$ as a function of $\sqrt{1/I}$ on the center of the plateau $\nu = 6$ on sample S2 at B=16.5 Tesla and T=4.2K. The linear behavior also confirms E-S VRH law

Bibliography

- [1] A. G. W. Cameron, “Abundances of the elements in the solar system,” *Space Science Reviews*, vol. 15, pp. 121–146, Sep 1973.
- [2] P. J. LU, N. YAO, J. F. SO, G. E. HARLOW, J. F. LU, G. F. WANG, and P. M. CHAIKIN, “The earliest use of corundum and diamond, in prehistoric china*,” *Archaeometry*, vol. 47, no. 1, pp. 1–12, 2005.
- [3] P. Schoetzenberger and L. Schoetzenberger, “Sur quelques faits relatifs a l histoire du carbone,” *CR Acad Sci Paris*, vol. 111, pp. 1774 – 1778, 1890.
- [4] L. Radushkevich and V. Lukyanovich, “O strukture ugleroda, obrazujucesja pri termiceskom razlozenii okisi ugleroda na zeleznom kontakte,” *Zurn Fisic Chim*, vol. 26, pp. 88 – 95, 1952.
- [5] M. Monthieux and V. L. Kuznetsov, “Who should be given the credit for the discovery of carbon nanotubes?,” *Carbon*, vol. 44, no. 9, pp. 1621 – 1623, 2006.
- [6] P. R. Wallace, “The band theory of graphite,” *Phys. Rev.*, vol. 71, pp. 622–634, May 1947.
- [7] S. M. D. J. Y. S. D. I. G. A. F. K.S Novoselov, A.K. Geim, “Electric field effects in atomically thin carbon films,” *SCIENCE*, vol. 306, octobre 2004.
- [8] C. Aslangul, “Applications de la mecanique quantique,” 2005. cours FIP ENS.
- [9] N. M. N.W.Ashcroft, *Physique des Solides*. EDP Science.
- [10] M. G. Jean Noel Fuchs, “Introduction to the physical properties of graphene,” 2008. cours ecole doctorale.
- [11] C. Schonberger, “Bandstructure of graphene and carbon nonotubes: An exercise in condensed matter physics,” avril 2006.
- [12] A. Bostwick, T. Ohta, T. Seyller, K. Horn, and E. Rotenberg, “Quasiparticle dynamics in graphene,” *Nat Phys*, vol. 3, pp. 36–40, Jan 2007.
- [13] A. Messiah, *Mecanique quantique*. Dunod, 1995.

BIBLIOGRAPHY

- [14] Y. Zhang, J. W. Tan, H. L. Stormer, and P. Kim, “Experimental observation of the quantum Hall effect and Berry’s phase in graphene,” *Nature*, vol. 438, pp. 201–204, 2005.
- [15] M. I. Katsnelson, K. S. Novoselov, and A. K. Geim, “Chiral tunneling and the Klein paradox in graphene,” *NATURE PHYS.*, vol. 2, p. 620, 2006.
- [16] N. Stander, B. Huard, and D. Goldhaber-Gordon, “Evidence for Klein tunneling in graphene $p - n$ junctions,” *Phys. Rev. Lett.*, vol. 102, p. 026807, Jan 2009.
- [17] A. F. Young and P. Kim, “Quantum interference and Klein tunnelling in graphene heterojunctions,” *Nat Phys*, vol. 5, pp. 222–226, Mar 2009.
- [18] E. McCann, D. S. Abergel, and V. I. Fal’ko, “The low energy electronic band structure of bilayer graphene,” *The European Physical Journal - Special Topics*, vol. 148, pp. 91–103, 2007. 10.1140/epjst/e2007-00229-1.
- [19] J. B. Oostinga, H. B. Heersche, X. Liu, A. F. Morpurgo, and L. M. K. Vandersypen, “Gate-induced insulating state in bilayer graphene devices,” *Nat Mater*, vol. 7, pp. 151–157, Feb 2008.
- [20] K. D. AGor’kov L.P., Larkin A.I., “Particle conductivity in a two-dimensional random potential,” *JETP Lett*, vol. 30, p. 228, 1979.
- [21] E. Abrahams, P. W. Anderson, D. C. Licciardello, and T. V. Ramakrishnan, “Scaling theory of localization: Absence of quantum diffusion in two dimensions,” *Phys. Rev. Lett.*, vol. 42, pp. 673–676, Mar 1979.
- [22] S. Datta, *Electronic Transport in Mesoscopic Systems*. 1985.
- [23] G.-L. I. B. K. G. S. W. Z. T. Dittrich, P. Hanggi, *Quantum Transport and Dissipation*. Wiley-VCH, 1998.
- [24] F. V. Tikhonenko, A. A. Kozikov, A. K. Savchenko, and R. V. Gorbachev, “Transition between electron localization and antilocalization in graphene,” *Phys. Rev. Lett.*, vol. 103, p. 226801, Nov 2009.
- [25] X. Du, I. Skachko, A. Barker, and E. Y. Andrei, “Approaching ballistic transport in suspended graphene,” *Nat Nano*, vol. 3, pp. 491–495, Aug 2008.
- [26] P. R. Wallace, “The band theory of graphite,” *Phys. Rev.*, vol. 71, pp. 622–634, May 1947.
- [27] M. Monteverde, C. Ojeda-Aristizabal, R. Weil, K. Bennaceur, M. Ferrier, S. Guéron, C. Glattli, H. Bouchiat, J. N. Fuchs, and D. L. Maslov, “Transport and elastic scattering times as probes of the nature of impurity scattering in single-layer and bilayer graphene,” *Phys. Rev. Lett.*, vol. 104, p. 126801, Mar 2010.

BIBLIOGRAPHY

- [28] D. S. Novikov, “Elastic scattering theory and transport in graphene,” *Phys. Rev. B*, vol. 76, p. 245435, Dec 2007.
- [29] K. Nomura and A. H. MacDonald, “Quantum transport of massless dirac fermions,” *Phys. Rev. Lett.*, vol. 98, p. 076602, Feb 2007.
- [30] J. Chen, “-H. et al. Charged impurity scattering in graphene,” *Nature Phys.*, vol. 4, pp. 377–381, 2008.
- [31] C. Jang, S. Adam, J.-H. Chen, E. D. Williams, S. Das Sarma, and M. S. Fuhrer, “Tuning the effective fine structure constant in graphene: Opposing effects of dielectric screening on short- and long-range potential scattering,” *Phys. Rev. Lett.*, vol. 101, p. 146805, Oct 2008.
- [32] L. A. Ponomarenko, R. Yang, T. M. Mohiuddin, M. I. Katsnelson, K. S. Novoselov, S. V. Morozov, A. A. Zhukov, F. Schedin, E. W. Hill, and A. K. Geim, “Effect of a high- κ environment on charge carrier mobility in graphene,” *Phys. Rev. Lett.*, vol. 102, p. 206603, May 2009.
- [33] F. Schedin, A. K. Geim, S. V. Morozov, E. W. Hill, P. Blake, M. I. Katsnelson, and K. S. Novoselov, “Detection of individual gas molecules adsorbed on graphene,” *Nat Mater*, vol. 6, pp. 652–655, Sep 2007.
- [34] K. Xu, P. Cao, and J. R. Heath, “Graphene Visualizes the First Water Adlayers on Mica at Ambient Conditions,” *Science*, vol. 329, no. 5996, pp. 1188–1191, 2010.
- [35] J.-H. Chen, C. Jang, S. Adam, M. S. Fuhrer, E. D. Williams, and M. Ishigami, “Charged-impurity scattering in graphene,” *Nat Phys*, vol. 4, pp. 377–381, May 2008.
- [36] J. Martin, N. Akerman, G. Ulbricht, T. Lohmann, J. H. Smet, K. von Klitzing, and A. Yacoby, “Observation of electron-hole puddles in graphene using a scanning single-electron transistor,” *Nat Phys*, vol. 4, pp. 144–148, Feb 2008.
- [37] K. Bolotin, K. Sikes, Z. Jiang, M. Klima, G. Fudenberg, J. Hone, P. Kim, and H. Stormer, “Ultrahigh electron mobility in suspended graphene,” *Solid State Communications*, vol. 146, no. 9-10, pp. 351 – 355, 2008.
- [38] C. R. Dean, A. F. Young, I. Meric, C. Lee, L. Wang, S. Sorgenfrei, K. Watanabe, T. Taniguchi, P. Kim, K. L. Shepard, and J. Hone, “Boron nitride substrates for high-quality graphene electronics,” *ArXiv e-prints*, May 2010.
- [39] K. von Klitzing, “The quantized hall effect,” *Nobel lectures*, 1985.
- [40] K. v. Klitzing, G. Dorda, and M. Pepper, “New method for high-accuracy determination of the fine-structure constant based on quantized hall resistance,” *Phys. Rev. Lett.*, vol. 45, pp. 494–497, Aug 1980.

BIBLIOGRAPHY

- [41] T. Ando and Y. Uemura, “Theory of oscillatory g factor in an mos inversion layer under strong magnetic fields,” *Journal of the Physical Society of Japan*, vol. 37, no. 4, pp. 1044–1052, 1974.
- [42] Z. F. Ezawa, *Quantum Hall Effects*. World Scientific, 2007.
- [43] M. O. Goerbig, “Electronic Properties of Graphene in a Strong Magnetic Field,” *ArXiv e-prints*, Apr. 2010.
- [44] K. S. Novoselov, Z. Jiang, Y. Zhang, S. V. Morozov, H. L. Stormer, U. Zeitler, J. C. Maan, G. S. Boebinger, P. Kim, and A. K. Geim, “Room-temperature quantum hall effect in graphene,” *Science*, vol. 315, p. 1379, 2007.
- [45] Z. Jiang, E. A. Henriksen, L. C. Tung, Y.-J. Wang, M. E. Schwartz, M. Y. Han, P. Kim, and H. L. Stormer, “Infrared spectroscopy of landau levels of graphene,” *Phys. Rev. Lett.*, vol. 98, p. 197403, May 2007.
- [46] L. Shubnikov and W. D. Haas *Proceedings of the Royal Netherlands Society of Arts and Science*, vol. 33, p. 130 and 163, 1930.
- [47] T. Ando, “Theory of quantum transport in a two-dimensional electron system under magnetic fields. iv. oscillatory conductivity,” *Journal of the Physical Society of Japan*, vol. 37, no. 5, pp. 1233–1237, 1974.
- [48] A. Isihara and L. Smrcka, “Density and magnetic field dependences of the conductivity of two-dimensional electron systems,” *Journal of Physics C: Solid State Physics*, vol. 19, no. 34, p. 6777, 1986.
- [49] M. Büttiker, “Four-terminal phase-coherent conductance,” *Phys. Rev. Lett.*, vol. 57, pp. 1761–1764, Oct 1986.
- [50] K. S. Novoselov, A. K. Geim, S. V. Morozov, D. Jiang, M. I. Katsnelson, I. V. Grigorieva, S. V. Dubonos, and A. A. Firsov, “Two-dimensional gas of massless dirac fermions in graphene,” *Nature*, vol. 438, pp. 197–200, Nov 2005.
- [51] Y. Zhang, Z. Jiang, J. P. Small, M. S. Purewal, Y.-W. Tan, M. Fazlollahi, J. D. Chudow, J. A. Jaszczak, H. L. Stormer, and P. Kim, “Landau-level splitting in graphene in high magnetic fields,” *Phys. Rev. Lett.*, vol. 96, p. 136806, Apr 2006.
- [52] K. I. Bolotin, F. Ghahari, M. D. Shulman, H. L. Stormer, and P. Kim, “Observation of the fractional quantum Hall effect in graphene,” *Nature*, vol. 462, pp. 196–9, Nov. 2009.
- [53] X. Du, I. Skachko, F. Duerr, A. Luican, and E. Y. Andrei, “Fractional quantum Hall effect and insulating phase of Dirac electrons in graphene,” *Nature*, vol. 462, no. November, pp. 10–13, 2009.

BIBLIOGRAPHY

- [54] F. Ghahari, Y. Zhao, P. Cadden-Zimansky, K. Bolotin, and P. Kim, “Measurement of the $\nu = 1/3$ fractional quantum Hall energy gap in suspended graphene,” *ArXiv e-prints*, Oct. 2010.
- [55] C. R. Dean, A. F. Young, P. Cadden-Zimansky, L. Wang, H. Ren, K. Watanabe, T. Taniguchi, P. Kim, J. Hone, and K. L. Shepard, “Multicomponent fractional quantum Hall effect in graphene,” *ArXiv e-prints*, Oct. 2010.
- [56] D. A. Abanin, K. S. Novoselov, U. Zeitler, P. A. Lee, A. K. Geim, and L. S. Levitov, “Dissipative quantum hall effect in graphene near the dirac point,” *Phys. Rev. Lett.*, vol. 98, p. 196806, May 2007.
- [57] J. G. Checkelsky, L. Li, and N. P. Ong, “Zero-energy state in graphene in a high magnetic field,” *Phys. Rev. Lett.*, vol. 100, p. 206801, May 2008.
- [58] L. Zhang, Y. Zhang, M. Khodas, T. Valla, and I. A. Zaliznyak, “Metal to insulator transition on the $n = 0$ landau level in graphene,” *Phys. Rev. Lett.*, vol. 105, p. 046804, Jul 2010.
- [59] S. M. D. J. K. K. S. D. I. G. A. F. K.S Novoselov, A.K. Geim, “Two dimensional gas of massless dirac fermions in graphene,” *nature*, vol. 438, Novembre 2005.
- [60] Z. Jiang, Y. Zhang, H. L. Stormer, and P. Kim, “Quantum hall states near the charge-neutral dirac point in graphene,” *Phys. Rev. Lett.*, vol. 99, p. 106802, Sep 2007.
- [61] A. J. M. Giesbers, U. Zeitler, M. I. Katsnelson, L. A. Ponomarenko, T. M. Mohiuddin, and J. C. Maan, “Quantum-hall activation gaps in graphene,” *Phys. Rev. Lett.*, vol. 99, p. 206803, Nov 2007.
- [62] A. J. M. Giesbers, L. A. Ponomarenko, K. S. Novoselov, A. K. Geim, M. I. Katsnelson, J. C. Maan, and U. Zeitler, “Gap opening in the zeroth landau level of graphene,” *Phys. Rev. B*, vol. 80, p. 201403, Nov 2009.
- [63] K. S. Novoselov, E. McCann, S. V. Morozov, V. I. Fal’ko, M. I. Katsnelson, U. Zeitler, D. Jiang, F. Schedin, and A. K. Geim, “Unconventional quantum hall effect and berry’s phase of $2[\pi]$ in bilayer graphene,” *Nat Phys*, vol. 2, pp. 177–180, Mar 2006.
- [64] O. Corbino *Z. Phys.*, vol. 12, p. 561, 1911.
- [65] P. F. Fontein, J. M. Lagemaat, J. Wolter, and J. P. Andre, “Magnetic field modulation—a method for measuring the hall conductance with a corbino disc,” *Semiconductor Science and Technology*, vol. 3, no. 9, p. 915, 1988.
- [66] B. Jeanneret, B. D. Hall, H.-J. Bühlmann, R. Houdré, M. Ilegems, B. Jeckelmann, and U. Feller, “Observation of the integer quantum hall effect by magnetic coupling to a corbino ring,” *Phys. Rev. B*, vol. 51, pp. 9752–9756, Apr 1995.

BIBLIOGRAPHY

- [67] K. Hashimoto, C. Sohrmann, J. Wiebe, T. Inaoka, F. Meier, Y. Hirayama, R. A. Römer, R. Wiesendanger, and M. Morgenstern, “Quantum hall transition in real space: From localized to extended states,” *Phys. Rev. Lett.*, vol. 101, p. 256802, Dec 2008.
- [68] J. Martin, N. Akerman, G. Ulbricht, T. Lohmann, K. von Klitzing, J. H. Smet, and a. Yacoby, “The nature of localization in graphene under quantum Hall conditions,” *Nature Physics*, vol. 5, pp. 669–674, July 2009.
- [69] S. A. Trugman, “Localization, percolation, and the quantum hall effect,” *Phys. Rev. B*, vol. 27, pp. 7539–7546, Jun 1983.
- [70] B. Huckestein and B. Kramer, “One-parameter scaling in the lowest landau band: Precise determination of the critical behavior of the localization length,” *Phys. Rev. Lett.*, vol. 64, pp. 1437–1440, Mar 1990.
- [71] J. T. Chalker and P. D. Coddington, “Percolation, quantum tunnelling and the integer hall effect,” *Journal of Physics C: Solid State Physics*, vol. 21, no. 14, p. 2665, 1988.
- [72] G.V.Mil’nikov and I. Sokolov *Pis’ma Zh. Eksp. Teor. Fiz*, vol. 48, no. 494, 1988.
- [73] M. Furlan, “Electronic transport and the localization length in the quantum hall effect,” *Phys. Rev. B*, vol. 57, pp. 14818–14828, Jun 1998.
- [74] F. Hohls, U. Zeitler, and R. J. Haug, “Hopping conductivity in the quantum hall effect: Revival of universal scaling,” *Phys. Rev. Lett.*, vol. 88, p. 036802, Jan 2002.
- [75] A. J. M. Giesbers, U. Zeitler, L. A. Ponomarenko, R. Yang, K. S. Novoselov, A. K. Geim, and J. C. Maan, “Scaling of the quantum hall plateau-plateau transition in graphene,” *Phys. Rev. B*, vol. 80, p. 241411, Dec 2009.
- [76] T. Haavasoja, H. Stormer, D. Bishop, V. Narayanamurti, A. Gossard, and W. Wiegmann, “Magnetization measurements on a two-dimensional electron system,” *Surface Science*, vol. 142, no. 1-3, pp. 294 – 297, 1984.
- [77] H. P. Wei, L. W. Engel, and D. C. Tsui, “Current scaling in the integer quantum hall effect,” *Phys. Rev. B*, vol. 50, pp. 14609–14612, Nov 1994.
- [78] H. Eyring, “The activated complex in chemical reactions,” *The Journal of Chemical Physics*, vol. 3, no. 2, pp. 107–115, 1935.
- [79] D. G. Polyakov and B. I. Shklovskii, “Activated conductivity in the quantum hall effect,” *Phys. Rev. Lett.*, vol. 73, pp. 1150–1153, Aug 1994.
- [80] S. S. Mandal and V. Ravishankar, “Activated resistivities in the integer quantum hall effect,” *Phys. Rev. B*, vol. 55, pp. 15748–15756, Jun 1997.

BIBLIOGRAPHY

- [81] M. Fogler, D. Polyakov, and B. Shklovskii, “Activated conductivity in the quantum hall effect,” *Surface Science*, vol. 361-362, pp. 255 – 260, 1996. Proceedings of the Eleventh International Conference on the Electronic Properties of Two-Dimensional Systems.
- [82] D. G. Polyakov and B. I. Shklovskii, “Universal prefactor of activated conductivity in the quantum hall effect,” *Phys. Rev. Lett.*, vol. 74, pp. 150–153, Jan 1995.
- [83] H. P. Wei, A. M. Chang, D. C. Tsui, and M. Razeghi, “Temperature dependence of the quantized hall effect,” *Phys. Rev. B*, vol. 32, pp. 7016–7019, Nov 1985.
- [84] S. Dorozhkin, M. Dorokhova, R. Haug, K. von Klitzing, and K. Ploog, “Thermally activated dissipative conductivity in the fractional quantum hall effect regime,” *JETP Letters*, vol. 63, pp. 76–82, 1996. 10.1134/1.566966.
- [85] M. Furlan, “Activated conductivities and nonuniversal behaviour in large high mobility hall bars,” *Physica B: Condensed Matter*, vol. 249-251, pp. 123 – 127, 1998.
- [86] A. E. B.I. Shklovskii, *Electronic Properties of Doped Semiconductors*, vol. 45. Springer, 1984.
- [87] A. L. Efros and B. I. Shklovskii, “Coulomb gap and low temperature conductivity of disordered systems,” *Journal of Physics C: Solid State Physics*, vol. 8, no. 4, p. L49, 1975.
- [88] H. Liu, A. Pourret, and P. Guyot-Sionnest, “Mott and efros-shklovskii variable range hopping in cdse quantum dots films,” *ACS Nano*, vol. 4, no. 9, p. 5211, 2010.
- [89] X. L. Hu, F. W. V. Keuls, Y. Carmi, H. W. Jiang, and A. J. Dahm, “Screening of the coulomb gap,” *Solid State Communications*, vol. 96, no. 2, pp. 65 – 68, 1995.
- [90] D. G. Polyakov and B. I. Shklovskii, “Variable range hopping as the mechanism of the conductivity peak broadening in the quantum hall regime,” *Phys. Rev. Lett.*, vol. 70, pp. 3796–3799, Jun 1993.
- [91] V.L.Nguen, “Two-dimensional hopping conduction in a magnetic field,” *Sov. Phys. Semicond.*, vol. 18, no. 2, p. 207, 1984.
- [92] A. Briggs, Y. Guldner, J. P. Vieren, M. Voos, J. P. Hirtz, and M. Razeghi, “Low-temperature investigations of the quantum hall effect in $in_xga_{1-x}as - inp$ heterojunctions,” *Phys. Rev. B*, vol. 27, pp. 6549–6552, May 1983.

BIBLIOGRAPHY

- [93] G. Ebert, K. von Klitzing, C. Probst, E. Schuberth, K. Ploog, and G. Weimann, "Hopping conduction in the Landau level tails in GaAs-AlGa_{1-x}As heterostructures at low temperatures," *Solid State Communications*, vol. 45, no. 7, pp. 625 – 628, 1983.
- [94] S. Koch, R. J. Haug, K. von Klitzing, and K. Ploog, "Variable range hopping transport in the tails of the conductivity peaks between quantum Hall plateaus," *Semiconductor Science and Technology*, vol. 10, no. 2, p. 209, 1995.
- [95] M. Shlimak, Issai, and Pepper, "Two-dimensional variable-range hopping conductivity: Influence of the electron-electron interaction," *Philosophical Magazine Part B*, vol. 81, no. 9, p. 1093.
- [96] I. Shlimak, K. J. Friedland, and S. D. Baranovskii, "Hopping conductivity in gated δ -doped GaAs: universality of prefactor," *Solid State Communications*, vol. 112, no. 1, pp. 21 – 24, 1999.
- [97] A. V. N. A. I. N. A. A. B. M. N. T. A. I. Yakimov, A. V. Dvurechenskii, "Two-dimensional phononless vrh conduction in arrays of Ge/Si quantum dots," *physica status solidi (c)*, vol. 1, pp. 51 – 54, 2004.
- [98] I. Aleiner and B. Shklovskii, "Effect of screening of the Coulomb interaction on the conductivity in the quantum Hall regime.," *Physical review. B, Condensed matter*, vol. 49, pp. 13721–13727, mai 1994.
- [99] B. Jeckelmann and B. Jeanneret, "The quantum Hall effect as an electrical resistance standard," *Reports on Progress in Physics*, vol. 64, no. 12, p. 1603, 2001.
- [100] G. Nachtwei, "Breakdown of the quantum Hall effect," *Physica E: Low-dimensional Systems and Nanostructures*, vol. 4, no. 2, pp. 79 – 101, 1999.
- [101] G. Eber, K. von Klitzing, K. Ploog, and G. Weinmann, "Two-dimensional magneto-quantum transport on GaAs/Ga_{1-x}Al_xAs heterostructures under non-ohmic conditions," *Journal of Physics C: Solid State Physics*, vol. 16, no. 28, p. 5441, 1983.
- [102] N. Q. Balaban, U. Meirav, and H. Shtrikman, "Crossover between different regimes of current distribution in the quantum Hall effect," *Phys. Rev. B*, vol. 52, pp. R5503–R5506, Aug 1995.
- [103] S. Komiyama and Y. Kawaguchi, "Heat instability of quantum Hall conductors," *Phys. Rev. B*, vol. 61, pp. 2014–2027, Jan 2000.
- [104] Y. Kawano and S. Komiyama, "Spatial distribution of nonequilibrium electrons in quantum Hall devices: Imaging via cyclotron emission," *Phys. Rev. B*, vol. 68, p. 085328, Aug 2003.

BIBLIOGRAPHY

- [105] Y. Kawano and S. Komiyama, “Breakdown of the quantized hall effect in the vicinity of current contacts,” *Phys. Rev. B*, vol. 61, pp. 2931–2938, Jan 2000.
- [106] Y. Kawaguchi, F. Hayashi, S. Komiyama, T. Osada, Y. Shiraki, and R. Itoh, “Disappearance of the breakdown of quantum hall effects in short devices,” *Japanese Journal of Applied Physics*, vol. 34, no. Part 1, No. 8B, pp. 4309–4312, 1995.
- [107] G. Ebert, K. von Klitzing, and G. Weimann, “Hall potential distribution in quantum hall experiments,” *Journal of Physics C: Solid State Physics*, vol. 18, no. 10, p. L257, 1985.
- [108] H. Z. Zheng, D. C. Tsui, and A. M. Chang, “Distribution of the quantized hall potential in $gaas - al_xga_{1-x}$ as heterostructures,” *Phys. Rev. B*, vol. 32, pp. 5506–5509, Oct 1985.
- [109] E. K. Sichel, M. L. Knowles, and H. H. Sample, “Equipotential distribution in the quantum hall effect in $gaas$ $ga_{1-x}al_x$ heterostructures,” *Journal of Physics C: Solid State Physics*, vol. 19, no. 28, p. 5695, 1986.
- [110] P. F. Fontein, J. A. Kleinen, P. Hendriks, F. A. P. Blom, J. H. Wolter, H. G. M. Lochs, F. A. J. M. Driessen, L. J. Giling, and C. W. J. Beenakker, “Spatial potential distribution in $gaas/ga_{1-x}al_x$ heterostructures under quantum hall conditions studied with the linear electro-optic effect,” *Phys. Rev. B*, vol. 43, pp. 12090–12093, May 1991.
- [111] M. Büttiker, “Absence of backscattering in the quantum hall effect in multiprobe conductors,” *Phys. Rev. B*, vol. 38, pp. 9375–9389, Nov 1988.
- [112] D. J. Thouless, “Edge voltages and distributed currents in the quantum hall effect,” *Phys. Rev. Lett.*, vol. 71, pp. 1879–1882, Sep 1993.
- [113] A. H. MacDonald, T. M. Rice, and W. F. Brinkman, “Hall voltage and current distributions in an ideal two-dimensional system,” *Phys. Rev. B*, vol. 28, pp. 3648–3650, Sep 1983.
- [114] A. M. M. Pruisken, “Universal singularities in the integral quantum hall effect,” *Phys. Rev. Lett.*, vol. 61, pp. 1297–1300, Sep 1988.
- [115] R. T. F. van Schaijk, A. de Visser, S. M. Olsthoorn, H. P. Wei, and A. M. M. Pruisken, “Probing the plateau-insulator quantum phase transition in the quantum hall regime,” *Phys. Rev. Lett.*, vol. 84, pp. 1567–1570, Feb 2000.
- [116] H. P. Wei, D. C. Tsui, and A. M. M. Pruisken, “Localization and scaling in the quantum hall regime,” *Phys. Rev. B*, vol. 33, pp. 1488–1491, Jan 1986.

BIBLIOGRAPHY

- [117] H. P. Wei, D. C. Tsui, M. A. Paalanen, and A. M. M. Pruisken, “Experiments on delocalization and universality in the integral quantum hall effect,” *Phys. Rev. Lett.*, vol. 61, pp. 1294–1296, Sep 1988.
- [118] S. Koch, R. J. Haug, K. v. Klitzing, and K. Ploog, “Experimental studies of the localization transition in the quantum hall regime,” *Phys. Rev. B*, vol. 46, pp. 1596–1602, Jul 1992.
- [119] S. W. Hwang, H. P. Wei, L. W. Engel, D. C. Tsui, and A. M. M. Pruisken, “Scaling in spin-degenerate landau levels in the integer quantum hall effect,” *Phys. Rev. B*, vol. 48, pp. 11416–11419, Oct 1993.
- [120] W. Li, G. A. Csáthy, D. C. Tsui, L. N. Pfeiffer, and K. W. West, “Scaling and universality of integer quantum hall plateau-to-plateau transitions,” *Phys. Rev. Lett.*, vol. 94, p. 206807, May 2005.
- [121] H. P. Wei, S. Y. Lin, D. C. Tsui, and A. M. M. Pruisken, “Effect of long-range potential fluctuations on scaling in the integer quantum hall effect,” *Phys. Rev. B*, vol. 45, pp. 3926–3928, Feb 1992.
- [122] B. Huckestein, “Scaling theory of the integer quantum hall effect,” *Rev. Mod. Phys.*, vol. 67, pp. 357–396, Apr 1995.
- [123] “The international system of units (si) 8th,” *BIPM*, 2006.
- [124] T. Quinn *Metrologia*, vol. 26, no. 69, 1989.
- [125] K. V. Emtsev, A. Bostwick, K. Horn, J. Jobst, G. L. Kellogg, L. Ley, J. L. McChesney, T. Ohta, S. A. Reshanov, J. Rohrl, E. Rotenberg, A. K. Schmid, D. Waldmann, H. B. Weber, and T. Seyller, “Towards wafer-size graphene layers by atmospheric pressure graphitization of silicon carbide,” *Nat Mater*, vol. 8, pp. 203–207, Mar 2009.
- [126] T. Shen, J. J. Gu, M. Xu, Y. Q. Wu, M. L. Bolen, M. A. Capano, L. W. Engel, and P. D. Ye, “Observation of quantum-hall effect in gated epitaxial graphene grown on sic (0001),” *Applied Physics Letters*, vol. 95, no. 17, p. 172105, 2009.
- [127] P. W. Sutter, J.-I. Flege, and E. A. Sutter, “Epitaxial graphene on ruthenium,” *Nat Mater*, vol. 7, pp. 406–411, May 2008.
- [128] Y. Hernandez, V. Nicolosi, M. Lotya, F. M. Blighe, Z. Sun, S. De, M. T., B. Holland, M. Byrne, Y. K. Gun’Ko, J. J. Boland, P. Niraaj, G. Duesberg, S. Krishnamurthy, R. Goodhue, J. Hutchison, V. Scardaci, A. C. Ferrari, and J. N. Coleman, “High-yield production of graphene by liquid-phase exfoliation of graphite,” *Nat Nano*, vol. 3, pp. 563–568, Sep 2008.
- [129] K. S. Kim, Y. Zhao, H. Jang, S. Y. Lee, J. M. Kim, K. S. Kim, J.-H. Ahn, P. Kim, J.-Y. Choi, and B. H. Hong, “Large-scale pattern growth of graphene films for stretchable transparent electrodes.,” *Nature*, vol. 457, pp. 706–10, Feb. 2009.

BIBLIOGRAPHY

- [130] S. Bae, H. Kim, Y. Lee, X. Xu, J.-S. Park, Y. Zheng, J. Balakrishnan, T. Lei, H. Ri Kim, Y. I. Song, Y.-J. Kim, K. S. Kim, B. Özyilmaz, J.-H. Ahn, B. H. Hong, and S. Iijima, “Roll-to-roll production of 30-inch graphene films for transparent electrodes,” *Nature Nanotechnology*, pp. 1–6, June 2010.
- [131] P. Blake, E. W. Hill, A. H. C. Neto, K. S. Novoselov, D. Jiang, R. Yang, T. J. Booth, and A. K. Geim, “Making graphene visible,” *Applied Physics Letters*, vol. 91, no. 6, p. 063124, 2007.
- [132] W. Bao, F. Miao, Z. Chen, H. Zhang, W. Jang, C. Dames, and C. N. Lau, “Controlled ripple texturing of suspended graphene and ultrathin graphite membranes,” *Nature nanotechnology*, vol. 4, pp. 562–6, Sept. 2009.
- [133] L. Wirtz and A. Rubio, “The phonon dispersion of graphite revisited,” *Solid State Communications*, vol. 131, no. 3-4, pp. 141 – 152, 2004.
- [134] P. Nemes-Incze, Z. Osvath, K. Kamaras, and L. Biro, “Anomalies in thickness measurements of graphene and few layer graphite crystals by tapping mode atomic force microscopy,” *Carbon*, vol. 46, no. 11, pp. 1435 – 1442, 2008.
- [135] A. C. Ferrari, J. C. Meyer, V. Scardaci, C. Casiraghi, M. Lazzeri, F. Mauri, S. Piscanec, D. Jiang, K. S. Novoselov, S. Roth, and A. K. Geim, “Raman spectrum of graphene and graphene layers,” *Phys. Rev. Lett.*, vol. 97, p. 187401, Oct 2006.
- [136] Y.-W. Tan, Y. Zhang, K. Bolotin, Y. Zhao, S. Adam, E. H. Hwang, S. Das Sarma, H. L. Stormer, and P. Kim, “Measurement of scattering rate and minimum conductivity in graphene,” *Phys. Rev. Lett.*, vol. 99, p. 246803, Dec 2007.
- [137] J.-H. Chen, C. Jang, S. Adam, M. S. Fuhrer, E. D. Williams, and M. Ishigami, “Charged-impurity scattering in graphene,” *Nat Phys*, vol. 4, pp. 377–381, May 2008.
- [138] J. Moser, A. Barreiro, and A. Bachtold, “Current-induced cleaning of graphene,” *Applied Physics Letters*, vol. 91, no. 16, p. 163513, 2007.
- [139] J. Moser and A. Bachtold, “Fabrication of large addition energy quantum dots in graphene,” *Applied Physics Letters*, vol. 95, no. 17, p. 173506, 2009.
- [140] M. Ishigami, J. H. Chen, W. G. Cullen, M. S. Fuhrer, and E. D. Williams, “Atomic structure of graphene on sio₂,” *Nano Letters*, vol. 7, pp. 1643–1648, May 2007. doi: 10.1021/nl070613a.
- [141] P. G. Silvestrov and K. B. Efetov, “Charge accumulation at the boundaries of a graphene strip induced by a gate voltage: Electrostatic approach,” *Phys. Rev. B*, vol. 77, p. 155436, Apr 2008.

BIBLIOGRAPHY

- [142] D. Horsell, A. Savchenko, F. Tikhonenko, K. Kechedzhi, I. Lerner, and V. Fal'ko, "Mesoscopic conductance fluctuations in graphene," *Solid State Communications*, vol. 149, no. 27-28, pp. 1041 – 1045, 2009. Recent Progress in Graphene Studies.
- [143] C. Ojeda-Aristizabal, M. Monteverde, R. Weil, M. Ferrier, S. Guéron, and H. Bouchiat, "Conductance fluctuations and field asymmetry of rectification in graphene," *Phys. Rev. Lett.*, vol. 104, p. 186802, May 2010.
- [144] J. Berezovsky, M. F. Borunda, E. J. Heller, and R. M. Westervelt, "Imaging coherent transport in graphene (part i): mapping universal conductance fluctuations," *Nanotechnology*, vol. 21, no. 27, p. 274013, 2010.
- [145] B. Huard, N. Stander, J. A. Sulpizio, and D. Goldhaber-Gordon, "Evidence of the role of contacts on the observed electron-hole asymmetry in graphene," *Phys. Rev. B*, vol. 78, p. 121402, Sep 2008.
- [146] L. J. H., K. Balasubramanian, R. T. Weitz, M. Burghard, and K. Kern, "Contact and edge effects in graphene devices," *Nat Nano*, vol. 3, pp. 486–490, Aug 2008.
- [147] E. H. Hwang and S. Das Sarma, "Single-particle relaxation time versus transport scattering time in a two-dimensional graphene layer," *Phys. Rev. B*, vol. 77, p. 195412, May 2008.
- [148] Y. Zhang, Z. Jiang, J. P. Small, M. S. Purewal, Y.-W. Tan, M. Fazlollahi, J. D. Chudow, J. A. Jaszczak, H. L. Stormer, and P. Kim, "Landau-level splitting in graphene in high magnetic fields," *Phys. Rev. Lett.*, vol. 96, p. 136806, Apr 2006.
- [149] B. A.L.Efros, Nguyen Van Lien, "Variable range hopping in doped crystalline semiconductors," *Solid State Communications*, vol. 32, no. 10, pp. 851–854, 1979.